

Molecular basis for ribosomal protein protection from cellular degradation

Thesis by
Ferdinand Michael Huber

In Partial Fulfillment of the Requirements for the degree of
Doctor of Philosophy

The logo for the California Institute of Technology (Caltech), featuring the word "Caltech" in a bold, orange, sans-serif font.

CALIFORNIA INSTITUTE OF TECHNOLOGY
Pasadena, California

2019
(Defended May 21st, 2019)

© 2019

Ferdinand Michael Huber

ACKNOWLEDGEMENTS

Over the past years many people had a significant impact on the adventure of this PhD thesis and I apologize to those I forgot to mention here.

Most importantly, I would like to thank my entire family and in particular my parents for their unconditional, continuous, and steady support and love. They set the basis for my education and scientific mindset by encouraging me to always follow my passion and curiosity. Without their generous help I would not have had the comfort of focusing primarily on my education.

Second, I was incredibly lucky with the very dedicated and patient mentors I had at the various stages of this journey, starting with Stefan Allmann, who taught me the basics of experimental biochemistry during my Bachelor's thesis, and followed by Fuensanta Martinez, who taught me the value of time and inspired my interest in structural biology. During my Master's thesis and beyond I had the pleasure to work with and learn from Andrew Davenport. Without his mentorship things would not have been the same: from him I learned meticulous experimental design, quick and thorough execution, and careful analysis.

I very much would like to thank my PhD advisor, André Hoelz, who provided me with the opportunity to work in his group and always pushed me to work on myself to become a better scientist. I am very grateful for his trust and the freedom he provided me to work on a project outside the general scope of the group. The past seven years have been incredibly intense and certainly challenging at times but we always shared the passion to make new discoveries and ultimately strive to understand how a cell operates.

Undoubtedly, my collaborators had a great impact on me and I would like to thank all of them. Specifically, Philipp Stelter and Ed Hurt for a fruitful collaboration on the ribosome assembly project. Moreover, I am grateful to Min-Kyung Sung and Raymond Deshaies for reaching out and starting a very productive and enjoyable collaboration. The discussions I had with Ray were one of the most inspiring times at Caltech.

Scientific success can only occur with a team of great scientists. André has assembled a wonderful group of scientists who I had the pleasure to work with. Especially in my first years Andrew Davenport, Chris Bley, Dan Lin, Tobias Stuwe, Ana Correia, and

Karsten Thierbach taught me so much about science and life in general. They made this adventure fun and worthwhile and I (will) miss working with them. I would like to thank Stefan Petrovic for always being critical, having a wonderful sense of humor, and for the countless discussions we had to make the world a better place. Moreover, I would like to thank Taylor Stevens, Sarah Speed, and Jonas Weinrich as part of “Team Pom”, and Si Nie, Thibaud Perriches, George Mobbs, Dipanjan Samanta, Claudia Jette, Sho Harvey, Emily Rundlet, Aaron Tang, Bonnie Brown, Sarah Cai, Anna Gres, Xiaoyu Liu, David Akopian, and Dan Mayo for being wonderful colleagues and friends.

Furthermore, I had the pleasure to mentor several incredible undergraduate students. I want to particularly thank Ellen Yu, who worked with me for more than 3 years and shared the same passion for research, science, and knowledge in general. It was a fantastic time and I am very proud that I could be part of her path to becoming a scientist.

Last but not least, I would like to thank my friends in the U.S. Chengcheng Fan, Belinda Wenke, Andrew Buller, Emily Blythe, Andy Zhou, Griffin Chure, and Kyu-Hyun Lee, who made this a fun experience. I really enjoyed our game nights, drinks at Magnolia House, discussing the world over a cup of coffee, and just having a good time!

ABSTRACT

Ribosomes are large macromolecular machineries composed of both protein and RNA constituents with a species-dependent molecular mass of at least ~3.3 MDa for the fully assembled eukaryotic 80S ribosome. Their catalytic activity is dependent on ribosomal RNA; therefore, ribosomes are *bona fide* ribozymes, and as such they mediate the final step of gene expression from DNA to RNA to protein by peptide bond formation between amino acids. Importantly, spatial separation of ribosome function and biogenesis into distinct cellular compartments allows for intricate regulatory mechanisms and rigorous quality control. Ribosome biogenesis occurs predominantly in the nucleolus and nucleus of the cell with final cytoplasmic maturation and quality control steps. Briefly, nucleolar ribosomal RNA together with ~200 trans-acting assembly factors co-transcriptionally forms the 40S and 60S pre-ribosomal subunits into which ~80 ribosomal proteins are incorporated in a hierarchical fashion.

Recent studies, including this thesis, have identified a novel class of dedicated ribosome assembly chaperones, in addition to the ~200 trans-acting ribosome assembly factors, which facilitate ribosomal protein shuttling. Ribosomal proteins are generated in the cytoplasm, and with only few exceptions they all have to enter the nucleus for incorporation into the pre-ribosomal subunits. Assembly chaperones can bind and protect unassembled ribosomal proteins either co-translationally or following nuclear import and shuttle them in a timely fashion to their destination sites at the maturing pre-ribosomal subunits. The first chapter of this thesis describes the identification and characterization of a dedicated assembly chaperone for the large ribosomal subunit protein RpL4, termed Acl4. Interestingly, Acl4 and likely also other dedicated assembly chaperones not only interact with ribosomal proteins to avoid aggregation and to shield them from unfavorable interactions, but also protect their client proteins from cellular degradation by the ubiquitin-proteasome machinery.

Ribosomes are built by assembling equimolar amounts of ribosomal proteins, which generates a challenge for the cell to ensure stoichiometric quantities of ribosomal proteins. Recent studies have demonstrated that stoichiometric levels of ribosomal proteins are established by cellular degradation of excess protein via ubiquitination of unassembled components. The second chapter of this thesis describes a conserved degradation pathway,

which is dependent on the E3 ubiquitin ligase Tom1 to mark unprotected and unassembled ribosomal proteins and target them for degradation. Moreover, it is demonstrated in the third chapter for the first time how an assembly chaperone protects its client ribosomal protein from ubiquitination and proteasome-mediated degradation. High resolution structures of the Acl4•RpL4 complex as well as RpL4 in complex with the nuclear transport factor Kap104 visualize the molecular interactions of those proteins and uncover the molecular mechanism of protecting conserved Tom1-target sites within RpL4. Together, the reported results identify and characterize both a novel degradation pathway as well as a protection mechanism for ribosomal proteins and advance the understanding of the intricate regulation of ribosome biogenesis.

PUBLISHED CONTENT AND CONTRIBUTIONS

Philipp Stelzer[#], **Ferdinand M. Huber**[#], Ruth Kunze, Dirk Flemming, André Hoelz^{*}, Ed Hurt^{*} (2015). Coordinated ribosomal L4 protein assembly into the pre-ribosome is regulated by its eukaryote-specific extension, *Mol. Cell*, 58, 854-862.

DOI: 10.1016/j.molcel.2015.03.029

Contributions: Cloning; protein expression, purification, and crystallization; structure determination and mutational analysis; protein-protein interaction analysis.

Min-Kyung Sung, Tanya R. Porras-Yakushi, Justin M. Reitsma, **Ferdinand M. Huber**, Michael J. Sweredoski, André Hoelz, Sonja Hess, Raymond J. Deshaies^{*} (2016). A conserved quality-control pathway that mediates degradation of unassembled ribosomal proteins, *eLife*, 5, e19105.

DOI: 10.7554/eLife.19105

Contributions: Cloning; protein expression and purification, and protein complex assembly.

Ferdinand M. Huber & André Hoelz^{*} (2017). Molecular basis for protection of ribosomal protein L4 from cellular degradation, *Nat. Commun.*, 8, 14354.

DOI: 10.1038/ncomms14354

Contributions: Cloning; protein expression, purification, and crystallization; structure determination and mutational analysis; protein-protein interaction analysis; *in vivo* analysis in *S. cerevisiae*.

[#]denotes equal contribution

^{*}denotes corresponding authors

TABLE OF CONTENTS

Acknowledgements	iii
Abstract	v
Published Content and Contributions	vii
Table of Contents	viii
Introduction	1
Eukaryotic ribosome structure and function	1
Compartmentalization of ribosome function and assembly	1
Ribosome assembly steps	2
Structural studies of ribosome assembly intermediates	4
Transcription and processing of ribosomal RNA	5
Nuclear import of ribosomal proteins	5
Dedicated ribosome assembly chaperones	7
Symportin 1 as dedicated assembly chaperone of RpL5/11	8
Degradation of excess ribosomal proteins	9
Figures	12
References	18
Chapter I:	
Coordinated ribosomal L4 protein assembly into the pre-ribosome is regulated by its eukaryote-specific extension	25
Abstract	26
Introduction	27
Results and Discussion	29
Acknowledgements	34
Experimental Procedures	35
Figures	41
Tables	61
References	66
Chapter II:	
A conserved quality-control pathway that mediates degradation of unassembled ribosomal proteins	71
Abstract	72
Introduction	73
Results	74
Discussion	82
Acknowledgements	87
Experimental Procedures	88
Figures	101
Tables	132
References	136

Chapter III:
Molecular basis for protection of ribosomal protein L4 from cellular degradation 145

- Abstract 146
- Introduction 147
- Results 149
- Acknowledgements 155
- Experimental Procedures 156
- Figures 164
- Tables 193
- References 198

INTRODUCTION

Eukaryotic ribosome structure and function

Ribosomes are macromolecular machineries responsible for the final step of gene expression from DNA to RNA to protein, as they translate the genetic code from messenger RNA (mRNA) into proteins by connecting amino acids via peptide bond formation. Due to their heterogeneous composition of both protein constituents as well as a subclass of RNA, termed ribosomal RNA (rRNA), which harbors the catalytic activity for peptide bond formation, ribosomes are in fact ribozymes (Cech, 2000).

Whereas ribosomes are present and fulfill the same function throughout all kingdoms of life, prokaryotic and eukaryotic ribosomes display substantial compositional differences. The eukaryotic ribosome contains a large 60S ribosomal subunit and a small 40S ribosomal subunit, which assemble into the eukaryotic 80S ribosome. The large 60S subunit consists of three ribosomal RNAs, the 25S, 5.8S, and 5S RNA and 46 ribosomal proteins, whereas the small 40S subunit contains only a single ribosomal RNA, the 18S rRNA and 33 ribosomal proteins (Ben-Shem et al., 2011; Ben-Shem et al., 2010).

X-ray crystallographic studies in the early 2010s first revealed the partial structure of the fully assembled eukaryotic 80S ribosome, followed by higher resolution structures of the individual 40S and 60S ribosomal subunits (Ben-Shem et al., 2010; Klinge et al., 2011; Rabl et al., 2011). The compact nature, large size, and characteristic shape of ribosomes make them an excellent target for cryo-electron microscopy studies, which have in the past years generated a wealth of information about the molecular mechanism of translation. More recently, new technological advances and developments in electron microscopy have enabled the determination of near-atomic resolution structures of assembly intermediates at various stages of ribosome biogenesis (see section below).

Compartmentalization of ribosome function and assembly

Membrane-dependent compartmentalization is one of the great hallmarks of eukaryotic cells that enables the separation of essential cellular processes into dedicated membrane-enclosed compartments (Hoelz et al., 2011). Not only does compartmentalization allow for generating optimized environments for specific cellular processes, such as protein

degradation in lysosomes or oxidative phosphorylation in mitochondria, it also provides a framework for efficient regulation and fine-tuning of these essential processes.

Eukaryotic ribosomes are an excellent example for this concept, as ribosomes generate proteins within the cytoplasm by translating mRNAs, which are, however, transcribed and processed in the nucleus of the cell. By separating mRNA transcription and translation into distinct membrane-enclosed compartments, mRNA transport through the nuclear pore complex (NPC) functions as a critical quality control step and as a basis for regulation of gene expression (Hoelz et al., 2011).

Moreover, eukaryotic ribosome assembly occurs primarily in the nucleolus and nucleus of the cell, whereas only the final steps of pre-ribosomal subunit maturation and quality control are carried out in the cytoplasm (Figure 1) (Pena et al., 2017). This allows on the one hand for the regulation and fine-tuning of ribosome biogenesis as desired by the current progress in the cell cycle as well as adapting to cellular stress signals and alterations in the cellular steady-state energy levels (Warner, 1999). On the other hand, compartmentalization ensures effective quality control mechanisms to eliminate incomplete ribosomal subunits and improperly assembled or malfunctioning ribosomes from the cellular pool.

In addition, early steps in the ribosome biogenesis pathway occur in a sub-compartment of the nucleus, the nucleolus, which is not separated by a membrane, but instead is a dense network at rDNA loci generated by the recruitment of RNA polymerases and rRNA processing factors (Lam et al., 2005). Even within the nucleolus dedicated sub-compartments exist for RNA transcription, modification, and cleavage to ensure efficient and unperturbed processing (Feric et al., 2016).

By separating eukaryotic ribosome function and assembly into different cellular compartments, evolution implemented a powerful regulatory mechanism for quality control and fine-tuning of ribosome biogenesis, which is one of the most energy consuming process in the cell (Madru et al., 2015; Strunk and Karbstein, 2009).

Ribosome assembly steps

Eukaryotic ribosome biogenesis is a complex interplay of pre-rRNA, ribosomal proteins, and more than 200 trans-acting assembly factors, such as AAA+-type ATPases, GTPases,

RNA helicases, and kinases, as well as ~80 small nucleolar RNAs (snoRNAs) involved in pre-rRNA processing (see below) (Bassler and Hurt, 2018; Strunk and Karbstein, 2009). All assembly factors orchestrate a hierarchical process reminiscent of a highly-efficient and well-controlled assembly line (Figure 1). Briefly, ribosome biogenesis starts with transcription of pre-rRNA and its co-transcriptional processing and recruitment of assembly factors to generate the 5 MDa 90S pre-ribosomal particle (also termed small subunit SSU processome) (Kornprobst et al., 2016). The 90S particle is composed of snoRNAs, such as the U3 snoRNP and ~70 other assembly factors that form distinct complexes, termed U three protein (UTP) complexes (Dragon et al., 2002; Kornprobst et al., 2016). UTP A, B, and C are multi-protein complexes that are recruited co-transcriptionally to 35S pre-rRNA and interact primarily with the 5'-ETS to facilitate the maturation of primarily the 40S pre-ribosomal subunit (Kornprobst et al., 2016).

Upon cleavage of the 5'-ETS by the nuclease Utp24 (Bleichert et al., 2006) at sites A0 and A1 and subsequent cleavage at site A2 within the ITS1, the 40S pre-ribosomal particle is released into its independent maturation pathway (Figure 2) (Kos and Tollervey, 2010; Pena et al., 2017). Whereas the 40S pre-ribosomal particle undergoes only minor additional maturation steps, the 60S pre-ribosomal particle is further assembled and processed in a co-transcriptional fashion, involving various distinct intermediate assembly steps (Chaker-Margot and Klinge, 2019).

The 60S pre-ribosomal intermediates are historically named after the presence of one or more assembly factors that are recruited to and define a specific stage in the pre-60S maturation pathway, such as the Nog2 or Rix1 particles (Barrio-Garcia et al., 2016; Wu et al., 2016). During the transition of the pre-60S subunit from the Nog2 particle into the Rix1 particle, the ITS2 between the 5.8S and 25S rRNA is cleaved and removed and the 5S rRNA is adopting its mature conformation (Pena et al., 2017). Further recruitment of the nuclear export adaptor NMD3 and the Mex67-Mtr2 complex along with the release of Nog2 and the Rix1 complex generate a pre-60S subunit that is competent for nuclear export (Ho et al., 2000; Sarkar et al., 2016). A number of recent reviews describe the eukaryotic ribosome assembly pathway in greater detail (Bassler and Hurt, 2018; Klinge and Woolford, 2019; Pena et al., 2017).

Upon nuclear export through the nuclear pore complex the pre-60S subunit undergoes further maturation steps, including the exchange of space-holder ribosomal proteins with their ultimate ribosomal protein counterparts (Lo et al., 2010; Warner, 2015). Following the removal of all assembly and nuclear export factors, the mature 60S ribosomal subunit can assemble with a mature 40S subunit to yield a fully assembled 80S ribosome, which is translation-competent.

Structural studies of ribosome assembly intermediates

Within the last five years, the revolution of resolution in cryo-electron microscopy technologies has had substantial impact on the determination of near-atomic resolution structures of various ribosome assembly intermediates. By endogenous tagging of specific assembly factors in *Saccharomyces cerevisiae* or the thermophilic fungus *Chaetomium thermophilum* and subsequently employing tandem affinity purification techniques, well-defined 60S pre-ribosomal subunits could be obtained and analyzed for their composition and structure. The aforementioned 90S, Nog2, and Rix1 particles, along with several other intermediates, could be purified from native source (Barrio-Garcia et al., 2016; Kater et al., 2017; Kornprobst et al., 2016; Wu et al., 2016). Their near-atomic resolution structures yielded a wealth of information about the complex molecular mechanisms, the composition of assembly intermediates, and the essential structural rearrangements of ribosomal RNA for various steps of the ribosome biogenesis pathway.

Among many advances in the understanding of ribosome assembly, comparison of assembly intermediate structures beautifully demonstrates the involvement of ribosome assembly factors that trigger successful transition through an assembly checkpoint (Kater et al., 2017). Energy consuming processes mediated by ATPases and GTPases facilitate large conformational rearrangements that ensure, amongst other mechanisms, the unidirectionality of the assembly process (Strunk and Karbstein, 2009). Further structural analysis of distinct and intact pre-ribosomal subunits is essential to understand the intricate structural rearrangements occurring at the maturing pre-ribosomal subunits. Moreover, structures of sequential intermediates will uncover how the large number of ribosome assembly factors and dedicated chaperones orchestrate the hierarchical incorporation of ribosomal proteins.

Transcription and processing of ribosomal RNA

The eukaryotic ribosome is built from four ribosomal RNAs, the 25S, 5.8S, 5S, and 18S rRNA. Intriguingly, the 25S, 18S, and 5.8S rRNA are generated as an individual 35S rRNA transcript that is subsequently cleaved, truncated, and processed into 25S, 18S, and 5.8S rRNA throughout various distinct assembly steps (Figure 2) (Turowski and Tollervey, 2015).

All three eukaryotic RNA polymerases are involved in the process of ribosome biogenesis. Transcription of 35S rRNA is dependent on RNA polymerase I, at rDNA repeat loci within the cellular nucleolus (Grummt, 2013). On the contrary, the 5S rRNA is transcribed by RNA polymerase III (Turowski and Tollervey, 2016). Besides direct production of ribosomal RNA by RNA polymerases I and III, RNA polymerase II has a more indirect role in ribosome biogenesis by producing the mRNA transcripts encoding for the translation of all ~80 ribosomal proteins.

The 35S RNA transcript contains additional external transcribed spacer sequences, the 5'- and 3'-ETS as well as internal transcribed spacer sequences, termed ITS, that separate the 18S, 5.8S, and 25S rRNA from one another (Turowski and Tollervey, 2015). Cleavage of the ITSs and subsequent truncation of the 5'- and 3'-ends that yield mature rRNAs are intricate processes that serve as quality control checkpoints and ensure the unidirectionality of ribosome biogenesis (Klinge and Woolford, 2019).

A large set of nucleases, RNA helicases, and small nucleolar RNAs (snoRNAs) are involved in rRNA processing. In addition to the aforementioned RNA cleavage events, ribosomal RNA is also heavily modified, for example by Kre33-dependent acetylation or Nep1/Emg1-dependent methylation at specific rRNA sites (Sharma and Lafontaine, 2015; Sharma et al., 2015; Thomas et al., 2011).

Importantly, rRNA processing is strongly intertwined with and dependent on the hierarchical incorporation of ribosomal proteins into the growing pre-ribosomal particles and recruitment of specific ribosome assembly factors serving as a trigger for transitioning through an assembly checkpoint (Pena et al., 2017).

Nuclear import of ribosomal proteins

Whereas separation of ribosome assembly and function into distinct cellular compartments

allows for efficient regulation and quality control, it generates the necessity of nuclear import of ribosomal proteins for incorporation into the maturing pre-ribosomal subunits. With the exception of only a few ribosomal proteins that are incorporated into the already exported pre-ribosomal subunits in the cytoplasm, such as RpL10 and RpL24, all ribosomal proteins are transported from the cytoplasm through the nuclear pore complex to the nucleus (Lo et al., 2010). Whereas the specific nuclear transport factors for each and every ribosomal protein have not yet been identified, a growing number of direct or indirect nuclear import mechanisms for ribosomal proteins are emerging (Pillet et al., 2017).

Nuclear import of proteins larger than ~40 kDa in size requires active transport through the diffusion barrier of the NPC by interacting through a nuclear localization signal (NLS) with nuclear transport factors that are collectively termed karyopherins (Lin and Hoelz, 2019; Timney et al., 2016). A classic NLS consists of either a monopartite or bipartite stretch of basic amino acids that interact with karyopherin- α import adaptors. In its cargo-bound state karyopherin- α can bind to karyopherin- β , which harbors intrinsic properties to interact with and cross the diffusion barrier of the NPC (Christie et al., 2016; Stuwe et al., 2015). Several ribosomal proteins or their dedicated adaptor proteins possess a different type of nuclear localization signal, termed PY-NLS according to its conserved proline-tyrosine consensus sequence that directly interacts with karyopherin- β 2 to be shuttled into the nucleus (Kressler et al., 2012; Lee et al., 2006).

Eukaryotic ribosomal proteins often contain elongated unstructured loops or termini and are highly positively charged as a prerequisite for rRNA interaction (Klinge et al., 2011). Due to these features, ribosomal proteins are prone to aggregation and have a tendency to form unfavorable interactions outside of their ribosomal destination (Koch et al., 2012; Pillet et al., 2015). Interestingly, karyopherins have been shown to not only function as nuclear import receptors, but are also thought to play an active role in preventing ribosomal proteins from aggregation, by binding to NLSs in their unstructured regions (Jakel et al., 2002).

Histone proteins are a very similar class of proteins compared to ribosomal proteins, as they harbor long unstructured termini and are highly positively charged to interact with DNA to form nucleosomes (Pillet et al., 2017). To prevent premature or unfavorable interactions of histones with DNA, histones interact with an acidic protein, nucleoplasmin,

which is the first identified member of a class of proteins termed molecular chaperones (Laskey et al., 1978). Similar molecular chaperoning mechanisms have been identified for various ribosomal proteins within the last decade, which will be discussed in the next section.

Dedicated ribosome assembly chaperones

The delicate structural and biochemical features of ribosomal proteins necessitated the co-evolution of a dedicated chaperoning system to protect ribosomal proteins until their delivery and incorporation into pre-ribosomal subunits at the correct time and location. Dedicated assembly chaperones have been identified for a small, but continuously growing set of ribosomal proteins of both the small and large ribosomal subunit (Pillet et al., 2017). One of the major challenges for the identification of novel ribosome assembly chaperones is their transient interaction with ribosomal proteins and their absence from mature ribosomal subunits. Whereas affinity tagging of a ribosomal protein and analyzing the obtained interaction partners has yielded trace amounts of assembly chaperone, other approaches, including pulse-chase labeling, have proven to be more powerful to study the biogenesis of macromolecular assemblies (Kressler et al., 2012; Stelter and Hurt, 2014; Stelter et al., 2012).

A total number of 8 dedicated ribosome assembly chaperones have been identified for 9 of the 79 eukaryotic ribosomal proteins (Pillet et al., 2017). Yar1, Tsr2, and Fap7 are chaperones for the small ribosomal subunit proteins (RpS) RpS3, RpS26, and RpS14, respectively (Hellmich et al., 2013; Koch et al., 2012; Schutz et al., 2018). The large ribosomal subunit proteins (RpL) RpL3, RpL4, RpL5 with RpL11, RpL10, and RpL23 have dedicated chaperones Rrb1, Acl4, Syo1, Sqt1, and Bcp1 (Calvino et al., 2015; Eisinger et al., 1997; Huber and Hoelz, 2017; Iouk et al., 2001; Kressler et al., 2012; Pausch et al., 2015; Stelter et al., 2015; Ting et al., 2017).

Whereas all ribosome assembly chaperones primarily fulfill a protective function for ribosomal proteins, the molecular mechanisms and structural details vary broadly. A comprehensive review of all mechanisms is outside the scope of this introduction, but some key concepts will be illustrated in the next section by an example that has been studied in

great detail (for a complete review of the current state of the field, see for example (Pillet et al., 2017)).

X-ray crystallographic studies have shown that ribosome assembly chaperones adopt a variety of different structural folds, ranging from β -propeller domains (Sqt1), TPR domains (Acl4), Ankyrin repeat domains (Yar1) to mixed domains containing both Armadillo and HEAT repeats (Syo1) (Figure 3) (Holzer et al., 2013; Kressler et al., 2012; Pausch et al., 2015; Stelter et al., 2015). Whereas assembly chaperones adopt a wide range of structural folds, some display similar binding preferences to their ribosomal protein clients at or around nuclear localization signals within unstructured regions, where they in fact compete with karyopherin-binding (Huber and Hoelz, 2017; Mitterer et al., 2016).

Further structural characterization of ribosomal proteins in complex with their dedicated chaperones is required to understand the various challenges ribosomal proteins are facing from their cytoplasmic generation to their incorporation into the pre-ribosomal subunits within the nucleus. Nature has evolved numerous molecular mechanisms to ensure efficient shuttling of ribosomal proteins to their destination to carefully balance efficient ribosome biogenesis (Pillet et al., 2017).

Symportin 1 as dedicated assembly chaperone for RpL5/11

One of the most unusual yet well-characterized assembly chaperones is Symportin 1 (Syo1), as it simultaneously binds, protects, and shuttles two ribosomal proteins of the large subunit, RpL5 and RpL11 (Bange et al., 2013; Kressler et al., 2012). Those two proteins are functionally connected because they form a complex with the 5S ribosomal RNA prior to its incorporation into the maturing ribosomal subunit (Calvino et al., 2015). Syo1 not only harbors two distinct binding sites for RpL5 and RpL11, but also a PY-NLS for assembling a transport-competent nuclear import complex with the karyopherin- β 2 homolog Kap104 (Kressler et al., 2012). Upon arrival in the nucleus the nuclear import complex is disassembled by the nuclear RanGTP gradient to release Syo1•RpL5•RpL11 into the nucleus, where it recognizes 5S rRNA (Calvino et al., 2015). Moreover, Symportin 1 is part of a molecular mimicry mechanism, as its client RpL11 interacts with helix 84 (H84) of the 25S rRNA upon delivery at the pre-60S subunit. In the

Syo1•RpL5•RpL11 complex the interface between RpL11 and H84 is occupied by a Syo1 helix, mimicking the RpL11-RNA interaction (Figure 3) (Calvino et al., 2015).

Whereas different assembly chaperones employ different molecular mechanisms to fulfill their function, the Syo1•RpL5•RpL11 chaperone-client complex beautifully illustrates the complex interplay of assembly chaperones, their ribosomal protein clients, karyopherins, and the surface of growing pre-ribosomal subunits.

Degradation of excess ribosomal proteins

The biogenesis of large macromolecular assemblies, such as the ribosome or the nuclear pore complex, generates a substantial challenge for the cell to ensure stoichiometric complex formation (Lin et al., 2016). In the eukaryotic ribosome, ribosomal proteins are present as a single copy, which requires identification and removal of non-incorporated ribosomal protein levels by a previously unknown mechanism. Protein levels could be balanced to similar stoichiometry on a transcriptional or translational level to generate only the amount of protein required for assembly. While it appears interesting to entertain the idea that avoiding the generation of excess ribosomal proteins could be most energy-efficient, the complex regulatory feedback circuits to ensure equal amounts of ~80 ribosomal proteins on a transcriptional or translational level seem unlikely. In fact, the evolution of assembly chaperones opens a plausible third mechanism, the cellular degradation of excess ribosomal proteins. It has recently been shown that excess ribosomal proteins are indeed degraded by the ubiquitin-proteasome system (Sung et al., 2016a; Sung et al., 2016b).

The first chapter of this thesis describes the identification of a novel ribosome assembly chaperone and its biochemical, structural, and mechanistic characterization. A pulse-chase approach was employed to identify the uncharacterized *S. cerevisiae* protein YDR161W as a transient interaction partner of the large subunit ribosomal protein RpL4. Biochemical and *in vivo* analysis in *S. cerevisiae* demonstrated that YDR161W possesses a chaperoning function and was consequently named Assembly Chaperone of RpL4 (Acl4).

Acl4 co-translationally recognizes and interacts with nascent RpL4 and releases it only at its final destination at the growing 60S pre-ribosomal subunit. Moreover, the 3.0 Å

X-ray crystal structure of Acl4 uncovers an all α -helical TPR domain that spans the majority of the protein's length. A structure-guided truncational approach identifies the general elements required for Acl4-RpL4 complex formation and highlights the preference of assembly chaperones to bind to unstructured and primarily basic regions of the client ribosomal proteins. For nuclear import of the Acl4•RpL4 complex, a PY-NLS on the RpL4 extension recruits karyopherin- β 2-type Kap104 to generate a heterotrimeric transport-competent Acl4•RpL4•Kap104 nuclear import complex.

Further mutational analysis and *in vivo* studies in *S. cerevisiae* demonstrate that the eukaryote-specific unstructured extension of RpL4 acts as a release-sensor for triggering timely RpL4 incorporation into the growing 60S pre-ribosomal subunit. The unstructured RpL4 extension recognizes and binds both RpL18 and the eukaryote-specific expansion segment 7 of the 25S ribosomal RNA at the pre-60S surface. Upon favorable interaction with both elements, RpL4 is released and incorporated into the pre-60S subunit.

The second chapter of this thesis reports the identification and characterization of a conserved cellular degradation pathway for excess ribosomal proteins by the ubiquitin-proteasome machinery. Previous work has shown that excess unbound or aggregated ribosomal proteins are efficiently cleared from the cell in a ubiquitin-dependent manner (Sung et al., 2016b). By performing a large-scale screen employing an *S. cerevisiae* knockout library of E3- and E2-enzymes, the E3-ubiquitin ligase Tom1 was identified to mediate ubiquitination of ribosomal protein targets. Importantly, the ubiquitination machinery for ribosomal proteins is conserved from yeast to humans and performed by the human E3 ubiquitin ligase Huw1.

Further analysis by SILAC and mass spectrometry uncovers a large set of ribosomal protein targets, primarily of the large ribosomal subunit, including RpL4 as one of the primary targets. In fact, RpL4 harbors three conserved lysine residues that serve as Tom1-dependent ubiquitination target sites. One site is located in the elongated unstructured loop and two sites are flanking the PY-NLS within the RpL4 C-terminal extension. *In vitro* ubiquitination assays with Tom1, Acl4•RpL4, and the karyopherin Kap104 demonstrate that both Acl4 and Kap104 are efficiently protecting RpL4 from Tom1-dependent ubiquitination and consequently from degradation by the proteasome. However, for further

molecular details additional structural studies are required to identify the underlying molecular mechanism of protection and to reveal whether other assembly chaperones could fulfill a similar protective function.

Chapter 3 of this thesis provides the molecular basis for protection of the ribosomal protein RpL4 from cellular degradation by Tom1-dependent ubiquitination and proteasomal degradation. The 2.4 Å X-ray crystal structure of Acl4•RpL4 is reported and offers detailed information about the determinants of Acl4-RpL4 complex formation at the atomic level. Upon Acl4 binding the otherwise elongated internal RpL4 loop is dramatically compacted and shielded by the Acl4 TPR domain. Importantly, the Tom1-target lysine in the RpL4 loop is inaccessible for ubiquitination when bound to Acl4.

Structure-guided mutagenesis of the Acl4-RpL4 complex uncovered an extensive interface between the RpL4 loop and the Acl4 concave surface. Surprisingly, biochemical interaction analysis of Acl4 surface mutations followed by *in vivo* validation show that mutation of a single Acl4 residue can abolish binding to RpL4. Moreover, mutagenesis of the RpL4 extension uncovers the determinants of karyopherin Kap104-binding to the RpL4 PY-NLS. A 3.0 Å X-ray crystal structure of RpL4•Kap104 provides the molecular details for protection of the remaining two Tom1-target lysines within the RpL4 extension. When in complex with Acl4 and Kap104, all three RpL4 lysines that are potential ubiquitination sites are inaccessible, keeping RpL4 protected from cellular degradation. Interestingly, a second Acl4 copy and Kap104 compete for a similar binding site on the RpL4 extension, explaining how the two Tom1-target sites within the extension are protected after nuclear import and disassembly of the Acl4•RpL4•Kap104 complex.

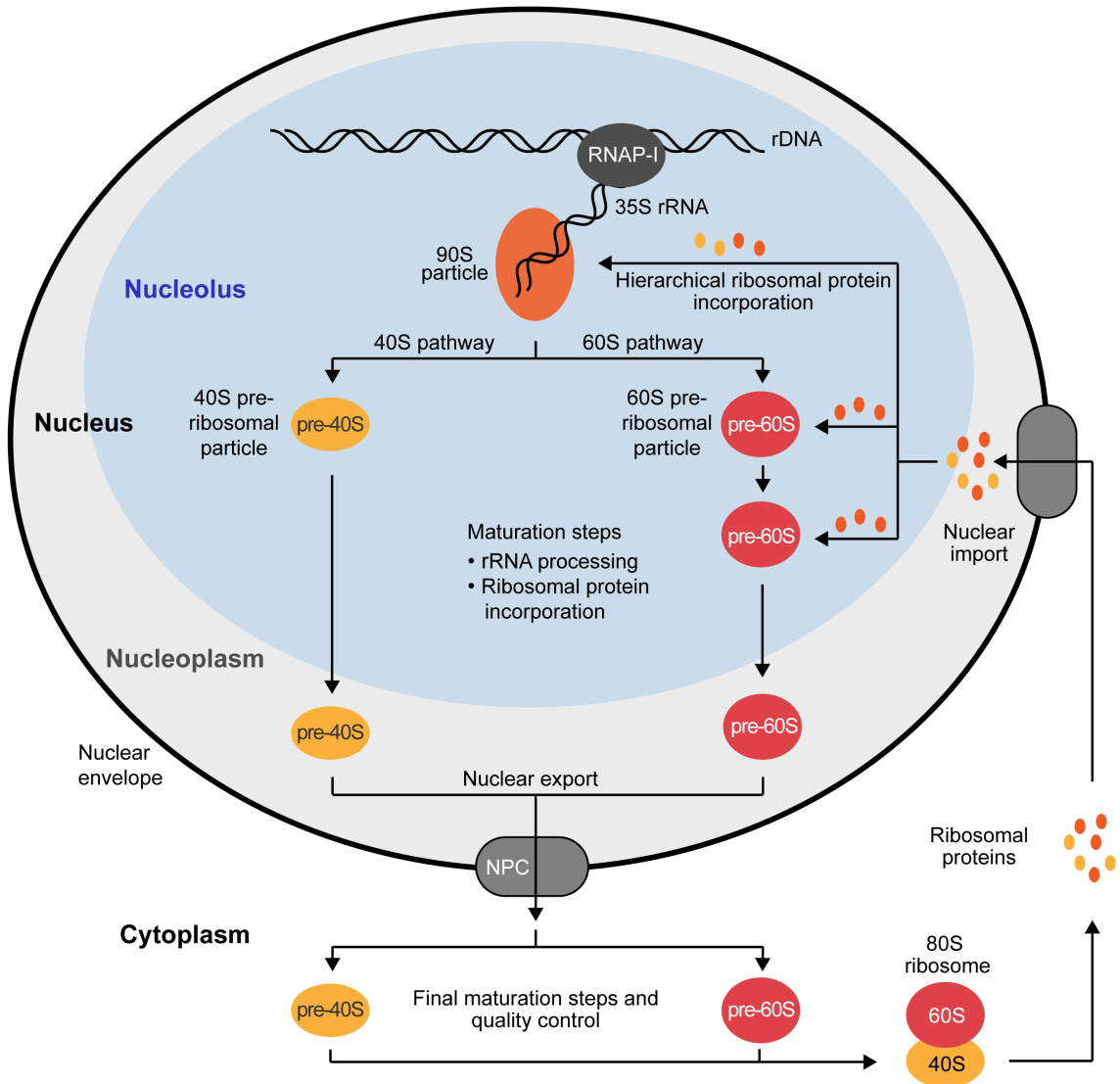


Figure 1: Simplified schematic of eukaryotic ribosome biogenesis

Ribosome assembly occurs predominantly in the cellular nucleolus, colored in light blue. During RNA polymerase I-dependent transcription of 35S rRNA, the 90S particle is formed by a large number of small nucleolar RNAs and assembly factors. Upon cleavage of an internal spacer sequence within the 35S rRNA, the 40S and 60S pre-ribosomal subunits are separated into their individual maturation pathways. Nuclear export and minor processing and quality control in the cytoplasm are the final steps in the biogenesis pathway to generate mature 80S ribosomes.

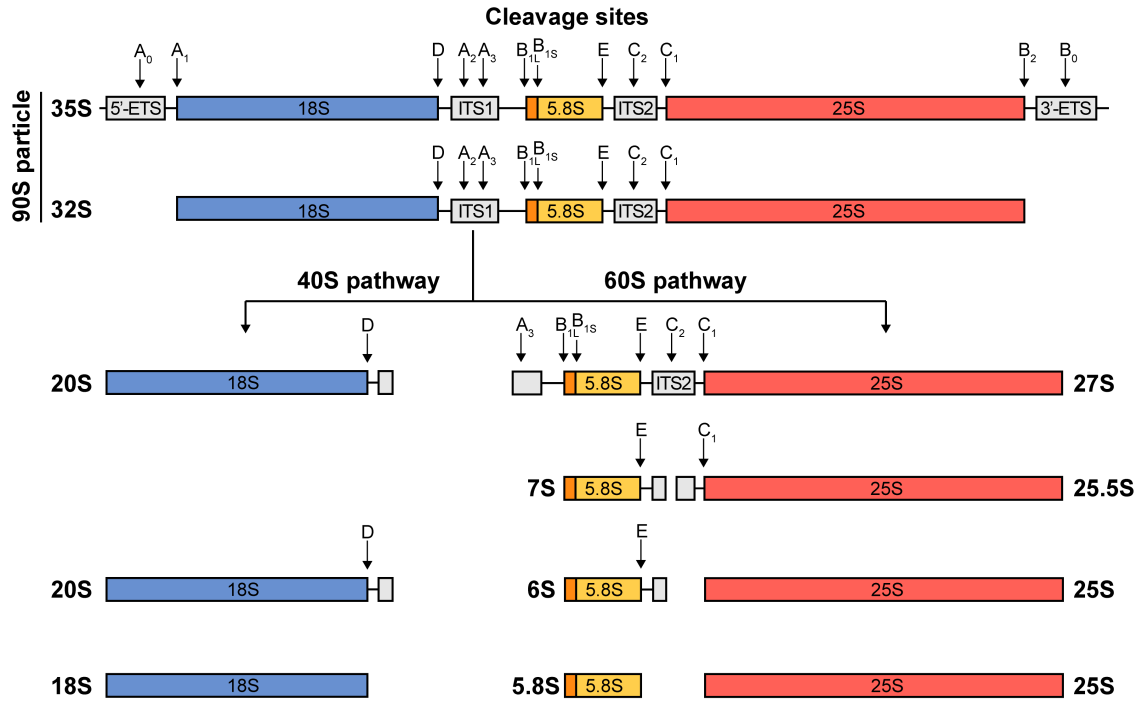
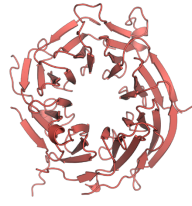


Figure 2: Processing of 35S ribosomal RNA at various stages of pre-ribosomal subunit assembly

The exo- and endo-nuclease cleavage sites are marked by an arrow. Co-transcriptionally, the 90S particle is assembled on the 35S rRNA transcript, which is cleaved at the A2 site to release the 40S and 60S pre-ribosomal subunits into their individual assembly pathways. Further processing of the resulting 20S and 27S rRNA in the nucleolus, nucleoplasm, and cytoplasm generates the mature 18S, 5.8S, and 25S rRNA.

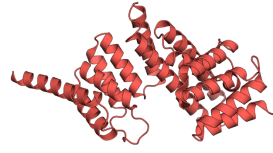
Individual assembly chaperones



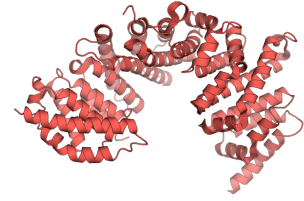
Sqt1



Tsr2

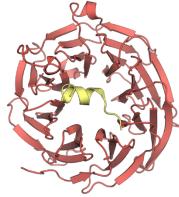


Acl4

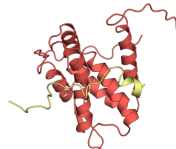


Syo1

Assembly chaperones with client ribosomal proteins



Sqt1-RpL10



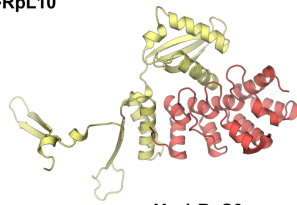
Tsr2-RpS26



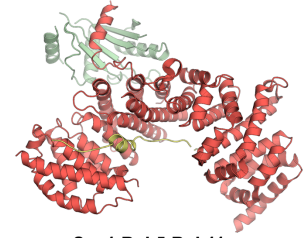
Acl4-RpL4



Syo1-RpL5



Yar1-RpS3



Syo1-RpL5-RpL11

Figure 3: Structures of ribosome assembly chaperones and assembly chaperone – client protein complexes

Assembly chaperones and their client proteins are shown in cartoon representation and are colored in red and yellow/green, respectively. X-ray crystal structures of Sqt1 (PDB ID: 4ZOY), Sqt1•RpL10 (PDB ID: 4ZOX), Acl4 (PDB ID: 4YNW), Acl4•RpL4 (PDB ID: 5TQB), Syo1 (PDB ID: 4GMO), Syo1•RpL5 (PDB ID: 4GMN), Syo1•RpL5•RpL11 (PDB ID: 5AFF), and Yar1•RpS3 (PDB ID: 4BSZ) as well as the solution NMR structures of Tsr2 (PDB ID: 6G03) and Tsr2•RpS26 (PDB ID: 6G04) are shown (Calvino et al., 2015; Holzer et al., 2013; Huber and Hoelz, 2017; Kressler et al., 2012; Pausch et al., 2015; Schutz et al., 2018; Stelter et al., 2015).

References

- Bange, G., Murat, G., Sinning, I., Hurt, E., and Kressler, D. (2013). New twist to nuclear import: When two travel together. *Commun Integr Biol* 6, e24792.
- Barrio-Garcia, C., Thoms, M., Flemming, D., Kater, L., Berninghausen, O., Bassler, J., Beckmann, R., and Hurt, E. (2016). Architecture of the Rix1-Rea1 checkpoint machinery during pre-60S-ribosome remodeling. *Nat Struct Mol Biol* 23, 37-44.
- Bassler, J., and Hurt, E. (2018). Eukaryotic Ribosome Assembly. *Annu Rev Biochem*.
- Ben-Shem, A., Garreau de Loubresse, N., Melnikov, S., Jenner, L., Yusupova, G., and Yusupov, M. (2011). The structure of the eukaryotic ribosome at 3.0 Å resolution. *Science* 334, 1524-1529.
- Ben-Shem, A., Jenner, L., Yusupova, G., and Yusupov, M. (2010). Crystal structure of the eukaryotic ribosome. *Science* 330, 1203-1209.
- Bleichert, F., Granneman, S., Osheim, Y.N., Beyer, A.L., and Baserga, S.J. (2006). The PINc domain protein Utp24, a putative nuclease, is required for the early cleavage steps in 18S rRNA maturation. *Proc Natl Acad Sci U S A* 103, 9464-9469.
- Calvino, F.R., Kharde, S., Ori, A., Hendricks, A., Wild, K., Kressler, D., Bange, G., Hurt, E., Beck, M., and Sinning, I. (2015). Symportin 1 chaperones 5S RNP assembly during ribosome biogenesis by occupying an essential rRNA-binding site. *Nat Commun* 6, 6510.
- Cech, T.R. (2000). Structural biology. The ribosome is a ribozyme. *Science* 289, 878-879.
- Chaker-Margot, M., and Klinge, S. (2019). Assembly and early maturation of large subunit precursors. *RNA* 25, 465-471.
- Christie, M., Chang, C.W., Rona, G., Smith, K.M., Stewart, A.G., Takeda, A.A., Fontes, M.R., Stewart, M., Vertessy, B.G., Forwood, J.K., *et al.* (2016). Structural Biology and Regulation of Protein Import into the Nucleus. *J Mol Biol* 428, 2060-2090.

Dragon, F., Gallagher, J.E., Compagnone-Post, P.A., Mitchell, B.M., Porwancher, K.A., Wehner, K.A., Wormsley, S., Settlege, R.E., Shabanowitz, J., Osheim, Y., *et al.* (2002). A large nucleolar U3 ribonucleoprotein required for 18S ribosomal RNA biogenesis. *Nature* *417*, 967-970.

Eisinger, D.P., Dick, F.A., Denke, E., and Trumpower, B.L. (1997). SQT1, which encodes an essential WD domain protein of *Saccharomyces cerevisiae*, suppresses dominant-negative mutations of the ribosomal protein gene QSR1. *Mol Cell Biol* *17*, 5146-5155.

Feric, M., Vaidya, N., Harmon, T.S., Mitrea, D.M., Zhu, L., Richardson, T.M., Kriwacki, R.W., Pappu, R.V., and Brangwynne, C.P. (2016). Coexisting Liquid Phases Underlie Nucleolar Subcompartments. *Cell* *165*, 1686-1697.

Grummt, I. (2013). The nucleolus-guardian of cellular homeostasis and genome integrity. *Chromosoma* *122*, 487-497.

Hellmich, U.A., Weis, B.L., Lioutikov, A., Wurm, J.P., Kaiser, M., Christ, N.A., Hantke, K., Kotter, P., Entian, K.D., Schleiff, E., *et al.* (2013). Essential ribosome assembly factor Fap7 regulates a hierarchy of RNA-protein interactions during small ribosomal subunit biogenesis. *Proc Natl Acad Sci U S A* *110*, 15253-15258.

Ho, J.H., Kallstrom, G., and Johnson, A.W. (2000). Nmd3p is a Crm1p-dependent adapter protein for nuclear export of the large ribosomal subunit. *J Cell Biol* *151*, 1057-1066.

Hoelz, A., Debler, E.W., and Blobel, G. (2011). The structure of the nuclear pore complex. *Annu Rev Biochem* *80*, 613-643.

Holzer, S., Ban, N., and Klinge, S. (2013). Crystal structure of the yeast ribosomal protein rpS3 in complex with its chaperone Yar1. *J Mol Biol* *425*, 4154-4160.

Huber, F.M., and Hoelz, A. (2017). Molecular basis for protection of ribosomal protein L4 from cellular degradation. *Nat Commun* *8*, 14354.

Iouk, T.L., Aitchison, J.D., Maguire, S., and Wozniak, R.W. (2001). Rrb1p, a yeast nuclear WD-repeat protein involved in the regulation of ribosome biosynthesis. *Mol Cell Biol* *21*, 1260-1271.

Jakel, S., Mingot, J.M., Schwarzmaier, P., Hartmann, E., and Gorlich, D. (2002). Importins fulfil a dual function as nuclear import receptors and cytoplasmic chaperones for exposed basic domains. *EMBO J* *21*, 377-386.

Kater, L., Thoms, M., Barrio-Garcia, C., Cheng, J., Ismail, S., Ahmed, Y.L., Bange, G., Kressler, D., Berninghausen, O., Sinning, I., *et al.* (2017). Visualizing the Assembly Pathway of Nucleolar Pre-60S Ribosomes. *Cell* *171*, 1599-1610 e1514.

Klinge, S., Voigts-Hoffmann, F., Leibundgut, M., Arpagaus, S., and Ban, N. (2011). Crystal structure of the eukaryotic 60S ribosomal subunit in complex with initiation factor 6. *Science* *334*, 941-948.

Klinge, S., and Woolford, J.L., Jr. (2019). Ribosome assembly coming into focus. *Nat Rev Mol Cell Biol* *20*, 116-131.

Koch, B., Mitterer, V., Niederhauser, J., Stanborough, T., Murat, G., Rechberger, G., Bergler, H., Kressler, D., and Pertschy, B. (2012). Yar1 protects the ribosomal protein Rps3 from aggregation. *J Biol Chem* *287*, 21806-21815.

Kornprobst, M., Turk, M., Kellner, N., Cheng, J., Flemming, D., Kos-Braun, I., Kos, M., Thoms, M., Berninghausen, O., Beckmann, R., *et al.* (2016). Architecture of the 90S Pre-ribosome: A Structural View on the Birth of the Eukaryotic Ribosome. *Cell* *166*, 380-393.

Kos, M., and Tollervey, D. (2010). Yeast pre-rRNA processing and modification occur cotranscriptionally. *Mol Cell* *37*, 809-820.

Kressler, D., Bange, G., Ogawa, Y., Stjepanovic, G., Bradatsch, B., Pratte, D., Amlacher, S., Strauss, D., Yoneda, Y., Katahira, J., *et al.* (2012). Synchronizing nuclear import of ribosomal proteins with ribosome assembly. *Science* *338*, 666-671.

- Lam, Y.W., Trinkle-Mulcahy, L., and Lamond, A.I. (2005). The nucleolus. *J Cell Sci* *118*, 1335-1337.
- Laskey, R.A., Honda, B.M., Mills, A.D., and Finch, J.T. (1978). Nucleosomes are assembled by an acidic protein which binds histones and transfers them to DNA. *Nature* *275*, 416-420.
- Lee, B.J., Cansizoglu, A.E., Suel, K.E., Louis, T.H., Zhang, Z., and Chook, Y.M. (2006). Rules for nuclear localization sequence recognition by karyopherin beta 2. *Cell* *126*, 543-558.
- Lin, D.H., and Hoelz, A. (2019). The Structure of the Nuclear Pore Complex (An Update). *Annu Rev Biochem*.
- Lin, D.H., Stuwe, T., Schilbach, S., Rundlet, E.J., Perriches, T., Mobbs, G., Fan, Y., Thierbach, K., Huber, F.M., Collins, L.N., *et al.* (2016). Architecture of the symmetric core of the nuclear pore. *Science* *352*, aaf1015.
- Lo, K.Y., Li, Z., Bussiere, C., Bresson, S., Marcotte, E.M., and Johnson, A.W. (2010). Defining the pathway of cytoplasmic maturation of the 60S ribosomal subunit. *Mol Cell* *39*, 196-208.
- Madru, C., Lebaron, S., Blaud, M., Delbos, L., Pipoli, J., Pasmant, E., Rety, S., and Leulliot, N. (2015). Chaperoning 5S RNA assembly. *Genes Dev* *29*, 1432-1446.
- Mitterer, V., Gantenbein, N., Birner-Gruenberger, R., Murat, G., Bergler, H., Kressler, D., and Pertschy, B. (2016). Nuclear import of dimerized ribosomal protein Rps3 in complex with its chaperone Yar1. *Sci Rep* *6*, 36714.
- Pausch, P., Singh, U., Ahmed, Y.L., Pillet, B., Murat, G., Altegoer, F., Stier, G., Thoms, M., Hurt, E., Sinning, I., *et al.* (2015). Co-translational capturing of nascent ribosomal proteins by their dedicated chaperones. *Nat Commun* *6*, 7494.
- Pena, C., Hurt, E., and Panse, V.G. (2017). Eukaryotic ribosome assembly, transport and quality control. *Nat Struct Mol Biol* *24*, 689-699.

Pillet, B., Garcia-Gomez, J.J., Pausch, P., Falquet, L., Bange, G., de la Cruz, J., and Kressler, D. (2015). The Dedicated Chaperone Acl4 Escorts Ribosomal Protein Rpl4 to Its Nuclear Pre-60S Assembly Site. *PLoS Genet* *11*, e1005565.

Pillet, B., Mitterer, V., Kressler, D., and Pertschy, B. (2017). Hold on to your friends: Dedicated chaperones of ribosomal proteins: Dedicated chaperones mediate the safe transfer of ribosomal proteins to their site of pre-ribosome incorporation. *Bioessays* *39*, 1-12.

Rabl, J., Leibundgut, M., Ataide, S.F., Haag, A., and Ban, N. (2011). Crystal structure of the eukaryotic 40S ribosomal subunit in complex with initiation factor 1. *Science* *331*, 730-736.

Sarkar, A., Pech, M., Thoms, M., Beckmann, R., and Hurt, E. (2016). Ribosome-stalk biogenesis is coupled with recruitment of nuclear-export factor to the nascent 60S subunit. *Nat Struct Mol Biol* *23*, 1074-1082.

Schutz, S., Michel, E., Damberger, F.F., Oplova, M., Pena, C., Leitner, A., Aebersold, R., Allain, F.H., and Panse, V.G. (2018). Molecular basis for disassembly of an importin:ribosomal protein complex by the escortin Tsr2. *Nat Commun* *9*, 3669.

Sharma, S., and Lafontaine, D.L.J. (2015). 'View From A Bridge': A New Perspective on Eukaryotic rRNA Base Modification. *Trends Biochem Sci* *40*, 560-575.

Sharma, S., Langhendries, J.L., Watzinger, P., Kotter, P., Entian, K.D., and Lafontaine, D.L. (2015). Yeast Kre33 and human NAT10 are conserved 18S rRNA cytosine acetyltransferases that modify tRNAs assisted by the adaptor Tan1/THUMP1. *Nucleic Acids Res* *43*, 2242-2258.

Stelter, P., Huber, F.M., Kunze, R., Flemming, D., Hoelz, A., and Hurt, E. (2015). Coordinated Ribosomal L4 Protein Assembly into the Pre-Ribosome Is Regulated by Its Eukaryote-Specific Extension. *Mol Cell* *58*, 854-862.

Stelter, P., and Hurt, E. (2014). A pulse-chase epitope labeling to study cellular dynamics of newly synthesized proteins: a novel strategy to characterize NPC biogenesis and ribosome maturation/export. *Methods Cell Biol* 122, 147-163.

Stelter, P., Kunze, R., Radwan, M., Thomson, E., Thierbach, K., Thoms, M., and Hurt, E. (2012). Monitoring spatiotemporal biogenesis of macromolecular assemblies by pulse-chase epitope labeling. *Mol Cell* 47, 788-796.

Strunk, B.S., and Karbstein, K. (2009). Powering through ribosome assembly. *RNA* 15, 2083-2104.

Stuwe, T., Bley, C.J., Thierbach, K., Petrovic, S., Schilbach, S., Mayo, D.J., Perriches, T., Rundlet, E.J., Jeon, Y.E., Collins, L.N., *et al.* (2015). Architecture of the fungal nuclear pore inner ring complex. *Science* 350, 56-64.

Sung, M.K., Porras-Yakushi, T.R., Reitsma, J.M., Huber, F.M., Sweredoski, M.J., Hoelz, A., Hess, S., and Deshaies, R.J. (2016a). A conserved quality-control pathway that mediates degradation of unassembled ribosomal proteins. *Elife* 5.

Sung, M.K., Reitsma, J.M., Sweredoski, M.J., Hess, S., and Deshaies, R.J. (2016b). Ribosomal proteins produced in excess are degraded by the ubiquitin-proteasome system. *Mol Biol Cell* 27, 2642-2652.

Thomas, S.R., Keller, C.A., Szyk, A., Cannon, J.R., and Laronde-Leblanc, N.A. (2011). Structural insight into the functional mechanism of Nep1/Emg1 N1-specific pseudouridine methyltransferase in ribosome biogenesis. *Nucleic Acids Res* 39, 2445-2457.

Timney, B.L., Raveh, B., Mironska, R., Trivedi, J.M., Kim, S.J., Russel, D., Wente, S.R., Sali, A., and Rout, M.P. (2016). Simple rules for passive diffusion through the nuclear pore complex. *J Cell Biol* 215, 57-76.

Ting, Y.H., Lu, T.J., Johnson, A.W., Shie, J.T., Chen, B.R., Kumar, S.S., and Lo, K.Y. (2017). Bcp1 Is the Nuclear Chaperone of Rpl23 in *Saccharomyces cerevisiae*. *J Biol Chem* 292, 585-596.

Turowski, T.W., and Tollervey, D. (2015). Cotranscriptional events in eukaryotic ribosome synthesis. *Wiley Interdiscip Rev RNA* 6, 129-139.

Turowski, T.W., and Tollervey, D. (2016). Transcription by RNA polymerase III: insights into mechanism and regulation. *Biochem Soc Trans* 44, 1367-1375.

Warner, J.R. (1999). The economics of ribosome biosynthesis in yeast. *Trends Biochem Sci* 24, 437-440.

Warner, J.R. (2015). Twenty years of ribosome assembly and ribosomopathies. *RNA* 21, 758-759.

Wu, S., Tutuncuoglu, B., Yan, K., Brown, H., Zhang, Y., Tan, D., Gamalinda, M., Yuan, Y., Li, Z., Jakovljevic, J., *et al.* (2016). Diverse roles of assembly factors revealed by structures of late nuclear pre-60S ribosomes. *Nature* 534, 133-137.

CHAPTER I

COORDINATED RIBOSOMAL L4 PROTEIN ASSEMBLY INTO THE PRE-RIBOSOME IS REGULATED BY ITS EUKARYOTE-SPECIFIC EXTENSION

This chapter was adapted from:

Philipp Stelter[#], **Ferdinand M. Huber**[#], Ruth Kunze, Dirk Flemming, André Hoelz^{*}, Ed Hurt^{*} (2015). Coordinated ribosomal L4 protein assembly into the pre-ribosome is regulated by its eukaryote-specific extension, *Mol. Cell*, 58, 854-862.

[#]denotes equal contribution

^{*}denotes corresponding authors

ABSTRACT

Eukaryotic ribosome biogenesis requires nuclear import and hierarchical incorporation of ~80 ribosomal proteins (RPs) into the ribosomal RNA core. In contrast to prokaryotes, many eukaryotic RPs possess long extensions that interdigitate in the mature ribosome. RpL4 is a prime example with a ~80 residue long surface extension of unknown function. Here, we identify assembly chaperone Acl4 that initially binds the universally conserved internal loop of newly synthesized RpL4 via its superhelical TPR domain, thereby restricting RpL4 loop insertion at its cognate nascent rRNA site. RpL4 release from Acl4 is orchestrated with pre-ribosome assembly, during which the eukaryote-specific RpL4 extension makes several distinct interactions with the 60S surface including a co-evolved site on neighboring RpL18. Consequently, mutational inactivation of this contact site, on either RpL4 or RpL18, impairs RpL4-Acl4 disassembly and RpL4 pre-ribosome incorporation. We propose that hierarchical ribosome assembly can be achieved by eukaryotic RP extensions and dedicated assembly chaperones.

INTRODUCTION

Ribosomes are huge (~4 MDa) ribonucleoprotein complexes, which translate the genetic code into polypeptide chains enabling the cell to manipulate their cellular environment. ~80 different ribosomal proteins (RP) are assembled coincident with transcription of pre-ribosomal RNA (rRNA) molecules, which are subsequently processed to mature rRNA molecules (25S, 18S, 5.8S and 5S) mediated by a complex interplay of more than 200 trans-acting assembly factors (Ben-Shem et al., 2011; Lafontaine and Tollervey, 2001; Woolford and Baserga, 2013). This highly energy consuming assembly process is tightly regulated within the cell to guarantee the rapid production of more than one million ribosomes per cell generation in mammalian cells (Grummt, 1999). In yeast, ~14 million RPs are generated per generation that translocate through the nuclear pore complex to meet the maturing ribosome in the nucleus (Schutz et al., 2014). Recent work demonstrates that RPs assemble in a hierarchical and cooperative manner onto the pre-rRNAs, which allow a rough classification of RPs into primary, secondary and tertiary binders (Gamalinda et al., 2014; Shajani et al., 2011). Ill-timed binding of RPs to the pre-ribosome or altered stoichiometry of RPs can disturb ribosome biogenesis, resulting in ribosomal stress. This stress signal can be transduced to other cellular pathways, potentially resulting in disease development including cancer (James et al., 2014; McCann and Baserga, 2013; Teng et al., 2013). Thus, synthesis of RPs must be tightly coordinated with their timely assembly into the pre-ribosome to avoid inadvertent defects in ribosomal biogenesis (Wang et al., 2014). Eukaryotic RPs often have composite protein structures located on the mature ribosome with folded and unfolded domains and/or long extensions. During evolution eukaryotic RPs acquired extensions on the ribosomal surface, which contact large stretches of the rRNA and other RPs (Ben-Shem et al., 2010; Melnikov et al., 2012). While the biological reason for the evolution of these RP extensions remains to be established, their involvement in translation, ribosome assembly, and masking the eukaryote-specific rRNA expansion segments (ESs) was suggested (Ben-Shem et al., 2011; Melnikov et al., 2012). The molecular mechanisms by which eukaryotic cells stabilize delicate largely unstructured RPs and coordinate their incorporation into the pre-ribosome are largely unknown. Dedicated chaperones were identified that bind to a number of RPs, disassemble

karyopherin•RP import complexes, or synchronize nuclear RP import (Eisinger et al., 1997; Holzer et al., 2013; Iouk et al., 2001; Jäkel et al., 2002; Koch et al., 2012; Kressler et al., 2012; Schaper et al., 2001; Schutz et al., 2014).

Here, we report that newly synthesized RpL4 is chaperoned by an uncharacterized protein, Ydr161w, which we name Assembly Chaperone of RpL4 (Acl4). We show that Acl4 binds to a protruding evolutionarily conserved loop of RpL4, which in the mature ribosome is buried deep in the rRNA core structure. Moreover, we demonstrate that the C-terminal RpL4 extension not only is involved in nuclear import of the Acl4•RpL4 complex, but also facilitates ribosome incorporation of RpL4 and associated disassembly of the Acl4•RpL4 complex. Thus, the eukaryotic cell acquired the ability to regulate ribosome maturation through C-terminal RP extensions and dedicated ribosomal assembly chaperones.

RESULTS AND DISCUSSION

Nascent RpL4 association with Acl4 ensures efficient 60S ribosome biogenesis

RpL4 is a typical RP with an ~80 residue C-terminal eukaryote-specific extension and an ~60 residue exposed evolutionarily conserved loop (Ben-Shem et al., 2011; Gamalinda and Woolford, 2014; Ramakrishnan and White, 1998). The loop protrudes from the globular folded core and deeply projects into the 25S rRNA core, lining the peptide exit tunnel of the mature ribosome (Figure 1A) (Zhang et al., 2013). The RpL4 extension meanders ~140 Å across the 60S surface with contacts to rRNA and RPs (Figure 1A).

To reveal the molecular details of how primarily unstructured RpL4 is assembled into the pre-ribosome and establish whether this process is assisted by additional biogenesis factors, we performed pulse-chase analyses combined with affinity-purification to study the fate of RpL4 during its early life (Stelter et al., 2012). After a 5 minute pulse newly synthesized RpL4 (for complementation, see Figure S1A; for yeast strains and constructs, see Table S1 and S2) co-precipitated an uncharacterized ~45 kDa protein (Ydr161w) (Figure 1B). Later, during the chase, RpL4 associated with other ribosomal proteins and assembly factors with concomitant dissociation of Ydr161w. At the end of the chase, pulse-labeled RpL4 was part of mature ribosomes, as indicated by co-precipitation of both 60S and 40S RPs (Figures 1B, 3B). Consistent with a transient interaction, affinity-purification of Ydr161w from yeast cells strongly co-enriched RpL4 (Figure 1C). We tested whether the eukaryote-specific RpL4 extension is linked to Ydr161w, for which a prokaryotic homolog was not found. However, Ydr161w, rather being impaired in the interaction, did not dissociate from newly synthesized RpL4 lacking its C-terminal extension (RpL4ΔExt) during the pulse-chase and was not assembled into the 60S subunit (Figure 1D). In contrast to a recent report (Gamalinda and Woolford, 2014), we observe that the RpL4 C-terminal extension is essential for cell growth and its absence from RpL4 induces a dominant growth defect, particular at higher temperatures (Figure S1B). Altogether, we conclude that Ydr161w, which we named Assembly Chaperone of L4 (Acl4), binds newly synthesized RpL4, whose release from Acl4 and subsequent ribosome incorporation depends on its eukaryote-specific extension domain (Figure 1B, D). Consistent with this interpretation, Acl4 directly binds RpL4, forming a stable complex that was reconstituted *in vitro* using

either *Chaetomium thermophilum* or yeast orthologs (Figure 2A). *In vivo*, Acl4 is distributed throughout the cell but is enriched in the nucleus (Figure 1E). Acl4 is not essential but *acl4*Δ cells display a slow growth phenotype (Figure 1F). The growth defect of *acl4*Δ cells can be partly rescued by expressing an extra *RPL4* copy (Figure 1F) and appears to be the consequence of a defective ribosome synthesis, indicated by reduction of free 60S relative to 40S subunits and the appearance of halfmer polysomes in ribosome profiles (Figure 1G).

RpL4 interacts with crescent-shaped Acl4 via an exposed loop

To gain structural insight into the Acl4-RpL4 interaction, we crystallized a *Chaetomium thermophilum* Acl4 fragment (for *E. coli* expression constructs, see Table S3), lacking the unstructured acidic C-terminal extension (residues 1-338), and solved its structure at a 2.9-Å resolution (Figure 2B, Table 1). *ctAcl4* exhibits a superhelical tetratricopeptide repeat (TPR) fold in its central α-helical region, which adopts an overall crescent-shaped structure (Figure 2B). *ctAcl4* is composed of 13 α-helices (αA-αM), which are arranged in a zig-zag fashion with a right-handed superhelical twist, forming 6.5 TPRs (Figure 2B). Whereas TPRs 1, 2, 5, and 6 adopt canonical TPRs, repeats 3 and 4 possess atypical extended helices (αF, αG) that form a characteristic tower in the middle of the domain, separating the protein into two halves (Figure S2C). No electron density was observed for the N-terminal basic region (residues 1-28) and thus this region is presumed to be disordered.

A multi-species sequence alignment shows that Acl4 is evolutionarily conserved with orthologs in fungi, insects, mollusks, worms, fish and plants (Figure S3A). As previously observed for other ribosome assembly chaperones (Holzer et al., 2013; Kressler et al., 2012), no mammalian Acl4 orthologs could be identified in database searches, suggesting that mammalian Acl4 protein sequences are evolutionarily more distant, or acquired an alternative shielding mechanism for nascent RpL4. Analysis of the conservation and electrostatic potential of the *ctAcl4* surface reveals that the concave and bottom surface are evolutionarily conserved and display a strong negative surface potential (Figure 2C, D).

These findings are in line with structure-based truncations of *ctAcl4* and *ctRpL4*, which revealed that the C-terminal *ctAcl4* half (residues 156-398), comprising the central

long helix αG , and the protruding *ctRpL4* loop, which is an evolutionarily conserved feature in all prokaryotic and eukaryotic RpL4s, are necessary and sufficient structural elements for the *ctAcl4-ctRpL4* interaction (Figures 2E, F). To identify mutants that impair *scAcl4* binding, we designed site-specific charge-swap mutations of invariant positively charged residues in the stem (R95E, R98E) and deleted the tip ($\Delta 63-87$) of the *scRpL4* loop, and found that they indeed disrupted the interaction (Figures 2G, S3B).

Negative-stain electron microscopy of the reconstituted *ctAcl4•ctRpL4* complex revealed a horseshoe-shaped structure that is large enough to accommodate the crescent shaped *ctAcl4*, binding to *ctRpL4* with its C-terminal half (Figures 2H, S2D). In this arrangement, the concave surface of *ctAcl4* could bind the protruding *ctRpL4* loop and shield it (Figure 2I). Consistent with this notion, the *ctRpL4* loop is protected against trypsin digestion only when bound to *ctAcl4* (Figure S4A). In contrast, the *ctRpL4* C-terminal extension, which is dispensable for the interaction with *ctAcl4* (Figure 2F), is sensitive to proteolysis in the *ctAcl4•ctRpL4* complex (Figure S4A). Thus, the C-terminal extension is accessible for other interactions in the cell (see below).

RpL4 loop mutants deficient in Acl4 binding enter ribosome biogenesis but display a growth defect

We investigated how *RPL4* loop mutants impaired in Acl4 binding affect yeast growth and cellular pathways. *RPL4 R95E R98E* was able to complement the non-viable *rpl4 Δ* null strain, but with a slower growth at higher temperatures (Figure 3A). As shown in the pulse-chase assay RpL4 R95E R98E was assembled into mature 60S subunits even though Acl4 was not found on nascent RpL4 in the 5 min pulse (Figure 3B). In contrast, the tip deletion variant *rpl4 $\Delta 63-87$* induced non-viability (Figure S1B). However, RpL4 $\Delta 63-87$ was not present in mature but rather in pre-60S particles that arrested at a late stage, as suggested by the co-enrichment of nuclear export factor Nmd3 and cytoplasmic assembly factors Lsg1 and Yvh1 (Figure 3B). Apparently, 60S subunits carrying RpL4 $\Delta 63-87$ cannot finally mature, indicating that correct insertion of the RpL4 loop into the lining of the peptide exit tunnel is linked to an unknown checkpoint control implemented in a late 60S maturation step. Altogether, the data indicate that Acl4 has an assisting role in RpL4 ribosome assembly.

The RpL4 C-terminal extension harbors a nuclear import signal and plays a pivotal role in the disassembly of the Acl4•RpL4 complex at the pre-ribosome

Owing to the finding that the RpL4 C-terminal extension is not required for Acl4 binding but is essential for cell growth (see Figures 3B, S1B), we looked for other eukaryote-specific functions. The RpL4 extension contains two putative PY-NLSs in series (residues 301-345), which induce a strong nuclear accumulation when fused to GFP (Figure 3D). Mutation of three lysine residues (K314A, K315A, K319A) in this extended NLS (residues 277-362) significantly diminished the NLS activity. Moreover, shorter constructs of this sequence (ranging from residues 303-320 or 311-333), which still carry these crucial lysine residues, have lost nuclear targeting activity. Altogether this data suggests that RpL4 contains an extended and complex NLS in its C-terminal extension.

Prompted by these findings, we tested interaction of the Acl4•RpL4 complex with nuclear import receptors. It was possible to bind *in vitro* the *ctAcl4•ctRpL4* heterodimer to the PY-NLS receptor *ctKap104* (Kressler et al., 2012; Suel and Chook, 2009), forming a stoichiometric *ctAcl4•ctRpL4•ctKap104* complex as determined by size-exclusion chromatography coupled to multiangle light scattering (Figure 2A). However, *scKap104* was not bound to the *scAcl4•scRpL4ΔExt* dimer, lacking the PY-NLS region (residues 277-362) (Figure 3E). These data suggest that Kap104 binds to the C-terminal extension of RpL4 to mediate nuclear import of the Acl4•RpL4 complex.

In the nucleus, RpL4 has to dissociate from Acl4 to be incorporated into the nascent ribosome. Previous studies established that RpL4 incorporation occurs early in ribosome formation together with several other RPs, including RpL18, RpL7, and RpL20 (Ben-Shem et al., 2011; Gamalinda and Woolford, 2014), which all reside in the vicinity of the C-terminal RpL4 extension in the fully assembled 60S ribosomal subunit (Figures 1A, 3C). Thus, we hypothesized that the interaction of the RpL4 extension with the pre-ribosomal surface could trigger the disassembly of the Acl4•RpL4 complex and would allow the insertion of the RpL4 molecule into the nascent pre-60S ribosome. To test this hypothesis, we mutated residues in two regions of the RpL4 extension that directly contact either RpL18 (corresponding mutation in RpL4: I289A, I290A, I295A) or the eukaryote-specific expansion segment 7 (ES7) of the 25S rRNA (corresponding mutation in RpL4: K332E and F334A) (Figure 3C). *In vivo*, both sets of RpL4 extension mutants were efficiently

imported into the nucleus, but exhibited a slow growth phenotype at elevated temperatures (Figures 4A, S4B). Pulse-chase assays showed that the RpL4 mutant deficient in RpL18 binding was inefficiently released from Acl4 with a delayed assembly into the 60S subunit (Figure 4B). The RpL4 mutant deficient in ES7 binding showed a similar albeit weaker defect, underlining that the RpL4 C-terminal extension uses multiple contact sites for recruitment to the nascent 60S subunit.

To verify that RpL18 is a critical factor assisting in the release of RpL4 from Acl4, we mutated hydrophobic RpL18 residues (L32E, V129D) that are in contact with hydrophobic RpL4 residues on the mature ribosome (Figures 3C, 4C). *In vivo*, the RpL18 mutant deficient in RpL4 binding showed similar defects as the RpL4 mutant deficient in RpL18 binding, with impaired cell growth at 37 °C and a defective 60S subunit synthesis (Figure 4A, D). Finally, the purification of chromosomally TAP-tagged RpL4 from strains harboring either wild-type RpL18 or the RpL4-binding deficient mutant revealed that the latter indeed showed an enrichment of Acl4 (Figure 4E). This data suggests that the C-terminal extension of RpL4 delivers the Acl4•RpL4 complex to the pre-ribosome, triggering RpL4 release from Acl4 and incorporation into the 60S ribosomal subunit.

In conclusion, we propose a model of how a nascent ribosomal protein (RpL4) can be incorporated into the pre-ribosome in a hierarchical fashion (Figure 4F). The key to this coordinated process is an assembly chaperone, Acl4, which shields RpL4 until timely release and insertion into the pre-ribosome is possible. RpL4 shielding could encompass the prevention of non-productive interactions or cellular degradation. RpL4 dissociation from Acl4 is triggered by the eukaryote-specific extension of RpL4, which contacts co-evolved sites on the pre-60S surface. The ~100 fold higher abundance of RpL4 suggests that Acl4 enters a new assembly cycle after RpL4 delivery. Such a mechanism could explain how eukaryotic cells achieve coordinated assembly of interdependent RPs into the maturing ribosome and shines light on the evolution of eukaryotic RP extensions regarding a role in ribosome assembly. The finding that no obvious mammalian Acl4 ortholog could be identified despite its sequence conservation in many eukaryotic species requires further investigation to allow for the generalization of this mechanism, but at the same time opens the door for the development of novel anti-fungal agents.

ACKNOWLEDGEMENTS

We thank Tobias Stuwe for help with crystallography and the scientific staff of APS Beamline GM/CA-CAT at the Argonne National Laboratory for their support with X-ray diffraction measurements. The operations at APS are supported by the Department of Energy and the National Institutes of Health. We also thank the EM core facility at Heidelberg University (Dr. Stefan Hillmer). F.M.H. was supported by a PhD student fellowship of the Boehringer Ingelheim Fonds. A.H. was supported by Caltech startup funds, the Albert Wyrick V Scholar Award of the V Foundation for Cancer Research, the 54th Mallinckrodt Scholar Award of the Edward Mallinckrodt, Jr. Foundation, and a Kimmel Scholar Award of the Sidney Kimmel Foundation for Cancer Research. This work was supported by grants from the Deutsche Forschungsgemeinschaft to E.H. (SFB638 B2; Hu363/10-4).

EXPERIMENTAL PROCEDURES

Recombinant protein expression and purification

Chaetomium thermophilum (*ct*) Acl4, RpL4, and Kap104 DNA fragments or *Saccharomyces cerevisiae* (*sc*) Acl4 and RpL4 fragments were amplified by PCR and ligated into the bacterial expression vectors pGEX-6P-1 (GE Healthcare), a modified pET28b vector (Novagene) (Mossessova and Lima, 2000). Quickchange mutagenesis (Stratagene) was performed to create mutant RpL4 and constructs were confirmed by DNA sequencing. *sc*Acl4, RpL4, and Kap104 ORFs were ligated into pETDuet-1 or pET24d-GST expression vectors. For further details on construct generation and a full list of constructs, see Table S3.

Bacterial expression constructs were transformed in *Escherichia coli* BL21-CodonPLUS(DE3)-RIL cells (Stratagene) and grown in LB medium to an OD₆₀₀ of approximately 0.6 prior to induction with 0.5 mM isopropyl β-D-thiogalactoside (IPTG). Cells were harvested after 20 hours of expression at 23 °C and resuspended in a buffer containing 20 mM TRIS (pH 8.0), 500 mM NaCl, 5 mM β-mercaptoethanol (β-ME, Sigma), 2 μM bovine lung aprotinin (Sigma) and complete EDTA-free protease inhibitor cocktail (Roche) and were subsequently flash frozen in liquid nitrogen. Cell lysis was performed with a cell disruptor (Avestin) and lysates were centrifuged for 1 hour with 40,000 x g at 4 °C. The supernatant fraction was applied to a Ni-NTA column, equilibrated with a buffer containing 20 mM TRIS (pH 8.0), 500 mM NaCl, 10 mM imidazole (pH 8.0) and 5 mM β-ME. Proteins were eluted with a linear gradient of buffer containing 20 mM TRIS (pH 8.0), 500 mM NaCl, 500 mM imidazole (pH 8.0), and 5 mM β-ME. The eluted protein was cleaved with ubiquitin-like-specific protease 1 (ULP1) and dialyzed against a buffer containing 20 mM TRIS (pH 8.0), 100 mM NaCl, and 5 mM β-ME. After cleavage, the protein was applied to an additional Ni-NTA column followed by further binding to a HiTrapQ HP (GE Healthcare) ion exchange column. The protein was eluted by applying a linear gradient of a buffer containing 20 mM TRIS (pH 8.0), 2 M NaCl, and 5 mM DTT. The protein was concentrated and loaded on a HiLoad 16/60 Superdex 75 or HiLoad 16/60 Superdex 200 column (GE Healthcare). *ct*Acl4¹⁻³³⁸ was purified in buffer containing

150 mM NaCl instead of 100 mM NaCl. Seleno-L-methionine-labeled (SeMet) proteins were produced in a synthetic medium that suppresses methionine biosynthesis, following standard protocols (Doublet, 1997).

Protein-protein interaction analysis

GST pull-down experiments were performed by incubating 100 μ l glutathione coupled Sepharose beads (GE Healthcare) with lysate of 1 liter bacterial expression cultures for 1 hour at 4 °C. The beads were washed three times with 50 ml of cold buffer containing 20 mM TRIS (pH 8.0), 100 mM NaCl and 5 mM DTT and were centrifuged at 500 x g at 4 °C. Bound proteins were eluted by incubating beads for 15 minutes on ice with a buffer containing 20 mM TRIS (pH 8.0), 100 mM NaCl, 5 mM DTT, and 20 mM reduced glutathione. The elution and load fractions were analyzed by SDS-PAGE and visualized with Coomassie brilliant blue staining. GST-coupled protein binding experiments of *E. coli* expressed yeast proteins were performed by incubating 50 μ l GST-bait coupled Sepharose beads (GE Healthcare) with purified protein eluates from *E. coli*. The beads were washed four times with 5 ml cold buffer containing 20 mM TRIS-HCl (pH 7.5), 150 mM NaCl, 50 mM potassium acetate, 2 mM magnesium acetate, 0.1 % (w/v) NP-40. Bound proteins were eluted by boiling beads with SDS-sample buffer for 3 minutes at 95 °C. The elution and load fractions were analyzed by SDS-PAGE and visualized with Coomassie brilliant blue staining.

Tandem-affinity purification from yeast cells

Tandem-affinity purifications were, unless otherwise indicated, performed in a buffer containing 20 mM TRIS-HCl (pH 7.5), 150 mM NaCl, 50 mM potassium acetate, 2 mM magnesium acetate, 0.1 % (w/v) NP-40 as previously described (Stelter et al., 2012). Cell pellets from 2 L cultures were broken in a mill (pulverisette FRITSCH) and extracts were centrifuged for 10 minutes at 3,400 x g, followed by centrifugation of the supernatant for 20 minutes at 35,000 x g. The supernatant was incubated with 300 μ l IgG beads (GE Healthcare) at 4 °C for 1 hour. IgG beads (GE Healthcare) with bound bait were washed four times with 10 ml purification buffer (0.01 % (w/v) NP-40). TEV cleavage was performed at 16 °C for 90 minutes in purification buffer (0.01 % (w/v) NP-40) and TEV-

eluates (450 μ l) were subsequently incubated with 30 μ l slurry of anti-Flag beads (Sigma-Aldrich) for 45 minutes. For Calmodulin binding, TEV eluate was supplemented with 2 mM CaCl_2 and incubated with 400 μ l slurry of Calmodulin beads (Sigma-Aldrich P4385) at 4 $^\circ\text{C}$. Protein bound anti-Flag beads were washed with 5 ml purification buffer (0.01 % (w/v) NP-40) and eluted with 35 μ l Flag peptide (100 $\mu\text{g}/\text{ml}$; Sigma-Aldrich E3290) for 45 minutes at 4 $^\circ\text{C}$. Protein bound to Calmodulin beads were washed with 10 ml purification buffer and eluted with 540 μ l elution buffer (10 mM TRIS-HCl (pH 8), 5 mM EGTA (pH 8.0), 50 mM NaCl) for 10 minutes at 30 $^\circ\text{C}$.

Multiangle light scattering

Purified *ctAcl4*²⁸⁻³³⁸, *ctAcl4*¹⁻³⁹⁸•*ctRpL4*¹⁻³⁶⁵ and *ctKap104*¹⁻⁹³⁸ were characterized by multiangle light scattering (MALS) followed by size exclusion chromatography (SEC). Protein samples were injected onto a Superdex 200 10/300 GL size exclusion column (GE Healthcare) pre-equilibrated with buffer containing 20 mM TRIS (pH 8.0), 100 mM NaCl, and 5 mM DTT. An 18-angle light scattering detector (DAWN HELEOS II; Wyatt Technology), a dynamic light scattering detector (DynaPro Nanostar; Wyatt Technology), and a refractive index detector (Optilab T-rEX; Wyatt Technology) were connected in series, following the size exclusion column. SEC-MALS data were collected at 25 $^\circ\text{C}$ at a flow rate of 0.5 ml/min every 1 second. ASTRA6 was used for data analysis to obtain the molecular mass and mass distribution (polydispersity) of the proteins (Wyatt, 1997).

Crystallization and data collection

Diffracting crystals of *ctAcl4*¹⁻³³⁸ and *ctAcl4*²⁸⁻³³⁸ were obtained by hanging drop vapor diffusion, combining 1 μ l of protein solution and 1 μ l of crystallization buffer and incubation at 21 $^\circ\text{C}$. Crystals of *ctAcl4*¹⁻³³⁸ grew at a protein concentration of 15 mg/ml in a crystallization buffer containing 0.2 M ammonium citrate tribasic (pH 7.0) and 20 % (w/v) PEG 3350. Crystals of *ctAcl4*²⁸⁻³³⁸ crystallized in a buffer containing 0.2 M potassium formate and 20 % (w/v) PEG 3350. X-ray diffraction data were collected at 100 K at the GM/CA beamline at the Advanced Photon Source (APS) to a resolution of 2.9 Å from native and SeMet-labeled protein that both crystallized in the spacegroup P1. X-ray diffraction data were processed using HKL2000 denzo/scalepack package

(Otwinowski and Minor, 1997). The structure of *ctAcl4*²⁸⁻³³⁸ was solved by multi-wavelength anomalous dispersion (MAD) using anomalous scattering data collected at the selenium edge of SeMet-labeled protein. SHELXD was used to locate four selenium sites and SHARP was used to calculate initial phases (Bricogne et al., 2003; Sheldrick, 2008). Density modification with solvent flattening and histogram matching was performed using DM (Bailey, 1994). The obtained experimental electron density map was of high quality and allowed for generating a model for *ctAcl4*²⁸⁻³³⁸. Iterative rounds of model building in COOT and refinement in PHENIX yielded a final model of *ctAcl4*²⁸⁻³³⁸, consisting of residues 28 to 310. No electron density was observed for residues 311 to 338 and these residues are presumed to be disordered (Adams et al., 2010; Emsley and Cowtan, 2004). The structure was refined with R_{work} and R_{free} values of 21.9 % and 25.6 %, respectively. The structure of *ctAcl4*¹⁻³³⁸ was solved by molecular replacement using the structure of the *ctAcl4*²⁸⁻³³⁸ fragment as a search model in Phaser and refined with R_{work} and R_{free} values of 24.0 % and 26.1 %, respectively (Mccoy et al., 2007). The final model of *ctAcl4*¹⁻³³⁸ contained residues 28 to 310, no electron density was observed for residues 1 to 27 and 311 to 338. Both structures possess excellent stereochemistry with no residues in the disallowed region of the Ramachandran plot as determined with MolProbity (Davis et al., 2007). Details of the data collection and structure refinement statistics are summarized in Table 1.

Electron microscopy and image processing

The *ctAcl4*•*ctRpL4* complex was loaded onto a 200 μl cushion of 7.5 % (v/v) glycerol in a buffer containing NB (20 mM HEPES (pH 7.5), 150 mM NaCl, 50 mM potassium acetate, 2 mM magnesium acetate, 5 % (v/v) glycerol) followed by a linear 10-30 % (v/v) glycerol and 0-0.15 % (v/v) glutaraldehyde gradient (Kastner et al., 2008). Samples were centrifuged in a SW 60 Ti Rotor (Beckman Coulter) for 18 hours at 336,000 x g and 4 °C, before 200 μl fractions were collected and analyzed by a negative staining EM.

For negative staining, 5 μl of sample were placed on a freshly glow-discharged, carbon-coated grid, and then washed three times with water, stained with 2 % (w/v) uranyl acetate and dried. Micrographs were recorded using a JEOL JEM-1400 microscope equipped with a 2 K x 2 K Tietz-CCD camera (TVIPS F224) at a nominal magnification of 20,000,

operating at 120 kV. The nominal pixel size was 3.9 Å. 13,616 single particles were selected semi-automatically using “Boxer” with an 80×80-pixel window (Ludtke et al., 1999). Subsequent image processing was carried out in IMAGIC-4D (van Heel et al., 1996). Particles were band-pass filtered and normalized in their gray value distribution and mass centered. Two-dimensional alignment and iterative refinement of class averages followed the procedures described in (Liu and Wang, 2011). The calculation of the 3D maps followed the procedures described in (Lutzmann et al., 2005). Relative spatial orientations were determined by sinogram correlation. This process was started several times, beginning with different class averages for the initial determination of Euler angles. Three-dimensional maps were calculated using the exact weighted back projection algorithm. Determination of Euler angles and calculation of 3D maps were repeated until the map converged into a stable shape, from which projections could be generated that were similar to all of the initially observed class averages. A 3D map was further refined by projection matching. This process was repeated several times. The resolution was estimated by dividing images randomly into two equally populated sets, reconstructing separately and determining the Fourier shell correlation. The estimated resolution based on where the 1/2 bit curve crosses the FSC curve is 26 Å. The final volumes were visualized using the UCSF Chimera package software and Gaussian filtered (Pettersen et al., 2004).

Illustrations and figures

Structure figures were generated using PyMOL (www.pymol.org). The electrostatic potential was calculated using APBS (Baker et al., 2001). Sequence alignments were generated using ClustalX (Jeanmougin et al., 1998) and colored with ALSCRIPT (Barton, 1993).

Ribosome profiling

Ribosome polysome profiles were analyzed by sucrose gradient centrifugation. Logarithmic growing yeast strains at an OD₆₀₀ of ~0.8 were incubated with 0.1 mg/ml cycloheximide for 15 minutes. 200 ml of cells were harvested at an OD₆₀₀ of ~0.8 and lysed in 600 µl buffer, containing 20 mM HEPES (pH 7.5), 1 mM EGTA, 2.5 mM MgCl₂, and 10 mM KCl, using glass beads and vortexing. 200 µl of the cell extract were layered onto

a 10-45 (w/v) % linear sucrose gradient and centrifuged for 16 hours at 66,800 x g and 4 °C.

FIGURES

Main figures

Figure 1. Acl4 is a chaperone of nascent RpL4

Figure 2. Biochemical and structural analysis of the Acl4-RpL4 interaction

Figure 3. The conserved loop of nascent RpL4 is protected by Acl4 until ribosome insertion

Figure 4. The C-terminal extension of RpL4 coordinates the incorporation of RpL4 into the pre-ribosome

Supplemental figures

Figure S1. Growth analysis of *RPL4* wild-type and *rpl4* mutants in a *rpl4AA rpl4BA* shuffle strain

Figure S2. Further analyses of the *ctAcl4* crystal structure

Figure S3. Acl4 homologs are found up to vertebrates and RpL4 loop mutants are defective in Acl4 binding

Figure S4. RpL4-Acl4 interaction stabilizes the RpL4 core/loop but not the extension from tryptic digest, and mutations in the RpL4 extension impairing ribosome interaction still allow nuclear import

Figure S5. Original silver stained polyacrylamide gel (uncut) and Western blots

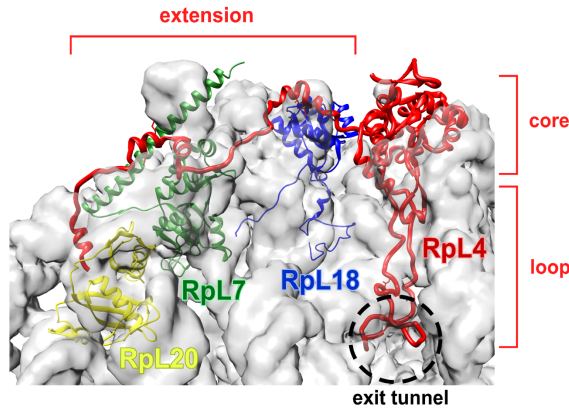
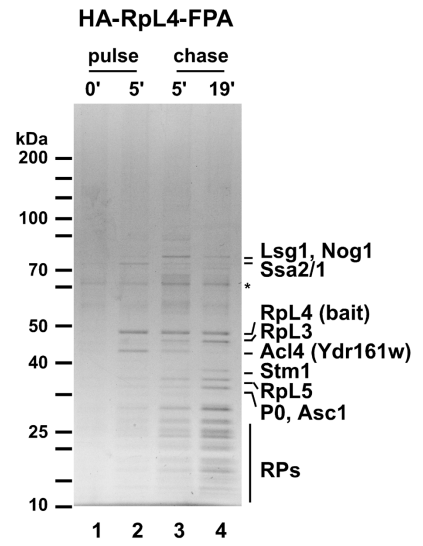
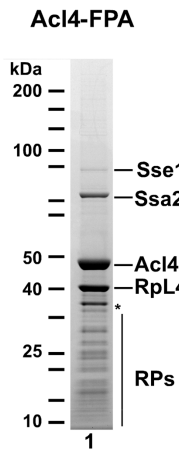
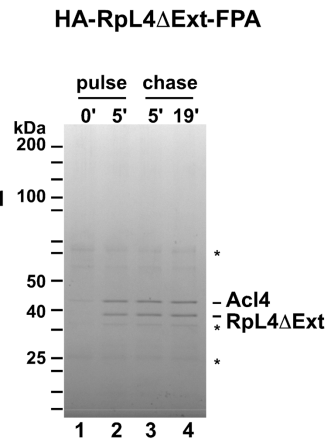
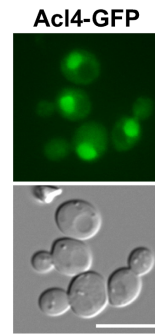
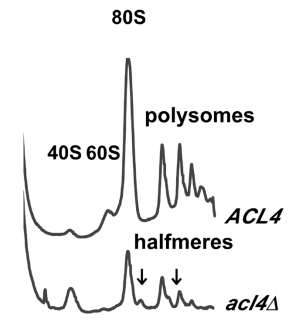
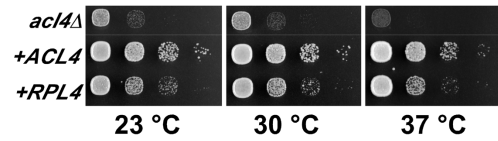
A**B****C****D****E****G****F**

Figure 1. Acl4 is a chaperone of nascent RpL4

(A) Structure of RpL4 as observed in the *S. cerevisiae* 80S ribosome (PDB IDs: 3U5E and 3U5D) (Ben-Shem et al., 2011). Surface of 25S and 5S rRNA are shown in grey. RpL4, RpL18, RpL7 and RpL20 are shown in red, blue, green, and yellow, respectively. Core, loop and C-terminal extension of RpL4 are indicated. (B) Epitope pulse-chase analysis of RpL4 in yeast cells. HA-RpL4-Flag-ProtA was pulsed for 0 (lane 1) or 5 minutes (lane 2), and chased for 5 (lane 3) and 19 minutes (lane 4). Newly synthesized RpL4 was tandem affinity-purified and analyzed by SDS-PAGE and Coomassie staining. Indicated proteins were identified by mass-spectrometry. Asterisk indicates keratin contaminant. (C) Tandem affinity-purification (Flag-ProtA) of chromosomal tagged Acl4 from yeast cells. Eluates were analyzed by SDS-PAGE, Coomassie staining and mass-spectrometry. Asterisk indicates RpL4 breakdown. (D) Epitope pulse-chase analysis of RpL4 Δ Ext. HA-RpL4 Δ Ext-Flag-ProtA was pulsed for 0 (lane 1) or 5 minutes (lane 2), and chased for 5 (lane 3) and 19 minutes (lane 4). Asterisks indicate keratin and IgG contaminants. (E) Acl4 localization in yeast cells. Acl4 was chromosomal tagged with GFP and the localization was assessed by fluorescence microscopy. Scale bar is 5 μ m. (F) Growth analysis of Δ acl4 strain. The impaired growth of Δ acl4 was partially rescued by expression of an additional copy of *RPL4* from a centromeric plasmid. (G) Polysome profiles of *ACL4* and Δ acl4 cells. Deletion of *ACL4* impairs the synthesis of the 60S ribosomal subunit. Free 80S, 60S, 40S, and polysomes are indicated. Arrows point to the observed halfmer polysomes. See also Figure S1.

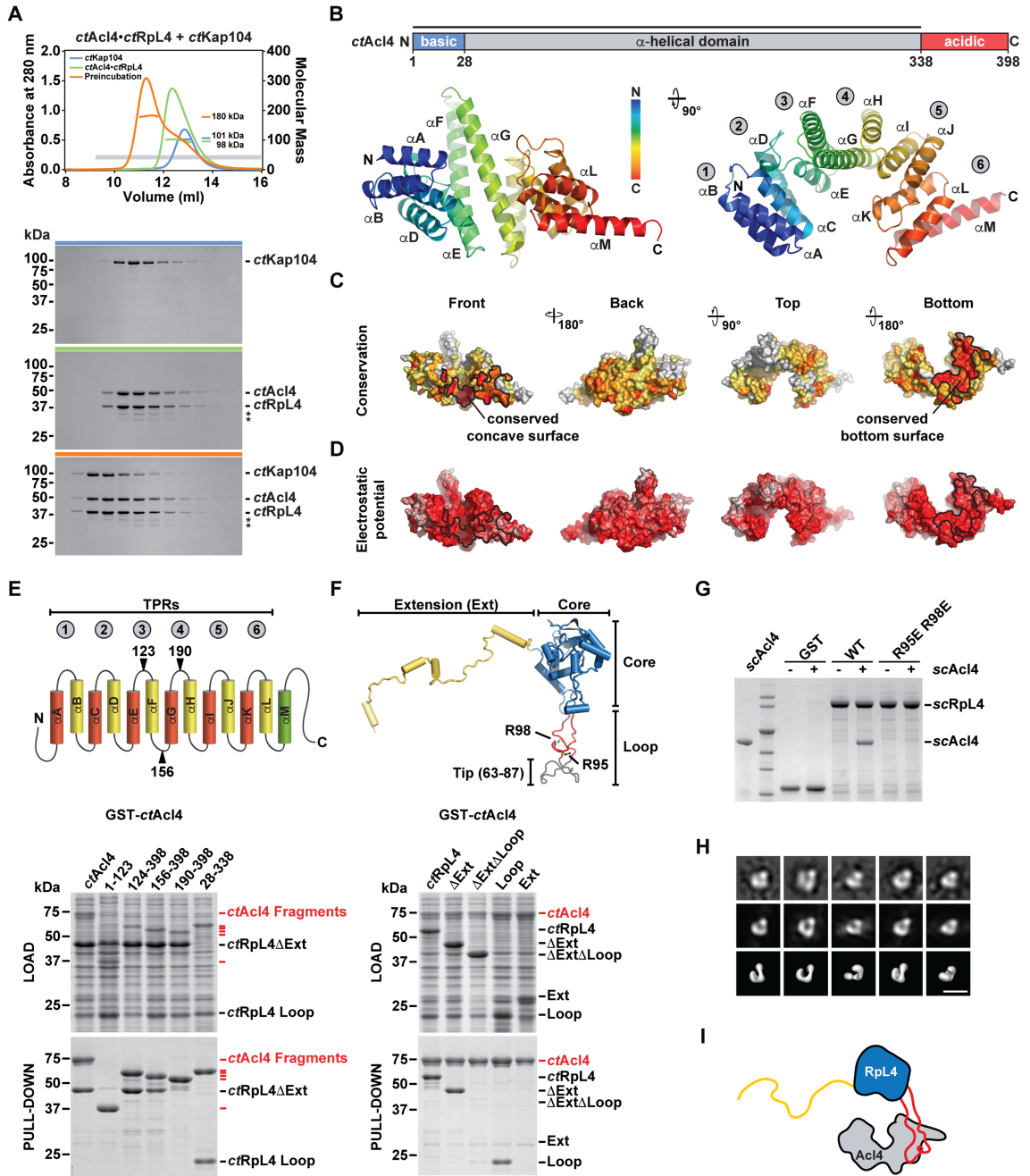


Figure 2. Biochemical and structural analysis of the Acl4-RpL4 interaction

(A) Size-exclusion chromatography coupled to multiangle light scattering (SEC-MALS) analysis of the *ctAcl4*•*ctRpL4*•*ctKap104* trimeric nuclear import complex. The absorbance at 280 nm is plotted against the elution volume of a Superdex 200 10/300 GL size exclusion column and overlaid with the molecular mass of the different proteins. Fractions that were resolved on a SDS-PAGE gel and visualized by Coomassie staining are indicated by a gray bar. Degradation products are labeled with asterisks. (B) Domain representation and crystal structure of *ctAcl4*. Blue, basic N-terminal region; grey, α -helical region; red, acidic C-terminal region. The crystallized fragment is indicated with a black bar. The *ctAcl4* crystal structure is shown in cartoon representation in two different orientations. (C) Surface representation of *ctAcl4* in four different orientations colored according to a multi-species sequence alignment (Figure S3A). Sequence conservation is shaded from white (< 40 % similarity) to yellow (40 % similarity) to red (100 % identity). (D) Surface representation colored according to electrostatic potential from -10 $k_B T/e$ (red) to +10 $k_B T/e$ (blue). (E) GST pull-down of *ctAcl4* variants. Red, GST-*ctAcl4* variants (bait); black, *ctRpL4* variants. Loaded (top, soluble lysate fraction) and pulled-down (bottom) fractions were analyzed by SDS-PAGE and Coomassie staining. *ctAcl4* fragment boundaries are shown above each lane and are depicted in a cartoon. (F) GST pull-down of *ctRpL4* variants. Red, GST-*ctAcl4* (bait); black, *ctRpL4* variants. *ctRpL4* fragment boundaries are shown above each lane and indicated in the *scRpL4* structure extracted from the *S. cerevisiae* ribosome (PDB ID: 1VXY) (Svidritskiy et al., 2014). (G) His-*scAcl4*, GST-*scRpL4* and GST-*scRpL4* R95E/R98E were purified from *E. coli*. GST, GST-*scRpL4* and GST-*scRpL4* R95E/R98E beads were incubated with excess of imidazole eluted His-*scAcl4*. Beads were boiled and eluates were resolved on a SDS-PAGE gel and visualized by Coomassie Brilliant Blue staining. (H) Negative stain electron microscopic analysis of recombinant purified *ctAcl4*•*ctRpL4* complex. Two-dimensional class average of *ctAcl4*•*ctRpL4* complex (top row) determined by multivariate statistical analysis matching with the projections of the final 3D model (middle row) and surface representations of equivalent orientations (bottom row). (I) Model of the Acl4•RpL4 complex. See also Figure S2 and S3.

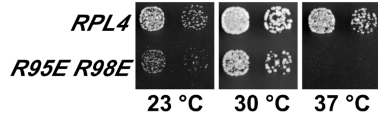
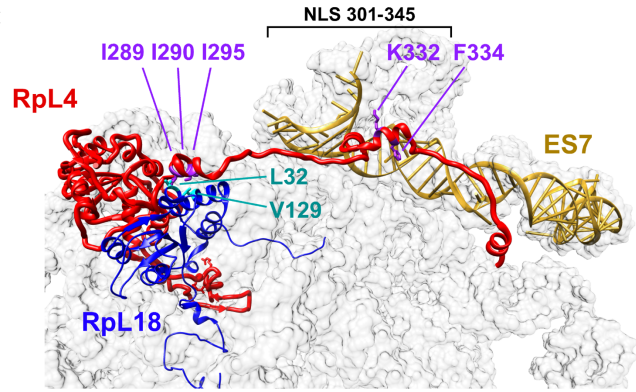
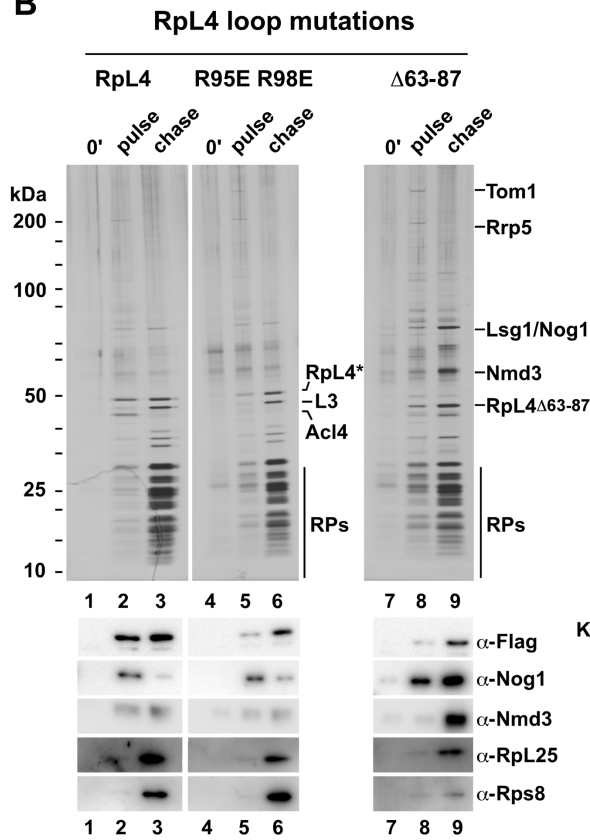
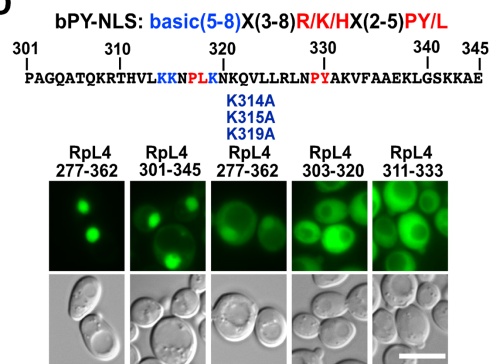
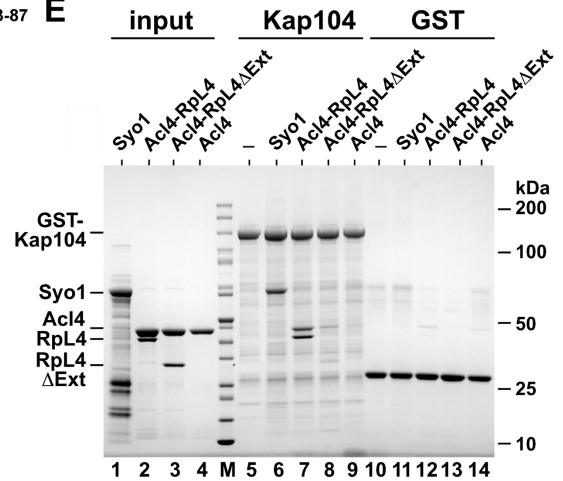
A**C****B****D****E**

Figure 3. The conserved loop of nascent RpL4 is protected by Acl4 until ribosome insertion

(A) *rpl4AA/rpl4BA* knockout strain was transformed with an empty vector or vectors containing *RPL4A* and *RPL4A R95E/R98E*. The *RPL4A* wild-type copy on the URA-plasmid was shuffled out on FOA. The respective clones were spotted on YPD plates and incubated at 23 °C, 30 °C and 37 °C for 2 days. (B) Epitope pulse-chase analysis of RpL4, RpL4 R95E/R98E and RpL4Δ63-87. Wild-type (lanes 1-3) or mutants (lanes 4-9) of RpL4 were pulsed for 0 minutes (lanes 1, 4, 7) or 5 minutes (lanes 2, 5, 8) as a GAL::tcapt-HA-RpL4-Flag-ProtA version and subsequently chased for 19 minutes (lanes 3, 6, 9). HA-RpL4-Flag-ProtA was affinity-purified and resolved on a SDS-PAGE gel and visualized by silver staining or western blot (lower panel). Indicated proteins were identified by mass-spectrometry. Acl4 was not found in the purification of RpL4 R95E/R98E and RpL4Δ63-87 (lanes 5, 8). The original blot and silver SDS-PAGE gel were sliced and put together from one gel/blot image (original blot and SDS-PAGE gel, see Figure S5). Accordingly, wild-type RpL4 (lanes 1-3) in Figures 3B and 4B are derived from the same gel. (C) Part of the 60S subunit with RpL4, RpL18 and the extended sequence of 25S RNA (ES7) are depicted. The RpL4 residues I289, I290 and I295 (violet) contacting RpL18 residues L32 and V129 (cyan), and RpL4 residues K332 and F334 (violet) contacting ES7 RNA (goldenrod) are shown. (D) The C-terminal extension (residues 277-362) of RpL4 targets the attached 3xyEGFP reporter to the nucleus. A 44-residue region of the C-terminal RpL4 extension (residues 301-345), containing two potential PY-NLS sequences (consensus is indicated above the amino acid sequence), is sufficient for efficient nuclear import. Mutation of three lysine residues (K314A, K315A, K319A) in the extended NLS (residues 277-362) or shorter constructs, ranging from residues 303-320 or 311-333, were also tested for NLS activity by monitoring nuclear accumulation of GFP. Scale bar is 5 μm. (E) The *scKap104* interaction with *scRpL4* is dependent on its C-terminal extension. GST-*scKap104*, His₆-*scAcl4*•*scRpL4*, His₆-*scAcl4*•*scRpL4*ΔExt, His₆-*scAcl4* and His₆-*scSyo1* (positive control for *scKap104* binding) (Kressler et al., 2012) were expressed in *E. coli* and affinity-purified (lanes 1-5, input). GST-*scKap104* (lanes 5-9) and GST (lanes 10-14) were immobilized on GSH-beads and incubated with excess of purified His₆-

scAcl4•scRpL4, *His₆-scAcl4•scRpL4ΔExt*, *His₆-scAcl4*, and *His₆-scSyo1*. Samples were analyzed by SDS-PAGE and Coomassie staining. See also Figures S4 and S5.

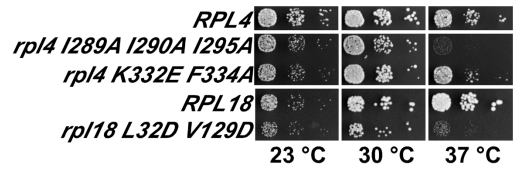
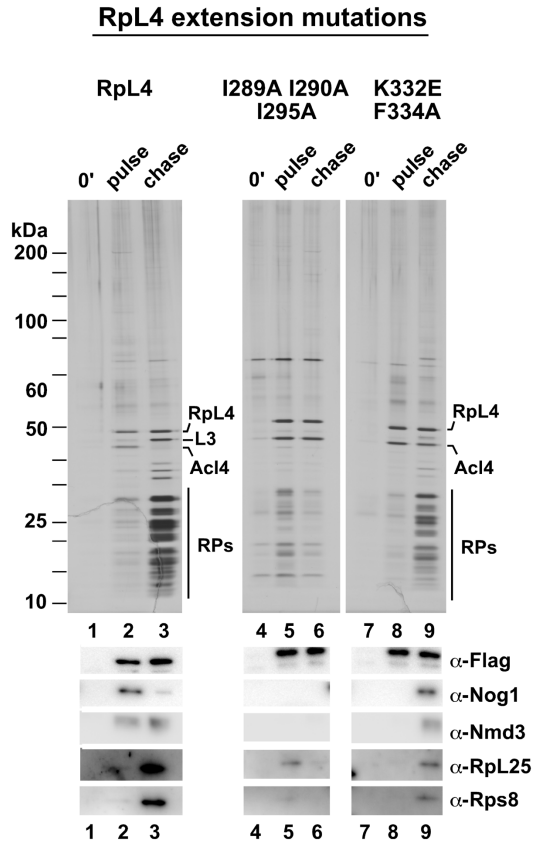
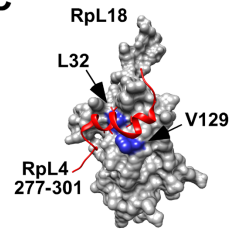
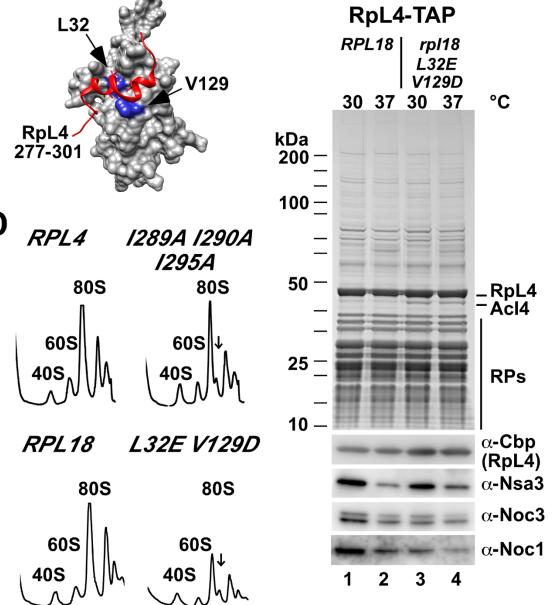
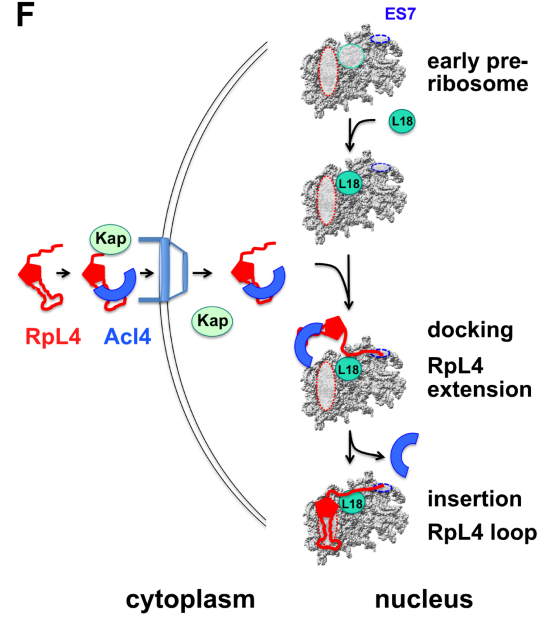
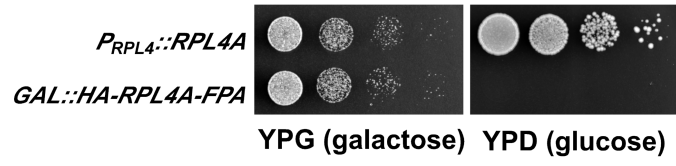
A**B****C****E****F**

Figure 4. The C-terminal extension of RpL4 coordinates the incorporation of RpL4 into the pre-ribosome

(A) Growth analysis of *RPL4* (wt), *RPL4-RPL18* contact and *RPL4-ES7* contact mutants. (B) Epitope pulse-chase analysis of RpL4 (lanes 1-3) and RpL4-RpL18 contact mutant (I289A, I290A, and I295A) (lane 4-6) and RpL4-ES7 contact mutant (K332E and F334A) (lanes 7-9). RpL4 and RpL4 mutants were pulsed for 0 minutes (lanes 1, 4, and 7) or 5 minutes (lanes 2, 5, and 8) as a GAL::tcapt-HA-RpL4-Flag-ProtA version and subsequently chased for 19 minutes (lanes 3, 6, and 9), tandem affinity-purified (TAP) and separated by SDS-PAGE and analyzed by silver staining and western blot. Blot and silver gel were sliced and put together from one gel/blot image (original blot and gel, see Figure S5). Accordingly, wild-type RpL4 (lanes 1-3) in Figures 3B and 4B are derived from the same gel. (C) Close up view of the RpL4-RpL18 interaction, as observed in the *S. cerevisiae* 80S ribosome (PDB ID: 3U5E) (Ben-Shem et al., 2011). Surface depiction of RpL18 (grey) and ribbon illustration of the RpL18 contact region of the C-terminal RpL4 extension (residues 277-301, red). Mutated RpL18 residues are indicated in blue (PDB IDs: 3U5E, 3U5D) (Ben-Shem et al., 2011). (D) Ribosome profiles of wild-type and *rpl4 I289A I290A I295A* or *rpl18 L32E V129D* (RpL4-RpL18 contact mutant) strains analyzed by sucrose gradient centrifugation of cell homogenate. (E) Tandem affinity-purification (TAP) of chromosomal tagged RpL4 in *RPL18* (lanes 1 and 2) and *rpl18 L32E V129D* (lanes 3 and 4) strains. Purified samples were separated by SDS-PAGE and analyzed by Coomassie staining and western blot (lower panel). Cells (lanes 2 and 4) were shifted to 37 °C for 2.5 hours. The band labeled as Acl4 was identified by mass spectrometry. (F) Model of coordinated RpL4 assembly into the maturing ribosome. Details as discussed in the text. See also Figures S4 and S5.

A



B

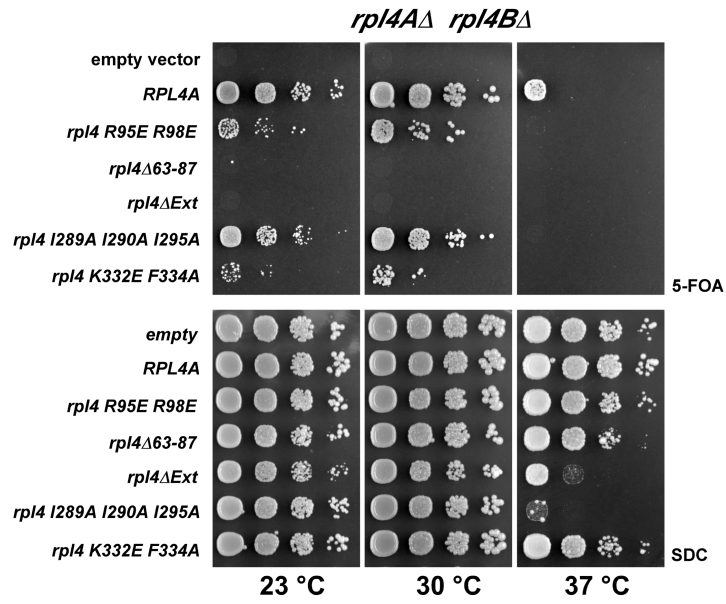


Figure S1. Growth analysis of *RPL4* wild-type and *rpl4* mutants in a *rpl4AΔ rpl4BΔ* shuffle strain (related to Figure 1)

(A) Growth complementation of HA-*RPL4*-FPA. *pGAL::HA-RPL4A*-FPA or *pP_{RPL4}-RPL4A* were transformed into *rpl4AΔ rpl4BΔ* shuffle strain and plated on SC-galactose plates. Transformants were transferred on 5-FOA plates and after 3 days spotted on YP-galactose and YP-glucose plates. It was incubated for 3 days at 30 °C. (B) Growth analysis of *rpl4* mutants. The indicated wild-type *RPL4A* and *rpl4A* mutants were cloned into centromeric plasmids under the endogenous *RPL4* promoter. Plasmids were transformed into *rpl4AΔ rpl4BΔ* shuffle strain. Transformants were spotted on 5-FOA and SC plates for 3 days at 23 °C, 30 °C, and 37 °C.

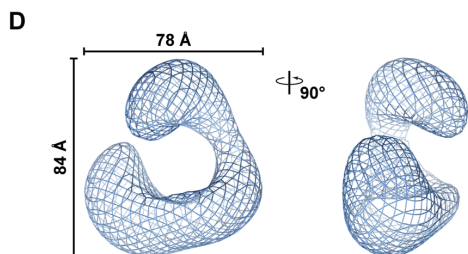
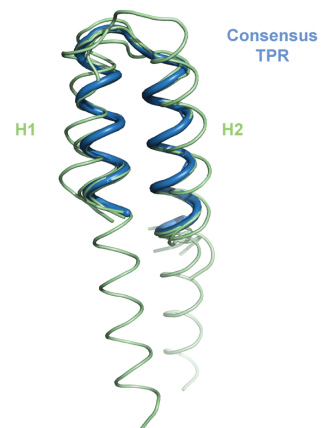
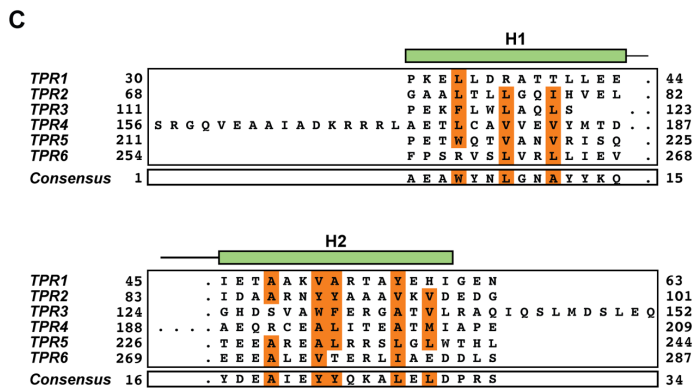
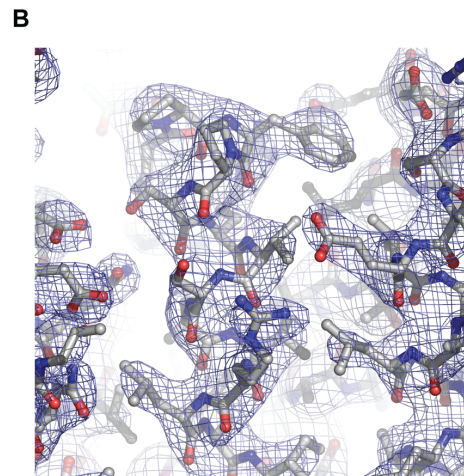
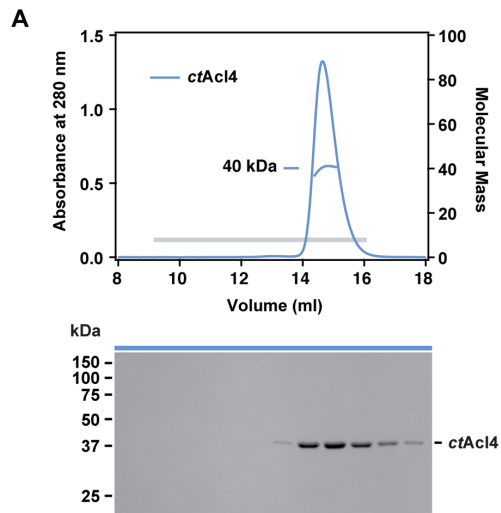
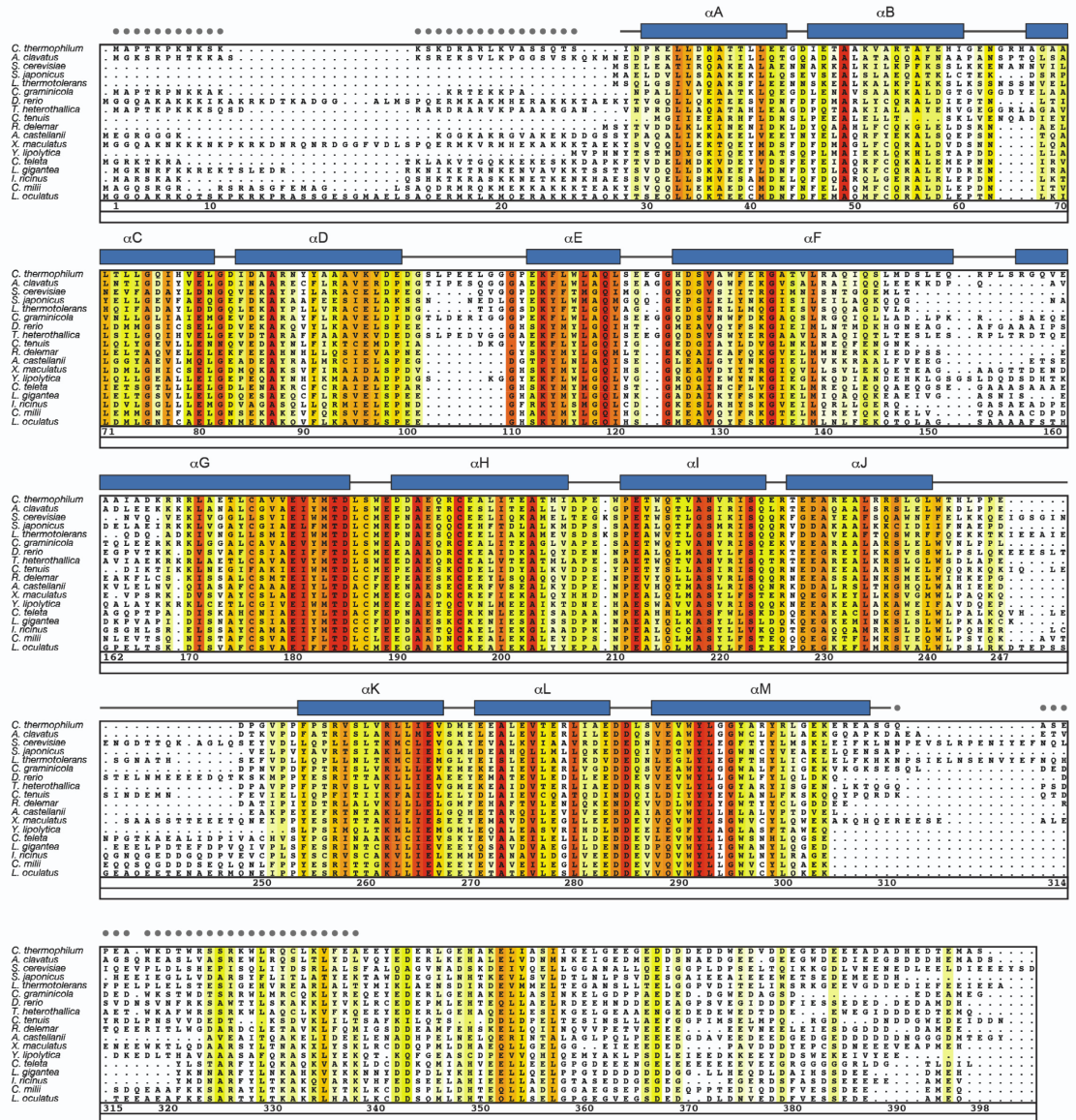


Figure S2. Further analyses of the *ctAcl4* crystal structure (related to Figure 2)

(A) Size-exclusion chromatography coupled to multiangle light scattering (SEC-MALS) analysis of the *ctAcl4*²⁸⁻³³⁸ fragment. The absorption at 280 nm is plotted against the elution volume from a Superdex 200 10/300 GL gel filtration column and overlaid with the observed molecular mass. The grey bar indicates fractions that were resolved on a SDS-PAGE gel and visualized by Coomassie staining. (B) Representative section of final 2|F_o|-|F_c| electron density map contoured at 1.0σ. (C) Structural superposition of the six *ctAcl4* TPRs and a canonical TPR (PDB ID: 2AVP) (Kajander et al., 2007). Structure-guided sequence alignment of *ctAcl4* TPRs and the canonical TPR. Consensus hydrophobic sequences are highlighted in orange. (D) Selected views of the volume representation of the *ctAcl4*•*ctRpL4* complex.

A



B

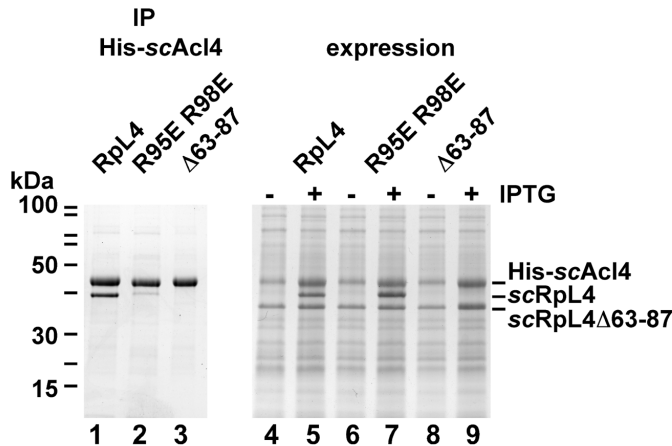


Figure S3. Acl4 homologs are found up to vertebrates and RpL4 loop mutants are defective in Acl4 binding (related to Figures 2 and 3)

(A) Acl4 protein sequences from 18 species were aligned and colored according to a Blosum62 matrix with white (< 40 % similarity), yellow (40 % similarity) to dark red (100 % identity). The residue numbering is according to the *ctAcl4* sequence. The α -helical regions are represented as blue rectangles and are numbered from αA to αM . Gray dots indicate residues of the crystallized construct that were not observed in the electron density map and are presumed to be disordered. (B) RpL4 loop mutants are impaired in Acl4 binding. Co-expression of His₆-*scAcl4*•*scRpL4*, His₆-*scAcl4*•*scRpL4* R95E/R98E loop mutant, and His₆-*scAcl4*•*scRpL4*Δ63-87 in *E. coli*. Right panel shows whole cell lysates before and after IPTG induction (lanes 4-9). The imidazole eluates (lanes 1-3) of purified His₆-*scAcl4*•*scRpL4*, His₆-*scAcl4*•*scRpL4* R95E/R98E loop mutant, and His₆-*scAcl4*•*scRpL4*Δ63-87 were analyzed by SDS-PAGE and Coomassie staining.

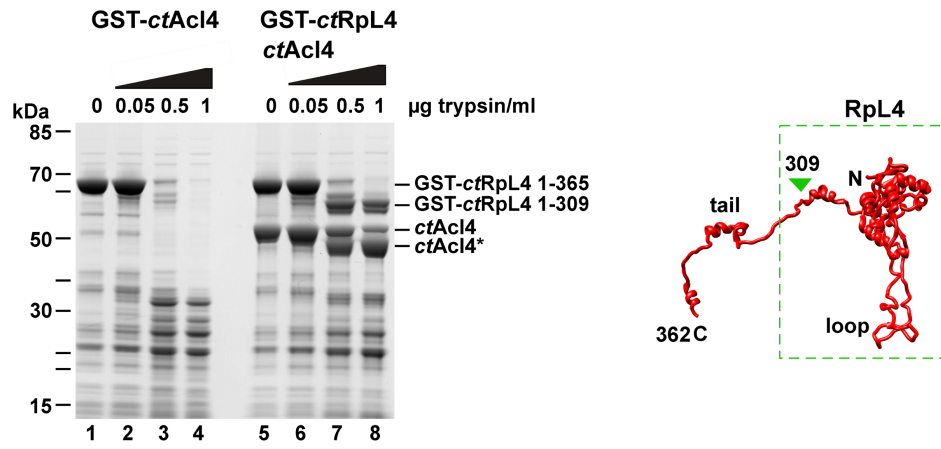
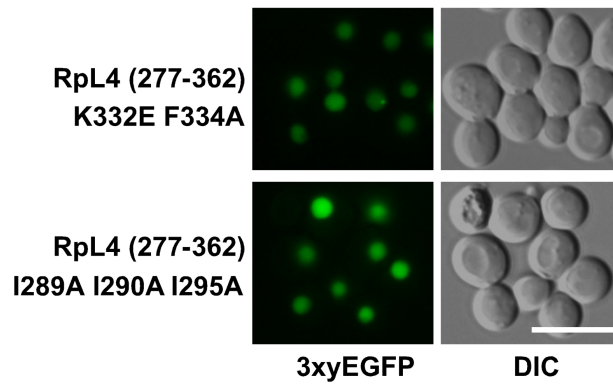
A**B**

Figure S4. RpL4-Acl4 interaction stabilizes the RpL4 core/loop but not the extension from tryptic digest, and mutations in the RpL4 extension impairing ribosome interaction still allow nuclear import (related to Figures 2 and 4)

(A) Tryptic digest of *ctRpL4* and *ctAcl4•ctRpL4*. GST-*ctRpL4* and His₆-*ctAcl4* were purified from *E. coli*. GST-*ctRpL4* was immobilized on GSH-beads and incubated with excess of His₆-*ctAcl4* (lanes 5-8). After washing, beads were incubated with increasing amounts of trypsin for 30 minutes at 37 °C. Beads were boiled with sample buffer and analyzed by SDS-PAGE and Coomassie staining. Tryptic fragments were analyzed by Orbitrap mass-spectrometry. Right panel illustrates the RpL4 (yeast) structure with the stable fragment highlighted by the dashed box (Ben-Shem et al., 2011). (B) The RpL4 extension mutants, RpL4²⁷⁷⁻³⁶² K332E/F334A and RpL4²⁷⁷⁻³⁶² I289A/I290A/I295A, target the 3xyEGFP reporter efficiently to the nucleus. Scale bar is 5 μm.

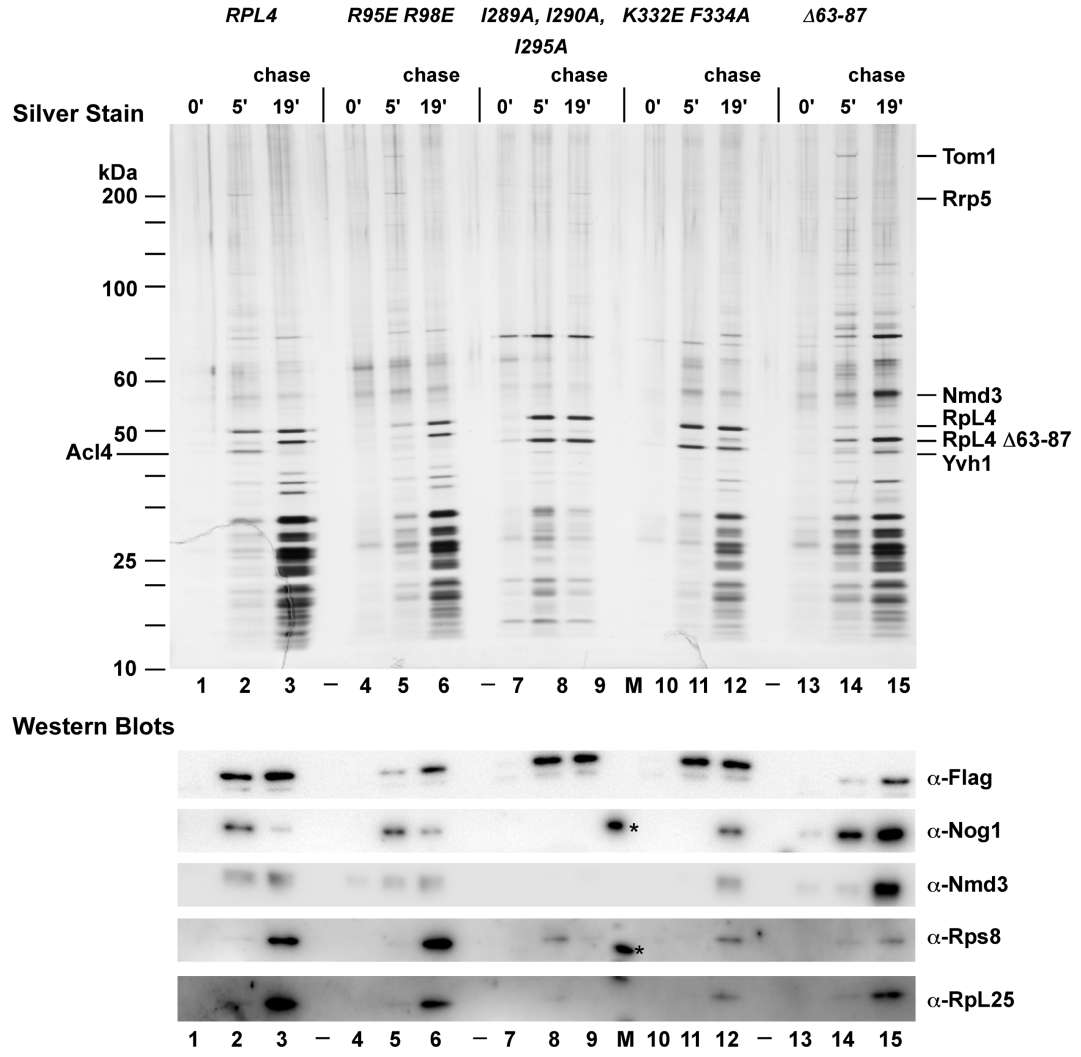


Figure S5. Original silver stained polyacrylamide gel (uncut) and Western blots (related to Figures 3 and 4)

Epitope pulse-chase analysis of RpL4 (lanes 1-3), RpL4 R95E/R98E (lanes 4-6) and RpL4 I289A/I290A/I295A (lanes 7-9), RpL4 K332E/F334A (lanes 10-12), RpL4 Δ 63-87 (lanes 13-15). RpL4 and RpL4 mutants were pulsed for 0 minutes (lanes 1, 4, 7, 10, and 13) or 5 minutes (lanes 2, 5, 8, 11, and 14) based on GAL::tcapt-HA-RpL4-Flag-ProtA constructs and subsequently chased for 19 minutes (lanes 3, 6, 9, 12, and 15), followed by tandem affinity-purification and SDS-PAGE. Shown is the initial SDS-PAGE gel, which was stained with silver (upper panel), and derived Western blots using the indicated antibodies (lower panels). Gel and blots were cut and arranged for better illustration of the data (see Figures 3B and 4B). Antibody cross-reaction with standard protein bands (M) is indicated by asterisks.

TABLES

Main table

Table 1. Crystallographic analysis

Supplemental tables

Table S1. Yeast strains (related to Figures 1, 3, and 4)

Table S2. Yeast constructs (related to Figures 1, 3, and 4)

Table S3. Bacterial expression constructs (related to Figures 2 and 3)

Table 1. Crystallographic analysis

Data collection				
Protein	<i>ctAc14</i> ¹⁻³³⁸	<i>ctAc14</i> ²⁸⁻³³⁸	<i>ctAc14</i> ²⁸⁻³³⁸	<i>ctAc14</i> ²⁸⁻³³⁸
PDB code	4YNW	4YNV	-	-
Synchrotron	APS ^a	APS	APS	APS
Beamline	GM/CA-CAT	GM/CA-CAT	GM/CA-CAT	GM/CA-CAT
Space group	P1	P1	P1	P1
Cell parameters				
<i>a</i> , <i>b</i> , <i>c</i> (Å)	49.1, 49.6, 80.3	49.5, 49.1, 80.1	49.5, 49.1, 80.0	49.5, 49.1, 80.0
α , β , γ (°)	98.6, 100.1, 98.5	98.7, 97.9, 100.0	98.7, 97.8, 100.0	98.7, 97.8, 100.0
	<i>Native</i>	<i>Se peak</i>	<i>Se inflection</i>	<i>Se remote</i>
Wavelength (Å)	0.97939	0.97936	0.97961	0.94937
Resolution (Å)	50.0 – 2.9	20.0 – 2.95	20.0 – 3.0	20.0 – 3.0
<i>R</i> _{sym} (%) ^b	4.6 (77.5)	5.9 (10.9)	6.1 (78.5)	6.5 (80.9)
$\langle I \rangle / \langle \sigma I \rangle$ ^b	40.3 (2.0)	22.4 (1.9)	21.2 (1.8)	20.5 (1.7)
Completeness (%) ^b	97.2 (85.8)	99.0 (98.3)	99.0 (98.3)	99.1 (98.6)
No. observations	125,935	119,531	115,067	113,041
No. unique reflections ^b	16,367 (1,424)	30,229 (3,037)	29,064 (2,926)	28,582 (2,895)
Redundancy ^b	7.7 (6.6)	4.0 (3.9)	4.0 (3.9)	4.0 (3.9)
Refinement				
Resolution (Å)	20.0 – 2.9	20.0 – 2.95		
No. reflections total	15,661	30,019		
No. reflections test set	1,577	1,497		
<i>R</i> _{work} / <i>R</i> _{free} (%)	24.0 / 26.1	21.9 / 25.6		
No. atoms	4,432	4,432		
Protein	4,432	4,432		
<i>B</i> -factors				
Protein	128.6	102.6		
R.m.s. deviations				
Bond lengths (Å)	0.002	0.003		
Bond angles (°)	0.5	0.6		
Ramachandran plot^c				
Favored (%)	94.7	94.5		
Additionally allowed (%)	5.3	5.5		
Outliers (%)	0.0	0.0		
Rotamer outliers (%) ^c	0.0	0.0		
C α outliers (%) ^c	0.0	0.0		
Clash score ^c	2.2	1.72		
MolProbity score ^c	1.36	1.30		

^a APS, Advanced Photon Source^b Highest resolution shell is shown in parentheses^c As determined by MolProbity (Davis et al., 2007)

Table S1. Yeast strains (related to Figures 1, 3, and 4)

Name	Genotype	Source
W303	<i>Matα, ade2-1, his3-11, 15, leu2-3,112, trp1-1, ura3-1, can1-100</i>	Kressler et al.
DS1-2b	<i>Matα, his3-Δ200, leu2Δ1, trp1-Δ63, ura3-52</i>	Lutzmann et al.
<i>rpl4AA/rpl4BA</i> shuffle	W303, <i>Matα, rpl4A::HIS3MX6, rpl4B::natNT2</i> pRS316- <i>RPL4A</i>	this study
<i>rpl18AΔ/rpl18BΔ</i> shuffle	W303, <i>Matα, rpl18A::HIS3MX6, rpl18B::natNT2</i> pRS316- <i>RPL18A</i>	this study
<i>rpl18AΔ/rpl18BΔ</i> shuffle	Ds1-2b, <i>Matα, rpl18A::HIS3MX6, rpl18B::natNT2</i> pRS316- <i>RPL18A</i>	this study
<i>acl4Δ</i>	W303, <i>Matα, acl4::HIS3MX6</i>	this study
<i>ACL4-GFP</i>	W303, <i>Matα, ACL4-GFP::HIS3MX6</i>	this study
<i>ACL4-FPA</i>	DS1-2b, <i>Matα, ACL4-FPA::natNT2</i>	this study
<i>RPL4-TAP</i>	Ds1-2b, <i>Matα, rpl18A::HIS3MX6, rpl18B::natNT2</i> pRS315- <i>RPL18A</i>	this study
<i>RPL4-TAP rpl18 L32E V129D</i>	Ds1-2b, <i>Matα, rpl18A::HIS3MX6, rpl18B::natNT2</i> pRS315- <i>rpl18A L32E V129D</i>	this study

Table S2. Yeast constructs (related to Figures 1, 3, and 4)

Name	Genotype	Source
Yeplac181-GAL::tcapt-HA-stop- <i>RPL4A</i> -FPA	2 μ , <i>LEU2</i> (Nde1/BamH1)	this study
Yeplac181-GAL::HA-stop- <i>RPL4A</i> -FPA	2 μ , <i>LEU2</i> (Nde1/BamH1)	this study
Yeplac181-GAL::HA- <i>RPL4A</i> -FPA	2 μ , <i>LEU2</i> (Nde1/BamH1)	this study
Yeplac181-GAL:: <i>RPL4A</i>	2 μ , <i>LEU2</i> (Nde1/BamH1)	this study
Yeplac181-GAL::tcapt-HA-stop- <i>RPL4A</i> (1-276)-FPA	2 μ , <i>LEU2</i> (Nde1/BamH1)	this study
Yeplac181-GAL::tcapt-HA-stop- <i>RPL4A</i> Δ 63-87-FPA	2 μ , <i>LEU2</i> (Nde1/BamH1) serine inserted	this study
Yeplac181-GAL::tcapt-HA-stop- <i>RPL4A</i> R95E R98E-FPA	2 μ , <i>LEU2</i> (Nde1/BamH1)	this study
Yeplac181-GAL::tcapt-HA-stop- <i>RPL4A</i> I289A I290A I295A-FPA	2 μ , <i>LEU2</i> (Nde1/BamH1)	this study
Yeplac181-GAL::tcapt-HA-stop- <i>RPL4A</i> K332E F334A-FPA	2 μ , <i>LEU2</i> (Nde1/BamH1)	this study
Yeplac112-GAL:: <i>RPL4A</i>	2 μ , <i>TRP1</i> (Nde1/BamH1)	this study
Yeplac112-GAL:: <i>ACL4</i>	2 μ , <i>TRP1</i> (Nde1/BamH1)	this study
pOME	CEN, <i>TRP1</i> tRNA ^{Ome} -Tyr, tRNA synthetase	Chin et al.
pUN100- <i>ACL4</i>	CEN, <i>LEU2</i> <i>PACL4</i> , <i>TACL4</i> (BamH1/Sac1)	this study
pUN100- <i>RPL4A</i>	CEN, <i>LEU2</i> <i>PRPL4A</i> , <i>TRPL4A</i> (BamH1/Xho1)	this study
pRS316- <i>RPL4A</i>	CEN, <i>URA3</i> <i>PRPL4A</i> , <i>TRPL4A</i> (BamH1/Xho1)	this study
pUN100- <i>RPL4A</i> - <i>TADH</i>	CEN, <i>LEU2</i> <i>PRPL4A</i> , <i>TADH</i> (BamH1/Xba1)	this study
pUN100- <i>RPL4A</i> R95E R98E- <i>TADH</i>	CEN, <i>LEU2</i> <i>PRPL4A</i> , <i>TADH</i> (BamH1/Xba1)	this study
pUN100- <i>RPL4A</i> Δ 63-87- <i>TADH</i>	CEN, <i>LEU2</i> <i>PRPL4A</i> , <i>TADH</i> (BamH1/Xba1)	this study
pUN100- <i>RPL4A</i> I298A I290A I295A	CEN, <i>LEU2</i> <i>PRPL4A</i> , <i>TRPL4A</i> (BamH1/Xho1)	this study
pUN100- <i>RPL4A</i> K332E F334A	CEN, <i>LEU2</i> <i>PRPL4A</i> , <i>TRPL4A</i> (BamH1/Xho1)	this study
pUN100- <i>RPL4A</i> 1-276	CEN, <i>LEU2</i> <i>PRPL4A</i> , <i>TRPL4A</i> (BamH1/Xho1)	this study
pADH111- <i>RPL4</i> (277-362)-(GA) ₅ -3xyEGFP	CEN, <i>LEU2</i> <i>PADH1</i> <i>TADH1</i>	this study
pADH111- <i>RPL4</i> (301-345)-(GA) ₅ -3xyEGFP	CEN, <i>LEU2</i> <i>PADH1</i> <i>TADH1</i>	this study
pADH111- <i>RPL4</i> (277-362K314AK315AK319A)-(GA) ₅ -3xyEGFP	CEN, <i>LEU2</i> <i>PADH1</i> <i>TADH1</i>	this study
pADH111- <i>RPL4</i> (303-320)-(GA) ₅ -3xyEGFP	CEN, <i>LEU2</i> <i>PADH1</i> <i>TADH1</i>	this study
pADH111- <i>RPL4</i> (311-333)-(GA) ₅ -3xyEGFP	CEN, <i>LEU2</i> <i>PADH1</i> <i>TADH1</i>	this study
pADH111- <i>RPL4</i> (277-362K332E F334A)-(GA) ₅ -3xyEGFP	CEN, <i>LEU2</i> <i>PADH1</i> <i>TADH1</i>	this study
pADH111- <i>RPL4</i> (277-362I289AI290AI295A)-(GA) ₅ -3xyEGFP	CEN, <i>LEU2</i> <i>PADH1</i> <i>TADH1</i>	this study
pRS315- <i>RPL18A</i>	CEN, <i>LEU2</i> <i>PRPL18A</i> <i>TRPL18A</i> (Not1/Xho1)	this study
pRS316- <i>RPL18A</i>	CEN, <i>URA3</i> <i>PRPL18A</i> <i>TRPL18A</i> (Not1/Xho1)	this study
pRS315- <i>RPL18A</i> L32E V129D	CEN, <i>LEU2</i> <i>PRPL18A</i> <i>TRPL18A</i> (Not1/Xho1)	this study

Table S3. Bacterial expression constructs (related to Figures 2 and 3)

Protein	Residues (Mutations)	Expression Vector	Restriction Sites 5', 3'	N-terminal overhang
<i>ctAcl4</i>	1-398	pET28b-SUMO	BamHI, NotI	S
<i>ctAcl4</i>	1-398	pGEX-6P-1	BamHI, NotI	GST-LEVLFQ ↓GMGS
<i>ctAcl4^a</i>	1-338	pET28b-SUMO	BamHI, NotI	S
<i>ctAcl4</i>	1-123	pGEX-6P-1	BamHI, NotI	GST-LEVLFQ ↓GMGS
<i>ctAcl4</i>	124-398	pGEX-6P-1	BamHI, NotI	GST-LEVLFQ ↓GMGS
<i>ctAcl4</i>	156-398	pGEX-6P-1	BamHI, NotI	GST-LEVLFQ ↓GMGS
<i>ctAcl4</i>	190-398	pGEX-6P-1	BamHI, NotI	GST-LEVLFQ ↓GMGS
<i>ctAcl4^a</i>	28-338	pET28b-SUMO	BamHI, NotI	S
<i>ctRpL4</i>	1-277	pET28b-SUMO	BamHI, NotI	His ₆ -SUMO-G ↓S
<i>ctRpL4</i>	1-277 (Δ49-111)	pET28b-SUMO	BamHI, NotI	His ₆ -SUMO-G ↓S
<i>ctRpL4</i>	49-111	pET28b-SUMO	BamHI, NotI	His ₆ -SUMO-G ↓S
<i>yAcl4</i>	1-387	pETDuet-1	BamHI, EcoRI	His ₆ -SQDP
<i>yAcl4-RpL4</i>	1-387, 1-362	pETDuet-1	BamHI, EcoRI	His ₆ -SQDP- <i>yAcl4</i>
<i>yAcl4-RpL4 ΔExt</i>	1-387, 1-276	pETDuet-1	BamHI, EcoRI	His ₆ -SQDP- <i>yAcl4</i>
<i>yAcl4-RpL4R95ER98E</i>	1-387, 1-362	pETDuet-1	BamHI, EcoRI	His ₆ -SQDP- <i>yAcl4</i>
<i>yAcl4-RpL4 Δ63-87</i>	1-362 (Δ63-87)	pETDuet-1	BamHI, EcoRI	His ₆ -SQDP- <i>yAcl4</i>
<i>ctAcl4</i>	1-398	pETDuet-1	BamHI, EcoRI	His ₆ -SQDP- <i>ctAcl4</i>
<i>ctAcl4-RpL4</i>	1-398, 1-365	pETDuet-1	BamHI, EcoRI	His ₆ -SQDP- <i>ctAcl4</i>
<i>ctRpL4</i>	1-365	pET24d	NdeI, BamHI	GST-TEV- <i>ctRpL4</i>
<i>ctKap104</i>	1-938	pET28b-SUMO	BamHI, NotI	S

^aConstructs that were used for crystallization of *ctAcl4*¹⁻³³⁸ and *ctAcl4*²⁸⁻³³⁸

↓Protease cleavage site

REFERENCES

- Adams, P.D., Afonine, P.V., Bunkoczi, G., Chen, V.B., Davis, I.W., Echols, N., Headd, J.J., Hung, L.W., Kapral, G.J., Grosse-Kunstleve, R.W., *et al.* (2010). PHENIX: a comprehensive Python-based system for macromolecular structure solution. *Acta Crystallogr D* 66, 213-221.
- Bailey, S. (1994). The Ccp4 Suite - Programs for Protein Crystallography. *Acta Crystallogr D* 50, 760-763.
- Baker, N.A., Sept, D., Joseph, S., Holst, M.J., and McCammon, J.A. (2001). Electrostatics of nanosystems: application to microtubules and the ribosome. *Proceedings of the National Academy of Sciences of the United States of America* 98, 10037-10041.
- Barton, G.J. (1993). ALSCRIPT: a tool to format multiple sequence alignments. *Protein engineering* 6, 37-40.
- Ben-Shem, A., Garreau de Loubresse, N., Melnikov, S., Jenner, L., Yusupova, G., and Yusupov, M. (2011). The structure of the eukaryotic ribosome at 3.0 Å resolution. *Science* 334, 1524-1529.
- Ben-Shem, A., Jenner, L., Yusupova, G., and Yusupov, M. (2010). Crystal structure of the eukaryotic ribosome. *Science* 330, 1203-1209.
- Bricogne, G., Vonrhein, C., Flensburg, C., Schiltz, M., and Paciorek, W. (2003). Generation, representation and flow of phase information in structure determination: recent developments in and around SHARP 2.0. *Acta Crystallogr D* 59, 2023-2030.
- Davis, I.W., Leaver-Fay, A., Chen, V.B., Block, J.N., Kapral, G.J., Wang, X., Murray, L.W., Arendall, W.B., Snoeyink, J., Richardson, J.S., *et al.* (2007). MolProbity: all-atom contacts and structure validation for proteins and nucleic acids. *Nucleic Acids Res* 35, W375-W383.

- Doublet, S. (1997). Preparation of selenomethionyl proteins for phase determination. *Method Enzymol* 276, 523-530.
- Eisinger, D.P., Dick, F.A., Denke, E., and Trumpower, B.L. (1997). SQT1, which encodes an essential WD domain protein of *Saccharomyces cerevisiae*, suppresses dominant-negative mutations of the ribosomal protein gene QSR1. *Mol Cell Biol* 17, 5146-5155.
- Emsley, P., and Cowtan, K. (2004). Coot: model-building tools for molecular graphics. *Acta Crystallogr D* 60, 2126-2132.
- Gamalinda, M., Ohmayer, U., Jakovljevic, J., Kumcuoglu, B., Woolford, J., Mbom, B., Lin, L., and Woolford, J.L., Jr. (2014). A hierarchical model for assembly of eukaryotic 60S ribosomal subunit domains. *Genes Dev* 28, 198-210.
- Gamalinda, M., and Woolford, J.L., Jr. (2014). Deletion of L4 domains reveals insights into the importance of ribosomal protein extensions in eukaryotic ribosome assembly. *Rna* 20, 1725-1731.
- Grummt, I. (1999). Regulation of mammalian ribosomal gene transcription by RNA polymerase I. *Prog Nucleic Acid Res Mol Biol* 62, 109-154.
- Holzer, S., Ban, N., and Klinge, S. (2013). Crystal structure of the yeast ribosomal protein rpS3 in complex with its chaperone Yar1. *J Mol Biol* 425, 4154-4160.
- Iouk, T.L., Aitchison, J.D., Maguire, S., and Wozniak, R.W. (2001). Rrb1p, a yeast nuclear WD-repeat protein involved in the regulation of ribosome biosynthesis. *Mol Cell Biol* 21, 1260-1271.
- Jäkel, S., Mingot, J.M., Schwarzmaier, P., Hartmann, E., and Görlich, D. (2002). Importins fulfil a dual function as nuclear import receptors and cytoplasmic chaperones for exposed basic domains. *EMBO J* 21, 377-386.
- James, A., Wang, Y., Raje, H., Rosby, R., and DiMario, P. (2014). Nucleolar stress with and without p53. *Nucleus* 5.

- Jeanmougin, F., Thompson, J.D., Gouy, M., Higgins, D.G., and Gibson, T.J. (1998). Multiple sequence alignment with Clustal X. *Trends Biochem Sci* 23, 403-405.
- Kajander, T., Cortajarena, A.L., Mochrie, S., and Regan, L. (2007). Structure and stability of designed TPR protein superhelices: unusual crystal packing and implications for natural TPR proteins. *Acta Crystallogr D Biol Crystallogr* 63, 800-811.
- Kastner, B., Fischer, N., Golas, M.M., Sander, B., Dube, P., Boehringer, D., Hartmuth, K., Deckert, J., Hauer, F., Wolf, E., *et al.* (2008). GraFix: sample preparation for single-particle electron cryomicroscopy. *Nat Methods* 5, 53-55.
- Koch, B., Mitterer, V., Niederhauser, J., Stanborough, T., Murat, G., Rechberger, G., Bergler, H., Kressler, D., and Pertschy, B. (2012). Yar1 protects the ribosomal protein Rps3 from aggregation. *J Biol Chem* 287, 21806-21815.
- Kressler, D., Bange, G., Ogawa, Y., Stjepanovic, G., Bradatsch, B., Pratte, D., Amlacher, S., Strauss, D., Yoneda, Y., Katahira, J., *et al.* (2012). Synchronizing nuclear import of ribosomal proteins with ribosome assembly. *Science* 338, 666-671.
- Lafontaine, D.L., and Tollervey, D. (2001). The function and synthesis of ribosomes. *Nat Rev Mol Cell Biol* 2, 514-520.
- Liu, X., and Wang, H.W. (2011). Single particle electron microscopy reconstruction of the exosome complex using the random conical tilt method. *J Vis Exp*.
- Ludtke, S.J., Baldwin, P.R., and Chiu, W. (1999). EMAN: semiautomated software for high-resolution single-particle reconstructions. *J Struct Biol* 128, 82-97.
- Lutzmann, M., Kunze, R., Stangl, K., Stelter, P., Toth, K.F., Bottcher, B., and Hurt, E. (2005). Reconstitution of Nup157 and Nup145N into the Nup84 complex. *The Journal of biological chemistry* 280, 18442-18451.
- McCann, K.L., and Baserga, S.J. (2013). Genetics. Mysterious ribosomopathies. *Science* 341, 849-850.

- Mccoy, A.J., Grosse-Kunstleve, R.W., Adams, P.D., Winn, M.D., Storoni, L.C., and Read, R.J. (2007). Phaser crystallographic software. *J Appl Crystallogr* *40*, 658-674.
- Melnikov, S., Ben-Shem, A., Garreau de Loubresse, N., Jenner, L., Yusupova, G., and Yusupov, M. (2012). One core, two shells: bacterial and eukaryotic ribosomes. *Nat Struct Mol Biol* *19*, 560-567.
- Mossessova, E., and Lima, C.D. (2000). Ulp1-SUMO crystal structure and genetic analysis reveal conserved interactions and a regulatory element essential for cell growth in yeast. *Molecular Cell* *5*, 865-876.
- Otwinowski, Z., and Minor, W. (1997). Processing of X-ray diffraction data collected in oscillation mode. *Method Enzymol* *276*, 307-326.
- Pettersen, E.F., Goddard, T.D., Huang, C.C., Couch, G.S., Greenblatt, D.M., Meng, E.C., and Ferrin, T.E. (2004). UCSF Chimera--a visualization system for exploratory research and analysis. *J Comput Chem* *25*, 1605-1612.
- Ramakrishnan, V., and White, S.W. (1998). Ribosomal protein structures: insights into the architecture, machinery and evolution of the ribosome. *Trends Biochem Sci* *23*, 208-212.
- Schaper, S., Fromont-Racine, M., Linder, P., de la Cruz, J., Namane, A., and Yaniv, M. (2001). A yeast homolog of chromatin assembly factor 1 is involved in early ribosome assembly. *Curr Biol* *11*, 1885-1890.
- Schutz, S., Fischer, U., Altvater, M., Nerurkar, P., Pena, C., Gerber, M., Chang, Y., Caesar, S., Schubert, O.T., Schlenstedt, G., *et al.* (2014). A RanGTP-independent mechanism allows ribosomal protein nuclear import for ribosome assembly. *Elife* *3*, e03473.
- Shajani, Z., Sykes, M.T., and Williamson, J.R. (2011). Assembly of bacterial ribosomes. *Annu Rev Biochem* *80*, 501-526.
- Sheldrick, G.M. (2008). A short history of SHELX. *Acta Crystallogr A* *64*, 112-122.

- Stelter, P., Kunze, R., Radwan, M., Thomson, E., Thierbach, K., Thoms, M., and Hurt, E. (2012). Monitoring spatiotemporal biogenesis of macromolecular assemblies by pulse-chase epitope labeling. *Mol Cell* 47, 788-796.
- Suel, K.E., and Chook, Y.M. (2009). Kap104p imports the PY-NLS-containing transcription factor Tfg2p into the nucleus. *J Biol Chem* 284, 15416-15424.
- Svidritskiy, E., Brilot, A.F., Koh, C.S., Grigorieff, N., and Korostelev, A.A. (2014). Structures of yeast 80S ribosome-tRNA complexes in the rotated and nonrotated conformations. *Structure* 22, 1210-1218.
- Teng, T., Thomas, G., and Mercer, C.A. (2013). Growth control and ribosomopathies. *Curr Opin Genet Dev* 23, 63-71.
- van Heel, M., Harauz, G., Orlova, E.V., Schmidt, R., and Schatz, M. (1996). A new generation of the IMAGIC image processing system. *J Struct Biol* 116, 17-24.
- Wang, W., Nag, S., Zhang, X., Wang, M.H., Wang, H., Zhou, J., and Zhang, R. (2014). Ribosomal Proteins and Human Diseases: Pathogenesis, Molecular Mechanisms, and Therapeutic Implications. *Med Res Rev*.
- Woolford, J.L., Jr., and Baserga, S.J. (2013). Ribosome biogenesis in the yeast *Saccharomyces cerevisiae*. *Genetics* 195, 643-681.
- Wyatt, P.J. (1997). Multiangle light scattering combined with HPLC. *Lc Gc-Mag Sep Sci* 15, 160-&.
- Zhang, Y., Wolfle, T., and Rospert, S. (2013). Interaction of nascent chains with the ribosomal tunnel proteins Rpl4, Rpl17, and Rpl39 of *Saccharomyces cerevisiae*. *J Biol Chem* 288, 33697-33707.

CHAPTER II

A CONSERVED QUALITY-CONTROL PATHWAY THAT MEDIATES DEGRADATION OF UNASSEMBLED RIBOSOMAL PROTEINS

This chapter was adapted from:

Min-Kyung Sung, Tanya R. Porras-Yakushi, Justin M. Reitsma, **Ferdinand M. Huber**, Michael J. Sweredoski, André Hoelz, Sonja Hess, Raymond J. Deshaies* (2016). A conserved quality-control pathway that mediates degradation of unassembled ribosomal proteins, *eLife*, 5, e19105.

ABSTRACT

Overproduced yeast ribosomal protein (RP) Rpl26 fails to assemble into ribosomes and is degraded in the nucleus/nucleolus by a ubiquitin-proteasome system quality control pathway comprising the E2 enzymes Ubc4/Ubc5 and the ubiquitin ligase Tom1. *tom1* cells show reduced ubiquitination of multiple RPs, exceptional accumulation of detergent-insoluble proteins including multiple RPs, and hypersensitivity to imbalances in production of RPs and rRNA, indicative of a profound perturbation to proteostasis. Tom1 directly ubiquitinates unassembled RPs primarily via residues that are concealed in mature ribosomes. Together, these data point to an important role for Tom1 in normal physiology and prompt us to refer to this pathway as ERISQ, for excess ribosomal protein quality control. A similar pathway, mediated by the Tom1 homolog Huwe1, restricts accumulation of overexpressed hRpl26 in human cells. We propose that ERISQ is a key element of the quality control machinery that sustains protein homeostasis and cellular fitness in eukaryotes.

INTRODUCTION

Protein quality control (PQC) has emerged as a major mechanism for maintaining protein homeostasis and cellular fitness. Defects in the cellular machinery that governs PQC cause multiple human diseases including multisystem proteinopathy (Brandmeir et al., 2008; Watts et al., 2004) and Amyotrophic Lateral Sclerosis (ALS) (Johnson et al., 2010; Kabashi and Durham, 2006). Other diseases, such as cancer, can exhibit heightened dependency on PQC pathways, which underlies the hypersensitivity of multiple myeloma cells to proteasome inhibitors (Cenci et al., 2012; Deshaies, 2014). Therefore, a deeper understanding of PQC will advance our understanding of both normal physiology and pathological states, and may enable novel approaches to treat multiple diseases.

Ribosome biogenesis is an intricate process involving many chaperones and assembly factors (Kressler et al., 2010; Warner, 1999). Ribosomal proteins made in excess over rRNA and other ribosomal proteins are among the most rapidly degraded proteins in eukaryotic cells (Abovich et al., 1985; Dephoure et al., 2014; Gorenstein and Warner, 1977; Torres et al., 2010; Torres et al., 2007; Warner, 1977), suggesting that proper coordination of synthesis and assembly is critical. Newly-synthesized human ribosomal proteins are subject to degradation by the proteasome in the nucleolus (Lam et al., 2007), and we recently found that overexpressed yeast ribosomal proteins that fail to assemble are conjugated with ubiquitin and degraded by the proteasome in the nucleus (Sung et al., 2016). Insoluble material that accumulates upon transient inhibition of the proteasome in yeast is strongly enriched for ribosomal proteins (Sung et al., 2016), pointing to PQC of unassembled ribosomal proteins as a major pathway of proteostasis. However, the PQC pathway that mediates ERISQ remains unknown - an important gap in our understanding of PQC that we set out to address.

RESULTS

Identification of Ubc4/5 and Tom1 as the E2 and E3 for ERISQ

We evaluated 115 mutant yeast strains, each lacking a different non-essential ubiquitin-proteasome system (UPS) gene, for those that accumulated non-essential ribosomal protein Rpl26a tagged with a FLAG epitope (Rpl26a^{FLAG}) upon its overexpression from the *GAL10* promoter. Accumulation of Rpl26a^{FLAG} in most mutants was similar to wild type (WT) and well below the level detected in *rpl26aΔrpl26bΔ* (Figure S1A, B), which accumulated overexpressed Rpl26a^{FLAG} due to lack of competition from endogenous Rpl26 (Sung et al., 2016). Notably, Rpl26a^{FLAG} accumulated to high levels in *tom1Δ* and *ubc4Δ* cells (Figures 1A and S1A, B).

Ubc4 is an ubiquitin-conjugating enzyme (E2) that is paralogous to and functionally redundant with Ubc5 (Seufert and Jentsch, 1990). Thus, subsequent experiments were performed with *ubc4Δubc5Δ* mutants. To test whether Ubc4/Ubc5 promoted ubiquitination of unassembled ribosomal proteins, we examined ubiquitin conjugates of overexpressed Rpl26a^{FLAG} that accumulated in proteasome-deficient *pre9Δ* cells (Sung et al., 2016). Ubiquitinated Rpl26a^{FLAG} was detected in *pre9Δ* but not in *ubc4Δubc5Δpre9Δ* cells (Figure 1B), indicating that Ubc4/Ubc5 promote ubiquitination of excess Rpl26a.

Tom1 is an E3 ubiquitin ligase of the HECT (homologous to E6AP C terminus) family. To investigate Tom1 function, we constructed *tom1^{CA}* strains in which the endogenous *TOM1* locus was mutated such that the catalytic cysteine3235 was changed to alanine (*tom1^{CA}*). We also appended a 3×HA epitope sequence to the 5' end of both *TOM1* and *tom1^{CA}*, and confirmed that the ^{3×HA}Tom1 and ^{3×HA}Tom1^{CA} proteins were expressed equivalently (Figure S2A) and the ^{3×HA}Tom1 was functional (Figure S2B-D). Using these strains, we established that Tom1 E3 activity was required for repression (Figure 1C) and ubiquitination (Figures 1D and S3A) of overexpressed Rpl26a^{FLAG}. Rpl26a^{FLAG} was co-immunoprecipitated with ^{3×HA}Tom1 (Figure 1E). Upon addition of an ubiquitination cocktail, immunoprecipitations of wild type but not mutant ^{3×HA}Tom1 ubiquitinated co-precipitated Rpl26a^{FLAG} (Figure S3B). Importantly, the activity defect of the ^{3×HA}Tom1^{CA} immunoprecipitate was complemented by adding ^{3×HA}Tom1 but not ^{3×HA}Tom1^{CA} prior to the ubiquitination reaction (Figures 1F and S3C).

To identify the population of Rpl26a^{FLAG} targeted by Tom1, we performed sucrose gradient fractionation. Mutant *tom1*^{CA} cells, like cells treated with the proteasome inhibitor bortezomib (Sung et al., 2016), accumulated unassembled Rpl26a^{FLAG} that co-fractionated with ^{3xHA}Tom1^{CA} (Figure 2A; note that ^{3xHA}Tom1 and ^{3xHA}Tom1^{CA} fractionated similarly). Co-immunoprecipitation of ^{3xHA}Tom1 or ^{3xHA}Tom1^{CA} with Rpl26a^{FLAG} was only detected in these low MW fractions (Figure 2B). Moreover, ubiquitinated Rpl26a^{FLAG} detected in low MW fractions from bortezomib-treated cells was almost entirely lost from *tom1*^{CA} cells (Figure 2B). Consistent with the reported localization of Tom1 (Huh et al., 2003), Rpl26a^{FLAG} or Rpl26a^{GFP} that accumulated upon their transient overexpression in *tom1*^{CA} cells were found in the nucleus and nucleolus (Figure 2C). Taken together, these data provide strong evidence that overexpressed Rpl26a failed to assemble into ribosomes and was directly bound and ubiquitinated by Tom1 in the nuclear/nucleolar compartments.

Tom1 targets a broad range of ribosomal proteins

To address whether Tom1 might have a broader role in promoting degradation of excess ribosomal proteins other than Rpl26a, we evaluated accumulation of a set of eight ectopically overexpressed ribosomal proteins in *tom1Δ* and WT cells. Similar to what we observed with bortezomib (Sung et al., 2016), deletion of *TOM1* enabled increased accumulation of at least seven of them (Figure S4A). We next sought to test whether Tom1 promoted degradation of unassembled ribosomal proteins in cells in which they were not deliberately overexpressed. We reasoned that if this is the case, Tom1 should directly associate with ribosomal proteins. Mass spectrometry of ^{3xHA}Tom1 immunoprecipitates from bortezomib-treated cells revealed enrichment for several ribosomal proteins, including Rpl26b (Figure S4B).

Ribosomal proteins are commonly identified in purified ubiquitin conjugates (Mayor et al., 2007; Mayor et al., 2005; Peng et al., 2003) or in ubiquitination site mapping experiments that rely on purification of the GlyGly dipeptide that remains attached to a lysine side chain following digestion of an ubiquitin conjugate with trypsin (Kim et al., 2011; Lesmantavicius et al., 2014; Porras-Yakushi and Hess, 2014; Porras-Yakushi et al., 2015; Sarraf et al., 2013; Swaney et al., 2013; Udeshi et al., 2013b; Wagner et al., 2011). Thus, we reasoned that if Tom1 plays a broad role in PQC of unassembled ribosomal

proteins as suggested by the experiments shown in Figure S4A and B, perhaps it accounts for the frequent recovery of ribosomal proteins in prior global ubiquitin conjugate profiling efforts. To address this possibility, we performed quantitative GlyGly profiling of *tom1Δ* and *TOM1* cells using SILAC (Figure S4C) to identify changes in the level of ubiquitination of specific lysines that occur upon loss of Tom1. Analysis of three biological replicates (Figures 3A and S5A) revealed 1,980 unique ubiquitination sites in 920 distinct proteins, of which 972 unique sites in 532 proteins were quantified. All three *tom1Δ* biological replicates exhibited lower overall ubiquitination than wild type, suggesting a major role for Tom1 in PQC. Of the 141 sites that exhibited a ≥ 2 -fold decrease in ubiquitination in *tom1Δ*, 51 (36%) were in ribosomal proteins (Figure S5B). Moreover, of the ubiquitinated peptides derived from ribosomal proteins, >50% (51 of 101) decreased in abundance in *tom1Δ*. By comparison, of 837 non-ribosomal sites identified, only 11% decreased in abundance in *tom1Δ*. SILAC analysis of the unfractionated cell lysates indicated that the reduction in ribosomal ubiquitin conjugates in *tom1Δ* was not due to reduction in total ribosomal protein levels (Figure 3B). Gene ontology analysis of the GlyGly profiling data confirmed that ubiquitination of ribosomal proteins (Figure 3C), particularly those of the large (60S) subunit (Figure 3D), was disproportionately impacted by loss of Tom1. These trends are clearly evident from a plot of the top 25 Tom1-dependent modification sites within all proteins (Figure S5C) or just ribosomal proteins (Figure 3E). To address whether the strong effects on ribosomal protein ubiquitination seen in *tom1Δ* cells were due specifically to loss of Tom1's E3 activity, the GlyGly SILAC analysis was repeated with WT and *tom1^{CA}* cells. Quantitative analysis of the data confirmed a disproportionate loss of ribosomal protein ubiquitination (Figure S5D).

Endogenous ribosomal proteins aggregate in *tom1Δ* mutants

If Tom1 mediates degradation of unassembled ribosomal proteins in unperturbed cells, there should not only be a decrease in ribosomal ubiquitin conjugates in *tom1* mutants, but a commensurate increase in unassembled ribosomal proteins that fail to be degraded. Since preliminary sucrose gradient fractionations did not reveal high levels of unassembled ribosomal proteins in *tom1Δ* cells (data not shown), we reasoned that over time, undegraded excess ribosomal proteins might aggregate and collect in insoluble deposits.

To investigate this matter, we prepared detergent-insoluble fractions from WT cells treated with or without bortezomib (btz) and *tom1* Δ cells, and evaluated them for their content of ribosomal proteins. Detergent-insoluble proteins, including Rpl1 and Rpl3, were greatly increased in *tom1* Δ cells compared to WT cells (Figure 3F, Pellet). High accumulation of insoluble proteins in *tom1* Δ cells was evident regardless of the method or buffer employed for cell lysis (Figure S6A). This observation was confirmed and extended by mass spectrometry coupled with label-free absolute quantification using iBAQ (intensity-Based Absolute Quantification) (Geiger et al., 2012). The insoluble proteins that exhibited the largest increase in *tom1* Δ cells were ribosomal proteins including Rpl1 and Rpl3 (Figures 3G and S6B). Gene ontology analysis (Figure 3H) and a plot of the top 20 detergent-insoluble proteins (Figure S6C) indicated that ribosomal proteins, including those of both the 60S and 40S subunits (Figure S6D), comprise the major class of aggregating proteins in *tom1* Δ cells.

Tom1 works through residues that are normally inaccessible in the structure of the mature ribosome

GlyGly profiling and analysis of insoluble proteins in *tom1* mutants both pointed to a broad role of Tom1 in ubiquitinating and degrading excess, unassembled ribosomal proteins. This raised a critical question that is common to all PQC pathways yet is poorly understood: how does Tom1 ubiquitinate so many different ribosomal proteins, yet manage to maintain some level of specificity for unassembled forms? To begin to address this question, we constructed a mutant Rpl26a that did not bind to rRNA. Two positively-charged clusters in Rpl26 – RRKARK (amino acids 12-17) and a patch formed by R27, R28, R51, and R52 – mediate binding to 5.8S rRNA and assembly into ribosomes (Babiano et al., 2012) (Figure 4A). We mutated various combinations of these residues to glutamate and observed that some mutants exhibited even less accumulation than overexpressed WT Rpl26a^{FLAG} (Figure 4B).

Unlike WT Rpl26a^{FLAG}, Rpl26-4E^{FLAG} (R12E, R13E, R16E, K17E) did not accumulate or assemble into ribosomes in *rpl26a* Δ *rpl26b* Δ cells (Figure 4C, top panels). However, upon inhibition of the proteasome with MG132 or bortezomib, Rpl26a-4E^{FLAG} accumulated (Figure S7A) and was detected in the low MW fractions of a sucrose gradient (Figure 4C, bottom panels), where it was ubiquitinated, albeit to a lesser extent than

unassembled WT Rpl26a^{FLAG} (Figure 4D). Strikingly, Rpl26a-4E^{FLAG} exhibited poor association with ^{3xHA}Tom1 (Figure 4E) and showed only very weak accumulation in *tom1Δ* (Figure 4F), suggesting that it is not primarily a Tom1 substrate but is re-directed to another QC pathway. Consistent with this idea, Rpl26a-4E^{FLAG} accumulated in *doa10* mutants (Figure S7B). The failure of Rpl26a-4E^{FLAG} to be targeted by Tom1 was not due to a defect in its nuclear localization (Figures 4G and S7C). We suggest that upon its import into the nucleus, Rpl26a-4E becomes a substrate for Doa10 that is localized to the inner nuclear membrane (Deng and Hochstrasser, 2006). Taken together, our results suggest that residues of Rpl26a that mediate interactions with rRNA and are buried when incorporated into the ribosome are also required for ubiquitination by Tom1 when Rpl26a fails to assemble.

To pursue this observation further and probe its potential generality, we focused on Rpl4, because assembly of Rpl4 has been studied in some depth (Stelter et al., 2015). Upon its synthesis, Rpl4 binds the dedicated chaperone Acl4. The Acl4•Rpl4 then recruits the karyopherin Kap104, for import into the nucleus. Importantly, a crystal structure is available for Acl4•Rpl4 (Huber and Hoelz, 2017), and the binding site of Kap104 on the complex has been mapped (Huber and Hoelz, 2017; Stelter et al., 2015). In our GlyGly profiling efforts, measurements were obtained for three ubiquitination sites on Rpl4: K55, K308, and K338 (10-, 8-, and 1.6-fold decrease in *tom1Δ*, respectively). The crystal structure of the ribosome indicates that K55 and K308, whose ubiquitinations exhibited the strongest dependence on Tom1, contact rRNA and are not accessible for modification in the mature ribosome (Ben-Shem et al., 2011). Interestingly, the crystal structure of the Acl4•Rpl4 complex revealed that Acl4 conceals K55, and a structural model of Kap104 docked to Acl4•Rpl4 indicates that it protects K308 and K338. Upon import of Acl4•Rpl4•Kap104 into the nucleus, Kap104 is dissociated through the action of Ran-GTP (Huber and Hoelz, 2017; Kressler et al., 2012). To test if this exposes the C-terminal region of Rpl4 to Tom1 (as would be the case if assembly of Rpl4 was delayed following nuclear import and release of Kap104), we performed an in vitro ubiquitination assay with purified substrates. ^{3xHA}Tom1 immunoprecipitates readily ubiquitinated Rpl4 in binary Acl4•Rpl4 complexes but not in ternary Acl4•Rpl4•*ct*Kap104 complexes, despite the fact that at least eight lysines of Rpl4 should remain exposed in the ternary complex (red circle, Figure 5A). Ubiquitination of Rpl4 within the binary complex required its extended C-terminus because

it was eliminated when the C-terminal region was truncated at residue 276 (Figure 5B). These data, along with those on Rpl26a, suggest that Tom1 selectively recognizes and ubiquitinates ribosomal proteins via residues that are only accessible in the unassembled state. Notably, pulse-chase labeling of yeast cells revealed that Rpl4 Δ 63-87, which lacks the loop region that binds Acl4, transiently associates with Tom1 (see Figure 3B of Stelter et al., 2015). However, it is unclear if loss of Tom1 during the chase was due to degradation or incorporation of Rpl4 Δ 63-87 molecules into ribosomes.

To assess more generally if Tom1 targets lysines that are inaccessible in the mature ribosome (PDB ID: 4V88), we examined the disposition of the major Tom1-dependent ubiquitination sites on large subunit proteins reported in Figure 3E. For this analysis, we used the structure of the HECT domain of Rsp5 covalently conjugated to both a donor ubiquitin and a substrate acceptor (PDB ID: 4LCD). We asked whether the epsilon amino group of a given lysine within the mature large subunit could conceivably make contact with the active site cysteine of Rsp5. Of the 18 lysines that could be observed in the 4V88 structure, 13 in the free 60S and 15 in the assembled 80S were not accessible to the probe (Figure 5C). Taken together, our data suggest strongly that Tom1-dependent ubiquitination events generally occur on ribosomal proteins prior to their assembly into the ribosome, on residues that normally are either buried in the ribosome, engage in salt bridges, or are otherwise shielded from contact.

Tom1 is required for maintaining cellular homeostasis of ribosomal proteins

We next turned our attention to the phenotypic effects of Tom1 deficiency. If a limited capacity to degrade excess ribosomal proteins contributes to the temperature-sensitive growth defect of *tom1* mutants (Utsugi et al., 1999) (Figure S2C, D), we reasoned that conditions that foster imbalances in the production of ribosome components should exacerbate this defect. To test this, we performed three different perturbations. First, *tom1*^{CA} cells (but not WT cells) were extremely sensitive to constitutive overexpression of *RPL26A* (Figure 6A) but not *RPL26A-4E* (Figure S8A) from the *GAL10* promoter. Second, we created a situation in which ribosomal proteins as a group are made in excess of rRNA via depletion (using the auxin-inducible degron (AID) (Morawska and Ulrich, 2013)) of proteins involved in rRNA synthesis including Rrn3 (transcription factor for RNA

polymerase I), Rpa190 (RNA polymerase I largest subunit) and Hmo1 (regulator of transcription by RNA polymerase I). Each of these depletions caused a synthetic growth defect when combined with *tom1^{CA}* (Figure S8B). The effect of combining *hmo1Δ* and *tom1^{CA}* mutations was even more severe (Figure 6B). Third, we manipulated cells such that assembly of a single ribosomal protein was impaired, via deletion of the Rpl4-selective chaperone Acl4 (Stelter et al., 2015). Inactivation of *TOM1* in an *acl4Δ* background caused a substantial synthetic growth defect (Figure 6C).

If the synthetic growth defects described above arose from a catastrophic failure of proteostasis, we reasoned that this might manifest itself in the detergent-insoluble fractions of double mutant cells. Strikingly, there was a massive increase in detergent-insoluble proteins when RNA Pol I transcription was diminished (*hmo1Δtom1^{CA}*; Figure 6D) or Rpl4 assembly was perturbed (*acl4Δtom1^{CA}*; Figure 6E) in a *tom1^{CA}* background.

Identification of Tom1 as a key mediator of ERISQ may rationalize numerous genetic interactions that have been reported for *tom1Δ*. In addition to suppressors that map to stress response/chaperone pathways and genes involved in ribosome protein expression (PKA pathway), deletions in 36 different genes encoding ribosomal proteins exhibit synthetic negative genetic interaction with *tom1Δ* (Costanzo et al., 2010) (Figure S8C). Based on the effects of the *acl4Δ* mutant (Figures 6C, E), deletions of one copy of duplicated ribosomal protein genes are predicted to create an imbalance in ribosomal proteins resulting in severe growth and proteostasis defects in a *tom1* background. Consistent with this prediction, deletion of one of the two copies of *RPS29* led to a synthetic growth defect (Figure S8D) and enormous accumulation of insoluble proteins in a *tom1Δ* mutant (Figure 6F).

Given the major role of ribosome production in the cellular economy, we evaluated the relative impact of the Tom1-dependent ERISQ pathway on overall proteostasis by comparing the amount of insoluble proteins in well-characterized PQC mutants including *doa10Δ* and *hrd1Δ* (ERAD; ER-associated degradation; (Vembar and Brodsky, 2008)), *ltn1Δ* (RQC; ribosome bound QC; (Bengtson and Joazeiro, 2010; Brandman et al., 2012; Defenouillere et al., 2013; Verma et al., 2013)), *san1Δ* (nuclear PQC; (Gardner et al., 2005)) and *ubr1Δ* (ERAD and cytoplasmic PQC; (Eisele and Wolf, 2008; Heck et al., 2010)). Under unperturbed conditions, *tom1Δ* cells contained significantly greater amounts

of insoluble proteins compared to these other PQC mutants (Figure 6G, Pellet), suggesting that ERISQ is a major player in maintaining proteostasis in yeast.

ERISQ pathway is conserved

A prior study in human cells demonstrated that a significant fraction of newly-synthesized ribosomal proteins imported into the nucleus is degraded by the UPS (Lam et al., 2007), suggesting that a PQC mechanism for unassembled ribosomal proteins is conserved in higher eukaryotes. To test this possibility, we evaluated transient expression of human Rpl26^{FLAG} (hRpl26^{FLAG}) in T-RExTM-293 cells treated with or without MG132 or bortezomib. Cells treated with these proteasome inhibitors accumulated greater amounts of overexpressed hRpl26^{FLAG} (Figure 7A), consistent with the existence of a UPS pathway that degrades overexpressed ribosomal proteins. The closest human homolog of Tom1 is Huwe1. Knockdown of Huwe1 by shRNA (Thompson et al., 2014) in both T-RExTM-293 and HeLa cells (Figure 7B) and knockout of *HUWE1* in HEK293T cells (Choe et al., 2016)(Figure 7C) enabled transient overexpression of hRpl26^{FLAG}. Importantly, a cycloheximide chase experiment indicated that hRpl26^{FLAG} overexpressed in *HUWE1* knockout cells was stable (Figure 7D).

To test if Huwe1 was required for ubiquitination of transiently overexpressed hRpl26^{FLAG}, control or Huwe1-depleted T-RExTM cells were co-transfected with plasmids encoding hRpl26^{FLAG} and HA-ubiquitin and then treated with MG132 to induce accumulation of ubiquitin conjugates. IP/Western blot analysis performed under denaturing conditions revealed that hRpl26^{FLAG} was modified by HA-ubiquitin in control but not Huwe1-depleted cells (Figure 7E). Consistent with this result, prior analysis of Huwe1-deficient cells by GlyGly profiling revealed reductions in the ubiquitination of multiple ribosomal proteins (Thompson et al., 2014).

DISCUSSION

Nearly 40 years ago Jonathan Warner and colleagues showed that multiple ribosomal proteins are rapidly degraded in both yeast and HeLa cells when ribosomal RNA synthesis is inhibited (Gorenstein and Warner, 1977; Warner, 1977). They and others went on to show that individual ribosomal proteins cannot be overexpressed from plasmids in yeast because the excess protein is rapidly degraded (Abovich et al., 1985; Warner et al., 1985). Essentially no progress was made towards understanding the underlying mechanism, until it was shown that ribosomal proteins are among the most abundant ubiquitin conjugates that accumulate in yeast cells with reduced proteasome activity (Mayor et al., 2007; Mayor et al., 2005), and that newly-synthesized ribosomal proteins are degraded by the proteasome in human nucleoli (Lam et al., 2007). More recently, we have shown that ribosome proteins produced in excess are ubiquitinated and then degraded in a proteasome-dependent manner (Sung et al., 2016). In the work reported here, we shed additional light on this old puzzle by showing that the ubiquitin ligase Tom1 collaborates with the E2 enzymes Ubc4 and Ubc5 to broadly mediate degradation of unassembled ribosomal proteins in yeast. We refer to this pathway as ERISQ, for Excess Ribosomal protein Quality control.

How are substrates recognized by the ERISQ pathway?

For ERISQ to work, two major challenges must be met. First, Tom1 has to detect many different ribosomal proteins. Second, it has to be able to distinguish their assembled versus unassembled forms. Although the exact structural basis for this discrimination remains to be determined, our analysis reveals that for Tom1 to act upon ribosomal proteins, residues that are normally concealed in the mature ribosome must be accessible. This was shown *in vivo* for the model substrate Rpl26 and *in vitro* for Rpl4. In addition, mapping of the major Tom1-dependent ubiquitination sites on the structure of the ribosome large subunit revealed that nearly 83% (15 of 18) of the sites on 12 different ribosomal proteins are no longer available to Tom1 following incorporation into the 80S ribosome. This suggests a very simple kinetic competition between Tom1 and rRNA for binding to ribosomal proteins newly arrived in the nucleolus. If the kinetic parameters for this race normally favor rRNA,

the correct outcome would dominate and only those proteins that fail to assemble would be targeted.

Tom1 has also been implicated in the degradation of unassembled histones (Singh et al., 2009), in which case a similar kinetic competition could apply. Although the domain employed by Tom1 to bind its substrates remains unknown, we note that the previously-described Tom1 substrates Dia2 (Kim and Koepp, 2012), Hht2 (Singh et al., 2009) and Yra1 (Iglesias et al., 2010) have pI values ranging from 9.3-12. Thus, Tom1, which is overall acidic (pI 4.8) may have a negatively-charged region that interacts electrostatically with basic substrates.

Conservation of the Tom1 ERISQ pathway in humans

Seminal studies from Warner indicated that human cells, like yeast, are unable to accumulate ribosomal proteins made in excess over rRNA due to rapid turnover (Warner, 1977), and subsequent proteomic studies revealed that a substantial fraction of newly-synthesized human ribosomal proteins are rapidly degraded by the proteasome (Lam et al., 2007). To test whether the mechanism we described in yeast also operates in human cells, we first demonstrated that the human ortholog (hRpl26) of yeast Rpl26 fails to accumulate upon transient overexpression, and then established that both ubiquitination and degradation of excess hRpl26 require Huwe1, which is the closest human homolog of Tom1. A recent proteome-wide profiling of ubiquitination sites that exhibit diminished occupancy upon depletion of Huwe1 revealed that, excluding Huwe1 itself, six of the top ten affected sites and seventeen of fifty-six that exhibited ≥ 2 -fold decreased occupancy were from ribosomal proteins (Thompson et al., 2014). These data point to a very general role for Huwe1 in ubiquitination of ribosomal proteins, similar to what we show here for yeast Tom1.

Physiological significance of Tom1/Huwe1 and ERISQ

Cells lacking Tom1 exhibit a variety of phenotypes besides ERISQ including cell cycle arrest, nucleolar fragmentation, defective mRNA export from the nucleus, reduced Ngg1/Ada3-dependent transcription, reduced polysomes, reduced rate of rRNA processing/maturation (Duncan et al., 2000; Saleh et al., 1998; Tabb et al., 2001; Utsugi et al., 1999), and sensitivity to paromomycin (Figure S8E). On the one hand it is possible that

all but one of these phenotypes are mainly secondary consequences of the primary defect. On the other hand, they may all arise independently from stabilization of different substrates. We can rule out that ERISQ is an indirect consequence of cell cycle arrest, nucleolar fragmentation, defective mRNA export, or a reduced rate of rRNA processing, because the defect in ERISQ is observed at temperatures that are permissive for growth of *tom1* mutants, whereas the other defects are only seen (or in the case of rRNA processing rate, is strongly enhanced) at the non-permissive temperature and thus are more likely to arise indirectly from exacerbation of a primary defect upon imposition of heat stress. It remains unclear to what extent a defect in ERISQ, when coupled to heat stress, might underlie these other phenotypes.

Some of the *tom1* phenotypes noted above are suggestive of a potential positive role for Tom1 in the assembly of functional ribosomes. However, this does not conflict with our observation that Tom1 plays a direct role in ubiquitinating and promoting the degradation of ribosome proteins that are overexpressed relative to their assembly partners. A speculative possibility is that Tom1 ubiquitinates a broad range of ribosomal proteins to promote their assembly (much as fusion to ubiquitin promotes assembly of Rps31; (Finley et al., 1989)), but if they fail to assemble within a given time interval, the ubiquitin conjugated by Tom1 serves to initiate degradation. However, the observation that genetic reductions of protein kinase A activity (which are predicted to diminish synthesis of ribosome proteins) suppress *tom1Δ* (Figure S8C) seems inconsistent with the idea that Tom1 plays a direct positive role in ribosome assembly.

A phenotype of *tom1^{CA}* cells that we describe here that is particularly notable is that they are exquisitely sensitive to perturbations that alter the balance between production of individual ribosomal proteins or total ribosomal proteins and rRNAs. Specifically, *tom1^{CA}* mutants are unable to sustain growth upon overexpression of *RPL26*, are sensitive to loss of the Rpl4-specific chaperone Acl4 (Stelter et al., 2015), are sensitive to reduction in expression (through deletion of one of two alleles) of a single ribosomal protein, and are hypersensitive to reduction of function in three different proteins involved in transcription by RNA polymerase I. Moreover, *tom1* mutants accumulate high levels of insoluble ribosomal proteins (which is consistent with their inability to degrade excess ribosomal proteins that may exist at any given point in time), and combining *tom1* with a mutation that

causes an imbalance in ribosome production (e.g. *tom1^{CA} acl4Δ*) leads to an enormous increase in insoluble protein, suggestive of a collapse in cellular proteostasis. Notably, even the *tom1Δ* single mutant accumulates more insoluble protein than any other PQC mutant that we examined, including the ERAD mutants *doa10Δ* and *hrd1Δ* (Vembar and Brodsky, 2008), the ribosome QC mutant *ltn1Δ* (Bengtson and Joazeiro, 2010; Brandman et al., 2012; Defenouillere et al., 2013; Verma et al., 2013), the nuclear QC mutant *san1Δ* (Gardner et al., 2005), or the cytosolic QC mutant *ubr1Δ* (Eisele and Wolf, 2008; Heck et al., 2010). Taken together with our observations that Tom1 directly binds and ubiquitylates unassembled ribosome proteins, these data point to a direct and critical role for Tom1 in the cellular proteostasis network.

The hypersensitivity of *tom1^{CA}* cells to stoichiometric imbalances in ribosome components raises interesting questions as to why unassembled ribosomal proteins would be toxic, and whether feedback mechanisms exist to monitor and respond to failures in ERISQ. Regarding the first question, given that ribosomal proteins are highly expressed, positively charged nucleic acid binding proteins, their accumulation might interfere with RNA biology. Regarding feedback mechanisms, it is interesting to note that in human cells, reduction of rRNA expression by low-dose actinomycin D treatment results in poor assembly of several ribosomal proteins including Rpl5 (Dai and Lu, 2004), Rpl11 (Lohrum et al., 2003; Zhang et al., 2003), Rpl26 (Zhang et al., 2010), Rps7 (Chen et al., 2007) and Rps14 (Zhou et al., 2013). These unassembled ribosomal proteins bind to and titrate ubiquitin ligase Mdm2, which leads to stabilization and accumulation of the Mdm2 substrate p53. This provides a sensitive feedback loop to reduce cell growth in response to stresses that impede ribosome assembly. It will be of great interest to determine whether a similar feedback mechanism operates in yeast, and how Huwe1 activity relates to the Mdm2–p53 feedback pathway described in human cells.

Is ERISQ relevant to cancer?

Dysfunctional ribosomal proteins and ribosome biogenesis has been linked to many diseases (Freed et al., 2010; Narla and Ebert, 2010). Particularly, given that one of the characteristic features of cancer is an increase in the overall rate of protein synthesis, it is clear that regulation of ribosome biogenesis is closely associated with tumor progression. Consistent

with this expectation, RNA Pol I activity is highly elevated in many cancer cells and leads to the enlargement of the nucleolus, which has been used as a marker for cancer for over 100 years (Derenzini et al., 2009). Furthermore, two major human tumor suppressor proteins, pRB and p53, have been shown to repress the production of rRNA and the loss of these factors cause an up-regulation of ribosome biogenesis in cancer tissues, consistent with a close relationship between cancer and ribosome synthesis (Montanaro et al., 2008). Up-regulation of ribosome production in cancer cells implies an enhanced dependency on QC mechanisms that survey ribosome assembly. However, the molecular pathway that mediates ERISQ in human cells has, up to now, remained unknown. Interestingly, several observations link Huwe1 function to cancer. Huwe1 is overexpressed in multiple human tumors, is essential for proliferation of a subset of tumors (Adhikary et al., 2005), and is required for activation of Myc-inducible target genes including ribosomal proteins in colon carcinoma cells (Peter et al., 2014). Our data suggest the intriguing hypothesis that accumulation of unassembled ribosomal proteins would titrate Huwe1, resulting in reductions in both Myc activity and transcription of genes that encode ribosomal proteins. Insights into the detailed molecular basis underlying ERISQ afforded by the discovery reported here will enable investigations into the biological relevance of ERISQ in human pathologies, including cancer, which may lead to novel concepts for therapy

ACKNOWLEDGEMENTS

We are grateful to members of the Deshaies laboratory for helpful advice and Rati Verma for critical reading of this manuscript. We thank Jonathan Warner, Christine Guthrie, Sarah Luchansky, Ling Song, Won-Ki Huh, George Moldovan, and Helle Ulrich for generously providing reagents and helpful discussions. We also thank Thang Nguyen and Rati Verma for numerous helpful suggestions regarding biochemical experiments. We thank Annie Moradian and Roxana Eggleston-Rangel for mass spectrometric assistance. R.J.D. is an Investigator of the HHMI.

EXPERIMENTAL PROCEDURES

Yeast strains, growth conditions, and transformation

All yeast strains used in this study (listed in Table S1) were derived from BY4741 (*MATa his3Δ1 leu2Δ0 met15Δ0 ura3Δ0*) or W303a (*MATa leu2-3,112 trp1-1 can1-100 ura3-1 ade2-1 his3-11,15*). All transformants were verified by auxotrophic selection or genomic PCR. Yeast was grown at 30°C in YPD or appropriate synthetic complete (SC) drop-out media. For ectopic expression of proteins from the *GAL1,10* promoter, cells grown in raffinose containing medium were treated with 2 % galactose for 60-90 min. We note that experiments were initiated with cells at OD₆₀₀ 3.0, because the ERISQ pathway was more prominent in cells at mid-log phase (OD₆₀₀ ~3.0) compared to early-log phase (OD₆₀₀ ~1.0) (data not shown). Yeast transformation was performed by lithium acetate method (Gietz and Schiestl, 2007). For several strains, PCR products were generated by the ‘gene splicing by overlap extension’ method (Horton et al., 1989).

Mammalian cell culture and transfection

T-REx™-293 (Thermo Fisher Scientific), HeLa (Thompson et al., 2014), HEK293 (Choe et al., 2016) cells were grown in Dulbecco’s modified Eagle’s medium (DMEM) supplemented with 10% fetal bovine serum (Atlanta Biologicals, Norcross, GA), penicillin, and streptomycin (Invitrogen) at 37 °C in 5 % CO₂. Mycoplasma contamination has been tested negative by MycoAlert Mycoplasma detection kit (Lonza). Cells used in this study were not in the database of cross-contaminated or mis-identified curated by the International Cell Line Authentication Committee (ICLAC). We haven’t authenticated cells by a third party. Transient transfections were performed using transfection reagents FuGENE® HD (Promega) according to manufacturer’s instructions. For lentiviral production, T-REx™-293 cell line (ThermoFisher) was transfected with the lentiviral construct along with helper plasmids. Forty eight hours after transfection, media supernatant containing the lentivirus was collected. The lentivirus-containing medium supplemented with polybrene was used to transduce the target cells. The doxycycline-inducible shRNA expression constructs (pLKO-Tet-ON vector (Thompson et al., 2014; Wiederschain et al., 2009)) containing the control (RDB3142; CAA CAA GAT GAA GAG

CAC CAA) and shHUWE1 (RDB3143; TGC CGC AAT CCA GAC ATA TTC) sequences were used (Thompson et al., 2014). shHUWE1 described previously as si5635 (Zhong et al., 2005) was used. Transduced T-REx™-293 cells transduced with the control or HUWE1 shRNA constructs were selected in the presence of 4 µg/ml of puromycin.

Plasmids and yeast molecular genetic manipulations

All plasmids used in this study are listed in Table S2. To construct pESC(HIS)-P_{GAL10}-RPL26A(mutants)-FLAG used in Figure 4, site-directed mutagenesis was performed using QuikChange Site-Directed Mutagenesis Kit (Agilent Technologies; 200519) according to manufacturer's instructions.

To construct N-terminally 3×HA-tagged Tom1, the ~1800 bp PCR product including the *KAN* selection marker and *RFAI* promoter was obtained using pKanMX6-P_{RFAI}-9Myc-AID* (Morawska and Ulrich, 2013) as a template, forward primer 5'-GAG AGG AAA AGA AGA AAA GGT AAA ACA ACG AAT ATT TTT CCG GAT CCC CGG GTT AAT TAA-3' and reverse primer 5'-TCT TGT AAG TAT AAT CTG GTC TTC T-3', and the ~180 bp PCR product encoding the 3×HA tag was obtained using pRS304-3×HA-TOM1 plasmid (Duncan et al., 2000) as a template, forward primer 5'- AGA AGA CCA GAT TAT ACT TAC AAG AAT GGA ATT CGG CCG CAT CTT TTA CC-3' and reverse primer 5'- GTT TCT CCT TTC TTG CCT TTT CAC ACC GAG TAA AAA GCA CAG ATC TGC ACT GAG CAG CGT-3'. With the two PCR products as templates, the ~2000 bp PCR product was obtained using forward primer 5'- GAG AGG AAA AGA AGA AAA GGT AAA ACA ACG AAT ATT TTT CCG GAT CCC CGG GTT AAT TAA-3' and reverse primer 5'- GTT TCT CCT TTC TTG CCT TTT CAC ACC GAG TAA AAA GCA CAG ATC TGC ACT GAG CAG CGT-3'. The obtained final PCR product was used for transformation, generating cells expressing 3×HA^TTom1 from the *RFAI* promoter.

To construct *tom1*^{CA} mutants, the ~145 bp PCR product including the 3' end region of *TOM1* with a C3235A mutation was obtained using pRS304-3×HA-TOM1^{CA} plasmid (Duncan et al., 2000) as a template, forward primer 5'-TGA TTT TGG TTC ATC AGA AAG ACT ACC ATC ATC ACA TAC C-3' and reverse primer 5'-CAA AAG CAG AGA GGC GCG CCT CAG GCA AGA CCA AAC CCT TCA TGC-3', and the ~1700 bp PCR product including the *KIURA3* was obtained using pFA6a-GFP-KIURA3 plasmid (Sung et

al., 2008) as a template, forward primer 5'-GCA TGA AGG GTT TGG TCT TGC CTG AGG CGC GCC TCT CTG CTT TTG-3' and reverse primer 5'-CAT GGC GCT ATA AAT TTA CAC GAA AAA TGA CGT CAT TGG TTC TGG AGG AAG TTT GAG-3'. With the two PCR products as templates, the ~1850 bp PCR product was obtained using forward primer 5'-TGA TTT TGG TTC ATC AGA AAG ACT ACC ATC ATC ACA TAC C-3' and reverse primer 5'-CAT GGC GCT ATA AAT TTA CAC GAA AAA TGA CGT CAT TGG TTC TGG AGG AAG TTT GAG-3'. The obtained final PCR product was used for transformation, generating *tomI^{CA}* strains.

Antibodies

Anti-Rpl1 and anti-Rpl3 were generous gifts from Jonathan Warner. Anti-FLAG (F1804; PRID:AB_262044; 1:10,000 dilution) was from Sigma, anti-Hexokinase (H2035-02; 1:10,000 dilution) was from USBiological, anti-HUWE1 (A300-486A; RRID:AB_2615536; 1:1,000 dilution) was from Bethyl laboratories, anti-HA (SC-7392; RRID:AB_627809; 1:5,000 dilution) was from Santa Cruz, anti-myc (MMS-150R; RRID:AB_291325; 1:5,000 dilution) was from Covance, anti-Ubiquitin (05-944; RRID:AB_441944; 1:5,000 dilution) and anti-GAPDH (MAB374; RRID:AB_2107445; 1:5,000 dilution) were from EMD Millipore, and anti-His₆ (200-332-382; RRID:AB_10704645; 1:5,000 dilution) was from Rockland. For secondary antibody, HRP-conjugated anti-rabbit IgG (A6154; RRID:AB_258284; 1:10,000 dilution) and HRP-conjugated anti-mouse IgG (M8770; RRID:AB_260711; 1:10,000 dilution) were from Sigma, IR680RD conjugated anti-rabbit (926-68071; RRID:AB_10956166; 1:10,000 dilution) and IR800CW conjugated anti-mouse (926-32210; RRID:AB_621842; 1:10,000 dilution) were from LI-COR Biosciences.

Microscopic analysis

Yeast cells grown in raffinose-containing SC medium at 30°C ($OD_{600} \leq 1.0$) were induced with galactose for 1 hour to express Rpl26a^{GFP} and placed in 384-well glass-bottom microplates (Whatman) pretreated with concanavalin A (Sigma; L7647) to ensure cell adhesion. Fluorescence images were taken using a Zeiss Axiovert 200M Inverted Microscope with an FITC filter set (excitation band pass filter, 450–490 nm; beam splitter,

510 nm; emission band pass filter, 515–565 nm) and a Rhodamine filter set (excitation band pass filter, 546 nm; beam splitter, 580 nm; emission long pass filter, 590 nm). We analyzed at least 50 cells and subcellular localization of GFP-fused proteins was reconfirmed by co-localization assay as described previously (Huh et al., 2003).

Immunoblotting

For denatured samples, yeast or mammalian cells were harvested, washed two times with PBS, and boiled in 2× SDS-containing sample buffer for 5 min followed by brief bead beating or sonication, respectively. For non-denatured samples, yeast cells were harvested and disrupted by bead beating in lysis buffer (50 mM Tris-HCl (pH 7.5), 150 mM NaCl, 1 % Triton X-100 and protease inhibitor cocktail (EDTA-free; Roche)). Cell debris was removed by centrifuging at 3,000 rpm for 5 min, and the remaining cell extract was centrifuged at 12,000 rpm for 10 min in an Eppendorf Centrifuge 5430R. For mammalian cells, harvested cells were washed twice with PBS, and then incubated with RIPA buffer (50 mM Tris-HCl (pH 7.5), 150 mM NaCl, 1 % IGEPAL, 0.5 % sodium deoxycholate, 0.1 % SDS and protease inhibitor cocktail (EDTA-free; Roche)) for 10 min. After centrifugation at 12,000 rpm for 10 min in an Eppendorf Centrifuge 5430R, the supernatant was transferred to a new tube and mixed with SDS-PAGE sample buffer. Hexokinase and GAPDH were used as an internal control. Myc-GFP was used as a control for transfection efficiency. Protein levels were quantified using Odyssey software.

Protein expression and purification

Acl4^{•FLAG}Rpl4, Acl4^{•FLAG}Rpl4Δext and *Chaetomium thermophilum* Kap104 were expressed in *E. coli* BL21-CodonPlus(DE3)-RIL cells (Stratagene) grown in LB media supplemented with appropriate antibiotics. Protein expression was induced at an OD₆₀₀ of approximately 0.6 with 0.5 mM isopropyl β-D-thiogalactoside (IPTG) for ~18 hours at 18 °C (Acl4^{•FLAG}Rpl4, Acl4^{•FLAG}Rpl4Δext) or 23 °C (*ctKap104*). Cells were harvested by centrifugation and resuspended in a buffer containing 20 mM Tris-Base (pH 8.0), 500 mM NaCl, 5 mM β-mercaptoethanol (Sigma), 2 μM bovine lung aprotinin (Sigma), and complete EDTA-free protease inhibitor cocktail (Roche), and subsequently flash frozen in liquid nitrogen. Thawed cells were lysed with a cell disrupter (Avestin) and the lysate was

centrifuged for 1 hour at 40,000 x g. Cleared lysate of *ctKap104* expression was applied to a glutathione sepharose column equilibrated in buffer containing 20 mM Tris-Base (pH 8.0), 100 mM NaCl, and 5 mM DTT (GE Healthcare) and eluted via a glutathione gradient. Pooled fractions were cleaved with PreScission protease (GE Healthcare) for 12 hours. Cleared lysate of Acl4^{FLAG}Rpl4, Acl4^{FLAG}Rpl4Δext expression was applied to a Ni-NTA column equilibrated in buffer containing 20 mM Tris-Base (pH 8.0), 500 mM NaCl, and 5 mM β-mercaptoethanol and eluted via an imidazole gradient. Pooled fractions were cleaved with ubiquitin-like-specific protease 1 (Ulp1) for 12 hours. Cleaved proteins were bound to a HiTrapQ HP (GE Healthcare) column equilibrated in buffer containing 20 mM Tris-Base (pH 8.0), 100 mM NaCl, and 5 mM DTT and eluted via a linear NaCl gradient, concentrated, and injected onto a HiLoad 16/60 Superdex 200 column equilibrated in 20 mM Tris-Base (pH 8.0), 100 mM NaCl, and 5 mM DTT. The Acl4^{FLAG}Rpl4•*ctKap104* complex was assembled by stoichiometric incubation for 1 hour at 4 °C and injection onto a HiLoad 16/60 Superdex 200 column equilibrated in 20 mM Tris-Base (pH 8.0), 100 mM NaCl, and 5 mM DTT.

***In vitro* ubiquitination assay**

Five hundred OD₆₀₀ units of cells expressing ^{3×HA}Tom1 (WT) and ^{3×HA}Tom1^{CA} were grown in raffinose medium and then induced to express Rpl26a^{FLAG} in galactose medium for 45 min followed by bortezomib (50 μM) treatment for an additional 45 min. Cells were harvested and disrupted by bead beating in 2.5 ml lysis buffer (50 mM Tris-HCl (pH 7.5), 150 mM NaCl, 0.5 % NP-40 and protease inhibitor cocktail (EDTA-free; Roche)). Cell debris was removed by centrifuging at 3,000 rpm for 5 min, and the remaining cell extract was centrifuged at 12,000 rpm for 10 min in an Eppendorf Centrifuge 5430R. Total lysates were incubated overnight with 150 μl anti-HA magnetic beads. Beads were washed three times with the same lysis buffer and then twice with 1× ubiquitin reaction buffer (50 mM Tris-HCl (pH 8.0), 10 mM MgCl₂, 0.2 mM CaCl₂, 1 mM DTT and 5 μM MG132). Beads were incubated with 2 mM ATP, 166 nM E1 (Ube1; BostonBiochem; E-305), 1 μM E2 (UbcH5a; BostonBiochem; E2-616), and 20 μg of His₆-ubiquitin (Ubiquitin; BostonBiochem; U-530) at 30°C for 1 hour. For Rpl4 ubiquitination, 10 μg of purified substrates (Acl4^{FLAG}Rpl4, Acl4^{FLAG}Rpl4Δext and Acl4^{FLAG}Rpl4•*ctKap104*) were used.

One-fifth volume of 5× SDS-containing sample buffer was added to stop the reactions and boiled for 5 min.

Binding to UBA columns and Usp2 treatment

Immunoprecipitation of ubiquitin conjugates was performed as described with some modifications (Verma et al., 2013). TUBE2-UBA resin (BostonBiochem; AM-130) was used to bind polyubiquitinated substrates. One hundred OD₆₀₀ units of cells were harvested and disrupted by bead beating in 500 µl lysis buffer (20 mM Tris-HCl (pH 7.5), 150 mM NaCl, 1 mM EDTA, 10 % Glycerol, 5 mM NEM, 1 % Triton X-100 and protease inhibitor cocktail (EDTA-free; Roche)). Cell debris was removed by centrifuging at 3,000 rpm for 5 min, and the remaining cell extract was centrifuged at 12,000 rpm for 10 min in an Eppendorf Centrifuge 5430R. TUBE2-UBA resin (30 µl) incubated overnight was washed three times with buffer (20 mM Tris-HCl (pH 8.0), 150 mM NaCl, 0.5 % Triton X-100). Fifty µl of 2× SDS-containing sample buffer was added to the resin and boiled for 5 min. Note that unmodified proteins can also potentially bind due to indirect interactions with ubiquitinated proteins. For Usp2 treatment, TUBE2-UBA resin prepared as described above was washed twice with 1× ubiquitin reaction buffer (50 mM Tris-HCl (pH 8.0), 10 mM MgCl₂, 0.2 mM CaCl₂, and 1 mM DTT) and mixed with 1 µM Usp2 (BostonBiochem; E-504) at 30 °C for 1 hour.

Nuclear fractionation of yeast cells

Subcellular fractionation was performed as described (Keogh et al., 2006). One hundred OD₆₀₀ units of cells grown in rich medium (OD₆₀₀ ≤1.0) were collected by centrifugation and then treated with 200 units Zymolyase for 1 hour at 30 °C in 1 ml SB buffer (1 M Sorbitol, 20 mM Tris-HCl (pH 7.5), 10 mM β-mercaptoethanol). Spheroplasts collected by centrifugation (2,000 rpm for 5 min at 4°C) were washed twice with SB buffer, and then resuspended in 500 µl EBX buffer (20 mM Tris-HCl (pH 7.5), 100 mM NaCl, 0.25 % Triton X-100, 15 mM β-mercaptoethanol and protease inhibitor cocktail (EDTA-free; Roche)). An aliquot was taken and used as a total cell extract, and the remainder of the lysate was layered over 1 ml NIB buffer (20 mM Tris-HCl (pH 7.5), 100 mM NaCl, 1.2 M Sucrose, 15 mM β-mercaptoethanol, and protease inhibitor cocktail (EDTA-free; Roche))

and centrifuged (12,000 rpm for 15 min at 4 °C in an Eppendorf Centrifuge 5430R). A sample of the upper soluble fraction was taken and used as cytosol and the rest of the supernatant discarded. The glassy white nuclear pellet was suspended in 500 µl EBX buffer and kept on ice for 10 min with gentle mixing and an aliquot taken and used as the nuclear fraction. 2× SDS-PAGE loading buffer was added to each fraction and samples were incubated at 95°C for 5 min and then subjected to SDS-PAGE and Western analyses.

Sucrose gradient and polysome profiling

Sucrose gradient and polysome profiling were performed as described (Verma et al., 2013). Yeast cells were grown to logarithmic phase in rich medium supplemented with glucose or raffinose at 30 °C, and treated with cycloheximide (100 µg/ml) for 15 min before cell lysis to stabilize polysomes. One hundred OD₆₀₀ units of cells were harvested and disrupted by bead beating in lysis buffer (0.5 mM DTT, 100 µg/ml cycloheximide, 200 µg/ml heparin, 20 mM Tris-HCl (pH 7.5), 140 mM KCl, 5 mM MgCl₂, and protease inhibitor cocktail (EDTA-free; Roche)). Cell debris was removed by centrifuging at 3,000 rpm for 5 min, and the remaining cell extract was centrifuged at 12,000 rpm for 10 min in an Eppendorf Centrifuge 5430R. Twenty five A₂₆₀ units of cell lysate layered on 7%~47% discontinuous sucrose gradient prepared in buffer (1 mM DTT, 140 mM KCl, 20 mM Tris-HCl (pH 7.5), and 5 mM MgCl₂) were centrifuged in SW55Ti rotor for 90 min at 50,000 rpm. For polysome profiling analysis, samples were fractionated while continuously recording the absorbance at 254 nm with a UV detector (ISCO, Lincoln, NE). For Western blot, 0.2 ml fractions collected from the top were treated with 0.02 % sodium deoxycholate for 30 min on ice and then precipitated by adding TCA to 10 % final concentration for 1 hour. Pellets were washed with ice-cold acetone, and then resuspended in 2× SDS-containing sample buffer.

Isolation of protein aggregates

Isolation of protein aggregates from yeast cells was performed as described previously (Koplin et al., 2010) with slight modifications. One hundred OD₆₀₀ units of exponentially growing cells were harvested, and cell pellets were frozen in liquid N₂. The cell pellets were resuspended in 1 ml lysis buffer (20 mM Na-phosphate (pH 6.8), 10 mM DTT, 1 mM

EDTA, 0.1 % Tween, 1 mM PMSF, protease inhibitor cocktail, and 100 units/ml zymolyase) and incubated at 30 °C for 30 min. Chilled samples were treated by tip sonication (20 %, 10 sec, twice) and centrifuged for 20 min at 600 g at 4 °C. Supernatants were adjusted to identical protein concentrations, and aggregated proteins were pelleted at 16,000 g for 20 min at 4 °C. After removing supernatants, insoluble proteins were washed once with Wash I buffer (20 mM Na-phosphate (pH 6.8), 500 mM NaCl, 5 mM EDTA, 2 % NP-40, 1 mM PMSF, and protease inhibitor cocktail), and centrifuged at 16,000 g for 20 min at 4 °C. Insoluble proteins were washed twice with Wash II buffer (20 mM Na-phosphate (pH 6.8)) and sonicated (10 %, 10 sec, twice) in 40 µl of Wash II buffer. Pellets were processed either as described below or solubilized in 10 µl SDS sample buffer. 1X of the total cell lysate (T) and soluble (S) fractions, and 20X of the isolated pellet (P) fraction were separated by SDS-PAGE, and analyzed by Coomassie Blue staining and immunoblotting. For the experiment in Figure S6A, the cells were lysed by agitation with glass beads as described by Kaganovich et al., (2008), in the presence of 3 different lysis buffers: 1) 100 mM Tris-Cl, 1 % Triton X-100, 150 mM KCl, 5 mM MgCl₂ and protease inhibitor; 2) 100 mM HEPES, 1 % Triton X-100, 300 mM NaCl and protease inhibitor (Lu et al., 2014); 3) 30 mM HEPES, 0.5 % Triton X-100, 150 mM NaCl, 1 % glycerol, 1 mM DTT and protease inhibitor (Kaganovich et al., 2008).

SILAC labeling of cells.

In order to determine the effect of deleting *TOM1* on ubiquitination *in vivo*, stable isotope labeling of amino acids in cell culture (SILAC) experiments were performed. Wild type or *tom1Δ* yeast strains were grown in either heavy or light medium and mixed 1:1. Three biological replicates of each strain was grown, one of which was a label swap. Yeast cells were grown in complete synthetic medium supplemented with 2 % dextrose and 20 mg/l of L-lysine and L-arginine. Yeast cells labelled “heavy”, were grown in L-¹³C₆¹⁵N₂-lysine (Lys 8) and L-¹³C₆-arginine (Arg 6) (Cambridge Isotope Laboratories), while yeast cells labelled “light” were grown in L-lysine (Lys 0) and L-arginine (Arg 0). Yeast cells were allowed to grow for 10 generations to log-phase (OD₆₀₀ 0.6~1.0) in the appropriate media to ensure full incorporation of the desired labels. Incorporation was determined by LC-MS analysis of the derivatized amino acid hydrolysate as previously described (Hess et al.,

2002). Cells were harvested by centrifugation at $5,000 \times g$ for 5 min, washed twice with sterile water, flash frozen in liquid N_2 and stored at $-80^\circ C$ until lysis.

Peptide preparation for mass spec.

Cell lysis, digestion and peptide desalting procedure were followed according to the PTMScan® Ubiquitin Remnant Motif (K- ϵ -GG) Kit #5562 from Cell Signaling Technology product manual with a few changes. Cells were lysed in 5 ml of lysis buffer (20 mM HEPES (pH 8.0), 9 M Urea, $1\times$ Protease Inhibitor cocktail (Promega), and 1 mM PMSF). Yeast cells were lysed by vortexing in the presence of glass beads. Cells were vortexed 1 min with 1 min rests on ice in between, for 7 cycles. Lysate was cleared by centrifugation at $20,000 \times g$ for 15 min at $15^\circ C$, after which protein concentration was determined by Bradford. Cleared lysate was mixed 1:1, by using 10 mg of each label. The mixed sample was reduced for 45 min with 1.25 M DTT, by adding 1/278 (v/v) to achieve a final concentration of 4.48 mM DTT. Cysteine alkylation was performed by treating the lysate with 10 mM NEM, for 30 min at room temperature (RT) in the dark. Proteins were then digested with LysC (Wako) at a ratio of 1:200 for 4 hours at RT. Lysate was then diluted to 2 M urea by adding 50 mM Tris (pH 8.0). The partially digested lysate was subsequently digested with sequence grade trypsin (Promega) at a protein ratio of 1:100 in the presence of 1 mM $CaCl_2$ overnight (≥ 15 hours) at room temperature in the dark. The following morning the reaction was quenched by adding trifluoroacetic acid (TFA) to a final concentration of 0.1%. Insoluble material was removed from the digest by centrifugation at $4,000 \times g$ for 15 min. Peptides were desalted using a 500 mg capacity Sep-pak column that initially was hydrated using 7 column volumes of ACN (21 ml), followed by an equilibration step with 7 column volumes of Buffer A (0.1 % TFA in H_2O) (21 ml). Cleared peptides were loaded onto the resin by gravity flow, washed with 7 column volumes of Buffer A, followed by 3 column volumes of Wash buffer (0.1 % TFA, 5 % ACN in H_2O). Desalted peptides were eluted using 2 column volumes of Elution buffer (0.1 % TFA, 40 % ACN in H_2O) (6 ml). The resulting peptide sample was frozen by storing at $-80^\circ C$ for at least 1 hour then lyophilized to dryness.

Basic reversed phase peptide fractionation.

Peptide fractionation, cross-linking of antibody, and K- ϵ -GG peptide immunoprecipitation procedure was followed as in Udeshi et al., (Udeshi et al., 2013a) with a few changes. Briefly, dried peptides were resuspended in 1.5 ml of bRP buffer A (5 mM ammonium formate (pH 10.0) and 2 % ACN v/v) and fractionated by HPLC using an Agilent Zorbax Extended C₁₈ 5 μ M column (dimensions 9.4 \times 250 mm). A 50 μ l fraction of load was saved to analyze later as an MS detectable sample during nanoLC-MS/MS analysis and for purposes of protein normalization. The sample was fractionated using a step gradient with Buffer B (5 mM ammonium formate (pH 10.0) and 80 % ACN v/v) as follows: 0-7.5 min (0-6 % B), 7.5-10.5 min (6-8 % B), 10.5-67.5 min (8-27 % B), 67.5-73.5 min (27-31 %), 73.5-79.5 min (31-39 % B), 79.5-90 min (39-60 %), and 90-116 min (60-80 % B) all at a flow rate of 2.0 ml/min. Fractions were collected in one-minute increments and mixed non-contiguously into 5 bins, beginning with fraction 8 and ending with fraction 103. Binned fractions were frozen by storing at -80 °C for more than 1 hour and subsequently lyophilized to dryness.

K- ϵ -GG peptide antibody cross-linking and immunoprecipitation.

In short, one aliquot of the K- ϵ -GlyGly peptide specific antibody (PTMScan® Ubiquitin Remnant Motif (K- ϵ -GlyGly) Kit #5562, Limited Use License, Cell Signaling Technology) was washed with 3-1 ml aliquots of 100 mM sodium borate (pH 9.0) and cross-linked in the presence of 1 ml of DMP cross-linking solution (100 mM sodium borate (pH 8.0), 20 mM dimethyl pimelimidate, DMP) for 30 min at room temperature with gentle rotation. Antibody bound beads were pelleted after each wash by centrifugation at 2,000 \times g for 30 sec and kept on ice whenever possible. The cross-linking reaction was performed to decrease contamination of K- ϵ -GG peptides with antibody during the final peptide elution step. The cross-linking reaction was quenched by washing the beads with 3-1 ml aliquots of 200 mM ethanolamine blocking buffer (pH 8.0) followed by incubating the cross-linked antibody for 2 hours at 4 °C with 1 ml of fresh ethanolamine blocking buffer. After blocking, the antibody-bound beads were washed with 3-1 ml aliquots of IAP buffer (50 mM MOPS (pH 7.2), 10 mM sodium phosphate, and 50 mM NaCl) and divided equally into 5 aliquots. Independently, the 5 desalted binned peptide samples were resuspended in

1.5 ml of 1× IAP buffer, the pH was measured (should be $\text{pH} \approx 7$), and cleared by spinning at maximum speed for 5 min. The peptide samples were allowed to incubate with the freshly cross-linked antibody for 2 hours at 4 °C. After immunoprecipitation the beads were pelleted by centrifugation at $2,000 \times g$ for 1 min, resuspended in 500 μl of 1× IAP, and transferred to 0.67 ml tubes and washed 3 times with 500 μl of 1× IAP buffer. Following the IAP washes, the beads were washed once with 500 μl of 1× PBS, followed by one 500 μl of wash with mass spectrometry grade water (Fluka). Finally, the bound K- ϵ -GG peptides were eluted with $2 \times 150 \mu\text{l}$ aliquots of 0.15 % TFA. With each elution aliquot, the beads were incubated for 10 min at RT with periodic tapping on the tube to achieve proper mixing. The resulting eluents were combined, dried, desalted by HPLC using a Michrom Bioresources C_{18} macrotrap, (Buffer A: 0.2 % Formic Acid in H_2O ; Buffer B: 0.2 % Formic Acid in ACN) and concentrated *in vacuo*.

NanoLC-MS/MS analysis.

The dried immunoprecipitated peptides were resuspend in Buffer A (0.2 % Formic Acid, 2 % ACN, nanoLC grade 97.8 % H_2O) and subjected to proteomic analysis using an EASY II nano-UPLC (Thermo Fisher Scientific) connected on-line to an Orbitrap Elite hybrid mass spectrometer with a nanoelectrospray ion source (Thermo Scientific) using settings similar to those previously described (Porrás-Yakushi et al., 2015). Peptides were separated using a 15 cm silica analytical column with a 75 μm inner diameter packed in-house with reversed phase ReproSil-Pur C_{18}AQ 3 μm resin (Dr Maisch GmbH, Amerbuch-Entringen, Germany). The flow rate was set to 350 nl/min, using a linear gradient of 2%-32% B (0.2% Formic Acid, 80 % ACN, 19.8 % nanoLC grade H_2O). Mass spectrometry detectable samples were analyzed on a 159 min gradient, while basic reversed phase immunoprecipitated samples were analyzed on a 90 min gradient. The mass spectrometer was set to collect data in a data-dependent mode, switching automatically between full-scan MS and tandem MS acquisition. All samples were analyzed by ETD and decision tree fragmentation. For ETD fragmentation, the fifteen most intense precursor ions were selected, while the 20 most intense ions were selected for fragmentation using the decision tree method. Data acquisition was managed using Xcalibur 2.0.7 and Tune 2.4 software (Thermo Fisher Scientific).

Mass spectrometry analyses of protein aggregates

Mass spectrometry analyses of protein aggregates were performed as described. Insoluble protein pellets were solubilized in an 8 M Urea buffer (40 mM Tris, 65 mM DTT, 100 mM Ammonium bicarbonate) containing cOmplete Protease Inhibitor Cocktail (Roche) and sonicated for 10 seconds at 10 % of maximum amplitude using a Branson Digital Sonifier. Samples were digested and prepared for mass spectrometry as described in (Pierce et al., 2013). One hundred fifty ng of digested peptides from *tom1Δ* cells and equal volume of peptides from WT cells were analyzed using an EASY-nLC 1000 coupled to an Orbitrap Fusion. Spectra were analyzed by MaxQuant (v 1.5.3.30). Digested peptides were loaded onto a 26-cm analytical HPLC column (75 μm ID) packed in-house with ReproSil-Pur C18AQ 1.9 μm resin (120 Å pore size, Dr. Maisch, Ammerbuch, Germany). After loading, the peptides were separated with a 120 min gradient at a flow rate of 350 nl/min at 50°C (column heater) using the following gradient: 2-6 % solvent B (7.5 min), 6–25 % B (82.5 min), 25-40 % B (30min), 40-100 % B (1min), and 100 % B (9 min) where solvent A was 97.8 % H₂O, 2 % ACN, and 0.2 % formic acid and solvent B was 19.8 % H₂O, 80 % ACN, and 0.2 % formic acid. The Orbitrap Fusion was operated in data-dependent acquisition (DDA) mode to automatically switch between a full scan ($m/z=350-1500$) in the Orbitrap at 120,000 resolving power and a tandem mass spectrometry scan of Higher energy Collisional Dissociation (HCD) fragmentation detected in the ion trap (using TopSpeed). AGC target of the Orbitrap and ion trap was 400,000 and 10,000 respectively.

Mass Spec Data analysis

Raw data was searched using MaxQuant (Cox and Mann, 2008; Wagner et al., 2011) (v 1.5.3.30) against the SGD yeast database (5911 entries) and a contaminant database (259 entries). Precursor mass tolerance was 4.5 ppm after automatic recalibration. Fragment ion tolerance was 0.5 Da. All default options were used except for SILAC diGly samples where the multiplicity was set to 2 with heavy labels Arg6 (+6.020129) and Lys8 (+8.014199). Trypsin digest was specified with up to two missed cleavages. Protein, peptide, and site false discovery rates were less than 1 % and were estimated using a target-decoy approach (Elias and Gygi, 2010). For non-GlyGly analysis, oxidation of methionine and protein N-terminal acetylation were specified as variable modifications and carbamidomethylation of

cysteine was specified as a fixed modification. For GlyGly analysis, N-ethylmaleimide modification of cysteine (+125.0477) was specified as a fixed modification, while N-terminal acetylation (+42.0106), methionine oxidation (+15.9949), and the GlyGly remnant (+114.0429, not on peptide C-terminus with neutral losses of 57.0215 and 114.0429 to account for fragmentation in the GlyGly remnant) were set as variable modifications, as previously described (Porras-Yakushi et al., 2015). iBAQ protein quantitation and “match between runs” were enabled.

For each pair of *tom1Δ* and WT samples, the difference between iBAQ abundances was used to identify the proteins that were most accumulated in the insoluble fraction in *tom1Δ*. The average difference between *tom1Δ* and WT samples across the three replicates was then used to identify the top 10 percent of proteins most accumulating. This set of 127 proteins was checked for annotation enrichment against all proteins identified in the sample using DAVID (Huang et al., 2009a, b). The most enriched terms included GO FAT cellular component annotations “ribosome” (p-value < 9.3E-40) and “mitochondrion” (p-value < 6.3E-2). The distribution of average Δ iBAQ values for all proteins and for proteins with those annotations is in Figure 3H. The distributions of average Δ iBAQ values for the large and small ribosomal subunits were compared with non-ribosomal proteins in Figure S6C. The individual ribosomal proteins Δ iBAQ values are displayed in Figure S6D with error bars representing the standard error of the mean (SEM).

FIGURES

Main figures

Figure 1. Ubc4/5 and Tom1 are the E2 and E3 enzymes responsible for ERISQ

Figure 2. Tom1 functions in non-ribosomal fractions

Figure 3. Diminished ubiquitination and accumulation of insoluble ribosomal proteins in *tom1* cells

Figure 4. A short stretch of positively-charged residues in Rpl26a that mediates rRNA binding promotes association with Tom1

Figure 5. Tom1 acts through residues that are normally inaccessible in the structure of the mature ribosome

Figure 6. Defective ribosome assembly homeostasis and proteostatic collapse in *tom1* mutant cells

Figure 7. ERISQ is conserved in human cells

Supplemental figures

Figure S1. Identification of ERISQ defect in *tom1Δ* and *ubc4Δ*

Figure S2. Characterization of tagged and ligase-dead Tom1

Figure S3. Tom1 mediates ubiquitination of overexpressed Rpl26a

Figure S4. Tom1 targets a broad range of overexpressed and endogenous ribosomal proteins

Figure S5. Quantitative GlyGly proteomic analyses of *tom1* mutants

Figure S6. Endogenous ribosomal proteins accumulate as insoluble species in *tom1Δ* mutants

Figure S7. Rpl26a-4E mutant is unstable and degraded by Doa10 in the nucleus/nucleolus

Figure S8. Tom1 is required for maintaining proteostasis

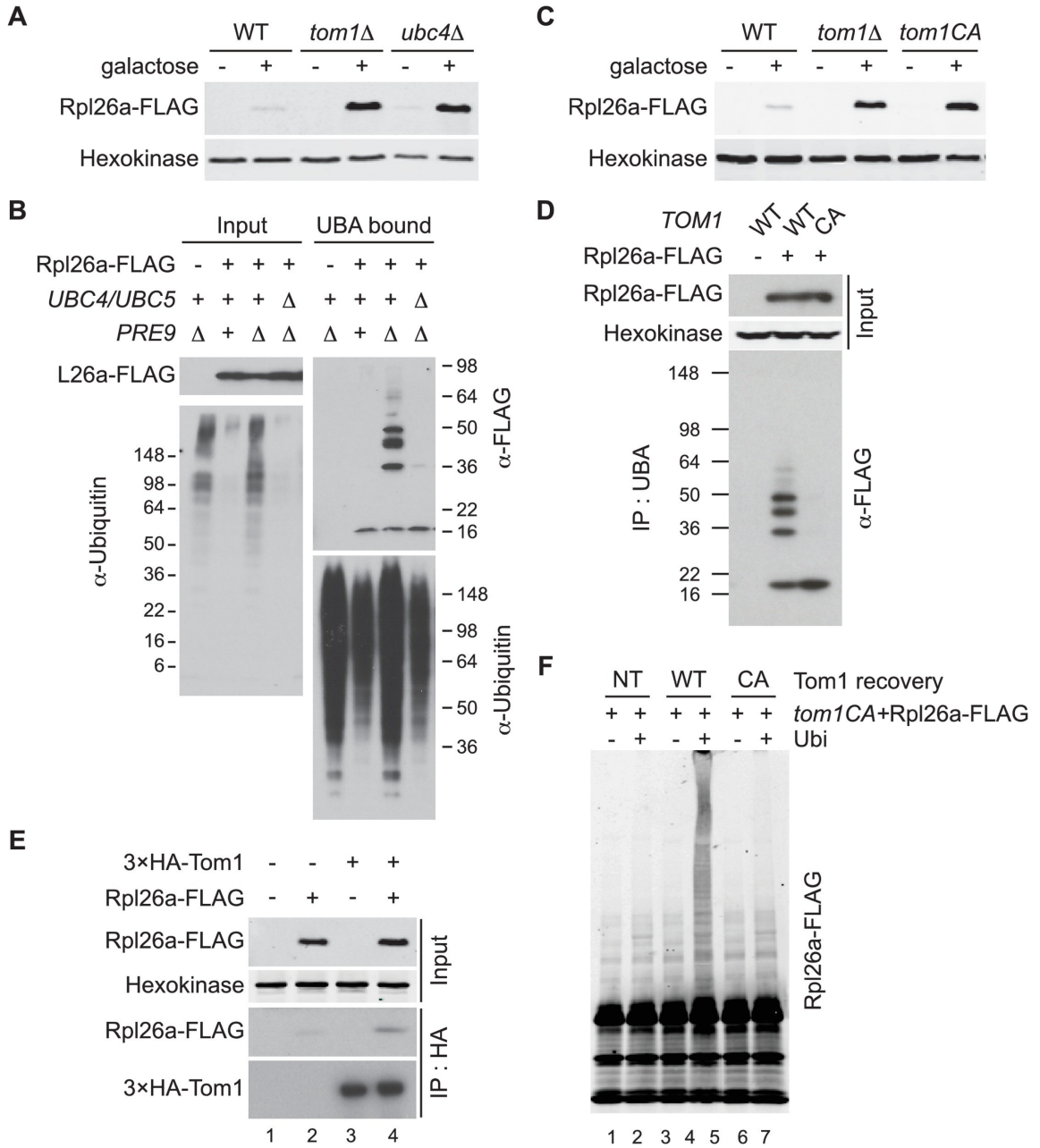


Figure 1. Ubc4/5 and Tom1 are the E2 and E3 enzymes responsible for ERISQ

(A) Rpl26a^{FLAG} accumulates in *tom1Δ* and *ubc4Δ*. Accumulation of Rpl26a^{FLAG} upon galactose induction in WT, *tom1Δ* and *ubc4Δ* cells was evaluated by SDS-PAGE and immunoblotting with the indicated antibodies. n = 3 biological replicates. (B) Rpl26a^{FLAG} ubiquitination depends on Ubc4/Ubc5. Rpl26a^{FLAG} was induced in cells of the indicated genotypes and cell lysates were prepared and subjected to pull-down with UBA domain resin. Input and bound proteins were evaluated as in (A). n = 3 biological replicates. (C) Rpl26a^{FLAG} accumulates in *tom1^{CA}* cells. As in (A) except that the Tom1 ligase-dead (*tom1^{CA}*) mutant was used. n = 3 biological replicates. (D) Rpl26a^{FLAG} ubiquitination depends on Tom1. As in (B) except that cells expressing WT Tom1 or Tom1^{CA} were treated with bortezomib for 45 min after addition of galactose. n = 3 biological replicates. (E) Rpl26a^{FLAG} binds ^{3xHA}Tom1. Anti-HA immunoprecipitates from cells expressing ^{3xHA}Tom1 and Rpl26a^{FLAG} were immunoblotted with antibodies to HA, FLAG, and hexokinase. n = 3 biological replicates. (F) In vitro ubiquitination of Rpl26a^{FLAG} by Tom1. Rpl26a^{FLAG} retrieved in ^{3xHA}Tom1^{CA} immunoprecipitates was supplemented or not with E1/E2/ubiquitin/ATP (Ubi) and Tom1 retrieved from untagged (NT), ^{3xHA}TOM1 (WT), or ^{3xHA}TOM1^{CA} (CA) cells, as indicated. See detailed methods in the experimental procedures section. n = 3 biological replicates.

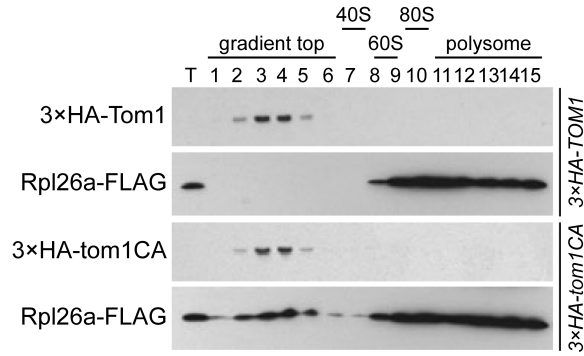
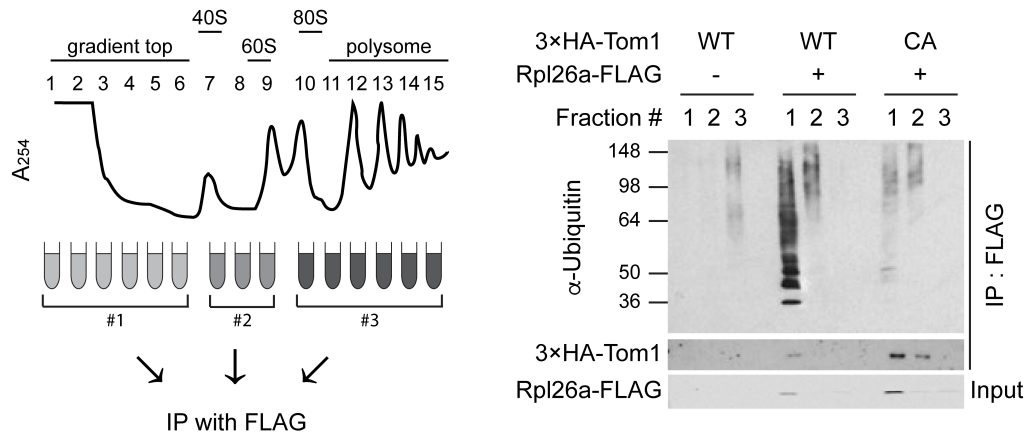
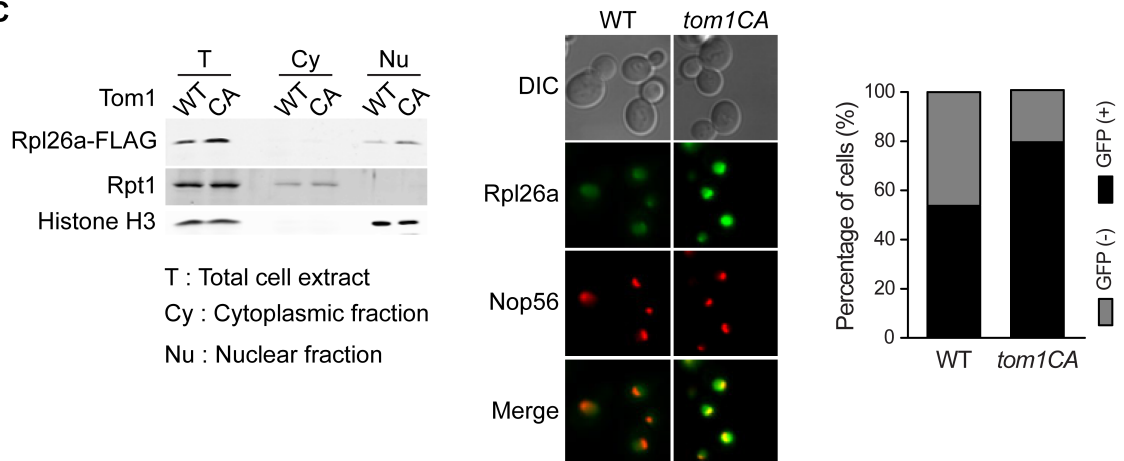
A**B****C**

Figure 2. Tom1 functions in non-ribosomal fractions

(A) Sucrose gradient fractionation behavior of 3xHA Tom1 and Rpl26a^{FLAG} upon galactose induction of Rpl26a^{FLAG} in 3xHA TOM1 or 3xHA TOM1^{CA} cells. T indicates total extract. n = 2 biological replicates. (B) Tom1 is required for ubiquitination of unassembled Rpl26a^{FLAG}. Left: experimental scheme. Right: cells were treated with bortezomib for 30 min after induction of Rpl26a^{FLAG} with galactose and then lysed and fractionated as in panel A prior to being processed as depicted in panel B. n = 2 biological replicates. (C) Rpl26a accumulates in the nucleus of *tom1*^{CA} cells. Left: Subcellular fractionation of Rpl26a^{FLAG} induced in WT and *tom1*^{CA} cells. Histone H3 and Hexokinase were used as nuclear and cytoplasmic markers, respectively. CA refers to Tom1-Cys3235Ala. Right: Fluorescence microscopy of Rpl26a^{GFP} induced in WT and *tom1*^{CA} cells. Nop56-RFP marks nucleoli. Shown at far right is the percentage of GFP positive cells. n = 2 biological replicates.

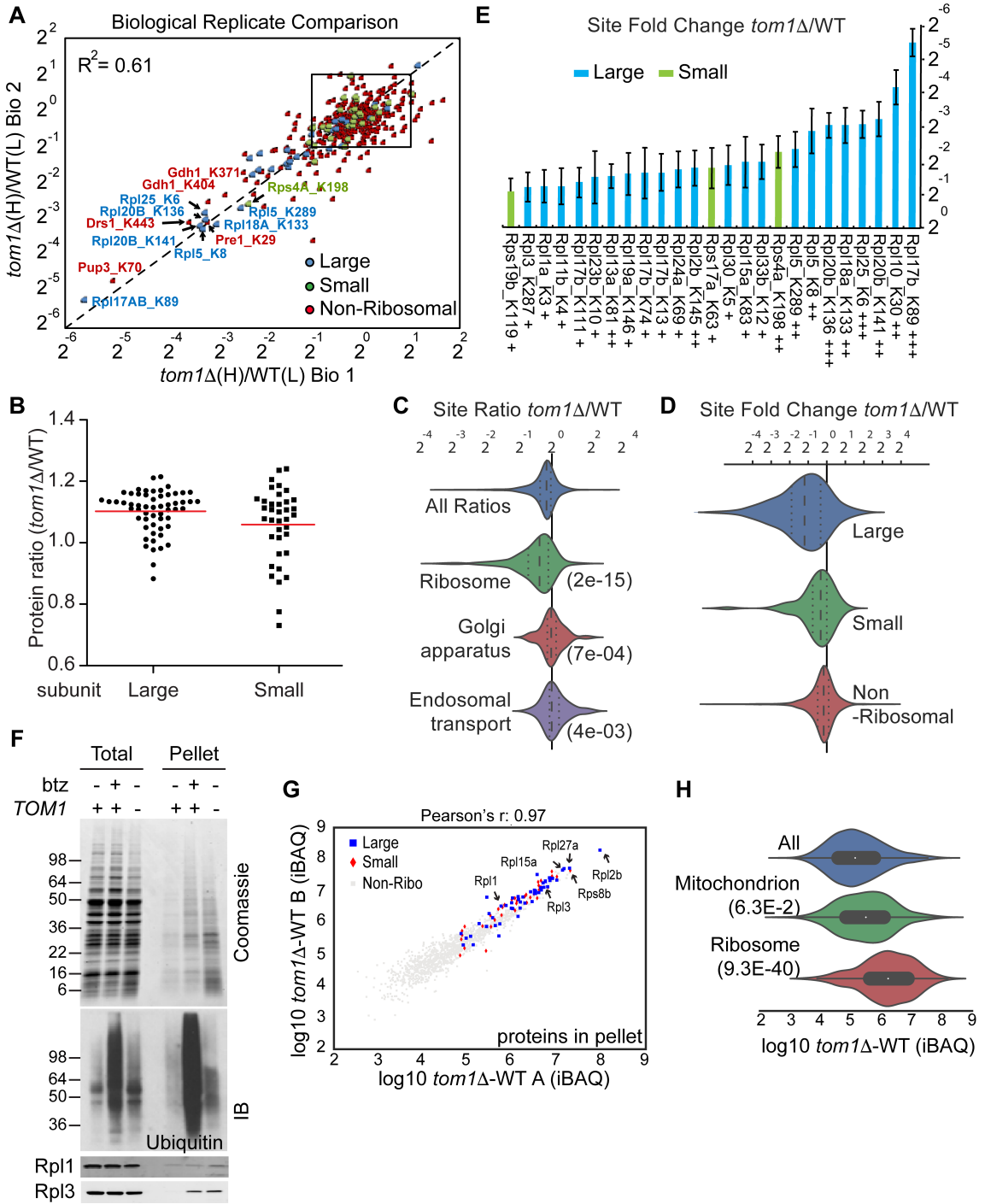


Figure 3. Diminished ubiquitination and accumulation of insoluble ribosomal proteins in *tom1* cells

(A) Diminished ubiquitination of ribosomal proteins in *tom1* Δ . Scatter plot of the SILAC ratios (*tom1* Δ /WT) for GlyGly-modified peptides identified in biological replicate 1 versus 2. Sites with the largest decrease in ubiquitination are annotated. The other pairwise comparisons are in Figure S5A. n = 3 biological replicates. (B) Column scatter plot representing the distribution of ratios (*tom1* Δ /WT) for proteins of the large (circles) and small (square) ribosome subunits. A red bar indicates the mean. (C) Violin plot of gene ontology analysis of ubiquitinated proteins that had one or more ubiquitination site that decreased by ≥ 2 -fold. The most strongly affected categories are shown. The number in parentheses refers to the disproportionate enrichment for the category in the top 10% of identifications and is the Benjamini and Hochberg corrected p-value from a Fisher Exact test. (D) Violin plot representing the distribution of ubiquitin site occupancy ratios (*tom1* Δ /WT) for the large (blue) and small (green) ribosome subunits, and non-ribosomal proteins (red). (E) The 25 ribosomal ubiquitination sites with the largest decrease in ubiquitin occupancy in *tom1* Δ . +++, p <0.001; ++, p <0.01; +, p <0.05. Each site was observed in at least two of the three biological replicates. The error bars represent 95% confidence intervals. Note that ubiquitination at K37 and K69 in Rpl26b was decreased by 2.4-fold and 1.6-fold in *tom1* Δ , respectively. (F, G) Insoluble ribosomal proteins accumulate in *tom1* Δ . (F) Detergent-insoluble pellet fractions isolated from lysate (Total) of indicated cells were analyzed by SDS-PAGE and staining with Coomassie blue or immunoblotting with the indicated antibodies. The pellet fraction is overloaded 20-fold compared to the total and supernatant fractions. n = 2 biological replicates. (G) Scatter plot representing Δ iBAQ of biological replicate B vs. A for insoluble proteins in *tom1* Δ mutants. Ribosomal proteins with the largest increase in the pellet fraction upon *TOM1* deletion, and Rpl1 and Rpl3 are annotated. Pearson's r-value is indicated on top of the plot. The other pairwise comparisons are in Figure S6B. n = 3 biological replicates. (H) Gene ontology analysis of proteins exhibiting increased insolubility in *tom1* Δ . Analysis is the same as for panel C.

A

MAKQSLDVSSD RRKARK AYFTAPSSQ RR VLLSAPLSKELRAQYGICALP RR DD

12 16 27 51

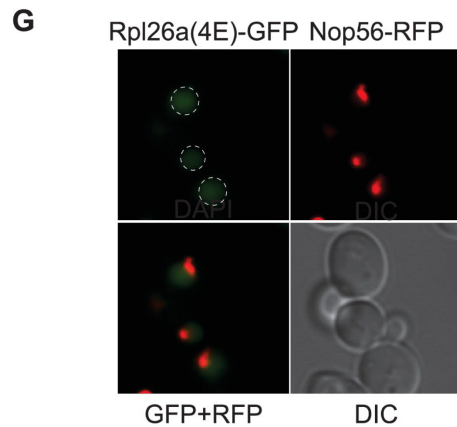
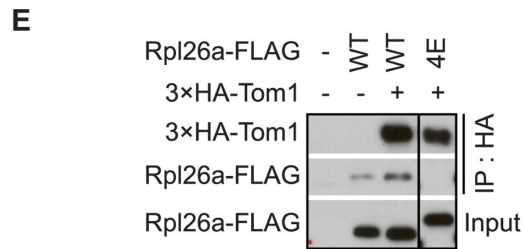
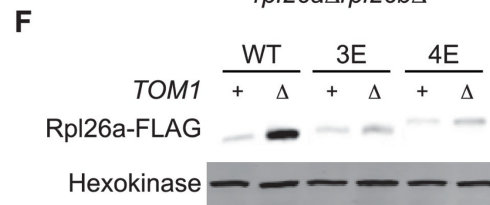
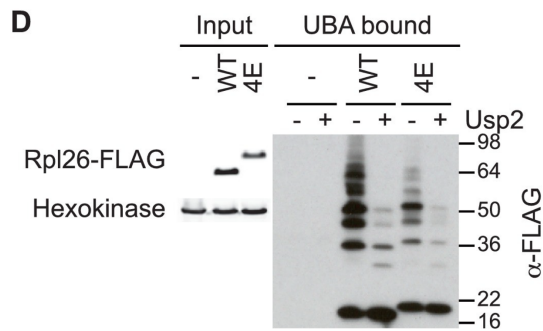
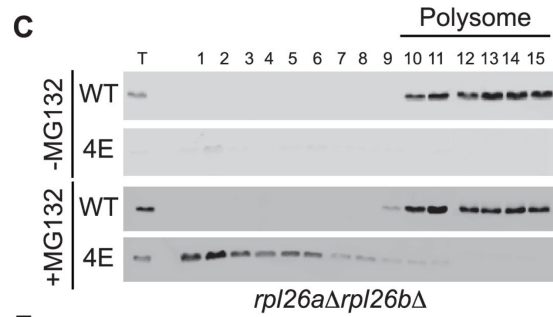
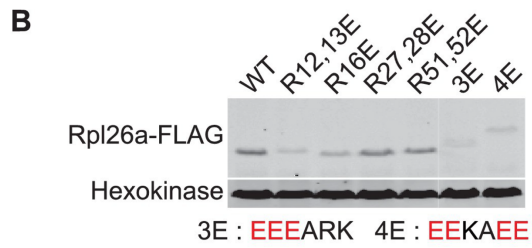
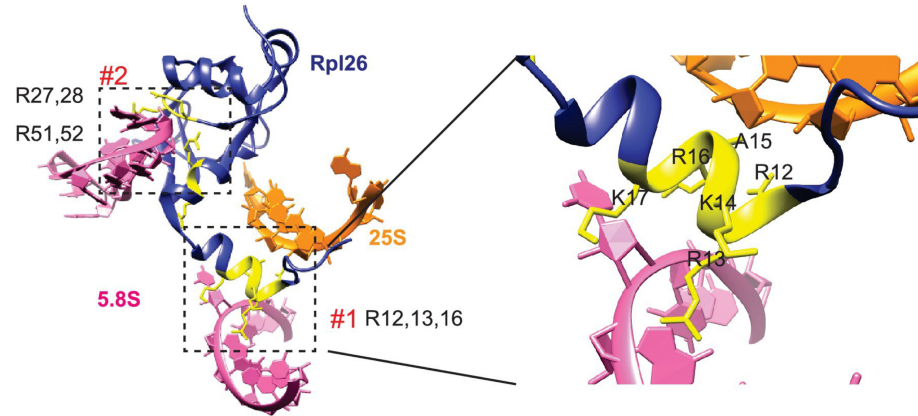
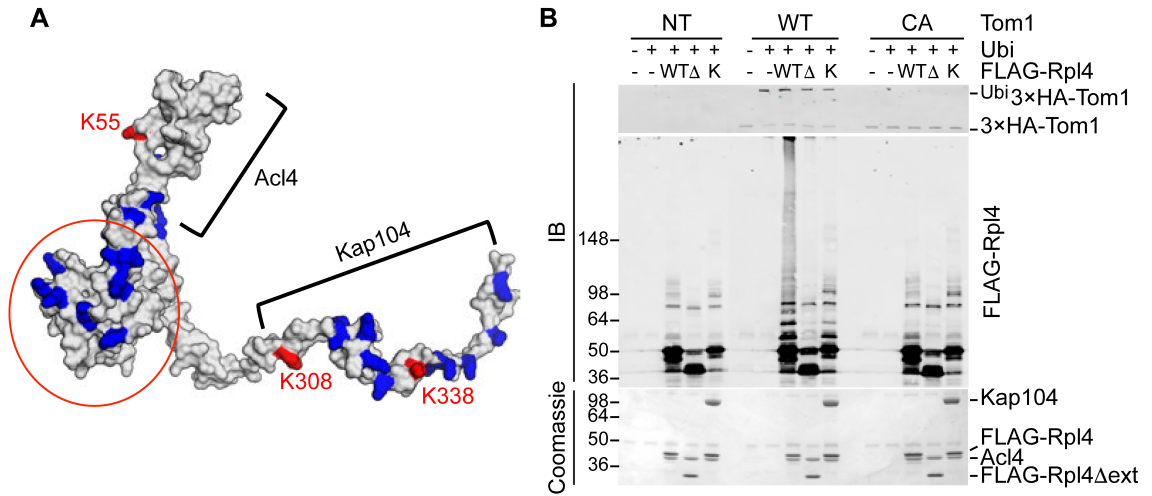


Figure 4. A short stretch of positively-charged residues in Rpl26a that mediates rRNA binding promotes association with Tom1

(A) Top: The first 54 amino acids of Rpl26a. Sequences adjacent to rRNA are boxed. Arginine residues targeted for mutation are in red. Bottom: Relative positions of arginines and rRNA based on the atomic model of the yeast 80S ribosome (PDB IDs: 3U5D and 3U5E). Orange and pink ribbons correspond to 25S and 5.8S rRNA, respectively. Blue ribbon corresponds to Rpl26. Predicted regions (#1 and #2) for rRNA binding are highlighted in yellow and boxed. (B) Differential accumulation of WT and mutant Rpl26a^{FLAG} upon galactose induction. n = 2 biological replicates. (C) Top: Ribosome assembly of WT Rpl26a^{FLAG} or Rpl26a-4E^{FLAG} induced in *rpl26aΔrpl26bΔ* cells. Bottom: Same as above except that MG132 was added 30 min after addition of galactose. T indicates total extract. n = 2 biological replicates. (D) Polyubiquitination of Rpl26a-4E^{FLAG}. Assay was performed as described for Figure 1D. Samples in '+' lanes were treated with deubiquitinating enzyme Usp2 prior to processing for SDS-PAGE, to demonstrate that high MW species were modified with ubiquitin. n = 2 biological replicates. (E) The Rpl26-4E mutation disrupts binding to Tom1. Lysates from cells of the indicated genotypes were subjected to pull-down with anti-HA followed by SDS-PAGE and immunoblotting for the indicated proteins. n = 2 biological replicates. (F) Protein level of Rpl26a^{FLAG} mutants upon galactose induction in WT and *tom1Δ* cells. n = 2 biological replicates. (G) Fluorescence images of Rpl26a^{4E}-GFP induced in WT cells. Nop56-RFP marks nucleoli. Dashed circles indicate nuclear region as judged by DAPI staining. n = 2 biological replicates.



C

RP_Lys	Comments
Rpl2_K145, Rpl5_K8, Rpl15_K83, Rpl17_K74, Rpl17_K89, Rpl23_K10, Rpl33_K12	Inaccessible (7 lysines)
Rpl3_K287, Rpl17_K13, Rpl17_K111	Accessible (3 lysines)
Rpl5_K289, Rpl13_K81, Rpl18_K133, Rpl19_K146, Rpl20_K136, Rpl20_K141, Rpl10_K30*, Rpl24_K69*	Exposed but not accessible to 25 Å probe (8 lysines) * exposed in 60S but not 80S

Figure 5. Tom1 acts through residues that are normally inaccessible in the structure of the mature ribosome

(A) Structure of Rpl4 within the mature ribosome (PDB ID: 4V88). Lysine residues are colored blue, with K55, K308, and K338 colored red. Areas involved in binding Acl4 and *ct*Kap104 are indicated. The exact boundaries of the Kap104 binding site are not known. The globular central domain, which is fully exposed in the ternary Acl4•Rpl4•Kap104 complex but is not ubiquitinated, is circled in red. (B) Ubiquitination of Acl4•Rpl4 by ^{3xHA}Tom1. Anti-HA immunoprecipitates from untagged (NT), ^{3xHA}TOM1 (WT), and ^{3xHA}*tom1*^{CA} (CA) cells were supplemented or not with E1/E2/ubiquitin/ATP (Ubi) and purified Acl4•^{FLAG}Rpl4, Acl4•^{FLAG}Rpl4Δext and Acl4•^{FLAG}Rpl4•*ct*Kap104 proteins. Samples were analyzed by SDS-PAGE and staining with Coomassie blue or immunoblotting with the indicated antibodies. WT, Δ, and K refer to Acl4•^{FLAG}Rpl4, Acl4•^{FLAG}Rpl4Δext and Acl4•^{FLAG}Rpl4•*ct*Kap104, respectively. See detailed methods in Experimental Procedures. n = 3 biological replicates. (C) Tom1 preferentially targets lysines that are inaccessible in mature ribosomes. Lysine residues shown are those from large subunit ribosomal proteins in Figure 3E that are incorporated in the model for the structure of the yeast ribosome (PDB ID: 4V88). The structure of a HECT domain–donor ubiquitin complex (PDB ID: 4LCD) predicts that a gap of radius 25 Å must be present for Tom1 to access a lysine for ubiquitination. Two of the sites (Rpl10 K30 and Rpl24 K69) are accessible in the 60S large subunit but become inaccessible upon formation of the 80S ribosome.

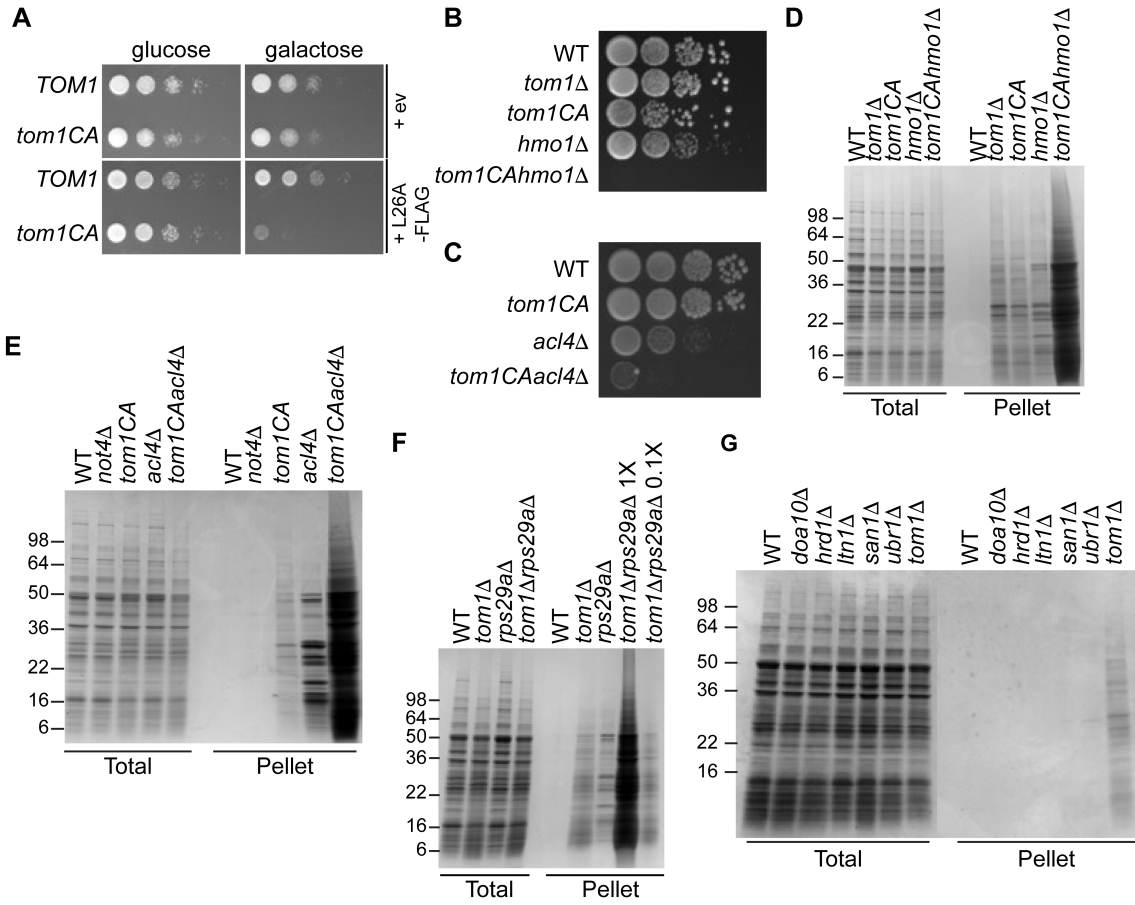


Figure 6. Defective ribosome assembly homeostasis and proteostatic collapse in *tom1* mutant cells

(A-C) Hypersensitivity of *tom1^{CA}* cells to imbalances in ribosome components. (A) Cells of the indicated genotypes were spotted in serial 10-fold dilutions on glucose or galactose medium and incubated at 30°C for 2 days. ev refers to empty vector. n = 2 biological replicates. (B, C) As in (A) except that cells of the indicated genotypes were spotted on YPD. n = 2 biological replicates. (D-G) Massive accumulation of insoluble proteins in *tom1* mutant cells. Cells of the indicated genotypes were lysed and fractionated into detergent-soluble and insoluble fractions, which were separated by SDS-PAGE and stained with Coomassie Blue. The pellet fraction is overloaded 20-fold compared to the total and supernatant fractions. n = 2 biological replicates.

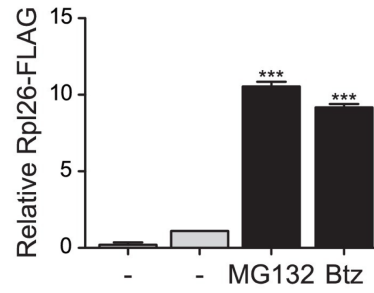
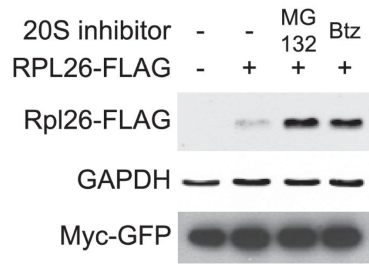
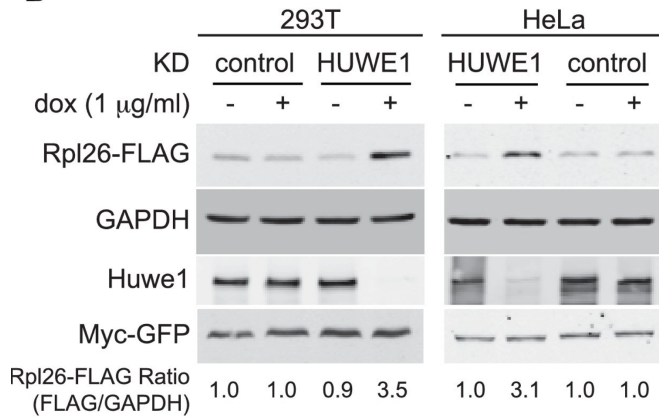
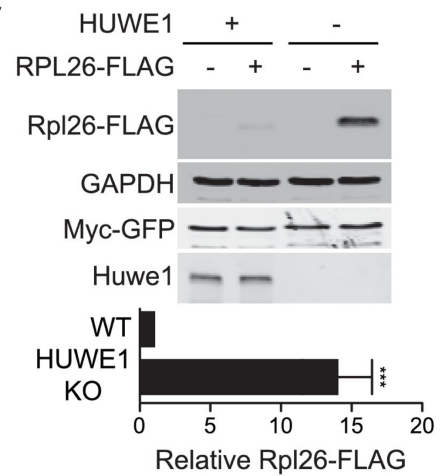
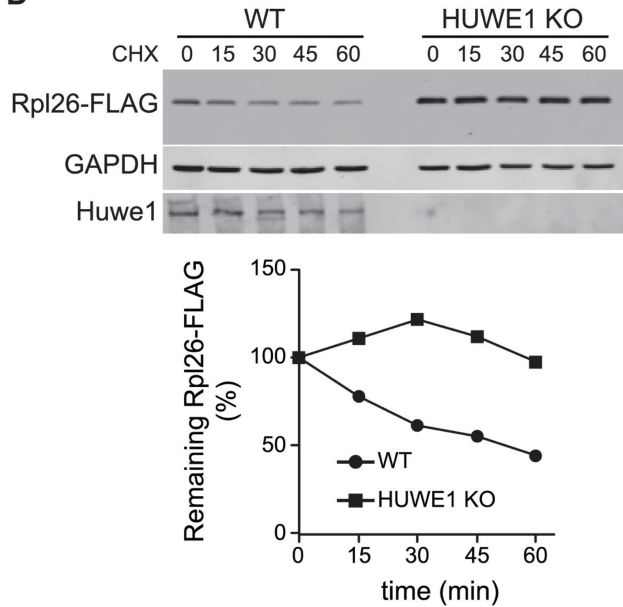
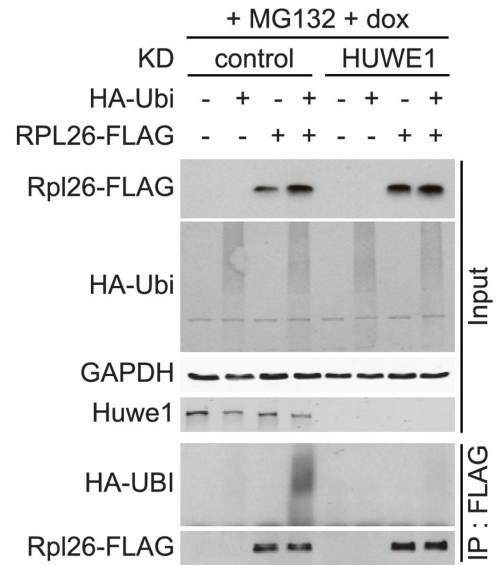
A**B****C****D****E**

Figure 7. ERISQ is conserved in human cells

(A) Proteasome inhibition enables overexpression of human Rpl26. Left: transiently expressed hRpl26^{FLAG} in T-RExTM-293 cells treated with 10 μ M MG132 or 1 μ M bortezomib (btz) for 3 hours. Right: quantification of blots. Values are the mean of three independent experiments and error bars indicate standard deviations. Asterisks indicate significant differences (two-tailed student's t-test, ***P <0.0001, compared with DMSO treatment). n = 3 biological replicates. (B) Depletion of HUWE1 enables overexpression of human Rpl26. As in (A) except that T-RExTM-293 (left) and HeLa (right) cells were induced with doxycycline for 3 days to express stably integrated shControl or shHUWE1. The relative ratio of hRpl26^{FLAG}/GAPDH is shown below each lane. n = 3 biological replicates. (C) Knockout of *HUWE1* enables overexpression of human Rpl26. Upper: as in (A) except that wild type and *HUWE1* knockout HEK293T cells were used. Bottom: quantification of blots. Values are the mean of three independent experiments and error bars indicate standard deviations. Asterisks indicate significant differences (two-tailed student's t-test, ***P <0.0001, compared with WT cells). n = 3 biological replicates. (D) Overexpressed human Rpl26 is stable in *HUWE1* knockout cells. Upper: wild type and *HUWE1* knockout HEK293T cells transiently expressing hRpl26^{FLAG} were treated with 10 μ g/ml cycloheximide (CHX). Bottom: quantification of blot. n = 1 biological replicate. (E) HUWE1 promotes ubiquitination of overexpressed human Rpl26. As in (B) except that HA^{ubiquitin} was co-expressed with Rpl26^{FLAG} and MG132 was added 3 hours prior to cell lysis. Total cell extract prepared under denaturing condition was adsorbed to FLAG resin and the bound fraction was immunoblotted with antibodies against FLAG and HA. n = 2 biological replicates.

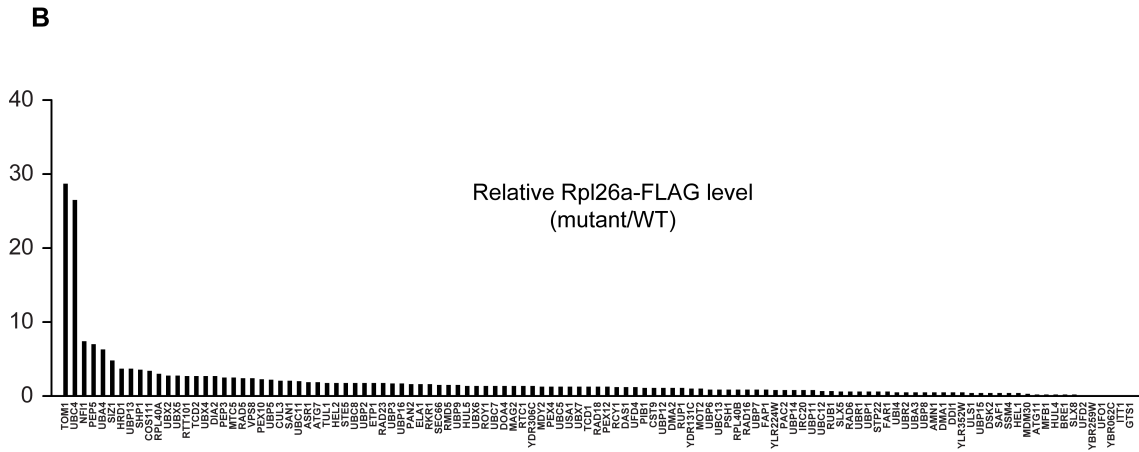
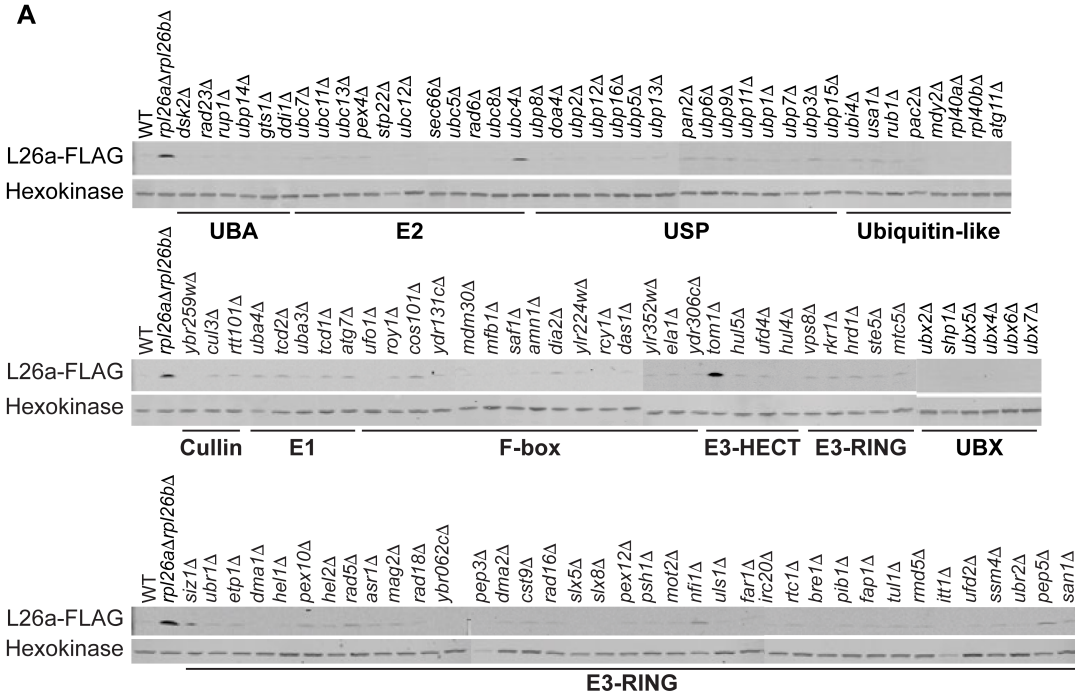


Figure S1. Identification of ERISQ defect in *tom1* Δ and *ubc4* Δ

(A) One hundred fifteen different knockout mutant strains each containing a plasmid that expressed Rpl26a^{FLAG} from the *GAL10* promoter were used. Rpl26a^{FLAG} induced in *rpl26a* Δ *rpl26b* Δ cells was used as a positive control. n = 1 biological replicate. (B) Quantification of data in (A).

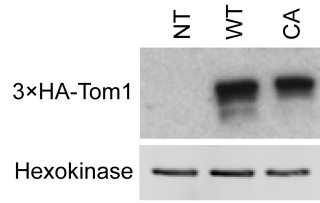
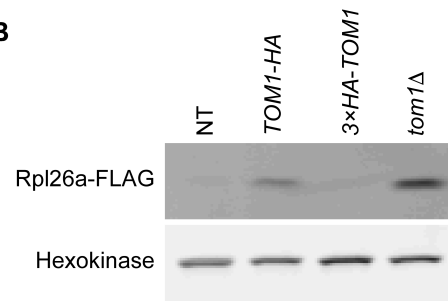
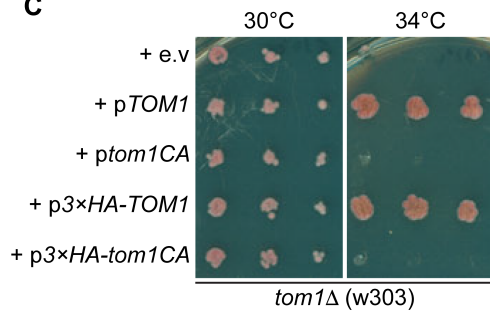
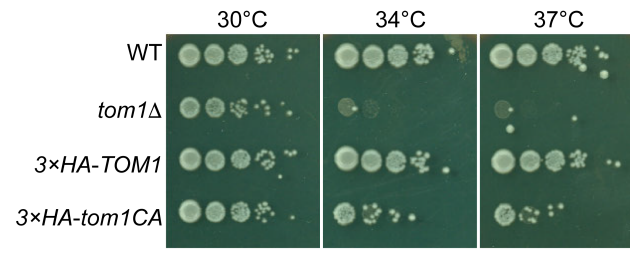
A**B****C****D**

Figure S2. Characterization of tagged and ligase-dead Tom1

(A) Protein level of $^{3\times\text{HA}}\text{Tom1}$ in cells expressing Tom1 (NT), $^{3\times\text{HA}}\text{Tom1}$ (WT) and $^{3\times\text{HA}}\text{Tom1}^{\text{CA}}$ (CA). n = 2 biological replicates. (B) Protein level of overexpressed Rpl26a^{FLAG} induced in cells expressing Tom1 (NT), Tom1^{HA}, $^{3\times\text{HA}}\text{Tom1}$ and *tom1*Δ. Note that a C-terminal tag on Tom1 compromises function, allowing for greater accumulation of galactose-induced Rpl26a^{FLAG}. n = 2 biological replicates. (C) Cells of the indicated genotypes were spotted on SC-TRP and incubated at 30 °C or 34 °C for 2 days. n = 2 biological replicates. (D) As in (C), except that cells of the indicated genotypes were spotted on YPD and incubated at the indicated temperatures for 2 days. n = 2 biological replicates.

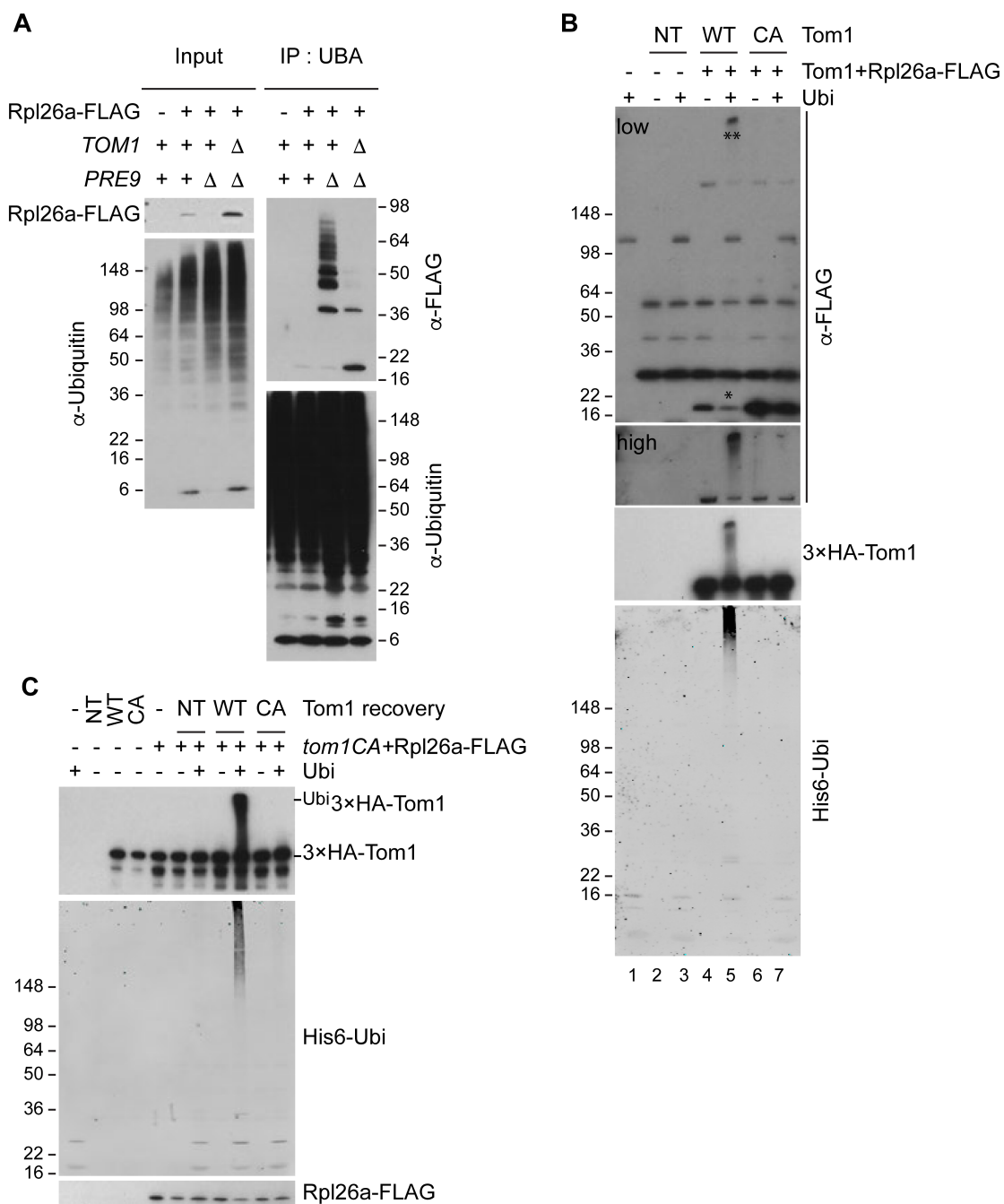


Figure S3. Tom1 mediates ubiquitination of overexpressed Rpl26a

(A) Polyubiquitination of Rpl26a^{FLAG}. Rpl26a^{FLAG} was induced in cells of the indicated genotypes and cell lysates were prepared and subjected to pull-down with UBA domain resin. Input and bound proteins were fractionated by SDS-PAGE and detected by immunoblot with the indicated antibodies. n = 2 biological replicates. (B) *In vitro* ubiquitination of Rpl26a^{FLAG} by Tom1. Lysates of cells expressing Rpl26a^{FLAG} and the indicated allele of ^{3xHA}Tom1 (NT is untagged control) were subjected to pull-down with anti-HA followed by addition of E1/E2/ubiquitin/ATP (Ubi) and incubation at 30°C for 1 hour. Reaction products were evaluated by immunoblot with the indicated antibodies. * indicates unmodified Rpl26a^{FLAG}. ** indicate ubiquitinated Rpl26a^{FLAG}. Note the increase in ubiquitinated Rpl26a^{FLAG} (**) and the loss of unmodified Rpl26a^{FLAG} (*). n = 2 biological replicates. (C) Additional immunoblots of samples in Figure 1F. n = 3 biological replicates.

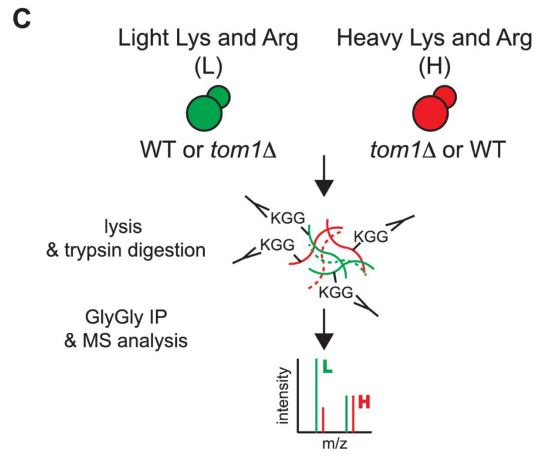
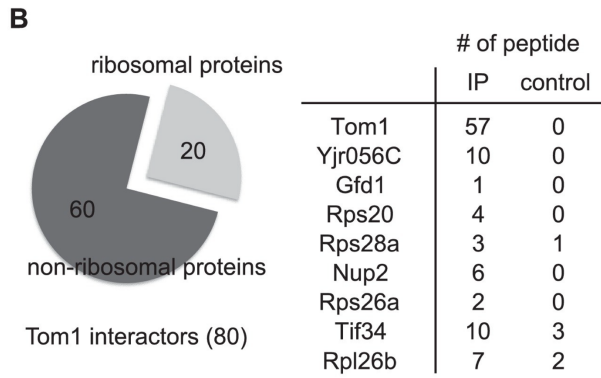
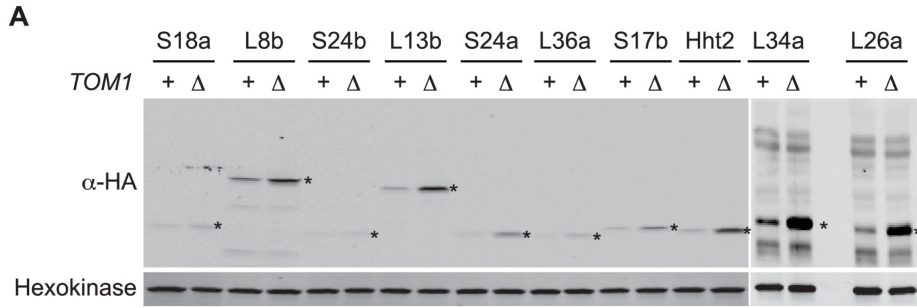


Figure S4. Tom1 targets a broad range of overexpressed and endogenous ribosomal proteins

(A) Relative levels of the transiently overexpressed, indicated ribosomal proteins (all tagged with a His6-HA-protein A ZZ domain epitope) in WT and *tom1* Δ mutants. n = 2 biological replicates. * indicates the expected size of protein. (B) Left: Cells expressing untagged-Tom1 or ^{3xHA}Tom1 were treated with bortezomib for 1 hour. Total cell extracts were adsorbed to HA resin and the bound fractions were analyzed by mass spectrometry. 80 proteins that increased >1.5 fold in ^{3xHA}Tom1 samples versus untagged samples were categorized into ribosomal or non-ribosomal proteins. Right: The number of peptides derived from the 9 proteins with the highest fold changes in ^{3xHA}Tom1 vs. untagged samples are shown. n = 1 biological replicate. (C) Schematic diagram of SILAC-based quantitative K- ϵ -GlyGly mass spectrometry (MS) strategy to identify Tom1-dependent ubiquitination sites.

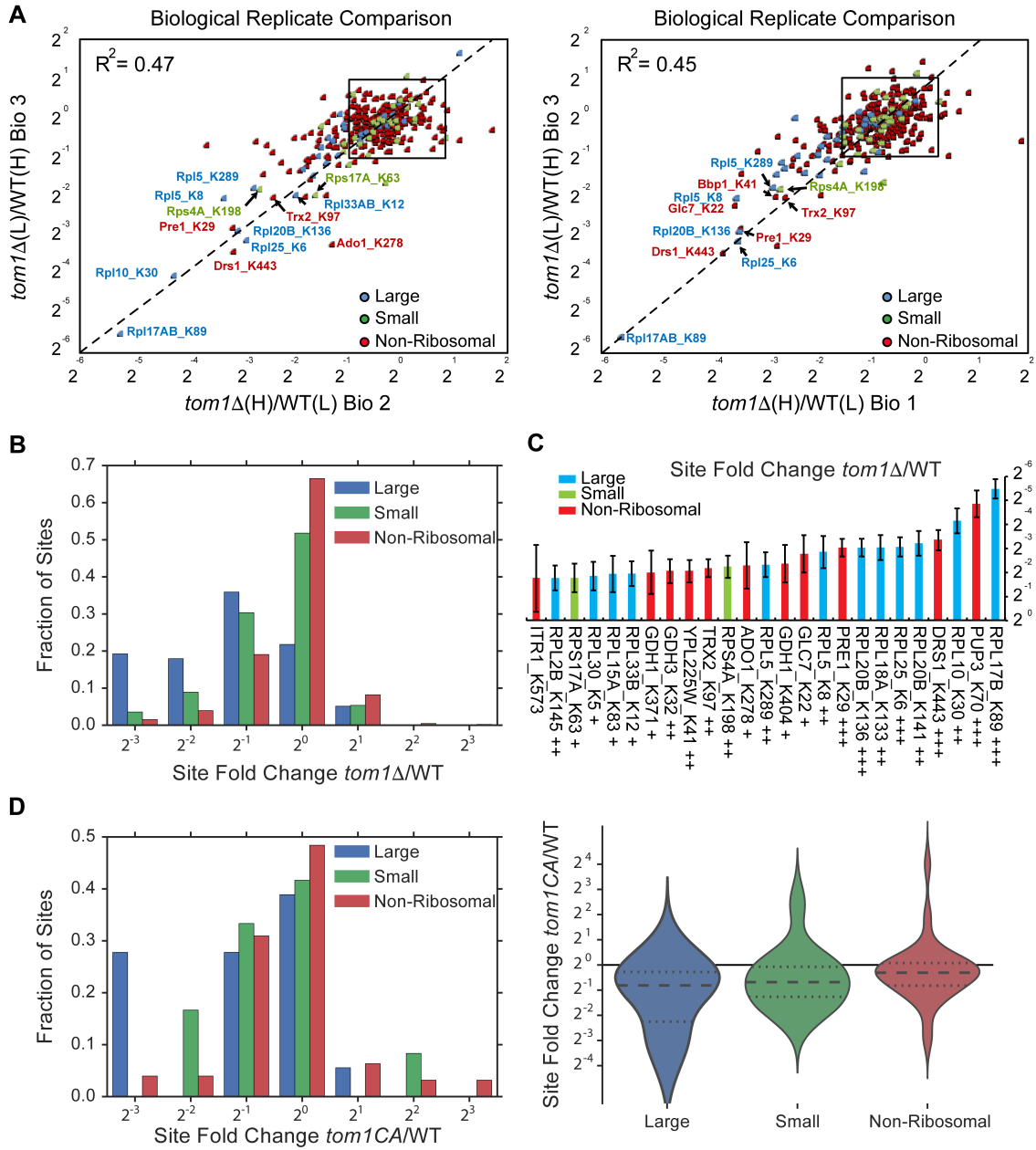


Figure S5. Quantitative GlyGly proteomic analyses of *tom1* mutants

(A) Scatter plots of the SILAC ratios (*tom1* Δ /WT) of biological replicate 3 vs. 2 (left) and biological replicate 3 vs. 1 (right) for GlyGly-modified peptides in *tom1* Δ and WT cells. Sites with the largest decrease in ubiquitination are annotated. These data accompany Figure 3A. n = 3 biological replicates. (B) Histogram of *tom1* Δ /WT ubiquitination site ratios for ribosomal proteins of the large and small subunits, and non-ribosomal proteins. For each protein category, the fraction of total with a given ratio is plotted. (C) The 25 ubiquitination sites with the largest decrease in ubiquitin occupancy in *tom1* Δ . +++, p <0.001; ++, p <0.01; +, p <0.05. Each site was observed in at least two of the three biological replicates. The error bars represent 95% confidence intervals. (D) Left: same as (B), except that a *tom1*^{CA} mutant was used instead of *tom1* Δ . Right: violin plot representing the distribution of ubiquitin site occupancy ratios for ribosomal proteins of the large (blue) and small (green) subunit, and non-ribosomal proteins (red). n = 3 biological replicates.

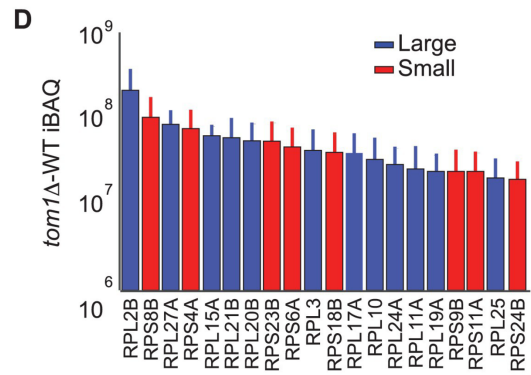
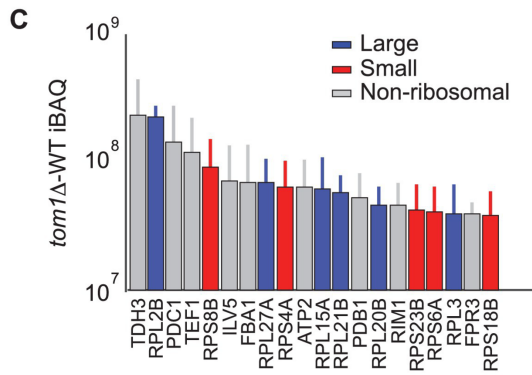
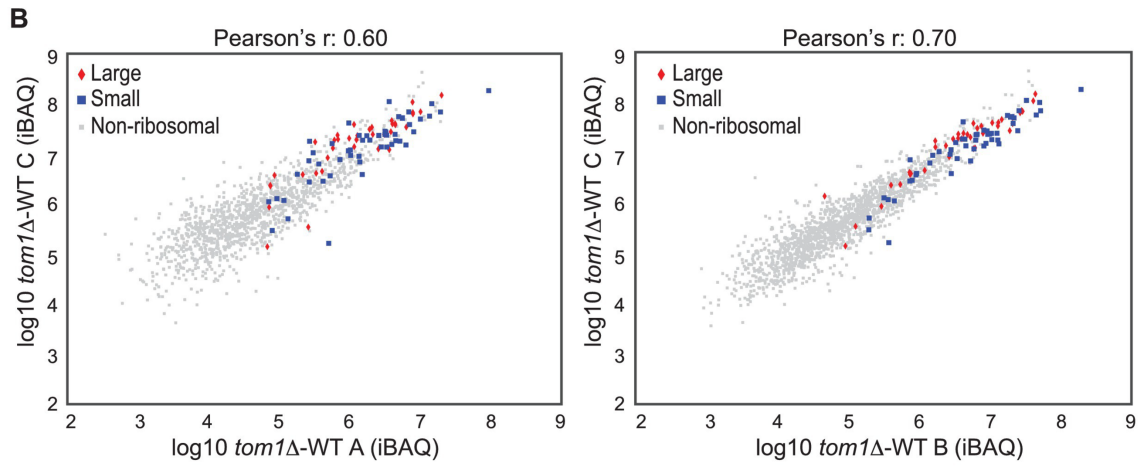
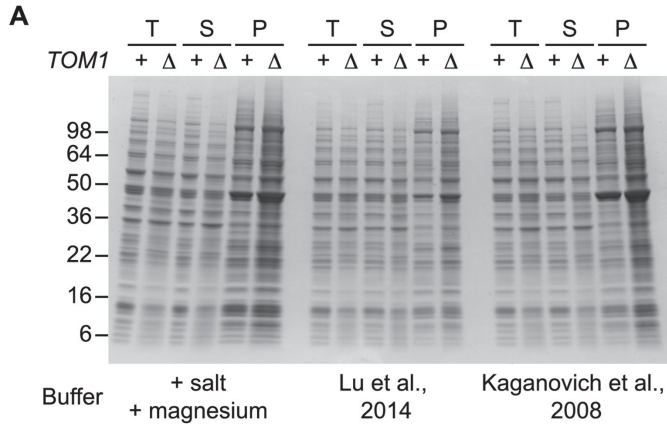


Figure S6. Endogenous ribosomal proteins accumulate as insoluble species in *tom1Δ* mutants

(A) Accumulation of insoluble proteins in *tom1* mutant cells is independent of lysis method or buffer. Cells of the indicated genotypes were lysed with glass beads in the presence of 3 different lysis buffers as indicated below gel image, and fractionated into detergent-soluble and insoluble fractions. Samples were separated by SDS-PAGE and stained with Coomassie Blue. The pellet fraction is overloaded 10-fold compared to the total and supernatant fractions. n = 2 biological replicates. T, S, and P indicate total, soluble, and pellet fractions, respectively. Note that results shown here are qualitatively similar to results in Figures 3F and 6D-G, even though the method employed to generate those figures employed lysis of spheroplasts in an EDTA-containing buffer. The reason for the higher background in this panel relative to the others is that the pellet fractions were not washed prior to analysis. (B) Scatter plots representing the Δ iBAQ of biological replicate C vs. A (left) and biological replicate C vs. B (right) for insoluble proteins in *tom1Δ* mutants. Pearson's r-value is indicated on top of the plot. These data accompany Figure 3G. n = 3 biological replicates. (C) The 20 proteins with the largest increase in the pellet fraction upon *TOM1* deletion. Bars represent the average Δ iBAQ values with error bars indicating the standard error of the mean (SEM). (D) Same as (C), except the top 20 ribosomal proteins are shown.

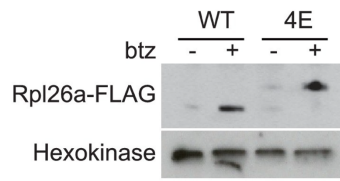
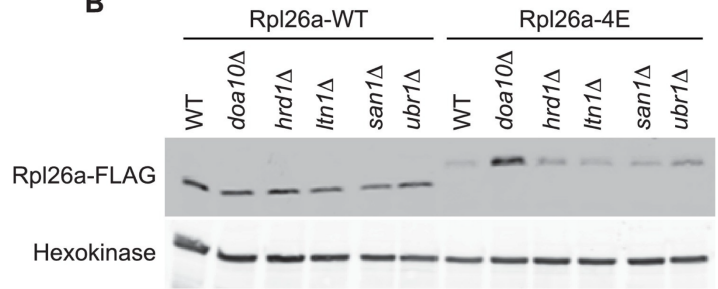
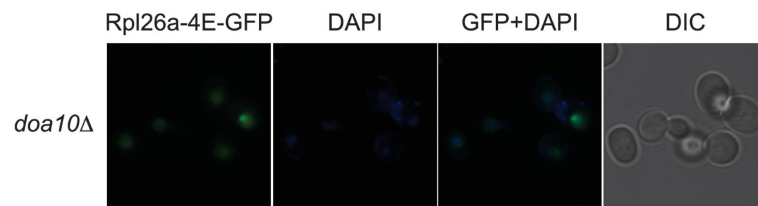
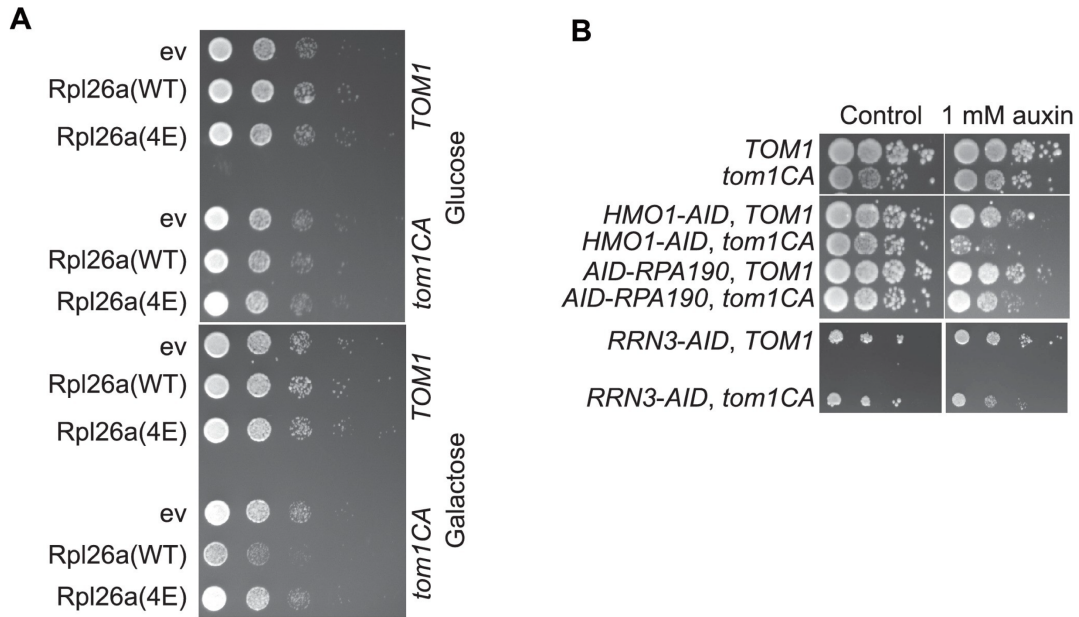
A**B****C**

Figure S7. Rpl26a-4E mutant is unstable and degraded by Doa10 in the nucleus/nucleolus

(A) Similar accumulation of Rpl26a^{FLAG} and Rpl26a-4E^{FLAG} upon galactose induction in the presence of bortezomib. Total cell lysates were evaluated by SDS-PAGE and immunoblotting with the indicated antibodies. n = 1 biological replicate. (B) Differential accumulation of WT and Rpl26a-4E upon galactose induction in WT and known PQC mutants was evaluated by SDS-PAGE and immunoblotting with the indicated antibodies. n = 1 biological replicate. (C) Fluorescence images of Rpl26a-4E^{GFP} induced in *doa10Δ* cells. n = 2 biological replicates.



C

Group	Gene	Genetic interaction with <i>tom1</i> Δ
Ribosomal Proteins	<i>RPL2A, RPL6B, RPL8A, RPL9B, RPL11B, RPL13A, RPL16A, RPL17B, RPL23A, RPL24A, RPL31B, RPL35B, RPL36A, RPL37A, RPL40A/B, RPL43B, RPS0A/B, RPS1A, RPS4B, RPS6B, RPS7B, RPS10B, RPS11B, RPS14A, RPS16A/B, RPS21A, RPS22B, RPS23A, RPS24A, RPS27A, RPS29A, RPS30A/B</i>	Double mutant exhibits reduced growth relative to either single mutant
Stress response	<i>MSN2, SSB1/2</i>	Overexpression suppresses <i>tom1</i> Δ
PKA	<i>CYR1, SCH9</i>	Deletion suppresses <i>tom1</i> Δ
	<i>BCY1, PDE2</i>	Overexpression suppresses <i>tom1</i> Δ



Figure S8. Tom1 is required for maintaining proteostasis

(A) Cells of the indicated genotypes were spotted in serial 10-fold dilutions on glucose or galactose medium and incubated at 30 °C for 2 days. *ev* refers to empty vector. n = 2 biological replicates. (B) Cells of the indicated genotypes were spotted as serial 10-fold dilutions on YPD with or without 1 mM auxin and incubated at 30 °C for 2 days. *AID* refers to auxin-inducible degron and *CA* refers to the Cys3235Ala mutation in *TOM1*. n = 2 biological replicates. (C) List of genetic interactions with *tom1Δ* as reported in the Saccharomyces Genome Database (www.yeastgenome.org). (D) Synthetic growth defects of *rps29aΔtom1Δ* double mutants. Cells of the indicated genotypes were spotted in serial 10-fold dilutions on YPD and incubated at 30 °C for 2 days. n = 2 biological replicates. (E) same as panel B except medium was supplemented or not with 2 mM paromomycin.

TABLES

Supplemental tables

Table S1. Yeast strains used in this study

Table S2. Plasmids used in this study

Table S1. Yeast strains used in this study

Strain	Genotype	Source
RJD1721	(BY4741) <i>MATa his3Δ1 leu2Δ0 met15Δ0 ura3Δ0</i>	-
RJD808	(W303a) <i>MATa can1-100 leu2-3,112 trp1-1 ura3-1 ade2-1 his3-11,15</i>	-
RJD6428	BY4741 <i>pdv5Δ::KanMX4</i> , p <i>GAL1-RPL13B-HHZ*</i>	(Sung et al., 2016)
RJD6429	BY4741 <i>pdv5Δ::KanMX4</i> , p <i>GAL1-RPL26A-HHZ*</i>	(Sung et al., 2016)
RJD6430	BY4741 <i>pdv5Δ::KanMX4</i> , p <i>GAL1-RPL34A-HHZ*</i>	(Sung et al., 2016)
RJD6431	BY4741 <i>pdv5Δ::KanMX4</i> , p <i>GAL1-RPL36A-HHZ*</i>	(Sung et al., 2016)
RJD6432	BY4741 <i>pdv5Δ::KanMX4</i> , p <i>GAL1-RPS17B-HHZ*</i>	(Sung et al., 2016)
RJD6433	BY4741 <i>pdv5Δ::KanMX4</i> , p <i>GAL1-RPS18A-HHZ*</i>	(Sung et al., 2016)
RJD6434	BY4741 <i>pdv5Δ::KanMX4</i> , p <i>GAL1-RPS24A-HHZ*</i>	(Sung et al., 2016)
RJD6435	BY4741 <i>pdv5Δ::KanMX4</i> , p <i>GAL1-RPS24B-HHZ*</i>	(Sung et al., 2016)
RJD6436	BY4741 <i>pdv5Δ::KanMX4</i> , p <i>GAL1-HOG1-HHZ*</i>	(Sung et al., 2016)
RJD6437	BY4741 <i>pdv5Δ::KanMX4</i> , p <i>GAL1-HHT2-HHZ*</i>	(Sung et al., 2016)
RJD6443	BY4741, pESC(HIS3)- <i>P_{GAL10}-RPL26A-FLAG</i>	(Sung et al., 2016)
RJD6444	BY4741 <i>rpl26aΔ::KanMX4 rpl26bΔ::KILEU2</i> , pESC(HIS3)- <i>P_{GAL10}-RPL26A-FLAG</i>	(Sung et al., 2016)
RJD6452	BY4741 <i>pdv5Δ::KanMX4</i> , pESC(HIS3)	(Sung et al., 2016)
RJD6453	BY4741 <i>pdv5Δ::KanMX4</i> , pESC(HIS3)- <i>P_{GAL10}-RPL26A-FLAG</i>	(Sung et al., 2016)
RJD6456	BY4741 <i>pre9Δ::KILEU2</i> , pESC(HIS3)	(Sung et al., 2016)
RJD6459	BY4741 <i>NOP56-RFP::KIUR43</i> , pESC(HIS3)- <i>P_{GAL10}-RPL26A-GFP</i>	(Sung et al., 2016)
RJD6462	BY4741 <i>pre9Δ::KILEU2</i> , pESC(HIS3)- <i>P_{GAL10}-RPL26A-FLAG</i>	(Sung et al., 2016)
RJD6468	BY4741 <i>tom1Δ::KanMX4</i>	OBS*
RJD6470	BY4741 <i>tom1Δ::KanMX4</i> , pESC(HIS3)- <i>P_{GAL10}-RPL26A-FLAG</i>	This study
RJD6473	BY4741 <i>ubc4Δ::KanMX4</i> , pESC(HIS3)- <i>P_{GAL10}-RPL26A-FLAG</i>	This study
RJD6475	BY4741 <i>ubc4Δ::KanMX4 ubc5Δ::KILEU2 pre9Δ::KIUR43</i> , pESC(HIS3)- <i>P_{GAL10}-RPL26A-FLAG</i>	This study
RJD6476	BY4741 <i>tom1C3235A::KIUR43</i>	This study
RJD6477	BY4741 <i>tom1C3235A::KIUR43</i> , pESC(HIS3)	This study
RJD6478	BY4741 <i>tom1C3235A::KIUR43</i> , pESC(HIS3)- <i>P_{GAL10}-RPL26A-FLAG</i>	This study
RJD6481	BY4741 <i>tom1C3235A::KIUR43 pdv5Δ::KILEU2</i> , pESC(HIS3)- <i>P_{GAL10}-RPL26A-FLAG</i>	This study
RJD6482	BY4741, pESC(HIS)	This study
RJD6484	BY4741 <i>tom1Δ::KanMX4 pre9Δ::KILEU2</i> , pESC(HIS3)- <i>P_{GAL10}-RPL26A-FLAG</i>	This study
RJD6485	BY4741 <i>TOM1-MYC::KIUR43</i>	This study
RJD6486	BY4741 <i>TOM1-HA::KIUR43</i>	This study
RJD6487	BY4741 <i>TOM1-FLAG::KIUR43</i>	This study
RJD6488	BY4741 <i>TOM1-GFP::KIUR43</i>	This study
RJD6489	BY4741 <i>TOM1-HA::KIUR43</i> , pESC(HIS3)- <i>P_{GAL10}-RPL26A-FLAG</i>	This study
RJD6491	W303 <i>tom1Δ::KILEU2</i> , pRS314	This study
RJD6492	W303 <i>tom1Δ::KILEU2</i> , pRS314- <i>TOM1</i>	This study
RJD6493	W303 <i>tom1Δ::KILEU2</i> , pRS314- <i>tom1C3235A</i>	This study
RJD6494	W303 <i>tom1Δ::KILEU2</i> , pRS314-3× <i>HA-TOM1</i>	This study
RJD6495	W303 <i>tom1Δ::KILEU2</i> , pRS314-3× <i>HA-tom1C3235A</i>	This study
RJD6496	BY4741 <i>KanMX6::P_{REF1}-3×HA-TOM1</i>	This study
RJD6498	BY4741 <i>KanMX6::P_{REF1}-3×HA-TOM1 pdv5Δ::KILEU2</i> , pESC(HIS)	This study
RJD6499	BY4741 <i>KanMX6::P_{REF1}-3×HA-TOM1 pdv5Δ::KILEU2</i> , pESC(HIS)- <i>P_{GAL10}-RPL26A-FLAG</i>	This study
RJD6500	BY4741 <i>KanMX6::P_{REF1}-3×HA-tom1C3235A::KIUR43</i>	This study
RJD6502	BY4741 <i>KanMX6::P_{REF1}-3×HA-tom1C3235A::KIUR43 pdv5Δ::KILEU2</i> , pESC(HIS)- <i>P_{GAL10}-RPL26A-FLAG</i>	This study
RJD6503	BY4741 <i>KanMX6::P_{REF1}-3×HA-TOM1</i> , pESC(HIS3)- <i>P_{GAL10}-RPL26A-FLAG</i>	This study
RJD6504	BY4741 <i>KanMX6::P_{REF1}-3×HA-tom1C3235A::KIUR43</i> , pESC(HIS3)- <i>P_{GAL10}-RPL26A-FLAG</i>	This study
RJD6507	BY4741 <i>NOP56-RFP-KIUR43 tom1C3235A::KILEU2</i> , pESC(HIS)- <i>P_{GAL10}-RPL26A-GFP</i>	This study
RJD6508	BY4741, pESC(HIS)- <i>P_{GAL10}-RPL26A(R12,13E)-FLAG</i>	This study
RJD6509	BY4741, pESC(HIS)- <i>P_{GAL10}-RPL26A(R16E)-FLAG</i>	This study
RJD6510	BY4741, pESC(HIS)- <i>P_{GAL10}-RPL26A(R27,28E)-FLAG</i>	This study
RJD6511	BY4741, pESC(HIS)- <i>P_{GAL10}-RPL26A(R51,52E)-FLAG</i>	This study
RJD6512	BY4741, pESC(HIS)- <i>P_{GAL10}-RPL26A(3E)-FLAG</i>	This study
RJD6513	BY4741, pESC(HIS)- <i>P_{GAL10}-RPL26A(4E)-FLAG</i>	This study
RJD6514	BY4741 <i>rpl26aΔ::KanMX4 rpl26bΔ::KILEU2</i> , pESC(HIS)- <i>P_{GAL10}-RPL26A(4E)-FLAG</i>	This study
RJD6515	BY4741 <i>rpl26aΔ::KanMX4 rpl26bΔ::KILEU2 pdv5Δ::KIUR43</i> , pESC(HIS)- <i>P_{GAL10}-RPL26A-FLAG</i>	This study
RJD6516	BY4741 <i>rpl26aΔ::KanMX4 rpl26bΔ::KILEU2 pdv5Δ::KIUR43</i> , pESC(HIS)- <i>P_{GAL10}-RPL26A(4E)-FLAG</i>	This study
RJD6517	BY4741 <i>pdv5Δ::KanMX4</i> , pESC(HIS)- <i>P_{GAL10}-RPL26A(4E)-FLAG</i>	This study
RJD6518	BY4741 <i>tom1Δ::KanMX4</i> , pESC(HIS)- <i>P_{GAL10}-RPL26A(3E)-FLAG</i>	This study
RJD6519	BY4741 <i>tom1Δ::KanMX4</i> , pESC(HIS)- <i>P_{GAL10}-RPL26A(4E)-FLAG</i>	This study
RJD6520	BY4741 <i>KanMX6::P_{REF1}-3×HA-TOM1 pdv5Δ::KILEU2</i> , pESC(HIS)- <i>P_{GAL10}-RPL26A(4E)-FLAG</i>	This study
RJD4781	W303 <i>lys2Δ::HIS3, arg4Δ::KanMX4</i>	-
RJD6522	W303 <i>lys2Δ::HIS3, arg4Δ::KanMX4 tom1Δ::KILEU2</i>	This study
RJD6523	W303 <i>lys2Δ::HIS3, arg4Δ::KanMX4 tom1C3235A::KILEU2</i>	This study
RJD6524	BY4741 <i>acl4Δ::KanMX4</i>	(Stelter et al., 2015)
RJD6525	BY4741 <i>acl4Δ::KanMX4 tom1C3235A::KIUR43</i>	This study
RJD6526	W303 <i>URA3::P_{ADHI}-AtTIR19myc</i>	This study
RJD6527	W303 <i>URA3::P_{ADHI}-AtTIR19myc tom1C3235A::KILEU2</i>	This study
RJD6528	W303 <i>URA3::P_{ADHI}-AtTIR19myc HMO1-GFP-AID*::hyg</i>	This study
RJD6529	W303 <i>URA3::P_{ADHI}-AtTIR19myc HMO1-GFP-AID*::hyg tom1C3235A::KILEU2</i>	This study
RJD6530	W303 <i>URA3::P_{ADHI}-AtTIR19myc Rrn3-GFP-AID*::hyg</i>	This study
RJD6531	W303 <i>URA3::P_{ADHI}-AtTIR19myc Rrn3-GFP-AID*::hyg tom1C3235A::KILEU2</i>	This study
RJD6532	W303 <i>URA3::P_{ADHI}-AtTIR19myc KanMX6::P_{REF1}-9myc-AID*-RPA190</i>	This study
RJD6533	W303 <i>URA3::P_{ADHI}-AtTIR19myc KanMX6::P_{REF1}-9myc-AID*-RPA190 tom1C3235A::KILEU2</i>	This study
RJD6428	BY4741 <i>pdv5Δ::KanMX4 tom1Δ::KILEU2</i>	This study
RJD6428	BY4741 <i>pdv5Δ::KanMX4 tom1Δ::KILEU2</i> , p <i>GAL1-RPL13B-HHZ*</i>	This study

Strain	Genotype	Source
RJD6429	BY4741 <i>pdv5Δ::KanMX4 tom1Δ::KILEU2</i> , pGAL1-RPL26A-HHZ*	This study
RJD6430	BY4741 <i>pdv5Δ::KanMX4 tom1Δ::KILEU2</i> , pGAL1-RPL34A-HHZ*	This study
RJD6431	BY4741 <i>pdv5Δ::KanMX4 tom1Δ::KILEU2</i> , pGAL1-RPL36A-HHZ*	This study
RJD6432	BY4741 <i>pdv5Δ::KanMX4 tom1Δ::KILEU2</i> , pGAL1-RPS17B-HHZ*	This study
RJD6433	BY4741 <i>pdv5Δ::KanMX4 tom1Δ::KILEU2</i> , pGAL1-RPS18A-HHZ*	This study
RJD6434	BY4741 <i>pdv5Δ::KanMX4 tom1Δ::KILEU2</i> , pGAL1-RPS24A-HHZ*	This study
RJD6435	BY4741 <i>pdv5Δ::KanMX4 tom1Δ::KILEU2</i> , pGAL1-RPS24B-HHZ*	This study
RJD6436	BY4741 <i>pdv5Δ::KanMX4 tom1Δ::KILEU2</i> , pGAL1-HOG1-HHZ*	This study
RJD6437	BY4741 <i>pdv5Δ::KanMX4 tom1Δ::KILEU2</i> , pGAL1-HHT2-HHZ*	This study
RJD6437	BY4741 <i>pdv5Δ::KanMX4</i> , pGAL1-RPL8B-HHZ*	This study
RJD6437	BY4741 <i>pdv5Δ::KanMX4 tom1Δ::KILEU2</i> , pGAL1-RPL8B-HHZ*	This study
RJD6525	BY4741 <i>hmo1Δ::KanMX4</i>	OBS*
RJD6525	BY4741 <i>hmo1Δ::KanMX4 tom1C3235A::KIURA3</i>	This study
RJD6459	BY4741 <i>NOP56-RFP::KIURA3</i> , pESC(HIS3)-P _{GAL10} -RPL26A(4E)-GFP	This study
RJD6656	BY4741 <i>rps29aΔ::KILEU2</i>	This study
RJD6657	BY4741 <i>tom1Δ::KanMX4 rps29aΔ::KILEU2</i>	This study
RJD2641	BY4741 <i>hrd1Δ::KanMX4</i>	OBS*
RJD2646	BY4741 <i>san1Δ::KanMX4</i>	OBS*
RJD2691	BY4741 <i>ubr1Δ::KanMX4</i>	OBS*
RJD4545	BY4741 <i>doa10Δ::KanMX4</i>	OBS*
RJD5400	BY4741 <i>ltn1Δ::KanMX4</i>	OBS*
RJD6708	BY4741 <i>hrd1Δ::KanMX4</i> , pESC(HIS3)-P _{GAL10} -RPL26A-FLAG	This study
RJD6709	BY4741 <i>san1Δ::KanMX4</i> , pESC(HIS3)-P _{GAL10} -RPL26A-FLAG	This study
RJD6710	BY4741 <i>ubr1Δ::KanMX4</i> , pESC(HIS3)-P _{GAL10} -RPL26A-FLAG	This study
RJD6711	BY4741 <i>doa10Δ::KanMX4</i> , pESC(HIS3)-P _{GAL10} -RPL26A-FLAG	This study
RJD6712	BY4741 <i>ltn1Δ::KanMX4</i> , pESC(HIS3)-P _{GAL10} -RPL26A-FLAG	This study
RJD6713	BY4741 <i>hrd1Δ::KanMX4</i> , pESC(HIS3)-P _{GAL10} -RPL26A(4E)-FLAG	This study
RJD6714	BY4741 <i>san1Δ::KanMX4</i> , pESC(HIS3)-P _{GAL10} -RPL26A(4E)-FLAG	This study
RJD6715	BY4741 <i>ubr1Δ::KanMX4</i> , pESC(HIS3)-P _{GAL10} -RPL26A(4E)-FLAG	This study
RJD6716	BY4741 <i>doa10Δ::KanMX4</i> , pESC(HIS3)-P _{GAL10} -RPL26A(4E)-FLAG	This study
RJD6717	BY4741 <i>ltn1Δ::KanMX4</i> , pESC(HIS3)-P _{GAL10} -RPL26A(4E)-FLAG	This study
RJD6718	BY4741 <i>doa10Δ::KanMX4</i> , pESC(HIS3)-P _{GAL10} -RPL26A(4E)-GFP	This study

OBS*: OpenBiosystems, yeast knockout collection

HHZ*: 6×His-HA-Protein A (ZZ domain)

Table S2. Plasmids used in this study

RDB	Plasmid	Source
1564	pCMV-HA-UBIQUITIN	(Kamitani et al., 1997)
3112	pGAL1-RPL26A-HHZ*	Open Biosystems
3113	pGAL1-RPL34A-HHZ*	Open Biosystems
3114	pGAL1-RPL36A-HHZ*	Open Biosystems
3115	pGAL1-RPL13B-HHZ*	Open Biosystems
3116	pGAL1-RPS18A-HHZ*	Open Biosystems
3117	pGAL1-RPS24A-HHZ*	Open Biosystems
3118	pGAL1-RPS24B-HHZ*	Open Biosystems
3119	pGAL1-RPS17B-HHZ*	Open Biosystems
3120	pGAL1-HOG1-HHZ*	Open Biosystems
3121	pGAL1-HHT2-HHZ*	Open Biosystems
3122	pESC (HIS)	Open Biosystems
3123	pESC (URA)	Open Biosystems
3124	pESC(HIS)-P _{GAL10} -RPL26A-FLAG	(Sung et al., 2016)
3125	pESC(HIS)-P _{GAL10} -RPL26A-GFP	(Sung et al., 2016)
3126	pRS314	(Duncan et al., 2000)
3127	pRS314-TOM1	(Duncan et al., 2000)
3128	pRS314-TOM1C3235A	(Duncan et al., 2000)
3129	pRS314-3xHA-TOM1	(Duncan et al., 2000)
3130	pRS314-3xHA-TOM1C3235A	(Duncan et al., 2000)
3132	pESC(HIS)-P _{GAL10} -RPL26A(4E)-FLAG	This study
3133	pESC(HIS)-P _{GAL10} -RPL26A(4E)-GFP	This study
3137	pHyg-AID*-GFP	(Morawska and Ulrich, 2013)
3140	pKanMX6-P _{RFA1} -9MYC-AID*	(Morawska and Ulrich, 2013)
3141	P _{ADH1} -OsTIR1-9MYC	NBRP (pNHK53)
3142	pLKO-Tet-ON_shControl	(Thompson et al., 2014)
3143	pLKO-Tet-ON_shHUWE1	(Thompson et al., 2014)
3144	P _{CMV} -hRPL26-FLAG	Addgene (cat# 19972)
3145	pKILEU2	EUROSCARF (pUG73)
3146	pFA6a-GFP-KIURA3	(Sung et al., 2008)
3151	pESC(HIS)-P _{GAL10} -RPL26A(3E)-FLAG	This study
3152	pESC(HIS)-P _{GAL10} -RPL26A(R12,13E)-FLAG	This study
3153	pESC(HIS)-P _{GAL10} -RPL26A(R16E)-FLAG	This study
3154	pESC(HIS)-P _{GAL10} -RPL26A(R27,28E)-FLAG	This study
3155	pESC(HIS)-P _{GAL10} -RPL26A(R51,52E)-FLAG	This study
3212	pGAL1-RPL8B-HHZ	Open Biosystems
	pcDNA3	Invitrogen
	pCDH-EF1-MCS-T2A-copMYCGFP	Hoelz lab
	pGEX-6P-1 GST- <i>ct</i> Kap104 ^{FL}	Hoelz lab
	pET28a His ₆ -SUMO- <i>scAcl4</i> ^{FL}	Hoelz lab
	pETDuet1 His ₆ -SUMO-3xFLAG- <i>scRpL4</i> ^{FL}	Hoelz lab
	pETDuet1 His ₆ -SUMO-3xFLAG- <i>scRpL4</i> ¹⁻²⁷⁶	Hoelz lab

HHZ*: 6×His-HA-Protein A (ZZ domain)

AID*: Auxin Inducible Degron

REFERENCES

- Abovich, N., Gritz, L., Tung, L., and Rosbash, M. (1985). Effect of Rp51 Gene Dosage Alterations on Ribosome Synthesis in *Saccharomyces-Cerevisiae*. *Mol Cell Biol* 5, 3429-3435.
- Babiano, R., Gamalinda, M., Woolford, J.L., Jr., and de la Cruz, J. (2012). *Saccharomyces cerevisiae* ribosomal protein L26 is not essential for ribosome assembly and function. *Mol Cell Biol* 32, 3228-3241.
- Ben-Shem, A., Garreau de Loubresse, N., Melnikov, S., Jenner, L., Yusupova, G., and Yusupov, M. (2011). The structure of the eukaryotic ribosome at 3.0 Å resolution. *Science* 334, 1524-1529.
- Bengtson, M.H., and Joazeiro, C.A. (2010). Role of a ribosome-associated E3 ubiquitin ligase in protein quality control. *Nature* 467, 470-473.
- Brandman, O., Stewart-Ornstein, J., Wong, D., Larson, A., Williams, C.C., Li, G.W., Zhou, S., King, D., Shen, P.S., Weibezahn, J., *et al.* (2012). A ribosome-bound quality control complex triggers degradation of nascent peptides and signals translation stress. *Cell* 151, 1042-1054.
- Brandmeir, N.J., Geser, F., Kwong, L.K., Zimmerman, E., Qian, J., Lee, V.M., and Trojanowski, J.Q. (2008). Severe subcortical TDP-43 pathology in sporadic frontotemporal lobar degeneration with motor neuron disease. *Acta Neuropathol* 115, 123-131.
- Cenci, S., Oliva, L., Cerruti, F., Milan, E., Bianchi, G., Raule, M., Mezghrani, A., Pasqualetto, E., Sitia, R., and Cascio, P. (2012). Pivotal Advance: Protein synthesis modulates responsiveness of differentiating and malignant plasma cells to proteasome inhibitors. *J Leukoc Biol* 92, 921-931.

Choe, K.N., Nicolae, C.M., Constantin, D., Imamura Kawasawa, Y., Delgado-Diaz, M.R., De, S., Freire, R., Smits, V.A., and Moldovan, G.L. (2016). HUWE1 interacts with PCNA to alleviate replication stress. *EMBO Rep* 17, 874-886.

Costanzo, M., Baryshnikova, A., Bellay, J., Kim, Y., Spear, E.D., Sevier, C.S., Ding, H., Koh, J.L., Toufighi, K., Mostafavi, S., *et al.* (2010). The genetic landscape of a cell. *Science* 327, 425-431.

Cox, J., and Mann, M. (2008). MaxQuant enables high peptide identification rates, individualized p.p.b.-range mass accuracies and proteome-wide protein quantification. *Nature Biotechnology* 26, 1367-1372.

Defenouillere, Q., Yao, Y., Mouaikel, J., Namane, A., Galopier, A., Decourty, L., Doyen, A., Malabat, C., Saveanu, C., Jacquier, A., *et al.* (2013). Cdc48-associated complex bound to 60S particles is required for the clearance of aberrant translation products. *Proc Natl Acad Sci U S A* 110, 5046-5051.

Deng, M., and Hochstrasser, M. (2006). Spatially regulated ubiquitin ligation by an ER/nuclear membrane ligase. *Nature* 443, 827-831.

Dephoure, N., Hwang, S., O'Sullivan, C., Dodgson, S.E., Gygi, S.P., Amon, A., and Torres, E.M. (2014). Quantitative proteomic analysis reveals posttranslational responses to aneuploidy in yeast. *Elife* 3.

Deshaies, R.J. (2014). Proteotoxic crisis, the ubiquitin-proteasome system, and cancer therapy. *BMC Biol* 12, 94.

Duncan, K., Umen, J.G., and Guthrie, C. (2000). A putative ubiquitin ligase required for efficient mRNA export differentially affects hnRNP transport. *Current Biology* 10, 687-696.

Eisele, F., and Wolf, D.H. (2008). Degradation of misfolded protein in the cytoplasm is mediated by the ubiquitin ligase Ubr1. *FEBS Lett* 582, 4143-4146.

- Elias, J.E., and Gygi, S.P. (2010). Target-decoy search strategy for mass spectrometry-based proteomics. *Methods Mol Biol* 604, 55-71.
- Finley, D., Bartel, B., and Varshavsky, A. (1989). The tails of ubiquitin precursors are ribosomal proteins whose fusion to ubiquitin facilitates ribosome biogenesis. *Nature* 338, 394-401.
- Gardner, R.G., Nelson, Z.W., and Gottschling, D.E. (2005). Degradation-mediated protein quality control in the nucleus. *Cell* 120, 803-815.
- Geiger, T., Wehner, A., Schaab, C., Cox, J., and Mann, M. (2012). Comparative Proteomic Analysis of Eleven Common Cell Lines Reveals Ubiquitous but Varying Expression of Most Proteins. *Molecular & Cellular Proteomics* 11.
- Gietz, R.D., and Schiestl, R.H. (2007). High-efficiency yeast transformation using the LiAc/SS carrier DNA/PEG method. *Nat Protoc* 2, 31-34.
- Gorenstein, C., and Warner, J.R. (1977). Synthesis and Turnover of Ribosomal-Proteins in Absence of 60s Subunit Assembly in *Saccharomyces-Cerevisiae*. *Mol Gen Genet* 157, 327-332.
- Heck, J.W., Cheung, S.K., and Hampton, R.Y. (2010). Cytoplasmic protein quality control degradation mediated by parallel actions of the E3 ubiquitin ligases Ubr1 and San1. *Proc Natl Acad Sci U S A* 107, 1106-1111.
- Hess, S., van Beek, J., and Pannell, L.K. (2002). Acid hydrolysis of silk fibroins and determination of the enrichment of isotopically labeled amino acids using precolumn derivatization and high-performance liquid chromatography-electrospray ionization-mass spectrometry. *Anal Biochem* 311, 19-26.
- Horton, R.M., Hunt, H.D., Ho, S.N., Pullen, J.K., and Pease, L.R. (1989). Engineering Hybrid Genes without the Use of Restriction Enzymes - Gene-Splicing by Overlap Extension. *Gene* 77, 61-68.

- Huang, D.W., Sherman, B.T., and Lempicki, R.A. (2009a). Bioinformatics enrichment tools: paths toward the comprehensive functional analysis of large gene lists. *Nucleic acids research* 37, 1-13.
- Huang, D.W., Sherman, B.T., and Lempicki, R.A. (2009b). Systematic and integrative analysis of large gene lists using DAVID bioinformatics resources. *Nat Protoc* 4, 44-57.
- Huber, F.M., and Hoelz, A. (2017). Molecular basis for protection of ribosomal protein L4 from cellular degradation. *Nat Commun* 8, 14354.
- Huh, W.K., Falvo, J.V., Gerke, L.C., Carroll, A.S., Howson, R.W., Weissman, J.S., and O'Shea, E.K. (2003). Global analysis of protein localization in budding yeast. *Nature* 425, 686-691.
- Johnson, J.O., Mandrioli, J., Benatar, M., Abramzon, Y., Van Deerlin, V.M., Trojanowski, J.Q., Gibbs, J.R., Brunetti, M., Gronka, S., Wu, J., *et al.* (2010). Exome Sequencing Reveals VCP Mutations as a Cause of Familial ALS. *Neuron* 68, 857-864.
- Kabashi, E., and Durham, H.D. (2006). Failure of protein quality control in amyotrophic lateral sclerosis. *Biochim Biophys Acta* 1762, 1038-1050.
- Kaganovich, D., Kopito, R., and Frydman, J. (2008). Misfolded proteins partition between two distinct quality control compartments. *Nature* 454, 1088-1095.
- Kamitani, T., Kito, K., Nguyen, H.P., and Yeh, E.T.H. (1997). Characterization of NEDD8, a developmentally down-regulated ubiquitin-like protein. *J Biol Chem* 272, 28557-28562.
- Keogh, M.C., Kim, J.A., Downey, M., Fillingham, J., Chowdhury, D., Harrison, J.C., Onishi, M., Datta, N., Galicia, S., Emili, A., *et al.* (2006). A phosphatase complex that dephosphorylates gamma H2AX regulates DNA damage checkpoint recovery. *Nature* 439, 497-501.

- Kim, W., Bennett, E.J., Huttlin, E.L., Guo, A., Li, J., Possemato, A., Sowa, M.E., Rad, R., Rush, J., Comb, M.J., *et al.* (2011). Systematic and quantitative assessment of the ubiquitin-modified proteome. *Mol Cell* *44*, 325-340.
- Koplin, A., Preissler, S., Ilina, Y., Koch, M., Scior, A., Erhardt, M., and Deuerling, E. (2010). A dual function for chaperones SSB-RAC and the NAC nascent polypeptide-associated complex on ribosomes. *J Cell Biol* *189*, 57-68.
- Kressler, D., Bange, G., Ogawa, Y., Stjepanovic, G., Bradatsch, B., Pratte, D., Amlacher, S., Strauss, D., Yoneda, Y., Katahira, J., *et al.* (2012). Synchronizing nuclear import of ribosomal proteins with ribosome assembly. *Science* *338*, 666-671.
- Kressler, D., Hurt, E., and Bassler, J. (2010). Driving ribosome assembly. *Biochim Biophys Acta* *1803*, 673-683.
- Lam, Y.W., Lamond, A.I., Mann, M., and Andersen, J.S. (2007). Analysis of nucleolar protein dynamics reveals the nuclear degradation of ribosomal proteins. *Curr Biol* *17*, 749-760.
- Lesmantavicius, V., Weinert, B.T., and Choudhary, C. (2014). Convergence of ubiquitylation and phosphorylation signaling in rapamycin-treated yeast cells. *Mol Cell Proteomics* *13*, 1979-1992.
- Lu, K., Psakhye, I., and Jentsch, S. (2014). Autophagic clearance of polyQ proteins mediated by ubiquitin-Atg8 adaptors of the conserved CUET protein family. *Cell* *158*, 549-563.
- Mayor, T., Graumann, J., Bryan, J., MacCoss, M.J., and Deshaies, R.J. (2007). Quantitative profiling of ubiquitylated proteins reveals proteasome substrates and the substrate repertoire influenced by the Rpn10 receptor pathway. *Mol Cell Proteomics* *6*, 1885-1895.
- Mayor, T., Lipford, J.R., Graumann, J., Smith, G.T., and Deshaies, R.J. (2005). Analysis of polyubiquitin conjugates reveals that the Rpn10 substrate receptor contributes to the turnover of multiple proteasome targets. *Mol Cell Proteomics* *4*, 741-751.

- Morawska, M., and Ulrich, H.D. (2013). An expanded tool kit for the auxin-inducible degron system in budding yeast. *Yeast* *30*, 341-351.
- Peng, J., Schwartz, D., Elias, J.E., Thoreen, C.C., Cheng, D., Marsischky, G., Roelofs, J., Finley, D., and Gygi, S.P. (2003). A proteomics approach to understanding protein ubiquitination. *Nat Biotechnol* *21*, 921-926.
- Pierce, N.W., Lee, J.E., Liu, X., Sweredoski, M.J., Graham, R.L.J., Larimore, E.A., Rome, M., Zheng, N., Clurman, B.E., Hess, S., *et al.* (2013). Cand1 Promotes Assembly of New SCF Complexes through Dynamic Exchange of F Box Proteins. *Cell* *153*, 206-215.
- Porras-Yakushi, T.R., and Hess, S. (2014). Recent advances in defining the ubiquitylome. *Expert Rev Proteomics* *11*, 477-490.
- Porras-Yakushi, T.R., Sweredoski, M.J., and Hess, S. (2015). ETD Outperforms CID and HCD in the Analysis of the Ubiquitylated Proteome. *J Am Soc Mass Spectrom* *26*, 1580-1587.
- Saleh, A., Collart, M., Martens, J.A., Genereaux, J., Allard, S., Cote, J., and Brandl, C.J. (1998). TOM1p, a yeast hect-domain protein which mediates transcriptional regulation through the ADA/SAGA coactivator complexes. *J Mol Biol* *282*, 933-946.
- Sarraf, S.A., Raman, M., Guarani-Pereira, V., Sowa, M.E., Huttlin, E.L., Gygi, S.P., and Harper, J.W. (2013). Landscape of the PARKIN-dependent ubiquitylome in response to mitochondrial depolarization. *Nature* *496*, 372-376.
- Seufert, W., and Jentsch, S. (1990). Ubiquitin-conjugating enzymes UBC4 and UBC5 mediate selective degradation of short-lived and abnormal proteins. *EMBO J* *9*, 543-550.
- Stelter, P., Huber, F.M., Kunze, R., Flemming, D., Hoelz, A., and Hurt, E. (2015). Coordinated Ribosomal L4 Protein Assembly into the Pre-Ribosome Is Regulated by Its Eukaryote-Specific Extension. *Molecular Cell* *58*, 854-862.

- Sung, M.K., Ha, C.W., and Huh, W.K. (2008). A vector system for efficient and economical switching of C-terminal epitope tags in *Saccharomyces cerevisiae*. *Yeast* 25, 301-311.
- Sung, M.K., Reitsma, J.M., Sweredoski, M.J., Hess, S., and Deshaies, R.J. (2016). Ribosomal proteins produced in excess are degraded by the ubiquitin-proteasome system. *Mol Biol Cell*.
- Swaney, D.L., Beltrao, P., Starita, L., Guo, A., Rush, J., Fields, S., Krogan, N.J., and Villen, J. (2013). Global analysis of phosphorylation and ubiquitylation cross-talk in protein degradation. *Nat Methods* 10, 676-682.
- Tabb, A.L., Utsugi, T., Wooten-Kee, C.R., Sasaki, T., Edling, S.A., Gump, W., Kikuchi, Y., and Ellis, S.R. (2001). Genes encoding ribosomal proteins Rps0A/B of *Saccharomyces cerevisiae* interact with TOM1 mutants defective in ribosome synthesis. *Genetics* 157, 1107-1116.
- Thompson, J.W., Nagel, J., Hoving, S., Gerrits, B., Bauer, A., Thomas, J.R., Kirschner, M.W., Schirle, M., and Luchansky, S.J. (2014). Quantitative Lys-epsilon-Gly-Gly (diGly) Proteomics Coupled with Inducible RNAi Reveals Ubiquitin-mediated Proteolysis of DNA Damage-inducible Transcript 4 (DDIT4) by the E3 Ligase HUWE1. *J Biol Chem* 289, 28942-28955.
- Torres, E.M., Dephoure, N., Panneerselvam, A., Tucker, C.M., Whittaker, C.A., Gygi, S.P., Dunham, M.J., and Amon, A. (2010). Identification of aneuploidy-tolerating mutations. *Cell* 143, 71-83.
- Torres, E.M., Sokolsky, T., Tucker, C.M., Chan, L.Y., Boselli, M., Dunham, M.J., and Amon, A. (2007). Effects of aneuploidy on cellular physiology and cell division in haploid yeast. *Science* 317, 916-924.
- Udeshi, N.D., Mertins, P., Svinkina, T., and Carr, S.A. (2013a). Large-scale identification of ubiquitination sites by mass spectrometry. *Nat Protoc* 8, 1950-1960.

- Udeshi, N.D., Svinkina, T., Mertins, P., Kuhn, E., Mani, D.R., Qiao, J.W., and Carr, S.A. (2013b). Refined preparation and use of anti-diglycine remnant (K-epsilon-GG) antibody enables routine quantification of 10,000s of ubiquitination sites in single proteomics experiments. *Mol Cell Proteomics* *12*, 825-831.
- Utsugi, T., Hirata, A., Sekiguchi, Y., Sasaki, T., Toh-e, A., and Kikuchi, Y. (1999). Yeast tom1 mutant exhibits pleiotropic defects in nuclear division, maintenance of nuclear structure and nucleocytoplasmic transport at high temperatures. *Gene* *234*, 285-295.
- Vembar, S.S., and Brodsky, J.L. (2008). One step at a time: endoplasmic reticulum-associated degradation. *Nat Rev Mol Cell Biol* *9*, 944-957.
- Verma, R., Oania, R.S., Kolawa, N.J., and Deshaies, R.J. (2013). Cdc48/p97 promotes degradation of aberrant nascent polypeptides bound to the ribosome. *Elife* *2*, e00308.
- Wagner, S.A., Beli, P., Weinert, B.T., Nielsen, M.L., Cox, J., Mann, M., and Choudhary, C. (2011). A proteome-wide, quantitative survey of in vivo ubiquitylation sites reveals widespread regulatory roles. *Mol Cell Proteomics* *10*, M111 013284.
- Warner, J.R. (1977). In the absence of ribosomal RNA synthesis, the ribosomal proteins of HeLa cells are synthesized normally and degraded rapidly. *J Mol Biol* *115*, 315-333.
- Warner, J.R. (1999). The economics of ribosome biosynthesis in yeast. *Trends Biochem Sci* *24*, 437-440.
- Watts, G.D., Wymer, J., Kovach, M.J., Mehta, S.G., Mumm, S., Darvish, D., Pestronk, A., Whyte, M.P., and Kimonis, V.E. (2004). Inclusion body myopathy associated with Paget disease of bone and frontotemporal dementia is caused by mutant valosin-containing protein. *Nat Genet* *36*, 377-381.
- Wiederschain, D., Wee, S., Chen, L., Loo, A., Yang, G., Huang, A., Chen, Y., Caponigro, G., Yao, Y.M., Lengauer, C., *et al.* (2009). Single-vector inducible lentiviral RNAi system for oncology target validation. *Cell Cycle* *8*, 498-504.

Zhong, Q., Gao, W.H., Du, F.H., and Wang, X.D. (2005). Mule/ARF-BP1, a BH3-only E3 ubiquitin ligase, catalyzes the polyubiquitination of Mcl-1 and regulates apoptosis. *Cell* 121, 1085-1095.

CHAPTER III

MOLECULAR BASIS FOR PROTECTION OF RIBOSOMAL PROTEIN L4 FROM CELLULAR DEGRADATION

This chapter was adapted from:

Ferdinand M. Huber & André Hoelz* (2017). Molecular basis for protection of ribosomal protein L4 from cellular degradation, *Nat. Commun.*, 8, 14354.

ABSTRACT

Eukaryotic ribosome biogenesis requires the nuclear import of ~80 nascent ribosomal proteins and the elimination of excess amounts by the cellular degradation machinery. Assembly chaperones recognize nascent unassembled ribosomal proteins and transport them together with karyopherins to their nuclear destination. We report the crystal structure of ribosomal protein L4 (RpL4) bound to its dedicated assembly chaperone of L4 (Acl4), revealing extensive interactions sequestering 70 exposed residues of the extended RpL4 loop. The observed molecular recognition fundamentally differs from canonical promiscuous chaperone-substrate interactions. We demonstrate that the eukaryote-specific RpL4 extension harbors overlapping binding sites for Acl4 and the nuclear transport factor Kap104, facilitating its continuous protection from the cellular degradation machinery. Thus, Acl4 serves a dual function to facilitate nuclear import and simultaneously protect unassembled RpL4 from the cellular degradation machinery.

INTRODUCTION

The spatial separation of cytoplasmic protein translation and nucleolar ribosome biogenesis requires the nuclear import of ~80 nascent ribosomal proteins (RPs) through the nuclear pore complex (NPC) and subsequent export of pre-ribosomal subunits into the cytoplasm (Johnson, 2014; Kressler et al., 2010). These NPC-dependent nucleocytoplasmic transport events generate a layer of regulation that facilitates the dynamic adjustment of total ribosome numbers along with RP quality control and rapid degradation (Gorenstein and Warner, 1977; Lafontaine, 2010, 2015; Roberts et al., 2003; Warner, 1977). Ribosome biogenesis is temporally and spatially coordinated by ~200 *trans*-acting ribosome assembly factors that mediate the hierarchical assembly of pre-ribosomal subunits (Fromont-Racine et al., 2003). Additionally, dedicated assembly chaperones assist ribosome biogenesis by recognizing and facilitating transport of nascent RPs to the pre-ribosome (Calvino et al., 2015; Eisinger et al., 1997; Holzer et al., 2013; Koch et al., 2012; Kressler et al., 2012; Pausch et al., 2015; Pillet et al., 2015; Stelter et al., 2015).

In the mature ribosome, ribosomal proteins form multiple intricate interactions with both neighboring RPs and ribosomal RNA (rRNA) (Ben-Shem et al., 2011). Contacts with rRNA are mediated predominantly by electrostatic contacts between the phosphate backbone and arginine- and lysine-enriched motifs of RP elements located at their termini or within protruding loops (Ben-Shem et al., 2011). The elongated ~70-residue loop of ribosomal protein L4 (RpL4) is devoid of secondary structure elements and extends deep into the large ribosomal subunit core, forming a series of interactions with rRNA and lines the peptide exit tunnel (Ben-Shem et al., 2011; Zhang et al., 2013). The mechanism by which nascent ribosomal proteins escape unfavorable interactions with nucleic acids, other RPs, and the cellular degradation machinery remains poorly understood. We have previously shown that the dedicated assembly chaperone Acl4 recognizes nascent RpL4, facilitates its nuclear import, and releases RpL4 upon engaging RpL18 at the pre-ribosome (Stelter et al., 2015). Moreover, Acl4 is required for the soluble expression of newly synthesized RpL4 and for the protection of RpL4 from the Tom1-dependent cellular degradation machinery (Pillet et al., 2015; Sung et al., 2016). Therefore, we hypothesized

that Acl4 generates a protective environment for RpL4 by sequestering elongated RpL4 elements until its incorporation into the pre-ribosome.

Here, we report the 2.4-Å resolution crystal structure of RpL4 in complex with its dedicated ribosome assembly chaperone Acl4. The structure reveals an extensive interaction encompassing 70 exposed residues of the internal RpL4 loop that are sequestered by the concave Acl4 surface upon complex formation. The observed binding mode differs dramatically from canonical chaperone-substrate interactions that generally recognize short exposed hydrophobic peptide stretches. Despite the considerable binding interface in the Acl4•RpL4 complex, we identified a single Acl4 residue that abolishes RpL4 binding and may serve as an intrinsic weak spot for complex disassembly. Moreover, we determined the 3.0-Å resolution crystal structure of the karyopherin transport factor Kap104 in complex with the eukaryote specific RpL4 extension. Our structural and biochemical analysis demonstrates that the RpL4 extension possesses overlapping binding sites for a second Acl4 copy and Kap104. Whereas unprotected RpL4 is targeted by the E3-ubiquitin ligase Tom1 for proteasome-dependent degradation, interactions with Acl4 and Kap104 sequester Tom1 ubiquitination sites in the RpL4 loop and extension. Thus, ribosome assembly chaperones serve a dual function to facilitate nuclear import and simultaneously protect unassembled ribosomal proteins from the cellular degradation machinery.

RESULTS

Crystal structure of the Acl4•RpL4 complex

Here, we set out to identify the molecular basis of Acl4-dependent RpL4 sequestration and protection. We generated a biochemical interaction map between RpL4, its assembly chaperone Acl4, and its transport factor Kap104 and gained insight into the Acl4-RpL4 binding mode at the atomic level. Crystals of the *Chaetomium thermophilum* Acl4•RpL4 complex, which included the Acl4 TPR domain (residues 28 to 361) and the globular core of RpL4 (RpL4^{CORE}) and the entire elongated loop (RpL4^{LOOP}), diffracted to 2.4-Å resolution (Figure 1a). The structure was solved by single-wavelength anomalous dispersion (SAD) using Seleno-L-methionine (SeMet) labeled proteins. The final model was refined to R_{work} and R_{free} values of 19.1 % and 22.7 %, respectively, with excellent stereochemistry (Table 1).

Acl4 adopts an α -helical tetratricopeptide repeat (TPR) fold composed of seven TPRs (α A- α N) and a C-terminal flanking helix (α O) with an overall right-handed superhelical twist that accommodates the entire 70-residue RpL4^{LOOP} with its concave surface (Figure 1b and S1). Whereas RpL4^{LOOP} forms numerous contacts with the Acl4 surface, RpL4^{CORE} contributes few additional interactions to the Acl4•RpL4 complex. Comparing the Acl4•RpL4 structure to our previously determined Acl4 *apo* structure revealed a conformational change upon RpL4^{LOOP} binding, which is unusual for TPR domains (Figure 1c) (Stelter et al., 2015). The longer central Acl4 helices α F and α G form a hinge between the N-terminal (α A- α F) and C-terminal halves (α G- α O) of Acl4, which rotate as rigid bodies by $\sim 10^\circ$ from an open to a closed conformation upon binding RpL4 (Figure 1c).

RpL4^{LOOP} undergoes dramatic rearrangement upon Acl4 binding

In the mature ribosome, the RpL4^{LOOP} adopts a remarkably elongated conformation, reaching deep into the rRNA core of the large ribosomal subunit, while the ~ 100 -residue RpL4 extension, RpL4^{EXT}, extends ~ 120 Å over the ribosomal surface (Figure 1d) (Ben-Shem et al., 2011). Whereas the conformation of RpL4^{CORE} remains largely unchanged, comparison of Acl4- and ribosome-bound RpL4 revealed a striking conformational change

of the elongated RpL4^{LOOP} (Figure 1d). Within the ribosome, RpL4^{LOOP} is fully extended and reaches ~50 Å into the center of the large subunit (Ben-Shem et al., 2011). In contrast, binding to Acl4 results in a great compaction of RpL4^{LOOP} by more than ~15 Å, sequestering a maximum number of residues into the protective environment of the concave Acl4 surface (Figure 1d). Acl4-binding induces the formation of an α -helix within RpL4^{LOOP} (α 3, residues 89 to 97), which is entirely devoid of secondary structure elements in the context of the intact ribosome. Thus, both Acl4 and RpL4 undergo dramatic conformational changes upon complex formation.

The majority of RpL4^{LOOP} is buried by the concave Acl4 surface and involves several interactions formed by predominantly invariant Acl4 residues (Figures S2-4). The extensive nature of the interactions is best illustrated by the sheer number of residues directly involved in Acl4-RpL4^{LOOP} binding: 42 out of 70 RpL4^{LOOP} residues and 87 out of 333 Acl4 residues (Figures 2a and S2). The interface is formed primarily by electrostatic interactions between the acidic Acl4 surface and the basic RpL4^{LOOP} (Figure S4b, d). However, additional hydrophobic and π -stacking interactions contribute to the stability of the Acl4•RpL4 complex as well (Figure 2a, b).

Acl4•RpL4 harbors an intrinsic weak spot for disassembly

While the extensive Acl4•RpL4 interface formed by a considerable number of direct interactions is ideally suited for substrate protection, this simultaneously represents a challenge for the eventual dismantling of the complex during ribosome biogenesis. To identify the underlying molecular mechanism, we employed a comprehensive structure- and conservation-guided mutagenesis approach with the goal of identifying Acl4 residues capable of triggering the disassembly of the Acl4-RpL4 interaction (Figure 2a-e). Individual mutations of most of the invariant Acl4 residues proved to be insufficient to disrupt or even weaken the Acl4-RpL4 interaction (Figure S5). We next focused on two highly conserved interaction sites in the concave Acl4 surface: the electrostatic interactions of Acl4 residues Glu180 and Glu212, both of which form a salt-bridge with RpL4 Arg108, and a hydrophobic pocket formed by Acl4 residues Tyr292 and Leu293, which engage RpL4 Phe101 (Figure 2b). However, neither the Acl4 E180R/E212R charge-swap nor the Acl4 Y292A/L293A double mutation had a major effect on the interaction with RpL4

(Figures 2b-d and S5). In contrast, we identified a single charge-swap Acl4 mutation, E266R that abolished the Acl4-RpL4^{LOOP} interaction almost completely (Figure S5). Glu266 is located on the top surface of Acl4•RpL4 and forms hydrogen bonds with the mainchain amides of RpL4 residues Met100 and Phe101, thereby anchoring the C-terminal end of RpL4 helix α 3 and compressing the RpL4^{LOOP} to the Acl4 surface (Figure 2b). Introducing the identified Acl4 mutants of the crystallized *C. thermophilum* protein into its *S. cerevisiae* homolog established that the overall architecture of the Acl4•RpL4 complex is evolutionarily conserved (Figures 2e and S5). In fact, despite limited sequence conservation, *C. thermophilum* Acl4 is capable of forming a chimeric complex with *S. cerevisiae* RpL4 (Figure 2e). These results suggest that the Glu266-mediated interactions constitute an intrinsic weak spot that is critical for Acl4•RpL4 complex disassembly. A structural comparison with the *apo* Acl4 reveals that disrupting these interactions upon engaging the pre-ribosomal surface leads to the simultaneous relaxation of the Acl4 TPR domain and elongation of RpL4^{LOOP}, reminiscent of a spring-loaded mechanism.

To validate the physiological relevance of our findings on the mechanism of Acl4-RpL4 binding and disassembly, we generated an *S. cerevisiae* Acl4 deletion (*acl4* Δ strain and analyzed various Acl4 mutants. Deletion of TPR1 and the acidic C-terminal region of Acl4 caused a growth defect at 37 °C, as did mutation of the conserved hydrophobic pocket with Tyr292 and Leu293 to alanines, consistent with the biochemical findings. In contrast, the E266R mutant displayed a severe growth defect, identical to the *acl4* Δ phenotype, demonstrating the physiological relevance of closely anchoring RpL4^{LOOP} to the Acl4 surface. Notably, the Acl4 E266R mutation exhibited identical behavior in size exclusion chromatography, confirming that the observed effect was not caused by improper Acl4 E266R protein folding (Figure S6). Surprisingly, the E180R/E212R double charge-swap mutation of the electrostatic binding site, which only moderately affected Acl4-RpL4 binding, also caused a substantial growth defect at all analyzed temperatures, suggesting a role of this binding site for the proper release of RpL4 into the maturing ribosome. Notably, all Acl4 variants were expressed at similar levels and predominantly localized to the nucleus with the RpL4-binding deficient mutants only displaying a slight increase in cytoplasmic localization (Figures 2g and S7).

Acl4 and Kap104 share an overlapping binding site on RpL4^{EXT}

By employing a more sensitive size exclusion chromatography assay, we identified an additional interaction between Acl4 and RpL4^{EXT}, which was previously missed in GST pull-down and yeast two-hybrid assays (Pillet et al., 2015; Stelter et al., 2015). We found that the heterodimeric Acl4•RpL4 complex is capable of interacting with an additional Acl4 molecule resulting in the formation of a heterotrimeric Acl4•RpL4•Acl4 complex with a 2:1 stoichiometry that is evolutionarily conserved (Figure 3a and Figure S8a). Mapping of the binding site established that RpL4^{EXT} is necessary and sufficient for binding of the second Acl4 copy (Figure 3b). Further truncation analysis identified an 18-residue region encompassing residues 311 to 328 of RpL4^{EXT} that is required for Acl4•RpL4•Acl4 complex formation. Alanine substitution of the three highly conserved basic residues in this region, Lys316, Lys317, and Arg321, substantially reduced binding of the second Acl4 copy to Acl4•RpL4 (Figure 3b-d). Notably, we observed no Acl4 exchange from the RpL4^{LOOP} binding site in the conditions of the performed pull-down experiments, demonstrating that the Acl4•RpL4 heterodimer is very stable in solution.

Previously, we found that the transport factor Kap104 binds to Acl4•RpL4 to form a heterotrimeric complex with equimolar stoichiometry (Stelter et al., 2015). Further mapping revealed that two distinct regions in Acl4•RpL4 are sufficient for Kap104 binding, one located in RpL4^{EXT} and another in the basic unstructured 28-residue N-terminal region of Acl4 (Figures 3h and S9). Consistently, the binding between Acl4•RpL4 and Kap104 is abolished when both regions are deleted (Figure S9c). RpL4^{EXT} harbors a canonical basic phenylalanine-tyrosine nuclear localization signal (PY-NLS) and alanine mutagenesis confirmed that all canonical elements of its consensus sequence are critical for the Kap104-RpL4^{EXT} interaction (Figure 3e) (Lee et al., 2006). Because Acl4 and Kap104 bind to overlapping sites in RpL4^{EXT} and Acl4•RpL4 possesses a second Kap104 binding site, we tested whether Kap104 is able to displace the RpL4^{EXT}-bound Acl4 copy. Indeed, in a competition experiment Kap104 replaced the RpL4^{EXT}-bound Acl4 copy to form an Acl4•RpL4•Kap104 complex (Figure 3f). As expected, RanGTP released Acl4•RpL4 from this nuclear import heterotrimer (Figure 3g). Additionally, the nuclear import adaptor Kap- α was also able to form a heterotrimeric Acl4•RpL4•Kap- α nuclear import complex, indicating that multiple karyopherins are capable of transporting

Acl4•RpL4 to the nucleus (Figures S8d, S9). However, Kap104 displaced Kap- α from the Acl4•RpL4•Kap- α heterotrimer in direct competition experiments, suggesting that Kap104 is the primary nuclear import factor for Acl4•RpL4 (Figure S8e).

Acl4 and Kap104 protect nascent RpL4 from degradation

We previously described a novel pathway for excess ribosomal protein quality control (ERISQ) involving the E3 ubiquitin ligase Tom1, which marks excess ribosomal proteins for proteasome-dependent degradation (Sung et al., 2016). RpL4^{LOOP} residue Lys56 along with RpL4^{EXT} residues Lys310 and Lys340 were identified as Tom1 recognition sites, which were ubiquitinated in the absence of Acl4 and Kap104 (Figure 4a) (Sung et al., 2016). The crystal structure of Acl4•RpL4 now shows that Lys56 is located in the highly conserved RpL4^{LOOP} and is sequestered by the Acl4 surface, thus shielded from Tom1-mediated ubiquitination (Figure 4b). These findings demonstrate that in the RpL4-binding deficient Acl4 E266R mutant Lys56 in RpL4^{LOOP} is not sequestered by Acl4 and therefore is a target for Tom1-dependent ubiquitination. Thus, the growth defect observed in the Acl4 E266R mutant likely is the consequence of Tom1-dependent RpL4 ubiquitination and degradation, resulting in reduced soluble levels of RpL4 and in turn of 60S pre-ribosomal particles (Pillet et al., 2015; Stelter et al., 2015).

To explore whether RpL4^{EXT} residues Lys310 and Lys340 are protected by Kap104 in a similar fashion, we determined the crystal structure of Kap104 in complex with RpL4^{EXT} to 3.0 Å resolution. The Kap104•RpL4^{EXT} structure revealed that the PY-NLS of RpL4^{EXT} engages the concave surface of Kap104 in the same binding mode as previously established for other PY-NLS sequences (Lee et al., 2006). Upon Kap104 binding to RpL4^{EXT} and formation of a nuclear import complex both Tom1-modification sites of RpL4^{EXT} are sequestered by the concave Kap104 surface, consistent with our previous protection results of an *in vitro* Tom1 ubiquitination assay (Figure 4c) (Sung et al., 2016).

In summary, these results together with our previous findings allow us to propose a model of the entire RpL4 life cycle (Figure 5): Nascent RpL4 binds two Acl4 copies, one via RpL4^{LOOP} and another via RpL4^{EXT}. Kap104 replaces one Acl4 copy and shuttles Acl4•RpL4 across the nuclear envelope. Once in the nucleus, Kap104 releases RpL4^{EXT} upon RanGTP binding, allowing the rebinding of a second Acl4 copy from the nuclear

Acl4 pool. RpL4 release from Acl4 and ribosome incorporation is dependent on the interaction of RpL4^{EXT} with RpL18 and is triggered by relaxation of the presumably spring-loaded Acl4•RpL4 complex at the pre-60S ribosomal subunit (Figure 5a) (Stelter et al., 2015). Whereas unprotected RpL4 is recognized and ubiquitinated by the E3 ligase Tom1, followed by its proteasome-dependent degradation, protection of RpL4 by Acl4 and Kap104 generates a pool of RpL4 available for ribosome biogenesis (Pillet et al., 2015; Sung et al., 2016). Thus, ribosome assembly chaperones not only facilitate nuclear import and pre-ribosome incorporation of their ribosomal protein substrates, but are also essential for their protection from the cellular degradation machinery (Figure 5b). It remains an open question how Acl4 and other ribosome assembly chaperones return to the cytoplasm after their substrate RPs are incorporated in the pre-ribosomal particle and whether this occurs in a karyopherin-dependent manner. However, the presence of only sub-stoichiometric amounts of Acl4 in the cell strongly suggests that Acl4 shuttles between nucleus and cytoplasm. Furthermore, because the NPC allows passive diffusion of small proteins with a mass of less than ~40 kDa, the re-export of free Acl4 may not require a dedicated transport factor. The next important steps will be to identify and characterize the assembly chaperones for the remaining ~70 ribosomal proteins to establish whether the principles identified for Acl4 are conceptually similar. Additionally, the development of an *in vitro* ribosomal assembly system will be essential for the elucidation of the complex interplay of chaperoned ribosomal proteins, the cellular degradation machinery, and the maturing pre-ribosomal particle.

Unlike promiscuous folding chaperones that recognize exposed short hydrophobic secondary structure elements, Acl4 serves a dedicated sequestering function and harbors an intrinsic trigger for RpL4 release. Thus, the Acl4-RpL4 interaction constitutes a prototype for a dedicated assembly chaperone-substrate interaction that exerts multiple functions. We envision that a similar mechanism is employed by other ribosomal assembly chaperones and by assembly factors of other multi-component macromolecular machineries.

ACKNOWLEDGEMENTS

We thank Daniel H. Lin, Alina Patke and Emily J. Rundlet, for critical reading of the manuscript, Raymond J. Deshaies, Min-Kyung Sung, and Andrew M. Davenport for helpful discussions, Christopher Markosian for technical support, Jens Kaiser and the scientific staff of SSRL Beamline 12-2 for their support with X-ray diffraction measurements and Yuh Min Chook and Raymond J. Deshaies for sharing material. The operations at SSRL are supported by the Department of Energy and the National Institutes of Health. We acknowledge the Gordon and Betty Moore Foundation, the Beckman Institute, and the Sanofi-Aventis Bioengineering Research Program for their support of the Molecular Observatory at the California Institute of Technology. F.M.H. was supported by a PhD fellowship of the Boehringer Ingelheim Fonds. A.H. is a Faculty Scholar of the Howard Hughes Medical Institute, an inaugural Principal Investigator of the Heritage Medical Research Institute for the Advancement of Medicine and Science at Caltech and was supported by Caltech startup funds, a Kimmel Scholar Award of the Sidney Kimmel Foundation for Cancer Research, and a Teacher-Scholar Award of the Camille & Henry Dreyfus Foundation.

EXPERIMENTAL PROCEDURES

Bacterial and yeast expression constructs

S. cerevisiae and *C. thermophilum* DNA fragments of Acl4, RpL4, Kap104, and Kap- α and of *H. sapiens* Ran were amplified by PCR and ligated into bacterial expression vectors pGEX-6P-1 (GE Healthcare), a modified pET28a and pETDuet1 vector (both Novagene) that contained an N-terminal His₆-SUMO (small ubiquitin-like modifier) tag (pET28a-SUMO, pETDuet1-SUMO), and a modified pET28a vector (Novagene) containing an N-terminal His₆ tag followed by a PreScission cleavage site (Hoelz et al., 2003; Mossessova and Lima, 2000). The expression construct of *H. sapiens* Kap104 in which the internal loop residues 337 to 367 were replaced with a GGSGGSG linker was a gift from Yuh Min Chook (Lee et al., 2006). Acl4 and RpL4 variants were amplified by PCR and ligated into yeast expression vectors pRS415, pRS415-mCherry, pRS415-HA-mCherry, and pRS413-eGFP. Mutants were generated using QuikChange mutagenesis (Stratagene) and confirmed by DNA sequencing. Details of all bacterial and yeast expression constructs are summarized in Tables S1 and S2.

Protein expression and purification

Bacterial expression constructs were transformed in *Escherichia coli* BL21-CodonPlus(DE3)-RIL cells (Stratagene) and grown in LB medium to an OD₆₀₀ of ~0.6 prior to induction with 0.5 mM isopropyl β -D-thiogalactoside (IPTG). Cultures containing *C. thermophilum* protein expression constructs were grown for 18 hours at 23 °C, while *S. cerevisiae* and *H. sapiens* proteins were expressed for 18 hours at 18 °C. Cells were harvested by centrifugation and resuspended in a buffer containing 20 mM TRIS (pH 8.0), 500 mM NaCl, 5 mM β -mercaptoethanol (β -ME), 2 μ M bovine lung aprotinin (Sigma), and complete EDTA-free protease inhibitor cocktail (Roche) and flash frozen in liquid nitrogen. Cells were supplemented with 1 mg DNase I (Roche), lysed with a cell disrupter (Avestin), and centrifuged at 4 °C with 40,000 x g for 1 hour. The supernatant was filtered through a 0.45 μ m filter (Millipore).

Purification of His₆-SUMO-tagged Acl4, RpL4, Acl4•RpL4, and Kap- α variants.

Filtered lysate of His₆-SUMO tagged proteins was applied to a Ni-NTA column (Qiagen)

equilibrated with a buffer containing 20 mM TRIS (pH 8.0), 500 mM NaCl, and 5 mM β -ME and eluted with a linear imidazole gradient. Protein containing fractions were pooled and cleaved with ubiquitin-like-specific protease 1 (ULP1) and dialyzed against a buffer containing 20 mM TRIS (pH 8.0), 100 mM NaCl, and 5 mM β -ME (His₆-SUMO-RpL4^{EXT} was dialyzed but not treated with ULP1). Dialyzed proteins were applied to a Ni-NTA column equilibrated with a buffer containing 20 mM TRIS (pH 8.0), 100 mM NaCl, and 5 mM β -ME and the unbound fraction was loaded onto a HiTrapQ HP (GE Healthcare) ion exchange column equilibrated in a buffer containing 20 mM TRIS (pH 8.0), 100 mM NaCl, and 5 mM DTT and eluted with a linear salt gradient. Protein-containing fractions were pooled, concentrated, and injected on a 16/60 HiLoad Superdex 200 size exclusion column (GE Healthcare) equilibrated with a buffer containing 20 mM TRIS (pH 8.0), 100 mM NaCl, and 5 mM DTT. Protein-containing fractions were pooled, concentrated to ~20 mg ml⁻¹, and flash frozen in liquid nitrogen for further use.

Purification of GST-tagged hsKap104, Kap104, and Acl4. Cleared cell lysate of proteins with N-terminal Glutathione-S-transferase (GST) tag was applied to a glutathione sepharose column equilibrated with a buffer containing 20 mM TRIS (pH 8.0), 100 mM NaCl, and 5 mM DTT and eluted with a linear gradient of reduced glutathione. Pooled fractions were cleaved with PreScission protease (GE Healthcare) for at least 10 hours and dialyzed against a buffer containing 20 mM TRIS (pH 8.0), 100 mM NaCl, and 5 mM DTT (GST-Kap104 and GST-Acl4 for subsequent GST pull-downs were dialyzed but not treated with PreScission protease). Dialyzed proteins were bound to a HiTrapQ HP (GE Healthcare) ion exchange column equilibrated in a buffer containing 20 mM TRIS (pH 8.0), 100 mM NaCl, and 5 mM DTT and eluted with a linear salt gradient. Protein-containing fractions were pooled, concentrated and injected on a 16/60 HiLoad Superdex 200 size exclusion column (GE Healthcare) equilibrated with a buffer containing 20 mM TRIS (pH 8.0), 100 mM NaCl, and 5 mM DTT. Protein-containing fractions were pooled, concentrated to ~20 mg ml⁻¹, and flash frozen in liquid nitrogen for further use.

Purification of Ran^{Q69L}. Cleared lysate of His₆-Ran^{Q69L} was applied to a Ni-NTA column (Qiagen) equilibrated with a buffer containing 20 mM TRIS (pH 8.0), 500 mM NaCl, and 5 mM β -ME and eluted with a linear imidazole gradient. Pooled fractions were cleaved with PreScission protease (GE Healthcare) for at least 10 hours and dialyzed

against a buffer containing 20 mM TRIS (pH 8.0), 100 mM NaCl, and 5 mM DTT. Cleaved protein was bound to a HiTrapQ HP (GE Healthcare) ion exchange column equilibrated in a buffer containing 20 mM TRIS (pH 8.0), 100 mM NaCl, and 5 mM DTT and eluted with a linear salt gradient. Protein containing fractions were pooled, concentrated and injected on a 16/60 HiLoad Superdex 75 size exclusion column (GE Healthcare) equilibrated with a buffer containing 20 mM TRIS (pH 8.0), 100 mM NaCl, and 5 mM DTT. Purified Ran^{Q69L} was charged with GTP by incubation with 10 mM EDTA and 2 mM GTP for 30 minutes at 4 °C. Nucleotide exchange was stopped by the addition of 25 mM MgCl₂ (Maertens et al., 2014). Ran^{Q69L}GTP was injected on a Superdex 200 10/300 GL size exclusion column (GE Healthcare) pre-equilibrated with a buffer containing 20 mM TRIS (pH 8.0), 100 mM NaCl, 5 mM DTT and 5 μM GTP. Protein containing fractions were pooled, concentrated to ~20 mg ml⁻¹, and flash frozen in liquid nitrogen for further use.

Purification of Acl4•RpL4. His₆-SUMO-tagged Acl4 and His₆-SUMO-tagged RpL4, encompassing residues 28 to 361 and 1 to 277, respectively, were coexpressed, as previously described (Stelter et al., 2015). Filtered lysate was applied to a Ni-NTA column (Qiagen) equilibrated with a buffer containing 20 mM TRIS (pH 8.0), 500 mM NaCl, and 5 mM β-ME and eluted with a linear imidazole gradient. Protein containing fractions were pooled and cleaved with ULP1 and dialyzed against a buffer containing 20 mM TRIS (pH 8.0), 100 mM NaCl, and 5 mM β-ME. Dialyzed proteins were applied to a Ni-NTA column equilibrated with a buffer containing 20 mM TRIS (pH 8.0), 100 mM NaCl, and 5 mM β-ME and the unbound fraction was loaded onto a HiTrapQ HP (GE Healthcare) ion exchange column equilibrated in a buffer containing 20 mM TRIS (pH 8.0), 100 mM NaCl, and 5 mM DTT and eluted with a linear salt gradient. Protein-containing fractions were pooled, concentrated and injected on a 16/60 HiLoad Superdex 200 size exclusion column (GE Healthcare) equilibrated with a buffer containing 20 mM TRIS (pH 8.0), 100 mM NaCl, and 5 mM DTT. Protein-containing fractions were pooled, concentrated to ~20 mg ml⁻¹, and used for crystallization.

Purification of hsKap104•RpL4^{EXT}, hsKap104, and RpL4^{EXT}, encompassing residues 308 to 332, were purified individually, as described above. The hsKap104•RpL4^{EXT} complex was assembled on a 16/60 HiLoad Superdex 200 size exclusion column (GE Healthcare) equilibrated with a buffer containing 20 mM TRIS

(pH 8.0), 100 mM NaCl, and 5 mM DTT. Complex assembly was carried out in the presence of a 5-fold molar excess of RpL4^{EXT} over *hsKap104* to yield a stoichiometric *hsKap104*•RpL4^{EXT} complex. Protein containing fractions were pooled, concentrated to ~20 mg ml⁻¹, and used for crystallization.

Structure determination and refinement of Acl4•RpL4

Crystals of the *C. thermophilum* Acl4•RpL4 complex, encompassing residues 28 to 361 and 1 to 277, respectively, were obtained by hanging drop vapor diffusion at 21 °C using 1 µl protein solution and 1 µl reservoir solution containing 0.1 M BIS-TRIS (pH 5.5), 2 % (v/v) Tacsimate (pH 5.5), and 13 % (w/v) PEG 3350. Acl4•RpL4 crystals grew in the orthorhombic space group P2₁2₁2 at a protein concentration of 17.5 mg ml⁻¹ and reached their maximum size of ~100 µm x 50 µm x 50 µm within one week. Cryo protection of the crystals was achieved with 0.1 M BIS-TRIS (pH 5.5), 2 % (v/v) Tacsimate (pH 5.5), 15 % (w/v) PEG 3350 and 20 % (v/v) ethylene glycol added in 5 % increments. Collection of X-ray diffraction data was performed at 100 K at beamline BL12-2 at the Stanford Synchrotron Radiation Lightsource (SSRL) and crystals diffracted to a resolution of 2.4 Å. X-ray data were processed using XDS (Kabsch, 2010). The structure of the Acl4•RpL4 complex was solved by single-wavelength anomalous dispersion (SAD) using anomalous scattering data collected at the selenium edge of SeMet-labeled crystals. Eight selenium sites were identified with SHELXD and initial phases were calculated with SHARP (Bricogne et al., 2003; Sheldrick, 2008). Density modification with solvent flattening and histogram matching was performed using DM (Bailey, 1994). The initial electron density map was of high quality and allowed for building of a complete model of the Acl4•RpL4 complex. A final model of the complex was generated by iterative rounds of model building and refinement in Coot and PHENIX, consisting of Acl4 residues 28 to 361 and RpL4 residues 4 to 272 (Adams et al., 2010; Emsley and Cowtan, 2004). No electron density was observed for RpL4 residues 1 to 3, 78 to 88, 189 to 202 and 273 to 277, which are presumed to be disordered. The structure was refined to R_{work} and R_{free} values of 19.1 % and 22.7 %, respectively. The Acl4•RpL4 model possesses excellent stereochemical parameters with no residues in disallowed regions of the Ramachandran plot as determined by MolProbity

(Davis et al., 2007). Further details of the data collection and refinement statistics are summarized in Table 1.

Structure determination and refinement of *hsKap104*•*RpL4*^{EXT}

Crystals of the *hsKap104*•*RpL4*^{EXT} complex were obtained by hanging drop vapor diffusion at 21 °C using 1 µl protein solution and 1 µl reservoir solution containing 0.1 M BIS-TRIS-propane (pH 7.0) and 0.5 M sodium citrate tribasic. *hsKap104*•*RpL4*^{EXT} crystals grew in the orthorhombic space group P2₁2₁2 at a protein concentration of 5 mg ml⁻¹ and reached their maximum size of ~100 µm x 50 µm x 50 µm within one week. Cryo protection of the crystals was achieved with 0.1 M BIS-TRIS-propane (pH 7.0) and 0.5 M sodium citrate tribasic and 24 % (v/v) glycerol added in 8 % increments. Collection of X-ray diffraction data was performed at 100 K at beamline BL12-2 at the Stanford Synchrotron Radiation Lightsource (SSRL) and crystals diffracted to a resolution of 3.0 Å. X-ray data were processed using XDS (Kabsch, 2010). The structure of the *hsKap104*•*RpL4*^{EXT} complex was solved by molecular replacement using the coordinates of *hsKap*-β2 (PDB ID: 4JLQ) as a search model in phaser (Adams et al., 2010; Soniat et al., 2013). The initial electron density map was of high quality and allowed for building of a complete model of the *Kap104*•*RpL4*^{EXT} complex. A final model of the complex was generated by iterative rounds of model building and refinement in Coot and PHENIX, consisting of *hsKap104* residues 1 to 890 and *RpL4*^{EXT} residues 326 to 332 (Adams et al., 2010; Emsley and Cowtan, 2004). No electron density was observed for *hsKap104* residues 1 to 4 and 321 to 367 and for *RpL4*^{EXT} residues 308 to 325, which are presumed to be disordered. The structure was refined to R_{work} and R_{free} values of 20.8 % and 23.8 %, respectively. The *hsKap104*•*RpL4*^{EXT} model possesses excellent stereochemical parameters with no residues in the disallowed regions of the Ramachandran plot as determined by MolProbity (Davis et al., 2007). Further details of the data collection and refinement statistics are summarized in Table 1.

GST pull-down interaction analysis

Interaction studies with GST-Acl4 coexpressed with SUMO-*RpL4*^{ΔEXT} were performed using GST pull-down experiments. 100 µl glutathione-coupled sepharose beads (GE

Healthcare) were equilibrated with a buffer containing 20 mM TRIS (pH 8.0), 100 mM NaCl, and 5 mM DTT and were incubated with cleared and filtered lysate from 1 L bacterial expression culture for 1 hour at 4 °C. GST-beads were washed three times with 15 ml buffer containing 20 mM TRIS (pH 8.0), 100 mM NaCl, and 5 mM DTT and centrifuged with 500 x g at 4 °C. Bound protein was eluted from the beads with 250 µl buffer containing 20 mM TRIS (pH 8.0), 100 mM NaCl, 5 mM DTT and 25 mM reduced glutathione. Eluted protein was resolved on a 12.5 % SDS-PAGE gel followed by visualization with Coomassie Brilliant Blue staining.

For GST pull-down experiments with pre-purified proteins, 20 µl of glutathione-coupled sepharose beads were equilibrated with a buffer containing 20 mM TRIS (pH 8.0), 100 mM NaCl, and 5 mM DTT and incubated for 1 hour with 35 nmol GST-tagged bait proteins and untagged prey proteins. After incubation, the beads were washed 4 times with 200 µl buffer containing 20 mM TRIS (pH 8.0), 100 mM NaCl, and 5 mM DTT and centrifuged with 500 x g at 4 °C. SDS-sample buffer was added to the beads, followed by boiling at 95 °C for 5 minutes and centrifugation at 30,000 x g for 5 minutes. Samples were resolved on a 12.5 % SDS-PAGE gel and visualized with Coomassie Brilliant Blue staining.

Size exclusion chromatography interaction analysis

Purified Acl4, RpL4, Kap104, and Kap- α variants were analyzed by size exclusion chromatography (SEC). Samples were injected on a Superdex 200 10/300 GL size exclusion column (GE Healthcare) pre-equilibrated with a buffer containing 20 mM TRIS (pH 8.0), 100 mM NaCl, and 5 mM DTT. Pre-incubation was performed for 1 hour at 4 °C prior to injection on a size exclusion column. Protein containing fractions were resolved on a 12.5 % SDS-PAGE gel and visualized with Coomassie Brilliant Blue staining.

Yeast strains, media and genetic methods

All yeast media was prepared and Lithium-acetate driven *S. cerevisiae* transformations were performed according to standard protocols. The *S. cerevisiae acl4* Δ strain was generated by replacing the Acl4 gene with a *kanMX4* cassette by homologous recombination, as previously described (Janke et al., 2004). Details of yeast expression

vectors are summarized in Table S2.

Growth analysis and fluorescence microscopy

The growth analysis was performed in *S. cerevisiae acl4Δ* strains that were transformed with pRS415 constructs carrying various mCherry-tagged Acl4 variants. Transformed cells were selected twice on SDC-LEU plates, prior to analysis. Ten-fold dilution series were prepared and 17.5 μl were spotted on SDC-LEU plates and grown at 23 °C, 30 °C, and 37 °C for 2-3 days. Localization assays were performed using pRS415 vectors carrying mCherry-tagged Acl4 variants and a pRS413 vector harboring eGFP-tagged RpL4. Transformed cells were selected twice on SDC-LEU-HIS plates prior to analysis. The variants were grown in SDC-LEU-HIS medium at 30 °C to mid-log phase. For heat-shock analysis, cells were grown at 30 °C to mid-log phase prior to shifting cells to 37 °C for 6 hours. For fluorescence microscopy 1 ml of cells was centrifuged at 500 x g and washed once with 1 ml of water. The cell pellet was resuspended in 100 μl water and 10 μl were analyzed using a Carl Zeiss Observer Z.1 equipped with a Hamamatsu C10600 Orca-R2 camera.

Western blot analysis

In vivo Acl4 expression levels were tested by transformation of *S. cerevisiae acl4Δ* strains with pRS415 constructs carrying various HA-mCherry-tagged Acl4 variants. Transformed cells were selected twice on SDC-LEU plates, prior to analysis. Protein extraction from cells was performed via NaOH and TCA treatment (Yaffe and Schatz, 1984). Specifically, cells were grown at 30 °C to an OD of ~1.0 prior to harvesting of 1 ml of culture. Cell pellets were resuspended and vortexed in 1 ml of a solution containing 1.85 M NaOH and 7.4 % (v/v) β-ME prior to incubation for 10 minutes on ice. Proteins were precipitated by addition of 150 μl of 50 % (w/v) TCA and incubation for 10 minutes on ice, followed by centrifugation at 30,000 x g for 2 minutes. The pellet was washed twice with 1 ml of ice-cold acetone and air-dried at room temperature prior to resuspension in SDS loading buffer. Western blot analysis was performed with a rabbit anti-hexokinase antibody (US Biological; H2035-02; 1:10,000 dilution), an anti-rabbit antibody fused to an IR800 fluorescent probe (Licor, 926-32211; 1:5,000 dilution), a mouse anti-HA antibody

(Covance; MMS-101P; 1:5,000 dilution), and an anti-mouse antibody coupled to alkaline phosphatase (Promega; S3721; 1:5,000 dilution). Antibodies were diluted in TBS-T supplemented with 5 % (w/v) milk powder and washes were carried out in TBS-T.

Animation of Acl4•RpL4 disassembly

Acl4 *apo* (PDB ID: 4YNV) and ribosome-bound RpL4 (PDB ID: 4V88) were superposed with Acl4•RpL4 structure as reference (Ben-Shem et al., 2011; Stelter et al., 2015). Morphing of the Acl4•RpL4 complex into the open Acl4 *apo* state and ribosome-bound RpL4 was animated using PyMOL (www.pymol.org).

Illustrations and figures

Size exclusion chromatography profiles were generated with IGOR (WaveMetrics) and assembled with Adobe Illustrator. All structure figures were generated with PyMOL (www.pymol.org). Sequence alignments were generated using ClustalX and colored with ALSCRIPT (Barton, 1993; Jeanmougin et al., 1998). Electrostatic potentials were calculated with APBS (Adaptive Poisson-Boltzmann Solver) software (Baker et al., 2001).

Data Availability

The coordinates and structure factors have been deposited with the Protein Data Bank with accession codes 5TQB (Acl4•RpL4) and 5TQC (Kap104•RpL4^{EXT}).

FIGURES

Main figures

Figure 1. Analysis of the Acl4•RpL4 structure

Figure 2. Acl4•RpL4 interaction analysis

Figure 3. Biochemical Acl4•RpL4•Kap104 interaction map

Figure 4. Shielding of Tom1 ubiquitination sites

Figure 5. Model for nuclear import and balancing of RpL4

Supplemental figures

Figure S1. Representations of the Acl4•RpL4 and Kap104•RpL4^{EXT} crystal structures

Figure S2. Multispecies sequence alignment of Acl4

Figure S3. Multispecies sequence alignment of RpL4

Figure S4. Conservation and electrostatic surface analysis of the Acl4•RpL4 crystal structure

Figure S5. Interaction analysis of *C. thermophilum* Acl4 surface mutations

Figure S6. Biochemical analysis of the *scAcl4* E266R mutant

Figure S7. *In vivo* localization analysis of Acl4 and RpL4

Figure S8. Biochemical analysis of RpL4^{EXT} interaction partners

Figure S9. Kap104 interaction with Acl4•RpL4

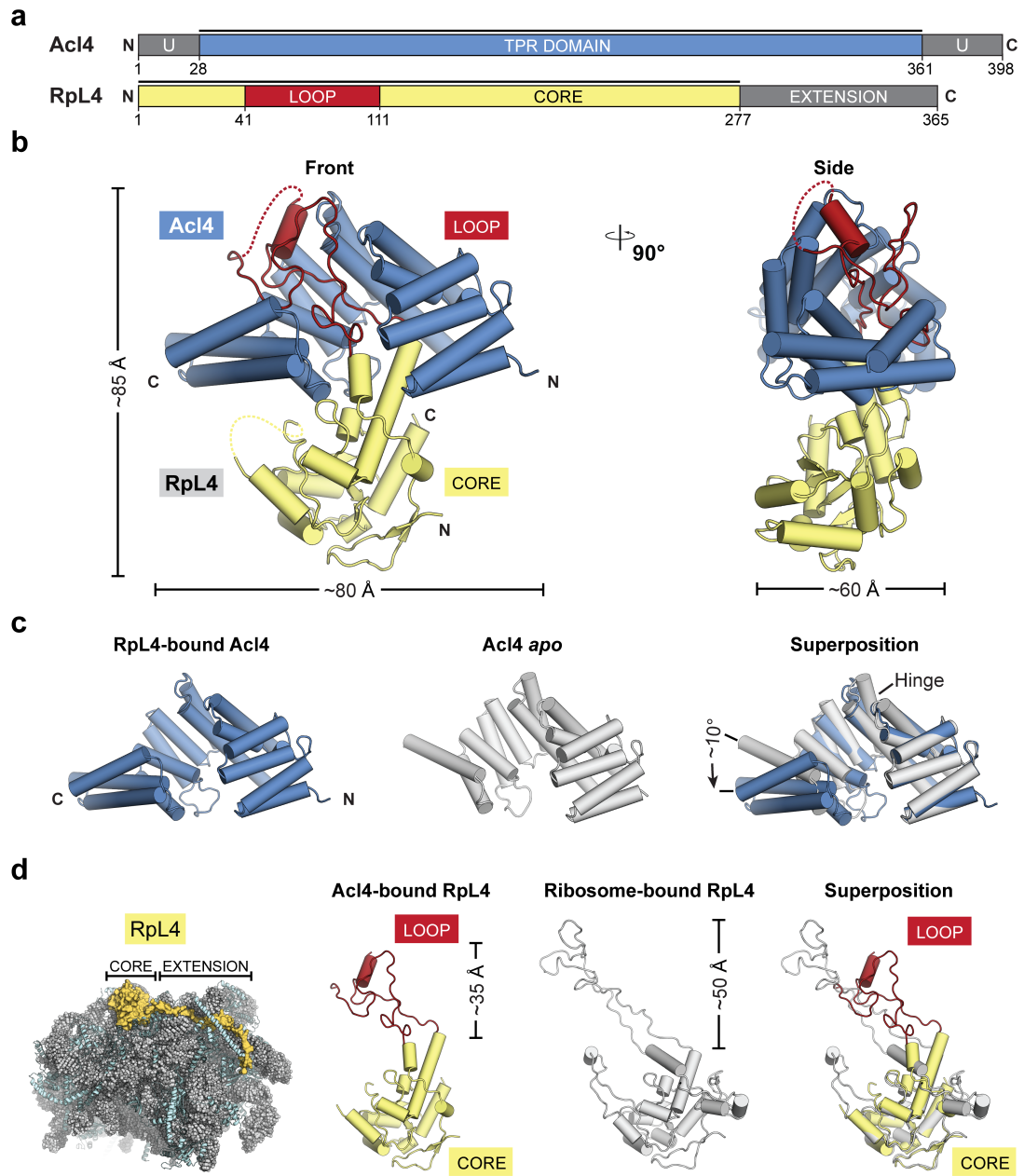


Figure 1. Analysis of the Acl4•RpL4 structure

(a) Domain representation of Acl4 and RpL4 from *Chaetomium thermophilum*. Acl4: unstructured N- and C-terminal regions (dark gray); central TPR domain (blue). RpL4: core (yellow); loop (red); C-terminal extension (dark gray). Black bars represent crystallized fragments. (b) Crystal structure of the *Chaetomium thermophilum* Acl4•RpL4 complex, shown in cartoon representation. A 90° rotation is shown on the right. Coloring is according to panel A. (c) Superposition of Acl4 *apo* (gray) (PDB ID: 4YNV) with Acl4•RpL4 (blue) (Stelter et al., 2015). (d) Cartoon representation of the *S. cerevisiae* large ribosomal subunit (PDB ID: 4V88) showing RNA (gray), proteins (teal), and RpL4 (yellow) (Ben-Shem et al., 2011). Superposition of Acl4-bound RpL4 with ribosome-bound RpL4 (gray).

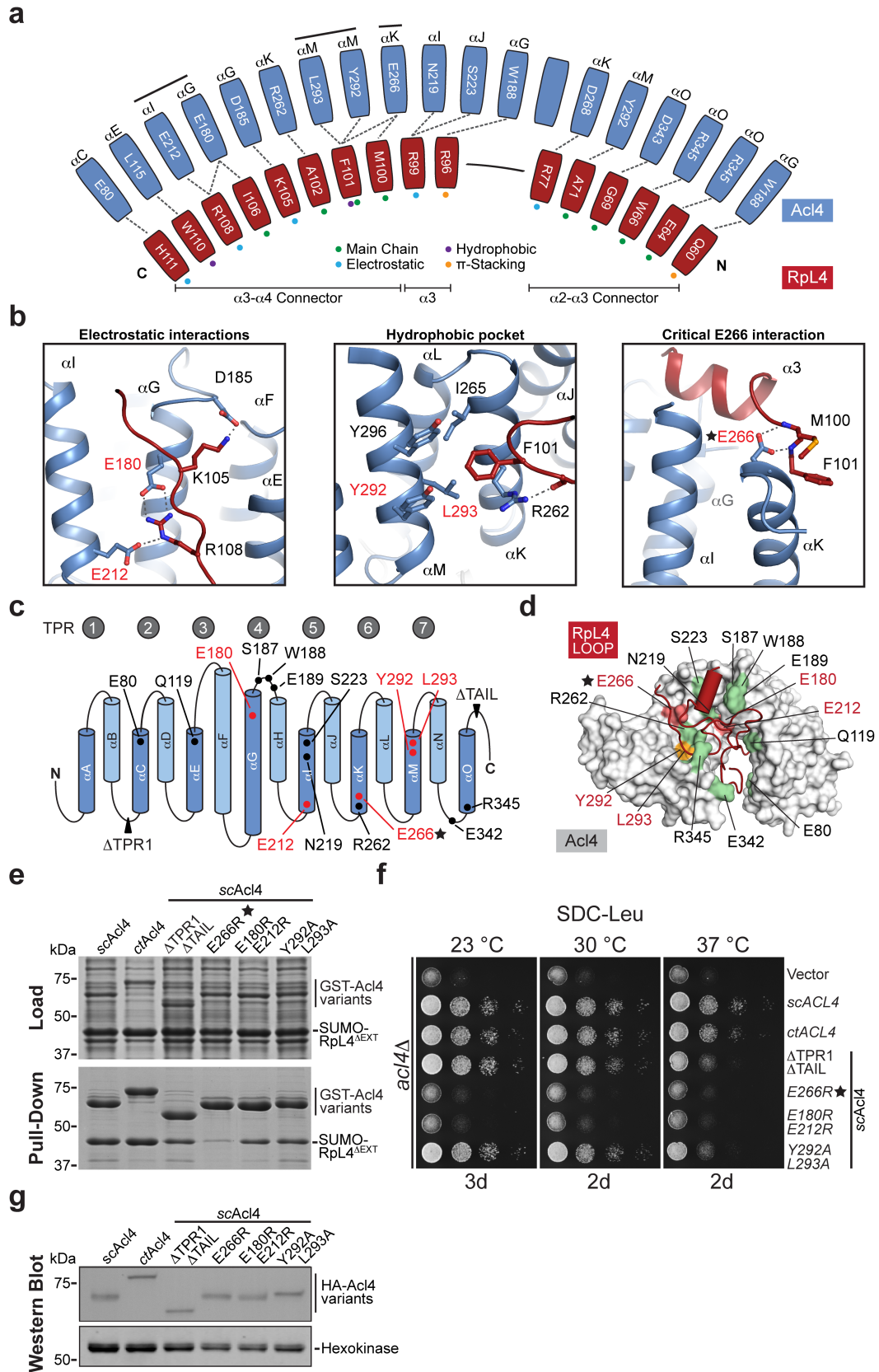


Figure 2. Acl4•RpL4 interaction analysis

(a) Schematic representation of the Acl4-RpL4 interface, colored as in Figure 1. Colored dots indicate the interaction type between depicted residues. (b) Acl4•RpL4 interaction hotspots. Boxes show three interactions between RpL4 (red) and Acl4 (blue) in cartoon representation. (c) Schematic representation of the Acl4 TPR domain fold architecture. The positioning of RpL4 interaction residues is indicated. (d) Mutational analysis of the Acl4-RpL4 interaction. Acl4 (gray) and RpL4^{LOOP} (red) are shown in surface and cartoon representation, respectively. Mutated Acl4 residues are plotted on the surface and colored according to effect on RpL4 binding: green, no effect; orange, medium effect; and red, strong effect. (e) Interaction analysis of Acl4 and RpL4^{ΔEXT}. Pull-down interaction analysis between *S. cerevisiae* GST-Acl4 variants (bait) and RpL4^{ΔEXT}. Loaded (top) and pulled-down (bottom) fractions are indicated and Acl4 mutations are depicted above each lane. (f) Growth analysis of Acl4 variants. Residue numbering is according to *C. thermophilum* Acl4. (g) Western blot analysis of the expression levels of Acl4 variants in *S. cerevisiae*. HA-tagged Acl4 variants and the hexokinase loading control were detected with anti-HA and anti-hexokinase antibodies, respectively.

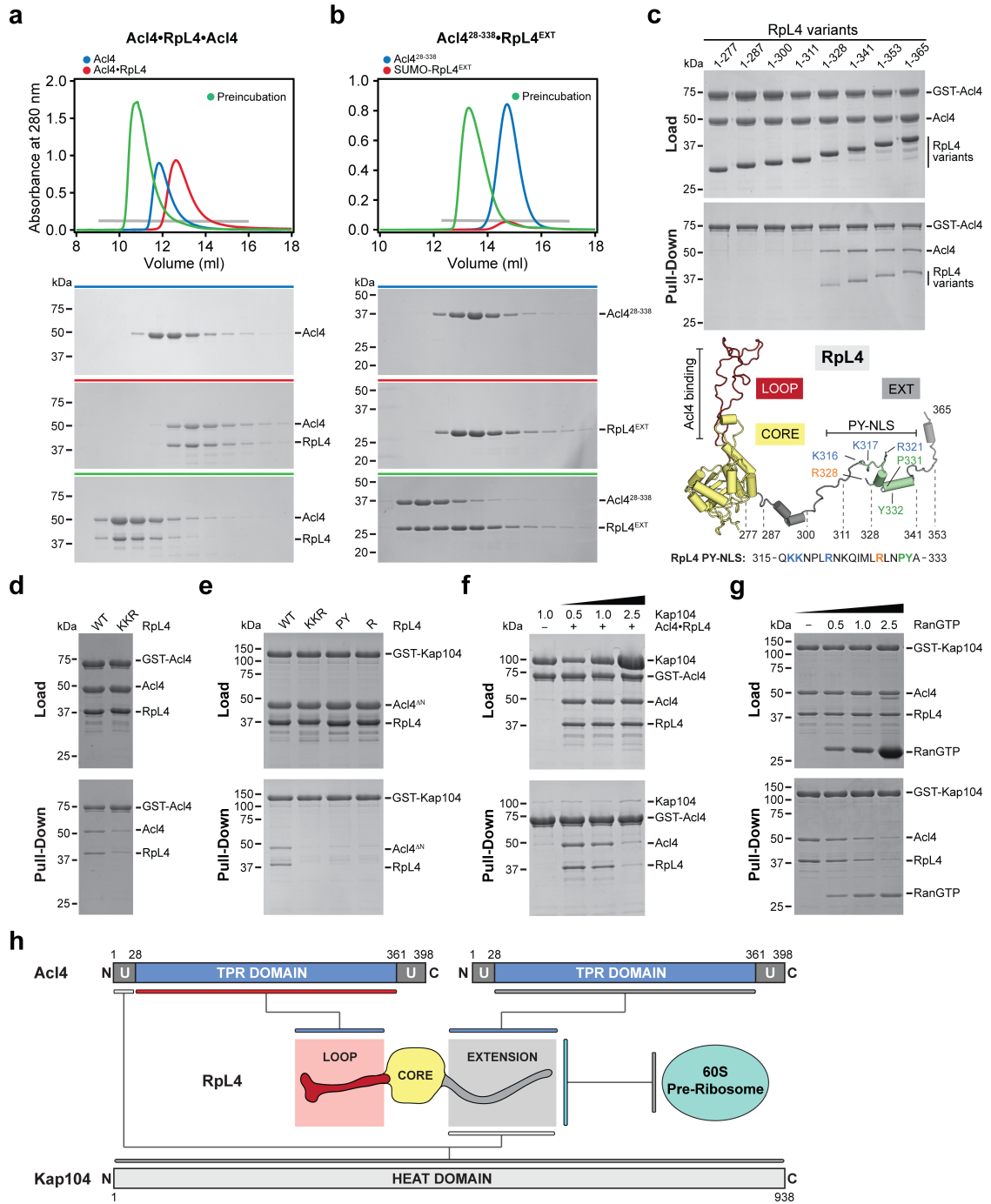


Figure 3. Biochemical Acl4•RpL4•Kap104 interaction map

(a, b) Size exclusion chromatography (SEC) analysis of Acl4, Acl4•RpL4, and SUMO-RpL4^{EXT}. SEC profiles of proteins or protein complexes are shown individually (blue and red) and after preincubation (green). (c) GST pull-down of pre-purified GST-Acl4 and Acl4•RpL4 C-terminal truncation variants. Loaded (top) and pulled-down (bottom) fractions are shown. Cartoon representation of RpL4 with RpL4^{LOOP}, RpL4^{CORE}, and RpL4^{EXT} colored as in Figure 1a. The basic PY-NLS is colored in green and the analyzed fragment boundaries are indicated. As reference, the primary sequence of the basic PY-NLS and the consensus residues are shown. (d) GST pull-down with pre-purified GST-Acl4 and Acl4•RpL4 variants. (e) GST pull-down with pre-purified GST-Kap104 and Acl4^{ΔN}•RpL4 variants. Labeling indicates RpL4 variants (WT, wild type; KKR, K316A/K317A/R321A; PY, P331A/Y332A; R, R328A). (f) GST pull-down with pre-assembled Acl4•RpL4•GST-Acl4 and increasing amounts of Kap104. (g) GST pull-down with pre-assembled Acl4•RpL4•GST-Kap104 and increasing amounts of RanGTP. (h) Schematic representation of the Acl4•RpL4•Kap104 interaction map.

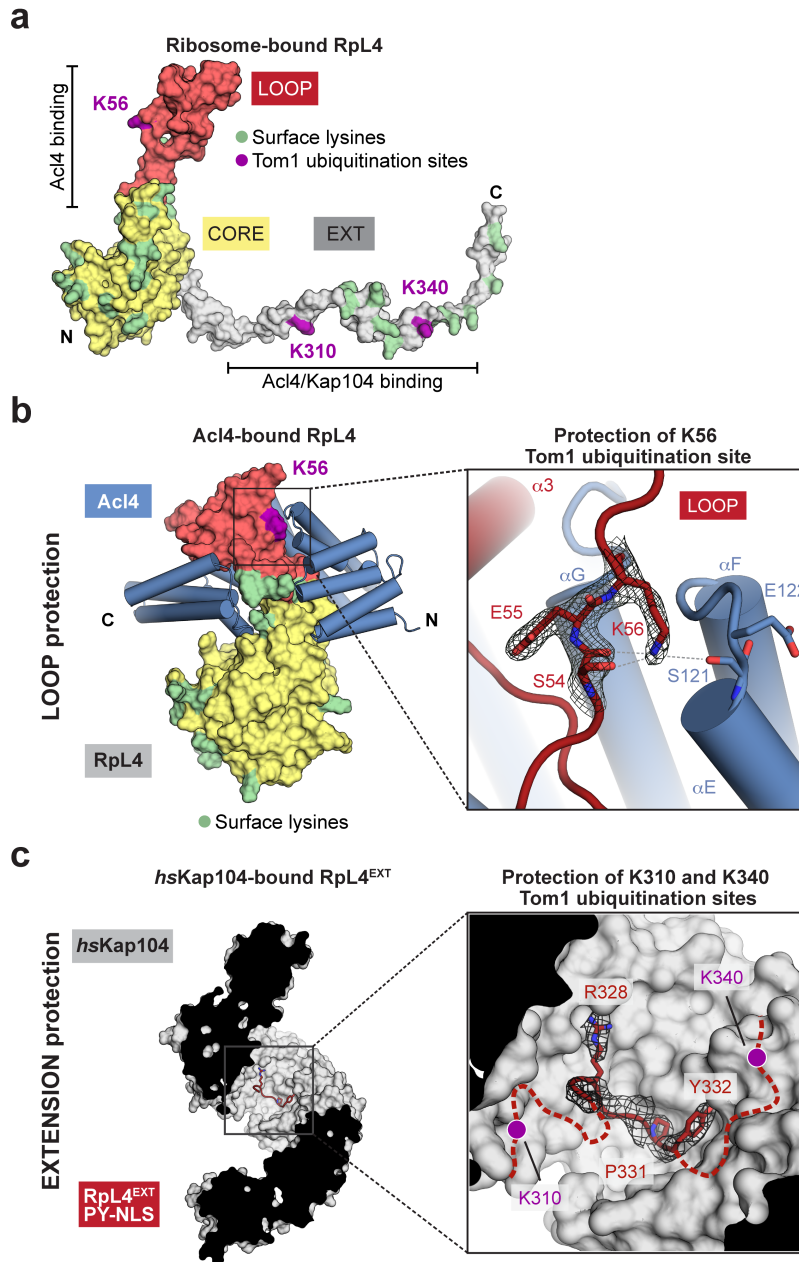
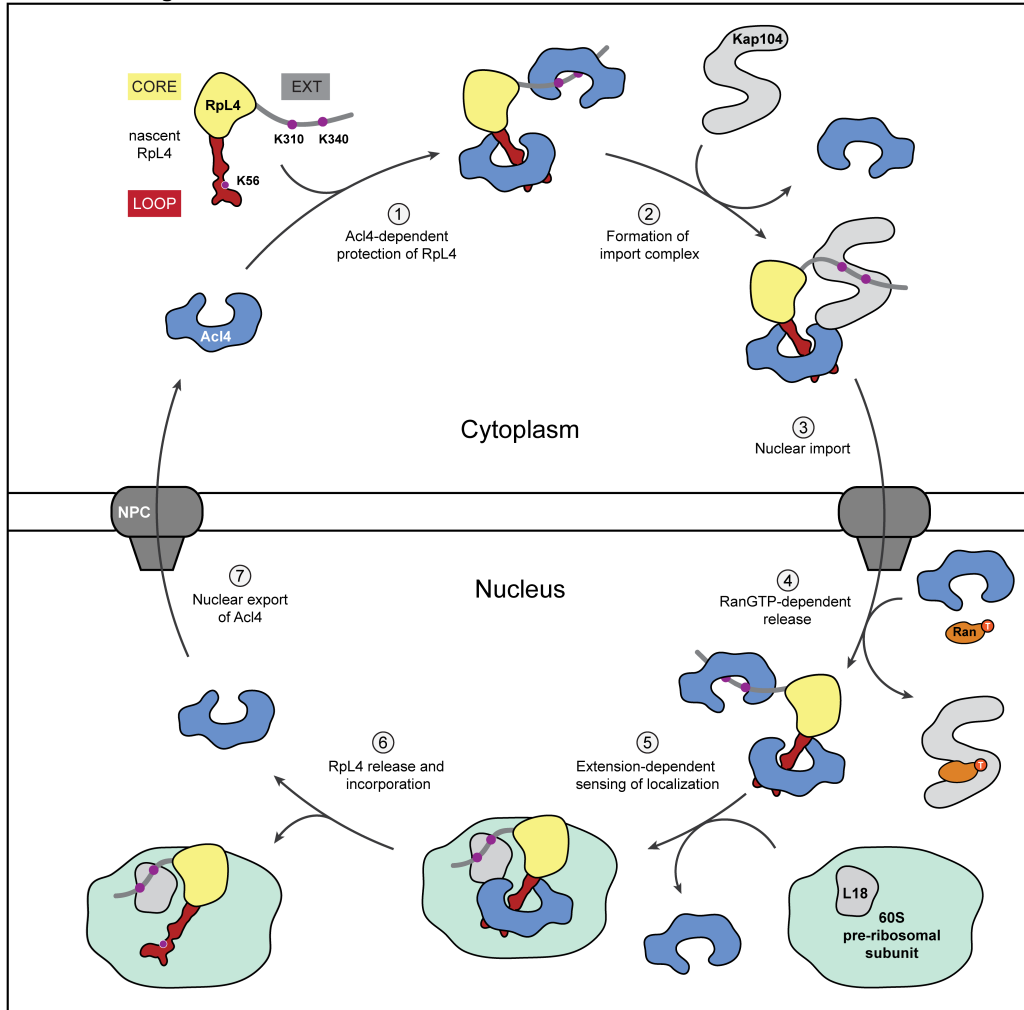


Figure 4. Shielding of Tom1 ubiquitination sites

(a) Surface representation of ribosome-bound RpL4 (PDB ID: 4V88) (Ben-Shem et al., 2011). Acl4 and Kap104 binding sites are indicated with black bars. (b) Acl4-bound RpL4 (colored as in Figure 1a) and Acl4 (blue) are shown in surface and cartoon representation, respectively. The inset marks the Tom1 ubiquitination site that is illustrated in detail on the right. Acl4 (blue) and RpL4 (red) and critical residues highlighted in stick representation with a section of the final $2|F_o|-|F_c|$ electron density map contoured at 1.0σ . (c) Crystal structure of the *hs*Kap104•RpL4^{EXT} complex. The inset marks the location of the Kap104 PY-NLS binding site that is illustrated in detail on the right. The residues of the PY-NLS consensus sequence, Arg328, Pro331 and Tyr332 are highlighted in stick representation with a section of the final $2|F_o|-|F_c|$ electron density map contoured at 1.0σ . Magenta circles indicate the approximate location of RpL4 residues K310 and K340 that are ubiquitinated by Tom1 in the absence of Kap104.

a
Ribosome biogenesis



b
Cellular degradation

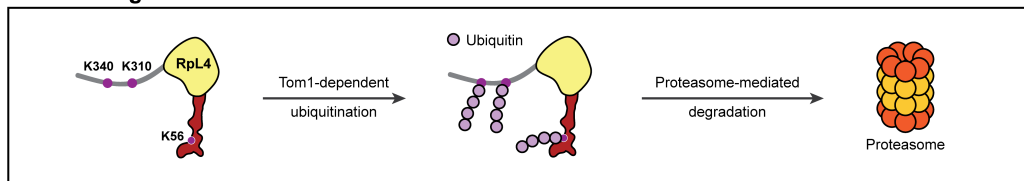


Figure 5. Model for nuclear import and balancing of RpL4

(a) Acl4- and Kap104-mediated nuclear import of RpL4. The cycle involves seven steps. (1) Following translation, nascent RpL4 is protected by two copies of Acl4 at its unstructured loop and at the unstructured C-terminal extension. (2) A stoichiometric hetero-trimeric nuclear import complex is formed by binding of Acl4•RpL4 to the transport factor Kap104. Kap104 binding occurs in a bi-partite fashion and involves the basic unstructured N-terminal region of Acl4 and RpL4^{EXT}, displacing the RpL4^{EXT}-bound Acl4 copy. (3) Kap104 dependent transport of Acl4•RpL4 through the NPC. (4) After successful transport, the Acl4•RpL4•Kap104 import complex is disassembled by nuclear RanGTP, releasing Acl4•RpL4 into the nucleoplasm. (5) RpL4^{EXT} contacts RpL18 and expansion segment 7 on the surface of the pre-60S subunit (Stelter et al., 2015). (6) Constructive interactions result in disassembly of the Acl4•RpL4 complex and incorporation of RpL4 into the large pre-ribosomal subunit. (7) Potential nuclear export of Acl4 allows its entering into the next RpL4 transport cycle. **(b)** Balancing of excess unassembled ribosomal proteins. In the absence of Acl4 and Kap104, unassembled RpL4 is ubiquitinated by Tom1 and degraded by the proteasome-dependent degradation machinery (Sung et al., 2016).

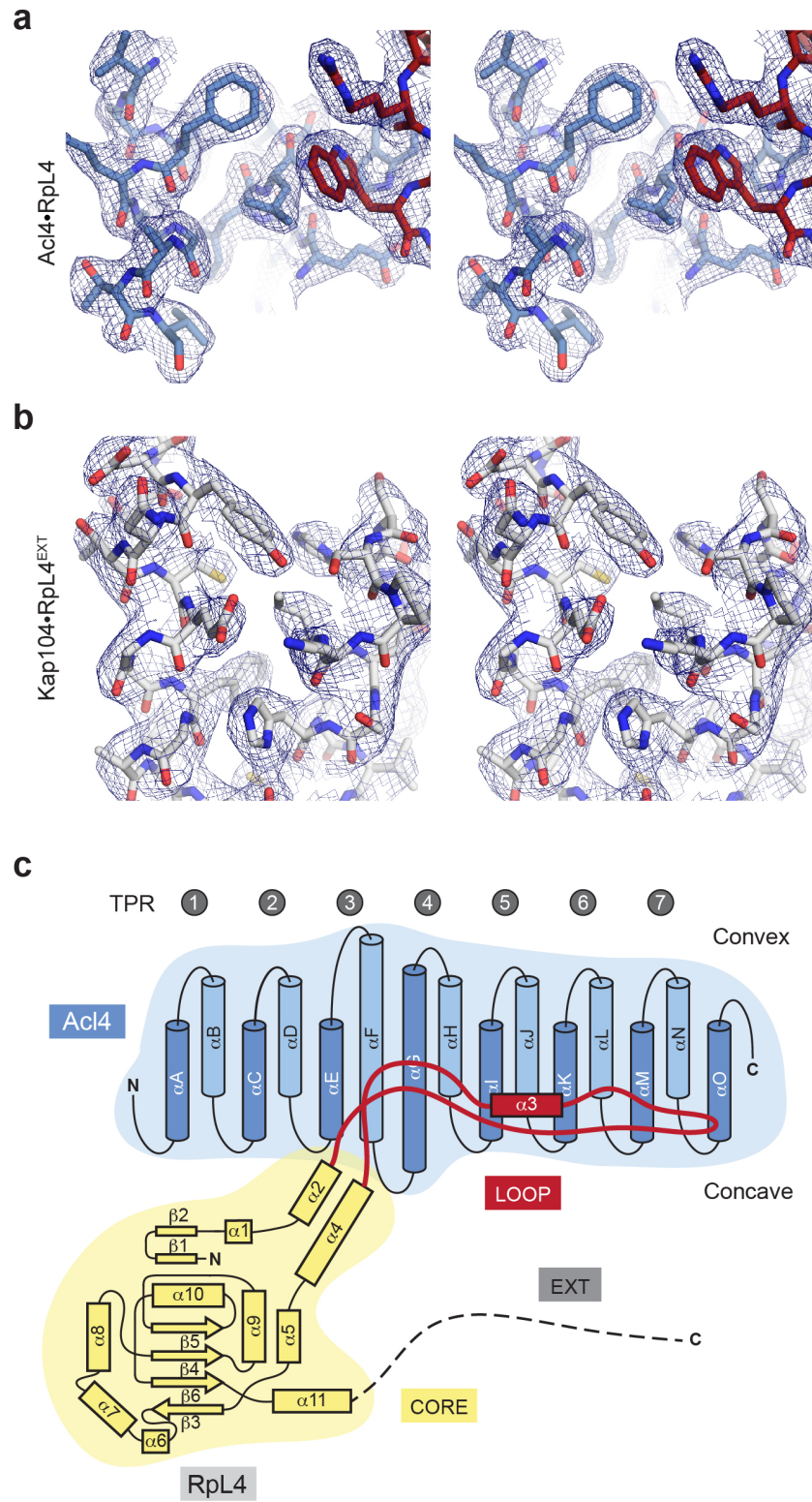


Figure S1. Representations of the Acl4•RpL4 and Kap104•RpL4^{EXT} crystal structures
(a) Stereo view of a stick representation of Acl4•RpL4 with a section of the final $2|F_o|-|F_c|$ electron density map contoured at 1.0σ . (b) Stereo view of a stick representation of Kap104•RpL4^{EXT} with a section of the final $2|F_o|-|F_c|$ electron density map contoured at 1.0σ . (c) The architecture of the Acl4•RpL4 complex is represented by the schematic arrangement of its secondary structure elements. The coloring is according to the color scheme in Figure 1a.

Acl4

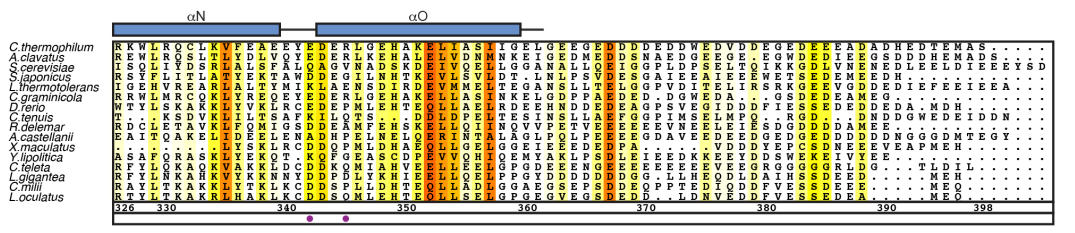
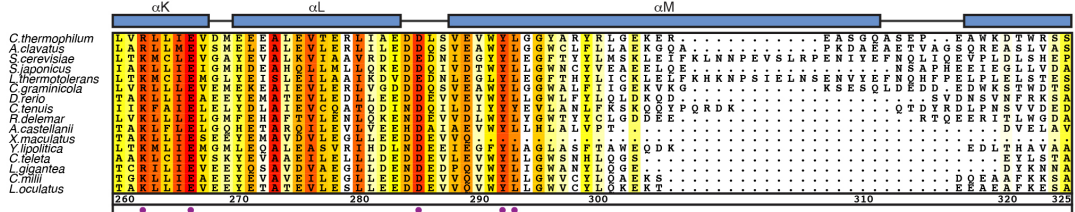
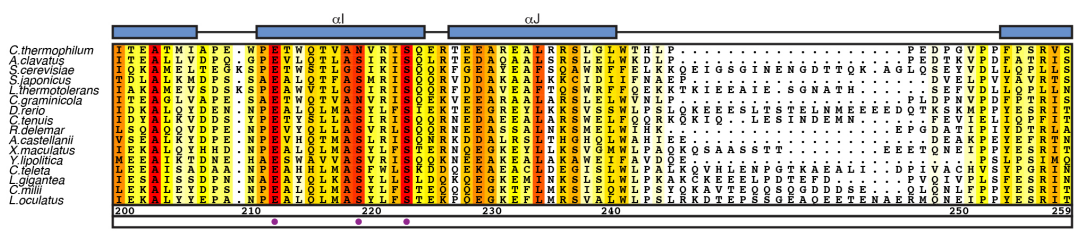
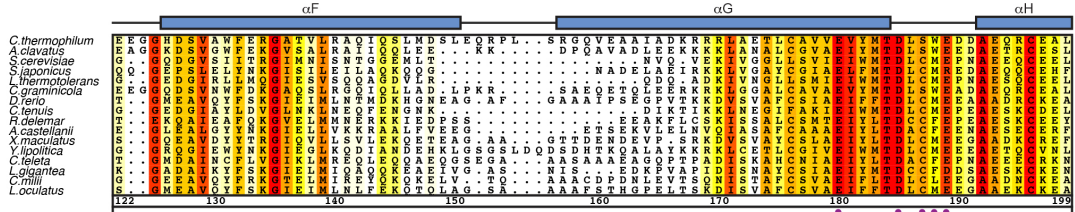
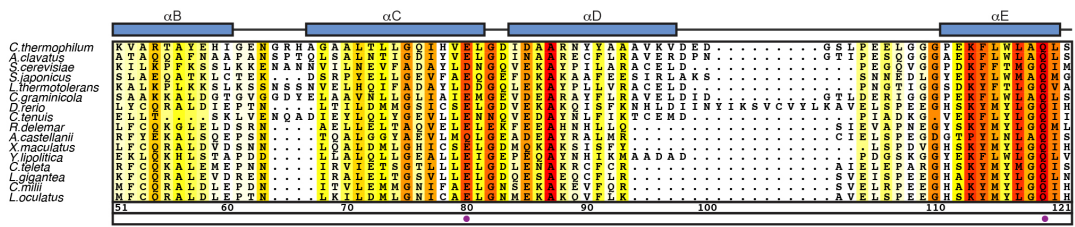
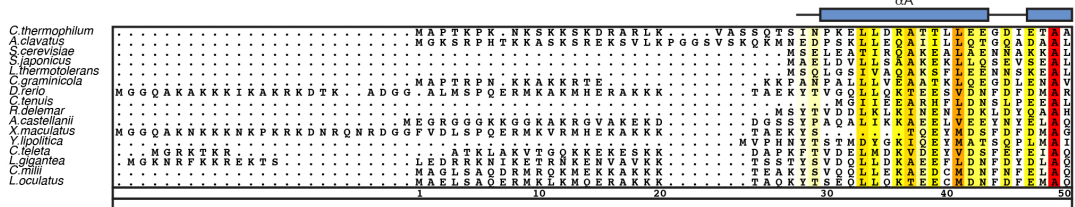


Figure S2. Multispecies sequence alignment of Acl4

Protein sequences of Acl4 from 16 species were aligned and colored according to a BLOSUM62 matrix. The sequence conservation is represented in shading from white (< 40 % similarity), yellow (40 % similarity) to dark red (100 % identity). Numbering of the alignment below is relative to the *C. thermophilum* Acl4 protein sequence. The secondary structure of Acl4 as observed in the Acl4•RpL4 structure is shown in blue rectangles, representing α -helices (α A to α O) and gray lines indicate coil regions. Purple dots indicate Acl4 surface residues that were mutated in this study.

RpL4

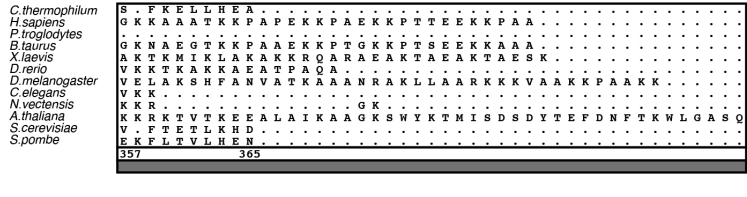
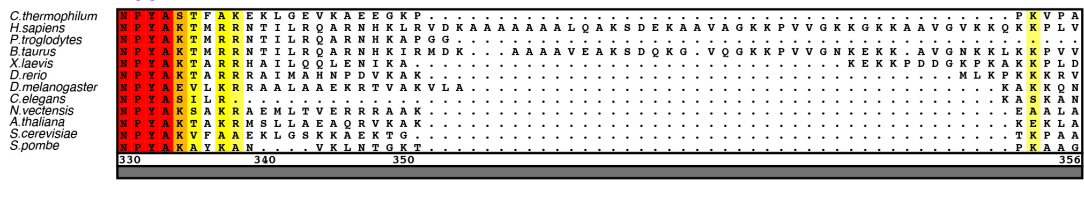
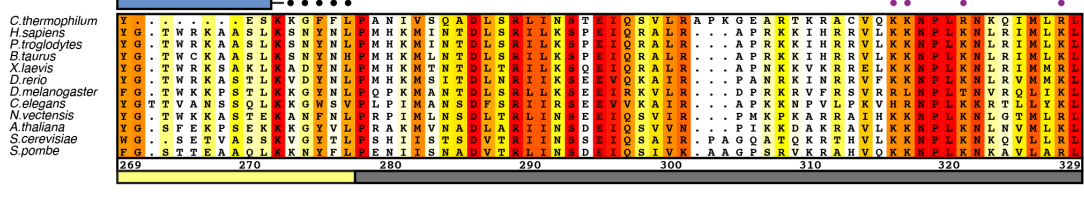
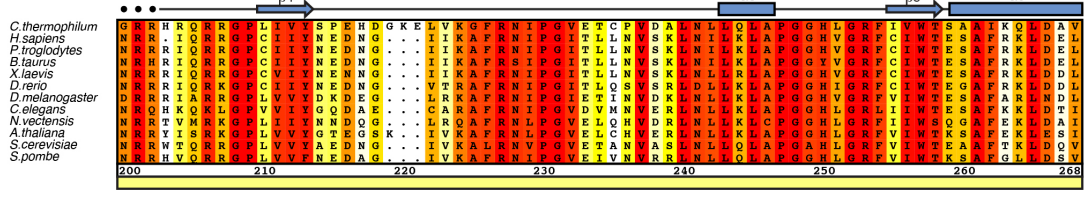
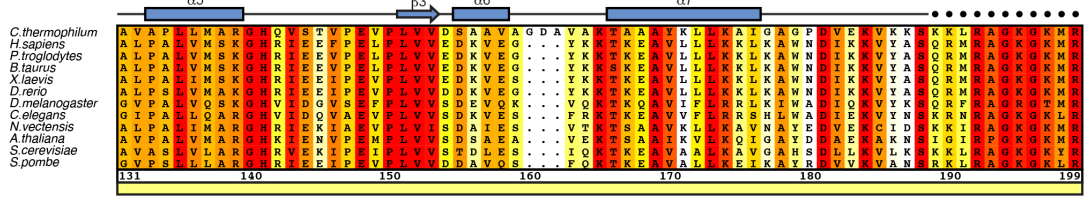
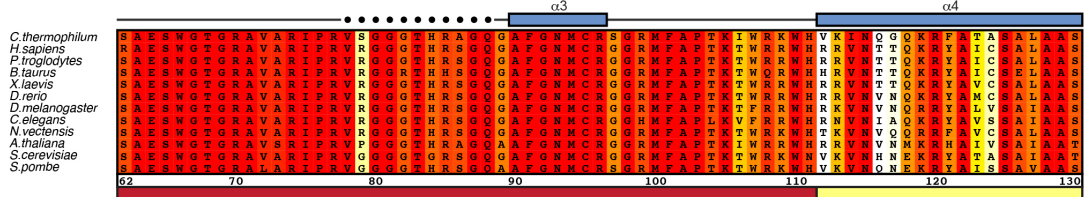
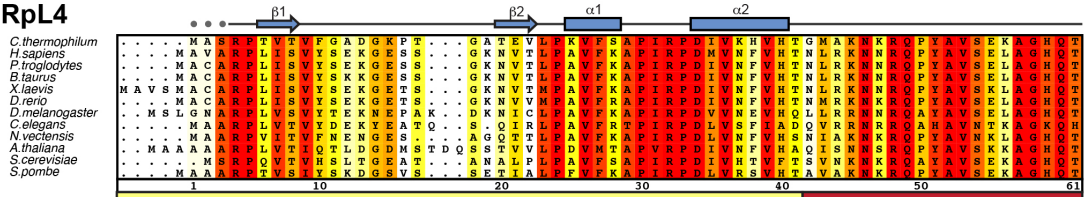


Figure S3. Multispecies sequence alignment of RpL4

Protein sequences of RpL4 from 12 species were aligned and colored according to a BLOSUM62 matrix. The sequence conservation is represented in shading from white (< 50 % similarity), yellow (50 % similarity) to dark red (100 % identity). Numbering of the alignment is relative to *C. thermophilum* RpL4. The secondary structure of RpL4 as observed in the Acl4•RpL4 crystal structure is illustrated with arrows and rectangles, representing beta-strands (β 1 to β 5) and α -helices (α 1 to α 9), respectively, and colored according to Figure 1a. Gray dots indicate residues that were part of the crystallization construct but were not observed in the final electron density map and thus are presumed to be disordered. Purple dots indicate RpL4^{EXT} residues that were mutated in this study. Residues corresponding to RpL4^{CORE}, RpL4^{LOOP}, and RpL4^{EXT} are highlighted by a yellow, red, and gray bar, respectively.

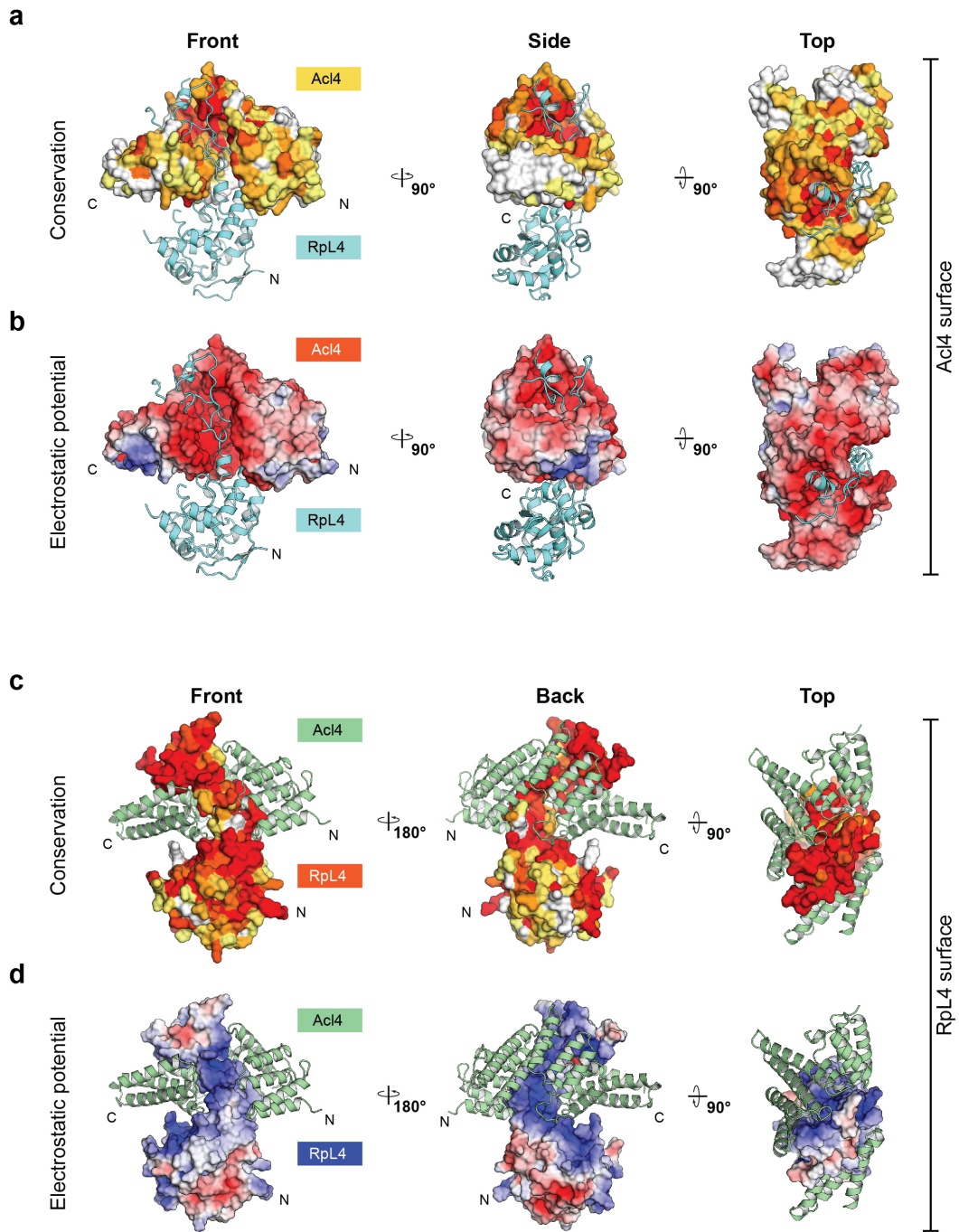


Figure S4. Conservation and electrostatic surface analysis of the Acl4•RpL4 crystal structure

(a) Surface representations of Acl4 colored according to the multi-species sequence alignment shown in Figure S2. RpL4 is shown in cartoon representation and colored in teal. The Acl4•RpL4 complex is shown from the front, side and top. (b) Surface representations of Acl4 colored according to its electrostatic surface potential from $-5 k_B T/e$ (red) to $+5 k_B T/e$ (blue). RpL4 is shown in cartoon representation and colored in teal. (c) Surface representation of RpL4 colored according to the multi-species sequence alignment shown in Figure S3. Acl4 is shown in cartoon representation and colored in green. (d) Surface representations of RpL4 colored according to its electrostatic surface potential from $-5 k_B T/e$ (red) to $+5 k_B T/e$ (blue).

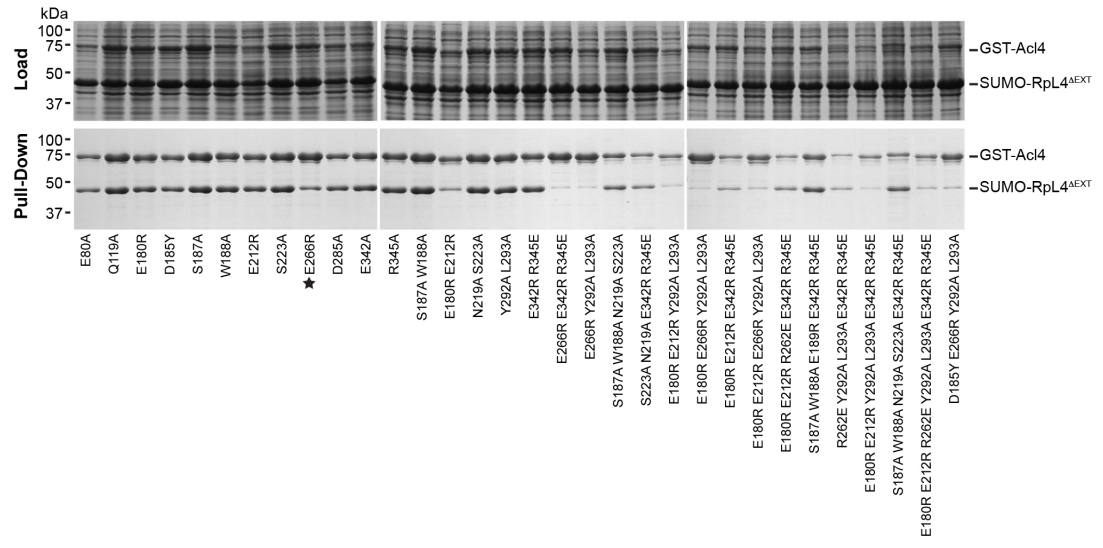


Figure S5. Interaction analysis of *C. thermophilum* Acl4 surface mutations

GST pull-down interaction analysis of His₆-SUMO-RpL4^{ΔEXT} and GST-Acl4 variants. Samples were resolved on SDS-PAGE gels and visualized by Coomassie Brilliant Blue staining. SDS-PAGE gels on top and bottom show the loaded soluble fraction that was incubated with glutathione beads and eluted pulled-down samples, respectively.

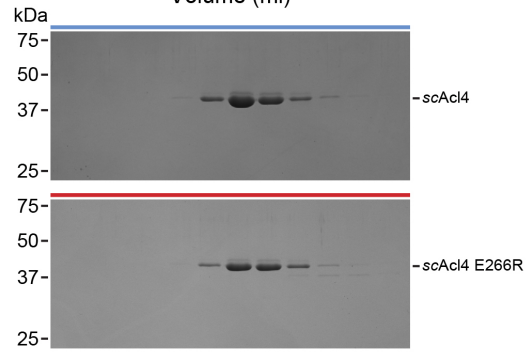
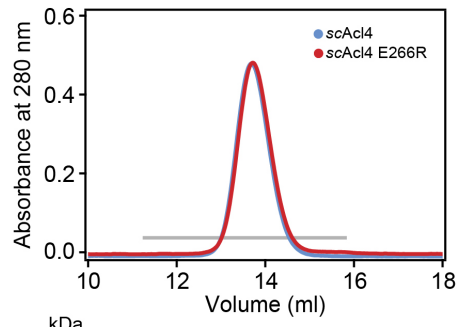
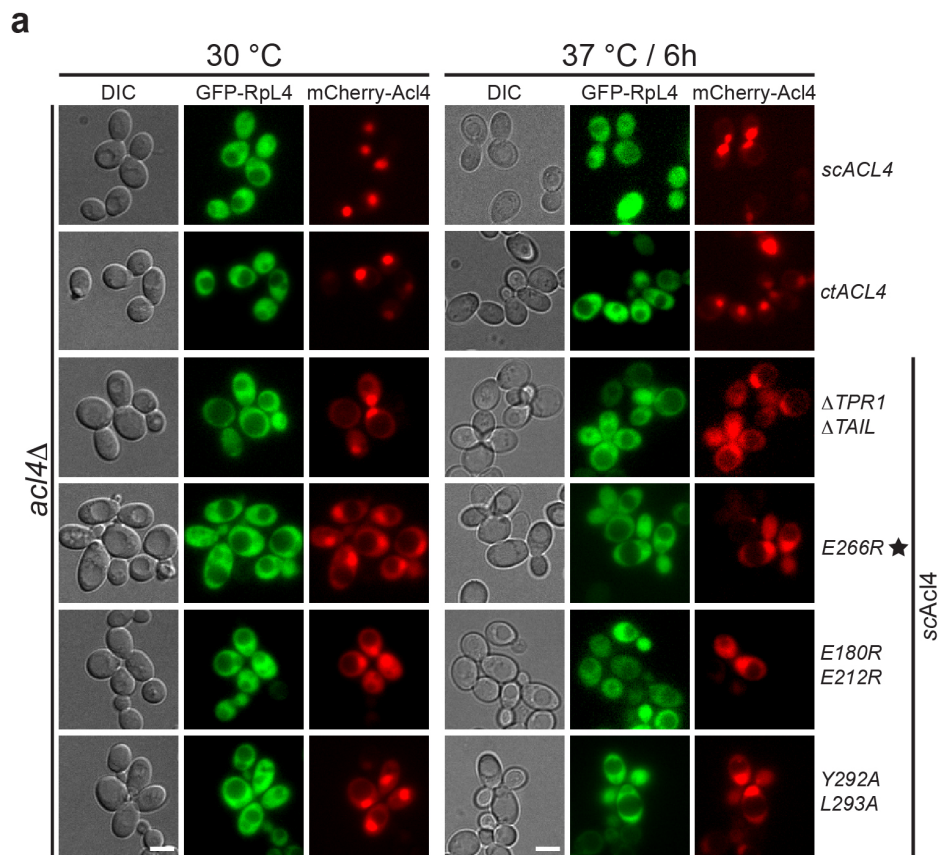


Figure S6. Biochemical analysis of the *scAcl4* E266R mutant

Size exclusion chromatography (SEC) analysis of the *scAcl4* E266R mutant. The absorbance at 280 nm is plotted against the elution volume of a Superdex 200 10/300 GL size exclusion column. Fractions indicated by a gray bar were resolved by SDS-PAGE gel and visualized by Coomassie Brilliant Blue staining.



b Fig. 2g, original Western blot

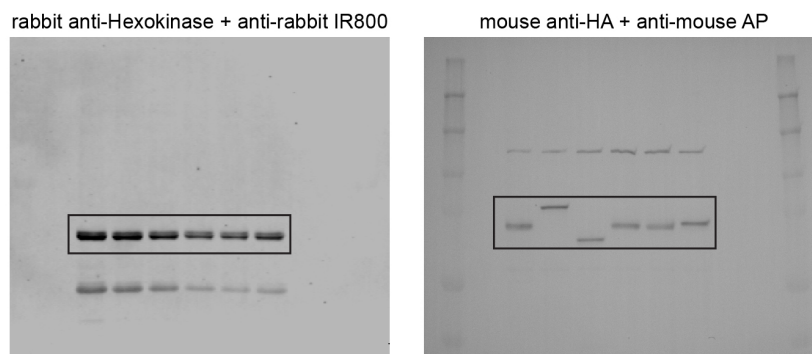


Figure S7. *In vivo* localization analysis of Acl4 and RpL4

(a) Subcellular localization analysis of mCherry-tagged Acl4 variants (red) and eGFP-tagged RpL4 (green) in a *S. cerevisiae acl4Δ* strain. Differential interference contrast (DIC) images are shown in gray scale. The left panel represents yeast grown to mid-log phase at 30 °C, while the right panel shows cells that were grown to mid-log phase at 30 °C and then shifted to 37 °C for 6 hours. Scale bars are 5 μm. (b) Original uncropped Western blots of Figure 2g. Black boxes indicate the cropped sections of the same membrane probed and visualized with different antibodies.

Figure S8. Biochemical analysis of RpL4^{EXT} interaction partners

(a) Size exclusion chromatography (SEC) analysis of the *S. cerevisiae* Acl4•RpL4•Acl4 complex. The absorbance at 280 nm is plotted against the elution volume of a Superdex 200 10/300 GL size exclusion column. (b) Protein sequences of RpL4 from 12 species were aligned and colored as in Figure S3. The consensus sequence of the basic PY-NLS is shown above the alignment. Numbering below the alignment is relative to *C. thermophilum* RpL4. Kap104 and Acl4 binding sites are indicated with black bars. (c) SEC analysis of the Acl4•RpL4•Kap104 complex. (d) SEC analysis of the Acl4•RpL4•Kap- α complex. (e) SEC analysis of a preformed Acl4•RpL4•Kap- α complex incubated with additional Kap104. Fractions indicated by a gray bar were resolved by SDS-PAGE gel and visualized by Coomassie Brilliant Blue staining.

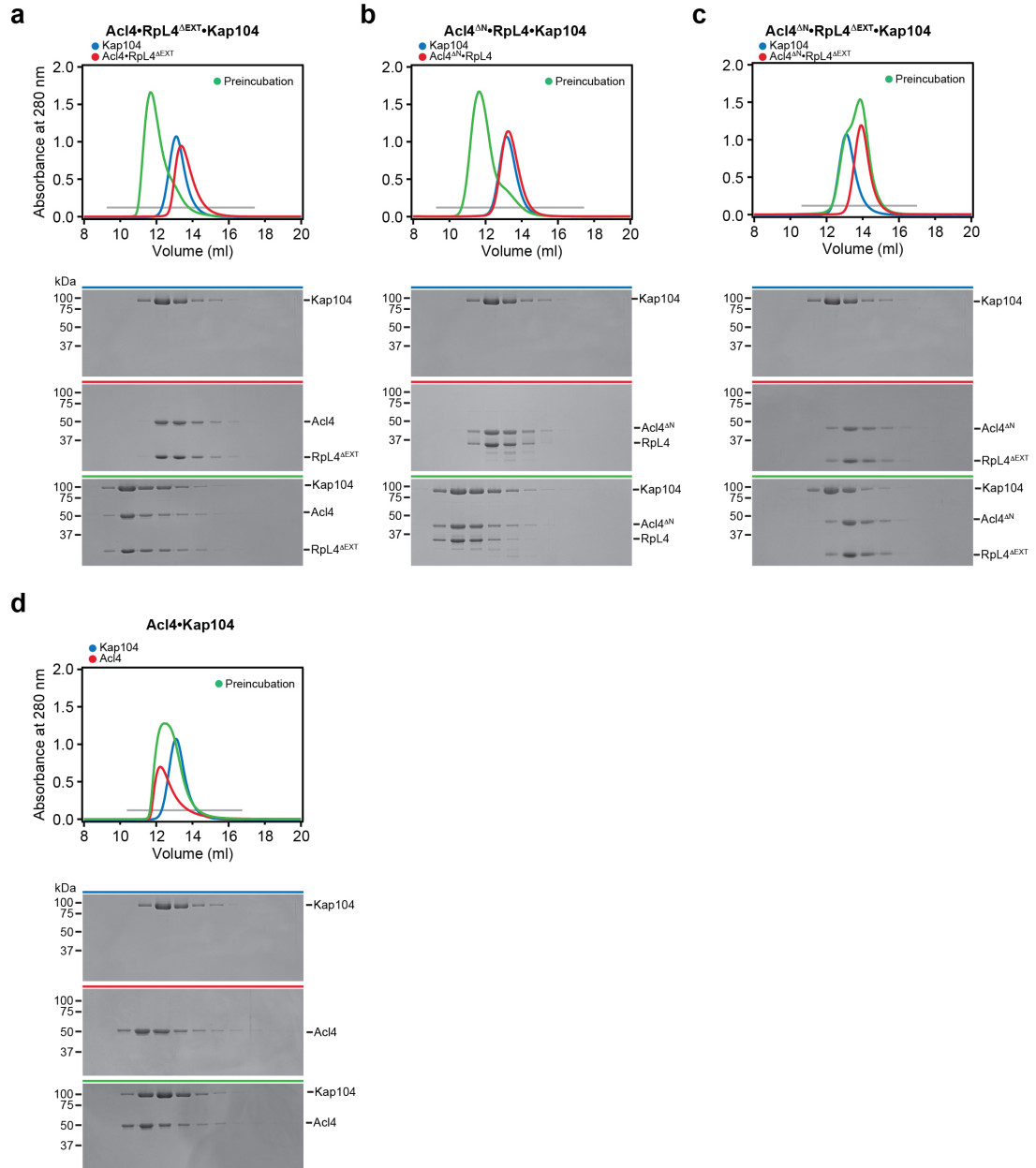


Figure S9. Kap104 interaction with Acl4•RpL4

(a) Size exclusion chromatography (SEC) analysis of the Acl4•RpL4^{ΔEXT}•Kap104 complex. The absorbance at 280 nm is plotted against the elution volume of a Superdex 200 10/300 GL size exclusion column. (b) SEC analysis of the Acl4^{ΔN}•RpL4•Kap104 complex. (c) SEC analysis of the Acl4^{ΔN}•RpL4^{ΔEXT}•Kap104 complex. (d) SEC analysis of Acl4•Kap104. The elution profile and SDS-PAGE gel of Kap104 is included in panels a-d as reference point for Kap104 elution. Fractions indicated by a gray bar were resolved by SDS-PAGE gel and visualized by Coomassie Brilliant Blue staining.

TABLES

Main table

Table 1. Data collection and refinement statistics

Supplemental tables

Table S1. Yeast expression constructs

Table S2: Bacterial expression constructs

Table 1. Data collection and refinement statistics

Data Collection		
Protein	AcI4 ²⁸⁻³⁶¹ •RpL4 ¹⁻²⁷⁷	hsKap104•RpL4 ³⁰⁸⁻³³²
PDB ID	5TQB	5TQC
Synchrotron	SSRL ^a	SSRL ^a
Beamline	12-2	12-2
Space group	P2 ₁ 2 ₁ 2	P2 ₁ 2 ₁ 2
Cell dimensions		
<i>a</i> , <i>b</i> , <i>c</i> (Å)	121.0, 127.9, 42.7	68.6, 130.7, 174.2
α , β , γ (°)	90.0, 90.0, 90.0	90.0, 90.0, 90.0
	<i>Se Peak</i>	<i>Native</i>
Wavelength (Å)	0.9792	1.0000
Resolution (Å)	50.0 – 2.4	50.0 – 3.0
<i>R</i> _{merge} (%) ^b	8.9 (99.0)	9.3 (192.7)
<i>R</i> _{pim} (%) ^b	2.6 (28.5)	2.7 (53.5)
$\langle I \rangle / \langle \sigma I \rangle$ ^b	13.6 (1.9)	20.7 (1.6)
CC _{1/2} ^b	99.9 (89.8)	99.9 (75.7)
Completeness (%) ^b	99.1 (99.1)	99.8 (99.9)
No. of observations	338,722	425,167
No. of unique reflections ^b	49,797 (8,039)	32,119 (5,078)
Redundancy ^b	6.8 (6.6)	13.2 (13.7)
Refinement		
Resolution (Å)	50.0 – 2.4	50.0 – 3.0
No. of reflections	49,767	32,065
No. of reflections test set	2,505 (5.0 %)	1,606 (5.0 %)
<i>R</i> _{work} / <i>R</i> _{free} (%)	19.1 / 22.7	20.8 / 23.8
No. atoms	4,605	6,750
Protein	4,510	6,750
Ligands	39	0
Water	56	0
<i>B</i> -factors		
Protein	73	103
Ligands	87	N/A
Water	60	N/A
RMSD		
Bond lengths (Å)	0.004	0.002
Bond angles (°)	0.7	0.7
Ramachandran plot^c		
Favored (%)	96.7	97.4
Outliers (%)	0.0	0.0
MolProbity		
Clash score ^c	1.98	1.77
MolProbity score ^c	1.17	1.05

^a SSRL, Stanford Synchrotron Radiation Lightsource

^b Highest-resolution shell is shown in parentheses

^c As determined by MolProbity (Davis et al., 2007)

Table S1. Yeast expression constructs

Plasmid	Protein	Residues (Mutations)	Vector	Restriction sites 5', 3'	Selection marker
pRS413-P _{Nop1} -eGFP-scRPL4	scRpL4	1-362	pRS413	BamHI, NotI	<i>HIS3</i>
pRS415-P _{Nop1} -mCherry-sc <i>ACL4</i>	scAcl4	1-387	pRS415	BamHI, NotI	<i>LEU2</i>
pRS415-P _{Nop1} -mCherry-sc <i>acl4</i> Δ TPR1 Δ TAIL	scAcl4	40-372	pRS415	BamHI, NotI	<i>LEU2</i>
pRS415-P _{Nop1} -mCherry-sc <i>acl4</i> E266R ^a	scAcl4	1-387 (E266R; E236R in <i>S. cerevisiae</i>)	pRS415	BamHI, NotI	<i>LEU2</i>
pRS415-P _{Nop1} -mCherry-sc <i>acl4</i> E180R E212R ^b	scAcl4	1-387 (E180R E212R; E131R E164R in <i>S. cerevisiae</i>)	pRS415	BamHI, NotI	<i>LEU2</i>
pRS415-P _{Nop1} -mCherry-sc <i>acl4</i> Y292A L293A ^a	scAcl4	1-387 (Y292A L293A; Y262A L263A in <i>S. cerevisiae</i>)	pRS415	BamHI, NotI	<i>LEU2</i>
pRS415-P _{Nop1} -mCherry-ct <i>ACL4</i>	scAcl4	1-398	pRS415	BamHI, NotI	<i>LEU2</i>
pRS415-P _{Nop1} -HA-mCherry-sc <i>ACL4</i>	scAcl4	1-387	pRS415	BamHI, NotI	<i>LEU2</i>
pRS415-P _{Nop1} -HA-mCherry-sc <i>acl4</i> Δ TPR1 Δ TAIL	scAcl4	40-372	pRS415	BamHI, NotI	<i>LEU2</i>
pRS415-P _{Nop1} -HA-mCherry-sc <i>acl4</i> E266R ^a	scAcl4	1-387 (E266R; E236R in <i>S. cerevisiae</i>)	pRS415	BamHI, NotI	<i>LEU2</i>
pRS415-P _{Nop1} -HA-mCherry-sc <i>acl4</i> E180R E212R ^b	scAcl4	1-387 (E180R E212R; E131R E164R in <i>S. cerevisiae</i>)	pRS415	BamHI, NotI	<i>LEU2</i>
pRS415-P _{Nop1} -HA-mCherry-sc <i>acl4</i> Y292A L293A ^a	scAcl4	1-387 (Y292A L293A; Y262A L263A in <i>S. cerevisiae</i>)	pRS415	BamHI, NotI	<i>LEU2</i>
pRS415-P _{Nop1} -HA-mCherry-ct <i>ACL4</i>	scAcl4	1-398	pRS415	BamHI, NotI	<i>LEU2</i>
pRS415-P _{Nop1} -mCherry ^b	N/A	N/A	pRS415	N/A	<i>LEU2</i>

^aMutants are listed with both *C. thermophilum* and the corresponding *S. cerevisiae* numbering

^b(Sikorski and Hieter, 1989)

Table S2: Bacterial expression constructs

Protein	Residues (Mutations)	Expression Vector	Restriction Sites 5', 3'	N-terminal overhang
<i>ctAcl4</i>	1-398	pET28b-SUMO	BamHI, NotI	S
<i>ctAcl4</i>	1-398	pGEX-6P-1	BamHI, NotI	GMGS
<i>ctAcl4</i>	1-398 (E80A)	pGEX-6P-1	BamHI, NotI	GMGS
<i>ctAcl4</i>	1-398 (Q119A)	pGEX-6P-1	BamHI, NotI	GMGS
<i>ctAcl4</i>	1-398 (D185Y)	pGEX-6P-1	BamHI, NotI	GMGS
<i>ctAcl4</i>	1-398 (E180R)	pGEX-6P-1	BamHI, NotI	GMGS
<i>ctAcl4</i>	1-398 (S187A)	pGEX-6P-1	BamHI, NotI	GMGS
<i>ctAcl4</i>	1-398 (W188A)	pGEX-6P-1	BamHI, NotI	GMGS
<i>ctAcl4</i>	1-398 (E212R)	pGEX-6P-1	BamHI, NotI	GMGS
<i>ctAcl4</i>	1-398 (E266R)	pGEX-6P-1	BamHI, NotI	GMGS
<i>ctAcl4</i>	1-398 (D285A)	pGEX-6P-1	BamHI, NotI	GMGS
<i>ctAcl4</i>	1-398 (E342R)	pGEX-6P-1	BamHI, NotI	GMGS
<i>ctAcl4</i>	1-398 (R345E)	pGEX-6P-1	BamHI, NotI	GMGS
<i>ctAcl4</i>	1-398 (E180R E212R)	pGEX-6P-1	BamHI, NotI	GMGS
<i>ctAcl4</i>	1-398 (S187A W188A)	pGEX-6P-1	BamHI, NotI	GMGS
<i>ctAcl4</i>	1-398 (N219A S223A)	pGEX-6P-1	BamHI, NotI	GMGS
<i>ctAcl4</i>	1-398 (Y292A L292A)	pGEX-6P-1	BamHI, NotI	GMGS
<i>ctAcl4</i>	1-398 (E342R R345E)	pGEX-6P-1	BamHI, NotI	GMGS
<i>ctAcl4</i>	1-398 (E266R Y292A L292A)	pGEX-6P-1	BamHI, NotI	GMGS
<i>ctAcl4</i>	1-398 (E266R E342R R345E)	pGEX-6P-1	BamHI, NotI	GMGS
<i>ctAcl4</i>	1-398 (S187A W188A N219A S223A)	pGEX-6P-1	BamHI, NotI	GMGS
<i>ctAcl4</i>	1-398 (N219A S223A E342R R345E)	pGEX-6P-1	BamHI, NotI	GMGS
<i>ctAcl4</i>	1-398 (E180R E212R Y292A L292A)	pGEX-6P-1	BamHI, NotI	GMGS
<i>ctAcl4</i>	1-398 (E180R E212R E342R R345E)	pGEX-6P-1	BamHI, NotI	GMGS
<i>ctAcl4</i>	1-398 (E180R E266R Y292A L292A)	pGEX-6P-1	BamHI, NotI	GMGS
<i>ctAcl4</i>	1-398 (D185Y E266R Y292A L293A)	pGEX-6P-1	BamHI, NotI	GMGS
<i>ctAcl4</i>	1-398 (E180R E212R E266R Y292A L292A)	pGEX-6P-1	BamHI, NotI	GMGS
<i>ctAcl4</i>	1-398 (E180R E212R R262E E342R R345E)	pGEX-6P-1	BamHI, NotI	GMGS
<i>ctAcl4</i>	1-398 (S187A W188A E189R E342R R345E)	pGEX-6P-1	BamHI, NotI	GMGS
<i>ctAcl4</i>	1-398 (R262E Y292A L293A E342R R345E)	pGEX-6P-1	BamHI, NotI	GMGS
<i>ctAcl4</i>	1-398 (E180R E212R Y292A L292A E342R R345E)	pGEX-6P-1	BamHI, NotI	GMGS
<i>ctAcl4</i>	1-398 (S187A W188A N219A S223A E342R R345E)	pGEX-6P-1	BamHI, NotI	GMGS
<i>ctAcl4</i>	1-398 (E180R E212R R262E Y292A L292A E342R R345E)	pGEX-6P-1	BamHI, NotI	GMGS
<i>ctAcl4</i>	28-398	pET28a-SUMO	BamHI, NotI	S
<i>ctAcl4</i> ^a	28-361	pET28a-SUMO	BamHI, NotI	S
<i>ctAcl4</i>	28-338	pET28a-SUMO	BamHI, NotI	S
<i>scAcl4</i>	1-387	pET28a-SUMO	BamHI, NotI	S
<i>scAcl4</i>	1-387	pGEX-6P-1	BamHI, NotI	GMGS
<i>scAcl4</i> ^b	1-387 (E266R; E236R in <i>S. cerevisiae</i>)	pET28a-SUMO	BamHI, NotI	S
<i>scAcl4</i> ^b	1-387 (E180R E212R; E131R E164R in <i>S. cerevisiae</i>)	pET28a-SUMO	BamHI, NotI	S
<i>scAcl4</i> ^b	1-387 (Y292A L293A; Y262A L263A in <i>S. cerevisiae</i>)	pET28a-SUMO	BamHI, NotI	S
<i>scAcl4</i>	40-372	pGEX-6P-1	BamHI, NotI	GMGS
<i>ctRpL4</i>	1-365	pETDuet1-SUMO	BamHI, NotI	S
<i>ctRpL4</i>	1-365 (K316A, K317A, R321A)	pETDuet1-SUMO	BamHI, NotI	S
<i>ctRpL4</i>	1-365 (R328A)	pETDuet1-SUMO	BamHI, NotI	S
<i>ctRpL4</i>	1-365 (P331A, Y332A)	pETDuet1-SUMO	BamHI, NotI	S
<i>ctRpL4</i>	1-353	pETDuet1-SUMO	BamHI, NotI	S

Protein	Residues (Mutations)	Expression Vector	Restriction Sites 5', 3'	N-terminal overhang
<i>ctRpL4</i>	1-341	pETDuet1-SUMO	BamHI, NotI	S
<i>ctRpL4</i>	1-328	pETDuet1-SUMO	BamHI, NotI	S
<i>ctRpL4</i>	1-311	pETDuet1-SUMO	BamHI, NotI	S
<i>ctRpL4</i>	1-300	pETDuet1-SUMO	BamHI, NotI	S
<i>ctRpL4</i>	1-287	pETDuet1-SUMO	BamHI, NotI	S
<i>ctRpL4</i> ^a	1-277	pETDuet1-SUMO	BamHI, NotI	S
<i>ctRpL4</i>	1-277	pET28a-SUMO	BamHI, NotI	S
<i>ctRpL4</i>	278-365	pET28a-SUMO	BamHI, NotI	S
<i>ctRpL4</i> ^a	308-332	pET28a-SUMO	BamHI, NotI	S
<i>scRpL4</i>	1-362	pETDuet1-SUMO	BamHI, NotI	S
<i>scRpL4</i>	1-276	pET28a-SUMO	BamHI, NotI	S
<i>ctKap104</i>	1-938	pGEX-6P-1	BamHI, NotI	GMGS
<i>ctKap-α</i>	81-506	pET28a-SUMO	BamHI, NotI	S
<i>hsRan</i>	1-216 (Q69L)	pET28a	NdeI, BamHI	GPHM
<i>hsKap104</i> ^a	1-890 (337-367 replaced by GGSGGSG)	pGEX-6P-1	BamHI, NotI	GMGS

^aConstructs that were used for crystallization of Acl4²⁸⁻³⁶¹•RpL4¹⁻²⁷⁷ and *hsKap104*¹⁻⁸⁹⁰•RpL4³⁰⁸⁻³³²

^bMutants are listed with both *C. thermophilum* and the corresponding *S. cerevisiae* numbering

REFERENCES

- Adams, P.D., Afonine, P.V., Bunkoczi, G., Chen, V.B., Davis, I.W., Echols, N., Headd, J.J., Hung, L.W., Kapral, G.J., Grosse-Kunstleve, R.W., *et al.* (2010). PHENIX: a comprehensive Python-based system for macromolecular structure solution. *Acta Crystallogr D* 66, 213-221.
- Bailey, S. (1994). The Ccp4 Suite - Programs for Protein Crystallography. *Acta Crystallogr D* 50, 760-763.
- Baker, N.A., Sept, D., Joseph, S., Holst, M.J., and McCammon, J.A. (2001). Electrostatics of nanosystems: application to microtubules and the ribosome. *Proceedings of the National Academy of Sciences of the United States of America* 98, 10037-10041.
- Barton, G.J. (1993). ALS-CRIP: a tool to format multiple sequence alignments. *Protein engineering* 6, 37-40.
- Ben-Shem, A., Garreau de Loubresse, N., Melnikov, S., Jenner, L., Yusupova, G., and Yusupov, M. (2011). The structure of the eukaryotic ribosome at 3.0 Å resolution. *Science* 334, 1524-1529.
- Bricogne, G., Vonrhein, C., Flensburg, C., Schiltz, M., and Paciorek, W. (2003). Generation, representation and flow of phase information in structure determination: recent developments in and around SHARP 2.0. *Acta Crystallogr D* 59, 2023-2030.
- Calvino, F.R., Kharde, S., Ori, A., Hendricks, A., Wild, K., Kressler, D., Bange, G., Hurt, E., Beck, M., and Sinning, I. (2015). Symportin 1 chaperones 5S RNP assembly during ribosome biogenesis by occupying an essential rRNA-binding site. *Nature communications* 6, 6510.
- Davis, I.W., Leaver-Fay, A., Chen, V.B., Block, J.N., Kapral, G.J., Wang, X., Murray, L.W., Arendall, W.B., 3rd, Snoeyink, J., Richardson, J.S., *et al.* (2007). MolProbity: all-atom contacts and structure validation for proteins and nucleic acids. *Nucleic acids research* 35, W375-383.

- Eisinger, D.P., Dick, F.A., Denke, E., and Trumpower, B.L. (1997). SQT1, which encodes an essential WD domain protein of *Saccharomyces cerevisiae*, suppresses dominant-negative mutations of the ribosomal protein gene QSR1. *Molecular and cellular biology* *17*, 5146-5155.
- Emsley, P., and Cowtan, K. (2004). Coot: model-building tools for molecular graphics. *Acta Crystallogr D* *60*, 2126-2132.
- Fromont-Racine, M., Senger, B., Saveanu, C., and Fasiolo, F. (2003). Ribosome assembly in eukaryotes. *Gene* *313*, 17-42.
- Gorenstein, C., and Warner, J.R. (1977). Synthesis and turnover of ribosomal proteins in the absence of 60S subunit assembly in *Saccharomyces cerevisiae*. *Molecular & general genetics : MGG* *157*, 327-332.
- Hoelz, A., Nairn, A.C., and Kuriyan, J. (2003). Crystal structure of a tetradecameric assembly of the association domain of Ca²⁺/calmodulin-dependent kinase II. *Molecular cell* *11*, 1241-1251.
- Holzer, S., Ban, N., and Klinge, S. (2013). Crystal structure of the yeast ribosomal protein rpS3 in complex with its chaperone Yar1. *Journal of molecular biology* *425*, 4154-4160.
- Janke, C., Magiera, M.M., Rathfelder, N., Taxis, C., Reber, S., Maekawa, H., Moreno-Borchart, A., Doenges, G., Schwob, E., Schiebel, E., *et al.* (2004). A versatile toolbox for PCR-based tagging of yeast genes: new fluorescent proteins, more markers and promoter substitution cassettes. *Yeast* *21*, 947-962.
- Jeanmougin, F., Thompson, J.D., Gouy, M., Higgins, D.G., and Gibson, T.J. (1998). Multiple sequence alignment with Clustal X. *Trends in biochemical sciences* *23*, 403-405.
- Johnson, A.W. (2014). Ribosomes: lifting the nuclear export ban. *Current biology : CB* *24*, R127-129.
- Kabsch, W. (2010). Xds. *Acta Crystallogr D* *66*, 125-132.

Koch, B., Mitterer, V., Niederhauser, J., Stanborough, T., Murat, G., Rechberger, G., Bergler, H., Kressler, D., and Pertschy, B. (2012). Yar1 protects the ribosomal protein Rps3 from aggregation. *The Journal of biological chemistry* 287, 21806-21815.

Kressler, D., Bange, G., Ogawa, Y., Stjepanovic, G., Bradatsch, B., Pratte, D., Amlacher, S., Strauss, D., Yoneda, Y., Katahira, J., *et al.* (2012). Synchronizing nuclear import of ribosomal proteins with ribosome assembly. *Science* 338, 666-671.

Kressler, D., Hurt, E., and Bassler, J. (2010). Driving ribosome assembly. *Biochimica et biophysica acta* 1803, 673-683.

Lafontaine, D.L. (2010). A 'garbage can' for ribosomes: how eukaryotes degrade their ribosomes. *Trends in biochemical sciences* 35, 267-277.

Lafontaine, D.L. (2015). Noncoding RNAs in eukaryotic ribosome biogenesis and function. *Nature structural & molecular biology* 22, 11-19.

Lee, B.J., Cansizoglu, A.E., Suel, K.E., Louis, T.H., Zhang, Z., and Chook, Y.M. (2006). Rules for nuclear localization sequence recognition by karyopherin beta 2. *Cell* 126, 543-558.

Maertens, G.N., Cook, N.J., Wang, W., Hare, S., Gupta, S.S., Oztop, I., Lee, K., Pye, V.E., Cosnefroy, O., Snijders, A.P., *et al.* (2014). Structural basis for nuclear import of splicing factors by human Transportin 3. *Proceedings of the National Academy of Sciences of the United States of America* 111, 2728-2733.

Mossessova, E., and Lima, C.D. (2000). Ulp1-SUMO crystal structure and genetic analysis reveal conserved interactions and a regulatory element essential for cell growth in yeast. *Molecular cell* 5, 865-876.

Pausch, P., Singh, U., Ahmed, Y.L., Pillet, B., Murat, G., Altegoer, F., Stier, G., Thoms, M., Hurt, E., Sinning, I., *et al.* (2015). Co-translational capturing of nascent ribosomal proteins by their dedicated chaperones. *Nature communications* 6, 7494.

Pillet, B., Garcia-Gomez, J.J., Pausch, P., Falquet, L., Bange, G., de la Cruz, J., and Kressler, D. (2015). The Dedicated Chaperone Acl4 Escorts Ribosomal Protein Rpl4 to Its Nuclear Pre-60S Assembly Site. *PLoS genetics* *11*, e1005565.

Roberts, P., Moshitch-Moshkovitz, S., Kvam, E., O'Toole, E., Winey, M., and Goldfarb, D.S. (2003). Piecemeal microautophagy of nucleus in *Saccharomyces cerevisiae*. *Molecular biology of the cell* *14*, 129-141.

Sheldrick, G.M. (2008). A short history of SHELX. *Acta crystallographica Section A, Foundations of crystallography* *64*, 112-122.

Sikorski, R.S., and Hieter, P. (1989). A system of shuttle vectors and yeast host strains designed for efficient manipulation of DNA in *Saccharomyces cerevisiae*. *Genetics* *122*, 19-27.

Soniat, M., Sampathkumar, P., Collett, G., Gizzi, A.S., Banu, R.N., Bhosle, R.C., Chamala, S., Chowdhury, S., Fiser, A., Glenn, A.S., *et al.* (2013). Crystal structure of human Karyopherin beta2 bound to the PY-NLS of *Saccharomyces cerevisiae* Nab2. *Journal of structural and functional genomics* *14*, 31-35.

Stelter, P., Huber, F.M., Kunze, R., Flemming, D., Hoelz, A., and Hurt, E. (2015). Coordinated Ribosomal L4 Protein Assembly into the Pre-Ribosome Is Regulated by Its Eukaryote-Specific Extension. *Molecular cell* *58*, 854-862.

Sung, M.K., Porras-Yakushi, T.R., Reitsma, J.M., Huber, F.M., Sweredoski, M.J., Hoelz, A., Hess, S., and Deshaies, R.J. (2016). A conserved quality-control pathway that mediates degradation of unassembled ribosomal proteins. *eLife* *5*.

Warner, J.R. (1977). In the absence of ribosomal RNA synthesis, the ribosomal proteins of HeLa cells are synthesized normally and degraded rapidly. *Journal of molecular biology* *115*, 315-333.

Yaffe, M.P., and Schatz, G. (1984). Two nuclear mutations that block mitochondrial protein import in yeast. *Proc Natl Acad Sci U S A* *81*, 4819-4823.

Zhang, Y., Wolfle, T., and Rospert, S. (2013). Interaction of nascent chains with the ribosomal tunnel proteins Rpl4, Rpl17, and Rpl39 of *Saccharomyces cerevisiae*. *The Journal of biological chemistry* 288, 33697-33707.